VERITAS, 1ES 1218 + 30.4 and the Extragalactic Background Light

Luis Valcárcel
Centre for High-Energy Physics
Department of Physics
McGill University
Montréal, Québec
Canada

November 11, 2008

A Thesis submitted to
McGill University
in partial fulfillment of the requirements for the degree of
Doctor of Philosophy

To my science teachers,
Mr. Louis Courcelles,
Mr. Boris Plante,
Mr. Jacques Beaulieu.
It is because of you that I like physics.
Your teaching remains an inspiration for all the work that I do.

Contents

List of Figures

Note: all figures of the camera pixels are generated with *vaDisplay*, the analysis viewer of the *VEGAS* analysis chain.

Abstract

Blazars are extremely powerful astrophysical objects that emit radiation up to the TeV regime. 1ES 1218 + 30.4 is one such object. It was observed from December 20, 2006, to March 20, 2007, by the γ-ray experiment VERITAS (Very Energetic Radiation Imaging Telescope Array System), an array of four 12-m atmospheric Čerenkov telescopes located in southern Arizona. These observations are analyzed and 1ES 1218 + 30.4 is detected with high significance. The observed spectrum is also found to be in agreement with previous results and is here measured to be $(2.2 \pm 0.3_{\mathrm{stat.}} \pm 0.4_{\mathrm{sys.}}) \times 10^{-12} \mathrm{cm}^{-2}\,\mathrm{s}^{-1}\,\mathrm{TeV}^{-1} (\frac{E}{0.8\,\mathrm{TeV}})^{-2.8 \pm 0.2_{\mathrm{stat.}} \pm 0.2_{\mathrm{sys.}}}$ in the 350 GeV to 1.9 TeV energy range. The spectrum is used to constrain the extragalactic background light by unfolding the intrinsic spectrum for many possibilities and keeping only the ones that lead to physically permissible intrinsic spectra. The direct measurements of the extragalactic background light at near infrared wavelengths are challenged by the limits derived in this work.

Résumé

Les blazars sont des objets astrophysiques extrêmement puissants qui émettent de la radiation jusqu'au régime TeV. 1ES 1218 + 30.4 est l'un de ces objets. Il a été observé du 20 décembre 2006 au 20 mars 2007 par le détecteur de rayons γ VERITAS (Very Energetic Radiation Imaging Telescope Array System), un réseau de quatre télescopes de 12 m situé au sud de l'Arizona, capables d'imager la lumière Čerenkov atmosphérique. Ces observations sont analysées et 1ES 1218 + 30.4 est détecté de manière significative. Le spectre observé est mesuré à $(2.2 \pm 0.3_{\mathrm{stat.}} \pm 0.4_{\mathrm{sys.}}) \times 10^{-12} \mathrm{cm}^{-2}\,\mathrm{s}^{-1}\,\mathrm{TeV}^{-1} (\frac{E}{0.8\,\mathrm{TeV}})^{-2.8 \pm 0.2_{\mathrm{stat.}} \pm 0.2_{\mathrm{sys.}}}$ dans la bande 350 GeV à 1.9 TeV. Le spectre est utilisé pour contraindre l'arrière-plan lumineux extragalactique en recouvrant le spectre intrinsèque à la source pour de nombreuses possibilités et en ne gardant que celles qui mènent à un spectre intrinsèque physiquement admissible. Les mesures directes de l'arrière-plan lumineux extragalactique aux longueurs d'onde du proche infrarouge sont mises à l'épreuve par les limites calculées dans ce travail.

Acknowledgments

This thesis is the result of long years of efforts and its writing could not have been possible without the help of many people whom I would like to thank.

First, I would like to thank my supervisor, Professor D. S. Hanna, for teaching me the rigor demanded by experimental work. He has always been available when I had questions and he has always had something to suggest for my work. He has also been very patient at times when I allowed myself to delay the submission of reports, so that I could scratch a little deeper on topics that interested me more, be them related to physics interest, mathematical tools or computer knowledge. With this extra time, I reached the understanding that I was seeking and that I deemed satisfactory.

Next, I would like to thank the other members of our group, current or past. Thanks to Professor K. Ragan who acted like a substitute supervisor when Prof. Hanna was away. His numerous questions at the group meetings have always enlightened the discussion. Special thanks go to Postdoc J. Kildea; he taught me a lot of what I know about γ-ray astrophysics. Postdocs G. Maier and P. Cogan were also important in answering some of the difficult questions that I had. Thanks to my colleagues, J.-P. Gagnon for showing me how to use the night-sky background instrument, A. MacLeod for help with gain measurements for this instrument, M. McCutcheon for help in making the night-sky background measurement during long cold nights and for incorporating my programs into the DQM, R. Guenette, M. Bautista and A. McCann for useful discussions about the experiment.

Many people from the VERITAS collaboration have also been of great help: J. Holder for lots of information and good times while observing, P. Fortin for advice on analysis, A. Falcone for teaching me the "art" of mirror mounting, T. C. Weekes, K. Gibbs, G. Gardner and all the personnel from the Fred Lawrence Whipple Observatory for making it possible for me to work on the telescopes.

People from Université de Montréal, Université Laval and the Observatoire du Mont-Mégantic have been very kind in showing me how to use the SIMON infrared instrument and analyze its data. P. Voyer, L. Albert, É. Artigau, B. Malenfant and G. Turcotte have helped in this respect. This experience diversified my knowledge of experimental astrophysics.

Thanks to the supporting staff of the physics department, P. Mercure and J. Gallego for technical support with the computers, E. Del Campo and S. Kecani for their

help in the machine shop, S. Biunno, M. Beauchamp and M. Della Neve for access to restricted parts of the Rutherford Physics building and for loan of equipment during early testing with the NSB instrument, P. Domingues, E. Shearon, S. Vieira, D. Koziol and L. Decelles for the paper work and special thanks to Mike for keeping my working environment clean and for his good advice.

Lastly, let me thank my friends and family. Thanks to my mother C. Gélinas and my father R. Valcárcel for teaching me the value of patience and transmitting me the desire to understand and to do things well. Thanks to my brother C. Valcárcel and to my life long friends C. Prévost, J.-F. Péloquin and J.-N. Morissette; without your moral support, I could not have brought this project to an end. Thanks to Ajanã, Peninha and everyone from Capoeira for the liberation of the mind that you provided through the art/sport, and especially to Poeta and Cholitinha for their encouragements and interest in my research. But, most of all, thanks to my girlfriend Dr. Josianne Lefebvre who has always been there for me, providing encouragements and help all along the way, especially during the last few weeks of the writing of this thesis.

Finally, thanks to McGill University, FQRNT and NSERC for providing financial support, which made this study possible.

Addendum for the final submission:
Thanks to my PhD examination committee, Prof. D. S. Hanna, Prof. K. Ragan, Prof. B. Rutledge, Prof. T. Webb and Prof. V. Zacek, and to my external examiner, Dr. J. McEnery. Your questions, criticism and comments have been well received and have been used to improve the final copy of this document.

Statement of Original Contributions

Over the course of his doctoral studies, the author of this thesis contributed in many different ways to the success of the VERITAS experiment and of its analysis.

He performed field work by traveling 13 times to Arizona where he undertook several construction, observation and maintenance shifts. Specifically, he participated in the building of the telescopes by installing a large fraction of the mirror mounts and mirror facets (see section 5.2), and helped perform regular and bias alignment of these. He conducted observations at both the Whipple 10-m telescope and the VERITAS array during its deployment (see section 5.5). He also acted as a daytime observer to fix the problems encountered by the regular observers during the night; as such he performed maintenance on the laser system (see section 5.6), measured the camera rotations and operated the charge injection system (see section 5.4.2). Most importantly, he measured the night-sky background at various sites in order to provide simulations with realistic parameters and to help in the decision to relocate the VERITAS array or not (see appendix C).

On the analysis side, he wrote more than 23 700 lines of code. The major softwares that he wrote include part of a photometry analysis for infrared data taken during 2 missions at Québec's Mont-Mégantic, a Monte Carlo analysis of the night-sky background instrument (see appendix C), a suite of five programs that now forms the basis of McGill's daily data quality monitoring products (see section 5.6 and appendix D), optimization scripts for the analysis cuts (see section 6.7), and an independent implementation of an algorithm that constrains the extragalactic background light (see section 7.2). Analysis of Whipple 10-m and of VERITAS data was also performed using the collaboration's official analysis packages (see section 7.1).

The author communicated results from his research at 3 student workshops, including one that he helped organize, at 2 of the Observatoire du Mont-Mégantic member's annual meeting, at the CASCA 2005 meeting, at 4 intra-departmental talks and at 3 collaboration meetings.

Of the material presented in this thesis, chapter 7 contains the most important results, which represent the author's own work. It presents an independent analysis of the 1ES 1218 + 30.4 VERITAS data and a derivation of an upper limit on the extragalactic background light from the spectrum of this source, which had never been done successfully before.

Foreword

The author tried to make the difficult subject of this thesis as comprehensible as possible in the hope of giving a chance to the uninitiated reader and of helping other graduate students understand more rapidly concepts that have evaded him for a long time. He has made special effort to present the material in as accessible a format as possible. To this end, and for purposes of clarity, when a **term is being defined** in the text, it is typeset in boldface and green color. When a variable is being defined, the symbols := or =: are used; the position of the colon indicates if it is the left or the right hand side term that is being defined. The **assumptions** used in the derivation of results have been clearly indicated by writing them in a blue color. Also, care has been taken to hyperlink the references when a web version was available. Hence, the reader curious about a reference only needs to click on its [ADS] or [LINK] icon, in the bibliography section of the pdf document, to view an online version, saving him the trouble to search for it himself.

It is the author's sincere hope that those who will read this thesis will learn something in the process. Enjoy the reading!

VERITAS, 1ES 1218 + 30.4 and the Extragalactic Background Light

INTRODUCTION

1

Introduction

At some places in the Universe, a very energetic radiation is emitted. So energetic in fact that it does not fit within the ordinary picture of the electromagnetic spectrum. In order to describe it, the scale must be extended by 15 orders of magnitude as shown in figure 1.1; this is the so called **γ-ray** part of the spectrum. The energies that are of particular interest in this thesis are those at the TeV (10^{12} eV) scale, the very-high-energy (VHE) regime. This is so energetic that this radiation cannot have been produced from thermal processes like those involved in the shining of ordinary stars. This radiation is more extreme; it is the result of violent phenomena, explosions and high-speed collisions of particles. The existence of these processes, that are part of what is called the **relativistic Universe** because their description requires Einstein's theories of relativity, is particularly interesting to particle physicists. It allows them to study fundamental physics at energies that they otherwise could not reach with their man-made accelerators.

In the searches for the origin of these energetic γ rays, it was found that a particular class of extraordinary astrophysical objects, called **blazars**, were particularly prolific at generating them. Of the γ rays that leave a blazar and head toward the Earth, not all survive the trip. Along their way lies the **extragalactic background light**, a photon field of low energy that permeates the intergalactic space. The γ rays that happen to collide with one of the infrared photons from this field have chances of mutating into an electron and a positron pair. Other than that, there are no other obstacles to keep them from reaching the Earth. They pass right through dust particles and are not deflected by electromagnetic fields. Once they have reached their desti-

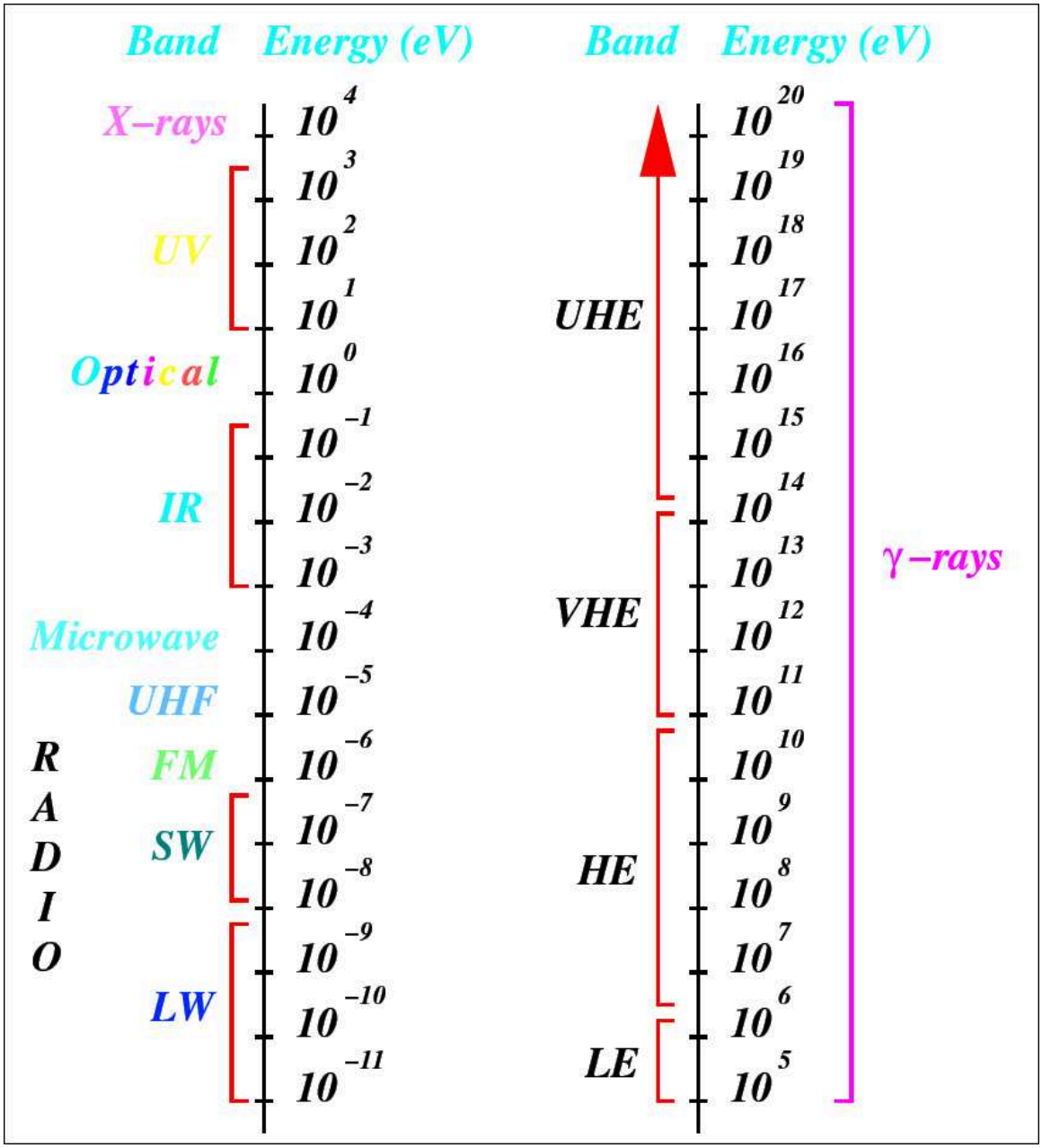

Figure 1.1: Electromagnetic spectrum. The band corresponding to γ rays takes as many orders of magnitude as all the other bands of the spectrum combined. Figure taken from [1].

nation they create the most amazing fireworks in interacting with the atmosphere.

If we had supernatural eyes capable to react to flashes of light of a few nanoseconds of duration and sensitive to UV wavelengths, then our view of the night sky would be filled with a perpetual display of these fireworks. A γ ray (or other very energetic cosmic particle) that enters the atmosphere is absorbed by it in a very peculiar way. It first interacts with the nucleus of one of the atmosphere's atoms to create an energetic electron/positron pair, whose components radiate energetic photons that may themselves create more energetic pairs of particles. A cascading effect is produced that forms an **extensive air shower** in the sky. The particles in the shower emit a faint mostly bluish-UV light. This induced atmospheric shower would then look just like a gigantic super fast birthday sparkler, with the difference that the sparks would mostly be going down in a narrow cone around the original γ-ray direction. Although the sparks begin at the top of the shower and make their way down, we would actually not see it that way. This is because the highly energetic particles in the shower travel faster than light in the atmosphere (incidently, it is this behaviour that makes them emit the bluish-UV light, this is called the **Čerenkov radiation**). Hence, they have time to go down the shower before the light emitted at the top reaches our supernatural eye. In fact, light emitted at the bottom is received almost simultaneously as the one emitted at the top. The difference in time is only a few nanoseconds. Thus the sparkler would appear to be almost instantaneously lighted all along its length and last very shortly.

A group of scientists from around the world, astro and particle physicists, became interested in seeing these showers and use them to study the γ rays from blazars and other exotic objects. They united with the goal of building supernatural eyes to see nature's biggest sparklers. They formed a collaboration, now comprising more than 120 members from more than 20 universities and institutes, that they called VERITAS, an acronym for Very Energetic Radiation Imaging Telescope Array System which is also both the motto for Harvard University[1] and the Latin word for *truth*.

[1]The Harvard-Smithsonian Center for Astrophysics is one of the VERITAS associated institutions.

They set out to build some of the largest telescopes on the planet, an array of four 12-m diameter telescopes located under the clear skies of southern Arizona in the hope of unveiling some of the *truth* behind the mysterious γ rays. The system they built is schematized in figure 1.2.

It is about this, the blazars, their γ rays, the interactions that they have with the extragalactic background light, the way in which we detect and recognize them in a sea of background showers due to other particles that make the problem feel like finding a needle in a haystack, that this thesis is concerned.

1.1 Thesis Outline

Over the course of this thesis, the reader will learn about the many different techniques used to detect γ rays, from satellite mounted experiments to imaging atmospheric Čerenkov telescope arrays. The history of the developments realized in these fields will also be highlighted (chapter 4). The VERITAS system will of course be described in greater detail; chapter 5 will be entirely devoted to it. This will show what remarkable apparatus has been built in order to "see" these gigantic extensive air shower. Then, chapter 6 will discuss how the data are analyzed, *i.e.* how the showers are reconstructed and parameterized so that they can be classified as γ ray or cosmic ray, and how statistical tools are used to extract conclusions from their counts. But before diving into the subject of experimental detection of γ rays, let us start by giving some of the scientific motivations for studying them. Chapter 2 gives the necessary theoretical background needed to understand blazars, while chapter 3 highlights the effect that the extragalactic background light can have on their TeV radiation and introduces the problem associated with the poor knowledge that we have of it. The thesis will conclude in chapter 7 by using the VERITAS observations of 1ES 1218 + 30.4, a blazar detected by the MAGIC collaboration (another γ-ray group), to confirm the detection of this source and to put a limit on the extragalactic background light.

Although the author found it more appropriate to describe the theory prior to the

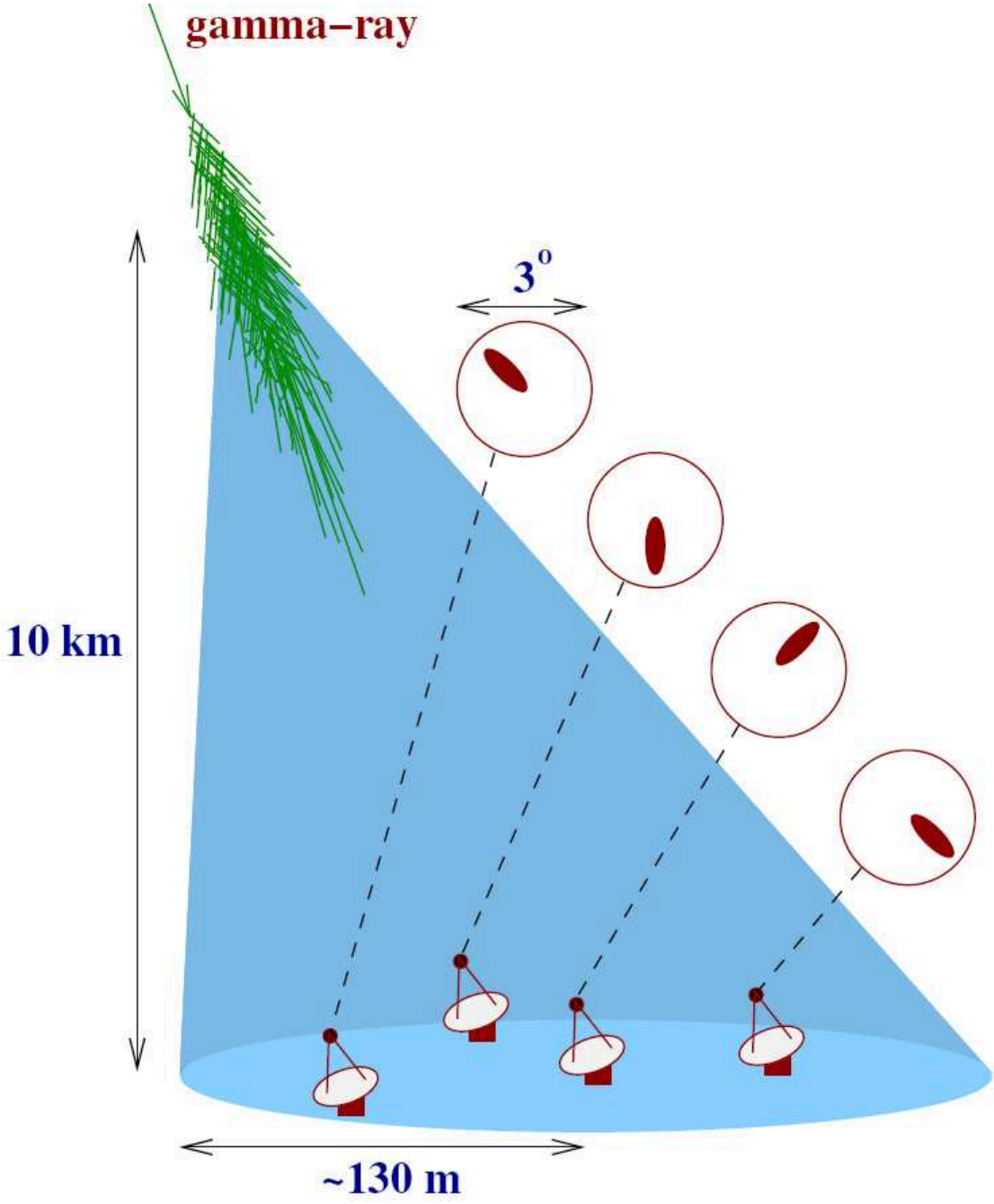

Figure 1.2: Array of imaging atmospheric Čerenkov telescopes. The telescopes capture an image of the extensive air shower from the Čerenkov light that it produces. Figure taken from [1].

description of the experiment, the first two chapters might be a little demanding for the non-specialized reader. It might therefore be more interesting for them to read chapters 4 and 5 first, which are probably more accessible.

Part I

THEORY

2

Blazar AGNs and 1ES 1218 + 30.4

Since very-high-energy astronomy started, many different types of astrophysical objects were found to emit γ rays in this band. Among these, one finds at least 5 binaries, 1 Wolf-Rayet binary, 6 shell-type supernova remnants, 8 pulsar wind nebulae, 19 blazars, 1 giant radio galaxy and many unidentified objects [2]. It is thus apparent that the blazar class of object is the most represented one in the TeV sky. To understand what blazars are and how they can emit such energetic radiation, the general class of active galactic nuclei must first be introduced. Then, after a general discussion about blazars, the main characteristics of 1ES 1218 + 30.4, the blazar which forms the center of this study, will be described.

2.1 Active Galactic Nuclei

Of the extragalactic objects observed at various wavelengths in the past, some were found to have extreme properties incompatible with those of other, normal, galaxies and presenting hints of non-thermal processes being at work to explain their atypical emission. These objects, which seemed to be more "active" than others and which seem to be tied to some phenomenon occurring at the center of some galaxies, have been called **Active Galactic Nuclei**, or **AGN** for short. Although there is now a paradigm to explain the AGN phenomenon, which will be described below, there is not yet a total confirmation of it and the best way to define AGNs is to list their observational properties, which are different from those of normal galaxies [3]. Some of the observables that could make an object part of the AGN class include:

- a **great luminosity**, that can go up to 10^{48} erg/s [1], whereas a typical galaxy has a luminosity around 10^{44} erg/s [2];
- a **very small angular size** that could imply that the huge luminosity comes from a volume $\ll 1\,\mathrm{pc}^3$ [3] (often, the AGN outshines its host galaxy, but when a host can be resolved, the AGN looks like a very bright point at its center);
- a radiation spectrum that spans a **very broad range of frequencies**, sometimes from radio to γ rays, and that cannot be explained from thermal processes;
- **strong emission lines**, sometimes narrow, sometimes very broad implying motions of several thousands of km/s;
- **linear polarization** that can be strong, although it is generally weak, but still stronger than in most stars;
- **bright radio emission**, sometimes compact, sometimes extended on enormous scales (hundreds of kpc) in the form of jets emanating from a central galaxy and terminated by double lobe features, which shows strong evidence for non-stellar activity;
- **strong variability** often correlated with strong polarization, compact radio structure and strong high-energy emission.

Since not all AGN exhibit all these properties simultaneously, sub-classes of AGNs have been formed to characterize the general groupings observed. Some classes are more the result of the historical context in which they were defined than the result of true physical differences. Over the years, some of these erroneous classifications have been resolved. A common way of organizing the different AGNs is shown in figure 2.1. As these groupings evolved to the current form, it was observed that some of the different classes could probably be explained by similar phenomena, only they

[1] $1\,\mathrm{erg} = 1\times10^{-7}\,\mathrm{J}$.
[2] There are also some AGNs with luminosities of a few percent that of typical galaxies.
[3] $1\,\mathrm{pc} = 3.086\times10^{16}\,\mathrm{m} = 3.262\,\mathrm{ly}$.

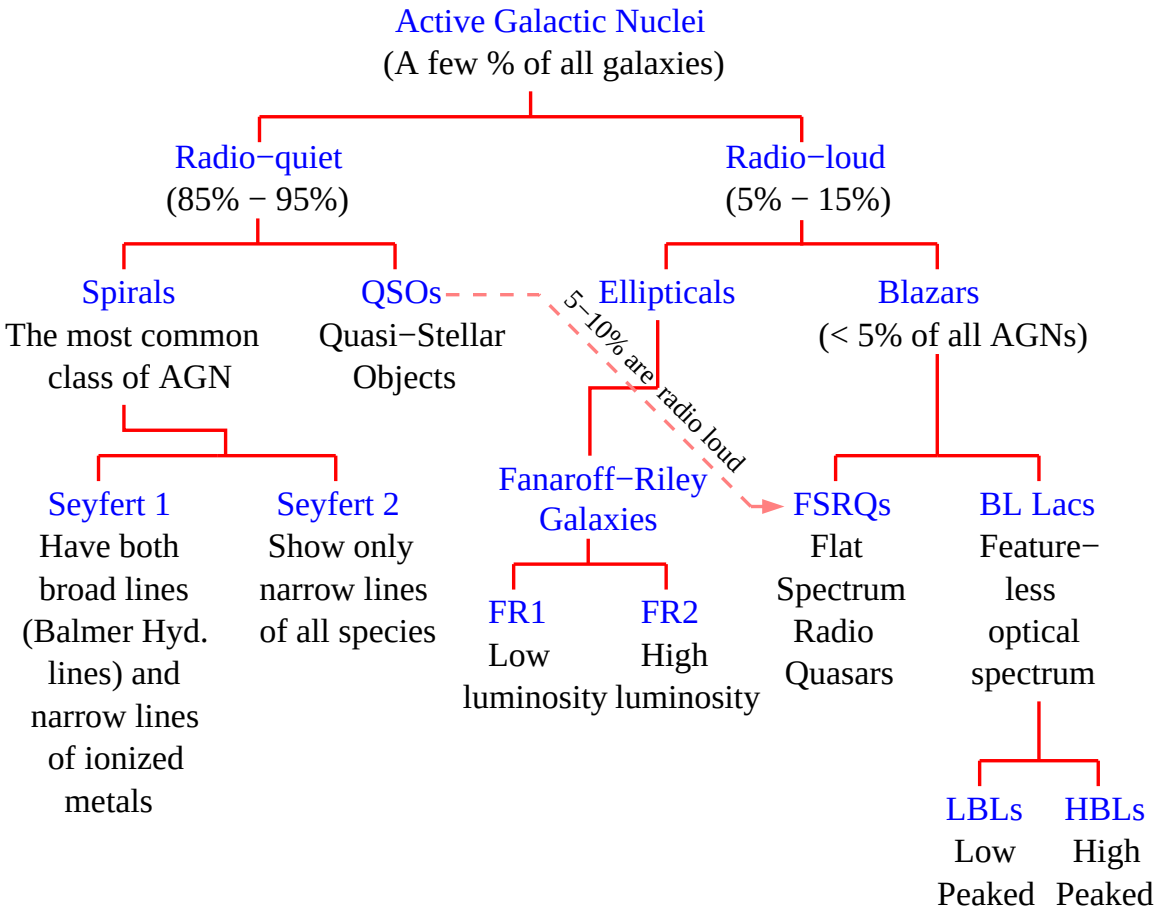

Figure 2.1: Classification of AGNs. Figure taken from [4].

appeared different when viewed under different conditions. Eventually, a generic model emerged to describe all the different AGNs [5]. It is shown in figure 2.2. In this picture, the incredible power of AGNs comes from strong-field relativistic gravity physics. At their center lies a super-massive black hole (10^7-$10^9\,M_\odot$ [4], radius $\sim 3\times10^{11}$ m) onto which material falls, gaining large amounts of kinetic energy that powers an accretion disk ($\sim10^{12}$ m) and heats it to UV wavelengths. Although it is still unclear exactly how they are formed, giant focused beams ($\sim10^{15}$-10^{22} m), called **jets**, of relativistically moving matter and energy, emerge normal to the plane of the disk, aligned with the rotation axis of the black hole[5]. Near the central black hole ($\sim10^{14}$ m) are clouds of fast moving material and farther out ($\sim10^{16}$-10^{18} m) are more clouds of colder material. Surrounding the accretion disk is a big dust torus ($\sim10^{15}$ m). Since the model is not spherically symmetric, it implies that the various classes are mainly the result of observing the AGNs from different angles[6]. If the AGN is viewed at right angles to the jets axis, then it is known as a Type-2. In this case, the dust torus obscures the view of the inner processes; narrow lines from the low-velocity gas clouds, as well as long extended radio jets (if present) are observable. Seyfert 2 and Fanaroff-Riley 1 and 2 are examples of these. If the AGN is viewed at some intermediate angle to the black hole rotation axis, then the core region becomes visible. Both the wide and narrow emission line regions may be visible, as well as the UV radiation from the accretion disk. Depending on the strength of the core emission with respect to that of the lobes of the jets, the object may be classified as core or lobe dominated. These AGNs are of Type-1. Examples are Seyfert 1 and most Quasi-Stellar Objects (QSOs or Quasars). In Type-0 AGNs, the jet axis is oriented toward the Earth and becomes the main observable. That situation permits one to study extreme physics occurring in the jets. There may or may not be emission lines present. Examples are, respectively, Flat Spectrum Radio Quasars (FSRQs) and BL

[4] Solar mass: $1\,M_\odot = 1.99\times10^{30}$ kg.

[5] The presence of jets is optional in the model. Some AGNs seem to have jets (radio-loud AGNs), others do not (radio-quiet AGNs).

[6] Other parameters of the model are the black hole mass and the accretion rate.

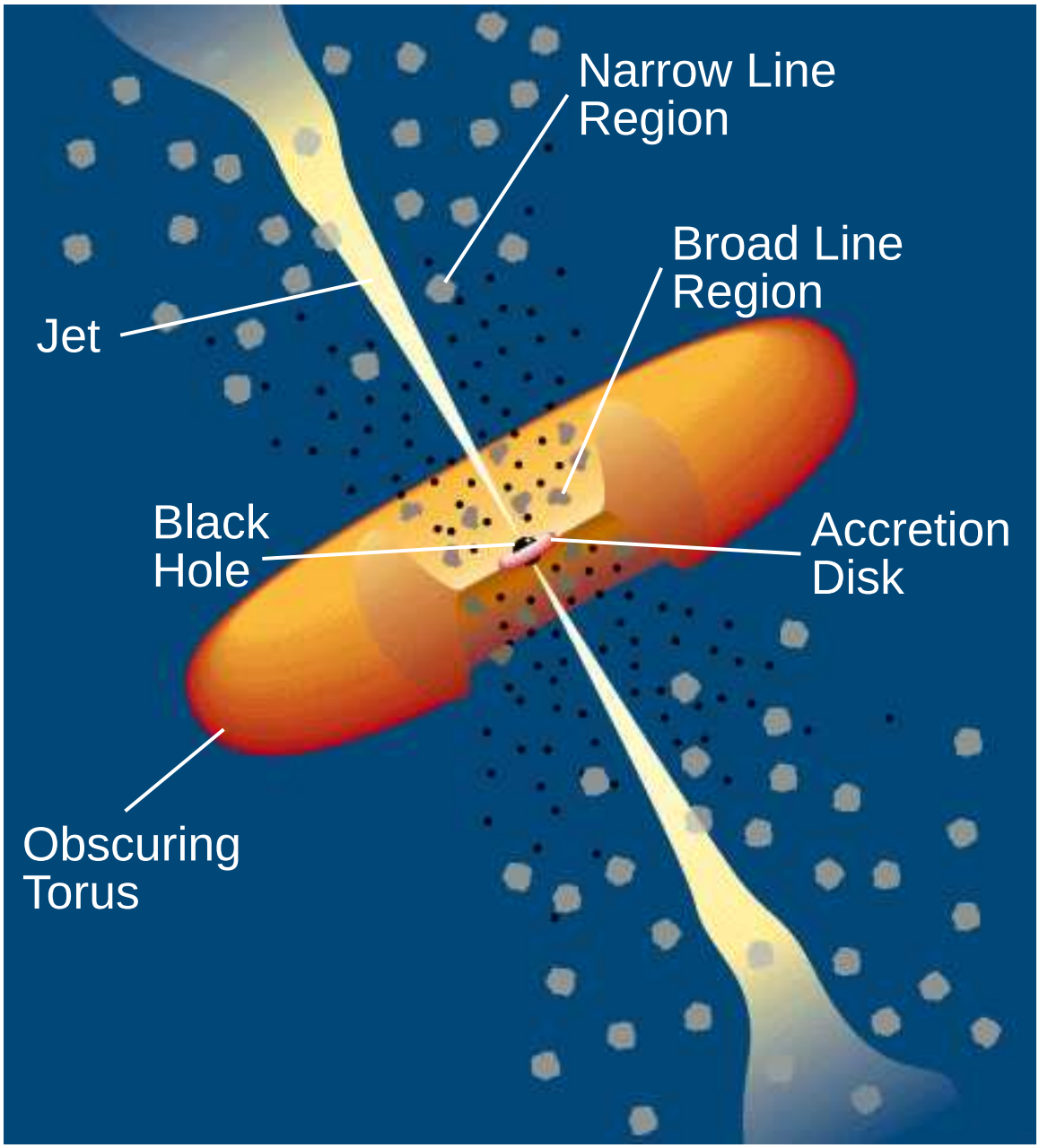

Figure 2.2: Schematic view of an AGN. Figure taken from [6], original illustration by C. Megan Urry and John Godfrey, Space Telescope Science Institute.

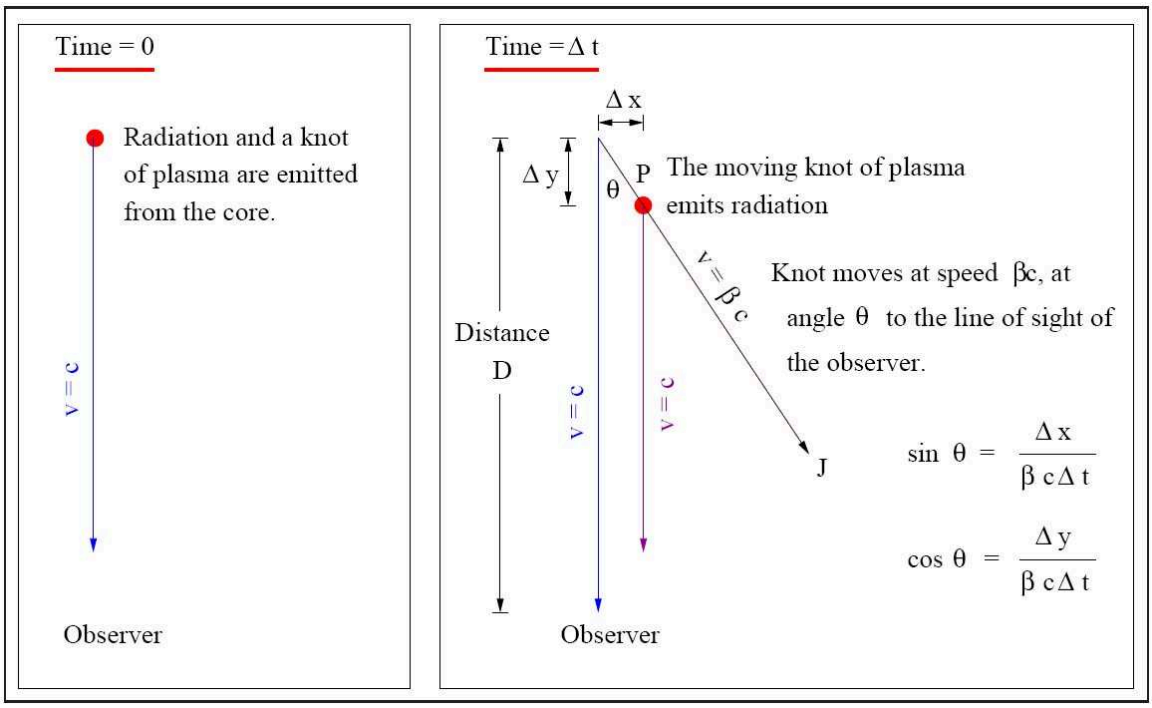

Figure 2.3: Diagram explaining superluminal motion. Figure taken from [4].

Lac objects.

2.1.1 Superluminal Motion

Interesting effects appear because of the relativistic nature of the radiating material traveling in the jets. One such effect is the apparent **superluminal motion** of the material. It is a geometric effect illustrated in figure 2.3 that was first predicted in 1966 by M. Rees in [7]. Imagine a blob of hot plasma moving at relativistic speed $\beta := v/c$ along the jet making an angle θ to the line of sight of the observer. Consider the radiation traveling at speed c emitted at times t_0 and Δt later. The observed transverse velocity is

$$\beta_\perp := \frac{\text{perpendicular distance traveled by the blob in time } \Delta t}{c\Delta t_{\text{obs}}}. \tag{2.1}$$

Now, the perpendicular distance traveled by the blob in time Δt is $\Delta x = \beta c \Delta t \sin\theta$, from simple trigonometry. However, $\Delta t_{\text{obs}} \neq \Delta t$ because the source moved partially in the observer's direction at a speed that is close to that of the radiation. Hence, Δt_{obs}, as measured from the arriving pulses of radiation is shorter than Δt (it would

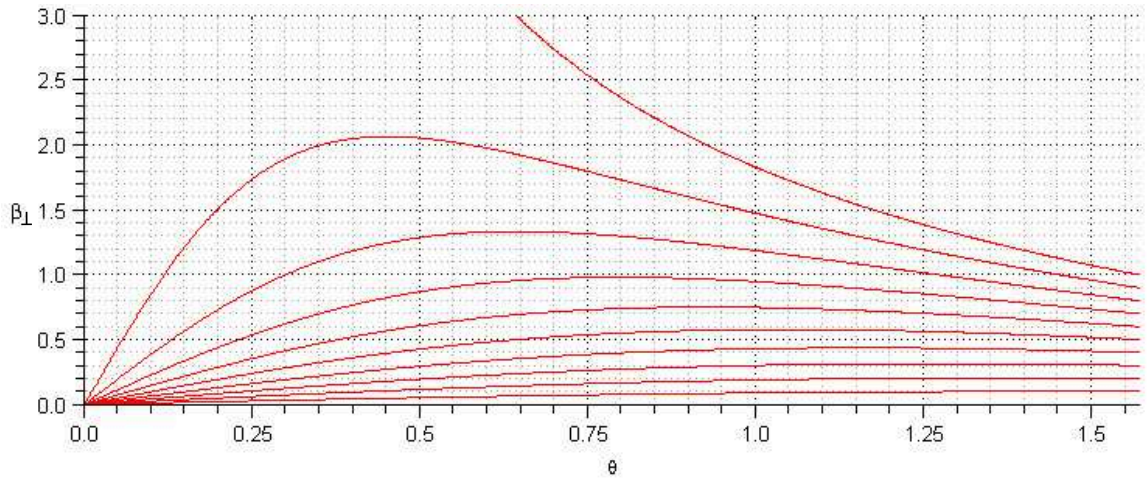

Figure 2.4: Plot of the apparent velocity as a function of θ (in radians) for different values of β. The 10 curves represent 10 values of β of 0.1, 0.2, ..., 1. The curve at the top is for $\beta = 1$ and the curves below go in order of decreasing β. As soon as $\beta > 1/\sqrt{2} \approx 0.7$, apparent superluminal motion can be observed for a certain range of angles of the jet orientation.

be null if the source was moving at 0 angle with the speed of light). It is easy to show that $\Delta t_{\text{obs}} = \Delta t - \Delta y/c = \Delta t(1 - \beta\cos\theta)$, hence,

$$\boxed{\beta_\perp = \frac{\beta\sin\theta}{1-\beta\cos\theta}}. \tag{2.2}$$

For $\beta > 1/\sqrt{2}$, certain values of θ will yield $\beta_\perp$ greater than unity, giving the apparency of superluminal motion (see figure 2.4). Moreover, it can be shown that $\beta_\perp < \Gamma\beta < \Gamma$, where

$$\Gamma := \frac{1}{\sqrt{1-\beta^2}} \tag{2.3}$$

is the **bulk Lorentz factor** (always > 1). So, by measuring $\beta_\perp$, a lower bound for Γ is obtained, which can serve to confirm relativistic motion of the source.

Five years after its prediction, apparent superluminal motion of ten times the speed of light was observed experimentally in very-long-baseline interferometry studies of 3C 279 [8]. Since then it has been observed in many AGNs at radio and optical wavelengths.

2.1.2 Doppler Beaming

Another interesting relativistic effect, called **Doppler Beaming** [9], happens because of time dilation. Considering again the situation described in figure 2.3, it was shown

that the true time interval between the two emission events is related to the *distorted* observed time interval by $\Delta t = \frac{\Delta t_{\text{obs}}}{(1-\beta\cos\theta)}$. However, this is in the reference frame of the observer. In the reference frame of the source (primed coordinates), which is moving at relativistic speed with respect to the observer, time dilation must be deconvoluted: $\Delta t' = \Delta t/\Gamma$. Therefore,

$$\boxed{\Delta t' = \delta \Delta t_{\text{obs}}}, \tag{2.4}$$

where

$$\delta := \frac{1}{\Gamma(1-\beta\cos\theta)} \tag{2.5}$$

is the **Doppler factor** (can be greater or less than 1).

2.1.3 *Luminosity Enhancement*

Doppler *beaming* takes its full meaning when considering its implications for the luminosity of the source. For an observer seeing the source move relativistically in the jet, it will appear as if the emission events were compressed[7] in time by the factor δ in equation 2.4, hence boosting the luminosity seen by the observer. While the source may be emitting isotropically in its rest frame, the angular dependence in δ results in beaming in the frame of the observer.

Another geometrical effect, called **relativistic aberration**, also acts as a luminosity enhancer. It appears because angles in trajectories change as a function of the relative motion of the observer. Again, if the source was emitting isotropically in its rest frame, to an outside observer seeing the source move, the radiation pattern will be warped into a cone along the source's trajectory (beaming). Transformation of the solid angle element from the source frame to the observer's frame results in $d\Omega' = \delta^2 d\Omega$ [3], hence contributing a factor δ^2 to the observed luminosity.

Lastly, the motion of the source changes the frequency of the observed radiation (red or blue-shifting). This turns out to also affect the calculation of the luminosity

[7] Here the case $\delta > 1$ is implicitly assumed, but inverted conclusions can be reached by treating the case $\delta < 1$.

observed at some frequency by some power α of δ, the exact value of which depends on the details of the population of particles that emits the radiation.

These three effects, Doppler beaming, relativistic aberration and red/blue-shifting, combine together into what is called **relativistic beaming** and they modify the observed luminosity in the following fashion:

$$\boxed{L_{\text{obs}} = \delta^p L'}, \tag{2.6}$$

where $p = 3 + \alpha$ [8].

The important beaming expressed in this equation explains why often only one jet is seen from an AGN. If one jet is oriented in the Earth's direction, its luminosity is enhanced. The counter-jet is then beamed in the opposite direction and appears consequently much dimmer.

2.2 Blazars

Given the importance of the Doppler factor in equations 2.4 and 2.6, and looking at its plot in figure 2.5, one quickly understands that since there is a region in the (β, θ) plane where δ grows quite rapidly to high values (high velocity and small angle part of the plane), a particular class of AGNs having these parameters will show extreme properties. This class has a relativistic jet oriented directly at Earth and its objects are called **blazars** (for "blazing stars"). People have often used the analogy of looking down the barrel of a gun to describe the situation. By looking down directly in the jet and examining the energy contents, one apprehends all the power contained within blazars, one of the most violent sources of high-energy photons in the Universe. Blazars emit at all wavelengths and can exhibit variability on various timescales. It is believed that blazars might be the source for ultra-high-energy cosmic rays (see section 2.3.2) and, because of their extreme properties, they form unique cosmic laboratories to study extreme physics.

[8] Depending on the jet modeling (continuous jet with rate measured in lab frame or jet formed of blobs, particle population spectra, isotropy or non-isotropy in the jet frame, etc.), the form taken by p can change somewhat; the p given here serves to illustrate the contributions discussed above.

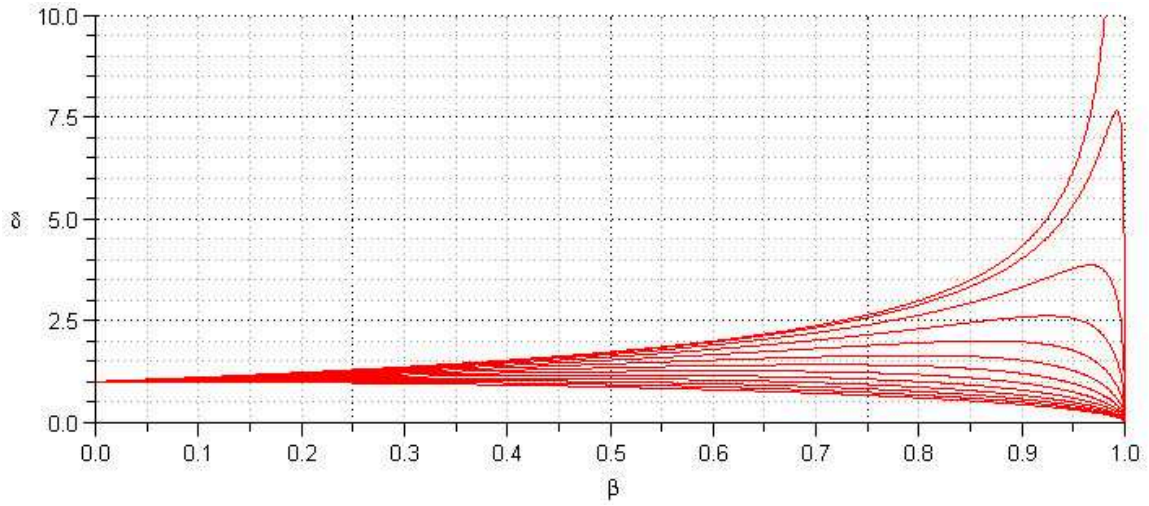

Figure 2.5: Plot of the Doppler factor as a function of β for different values of θ. The 13 curves represent 13 values of θ between 0 and $\pi/2$, in equal spacings. The curve at the top is for $\theta = 0$ and the curves below go in order of increasing θ.

2.2.1 Spectral Energy Distribution

A typical feature of blazars is the shape of their **spectral energy distribution (SED)**, a plot that represents the power observed at each frequency. To illustrate, figure 2.6 shows the SED for Markarian 501 (or Mrk 501 for short), an extreme blazar. The notable features are the two characteristic broad humps revealing the non-thermal nature of the emission. It is believed that the lower energy peak, usually from radio to UV or X rays, is due to synchrotron radiation emitted by the electrons moving ultra-relativistically in the jet, while the higher energy peak, from X to γ rays, has an origin which is debated (see section 2.3 for some models). Some blazars are thus capable of emitting up to TeV energies, which is remarkable and makes them a source of the highest energy photons that have been recorded.

Also notable from the previous picture is that the shape of the SED changes, depending on the epoch of the observation. These changes relate to the activity of the source. In active states, not only does the luminosity increase by a large amount, the peaks of the SED bumps also usually shift to higher frequencies. This is important because it implies that some objects that might be too faint to be detectable at TeV energies under normal conditions, might become detectable when the source is active;

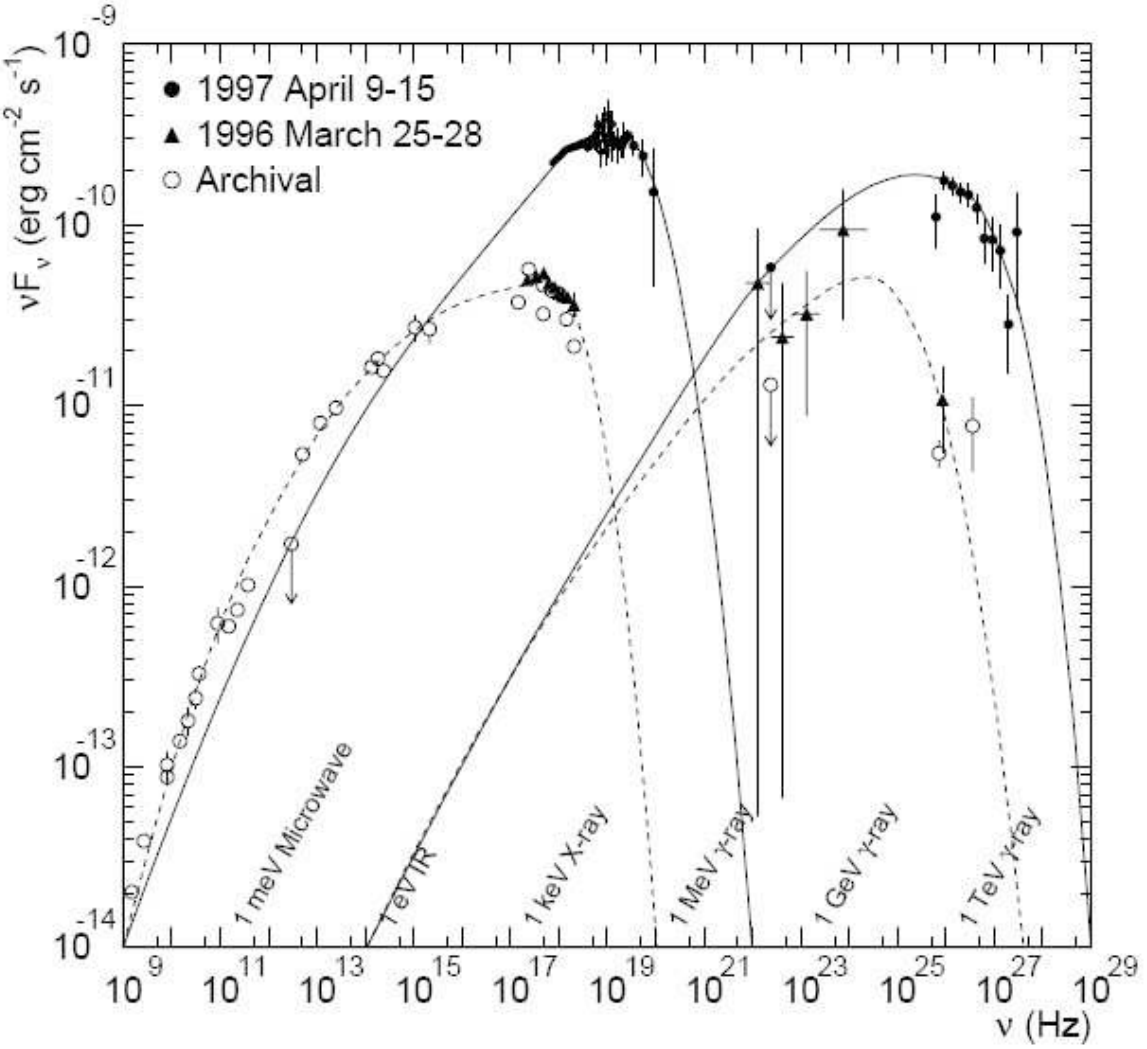

Figure 2.6: Spectral energy distribution of Mrk 501 during quiescent state (dashed curve) and active state (solid curve); the curves only serve to guide the eye and do not represent fits to the data. The two humps are characteristic of blazar emission, the low-energy one being attributed to synchrotron radiation and the high-energy one, possibly to inverse Compton scattering of low-energy photons. During a period of activity, the amplitudes of the humps increase, but their peaks also shift to higher frequencies. Figure taken from [10].

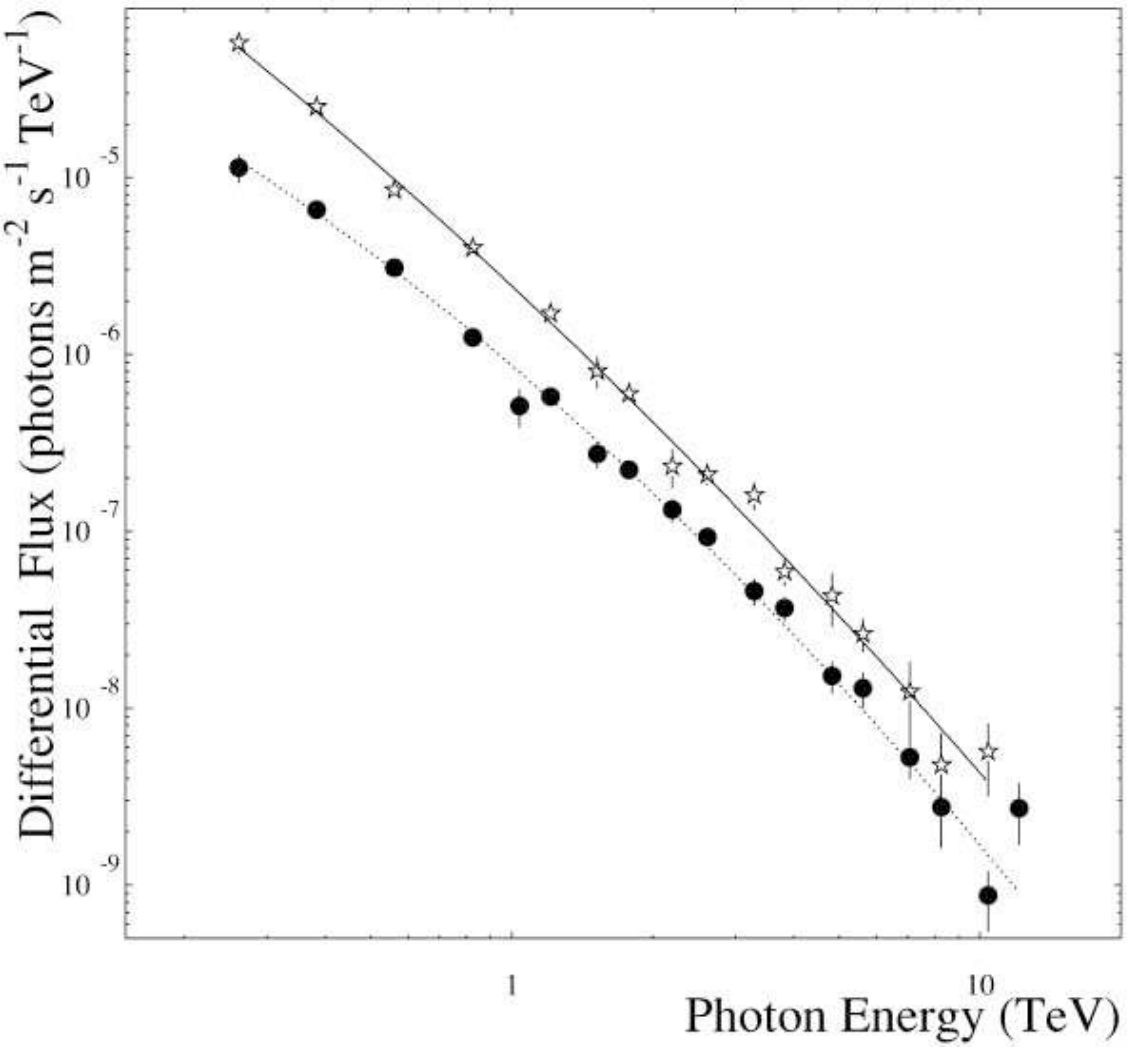

Figure 2.7: Differential flux of Mrk 421 (stars) and Mrk 501 (circles) at TeV energies during outbursts. The curves are obtained from best fits to the data. Figure taken from [13].

the TeV sky is not static, it changes constantly.

Since it is the TeV energies that are of interest in this thesis, it is appropriate to look a little closer at this range. Figure 2.7 shows the very-high-energy differential flux levels for Mrk 421 and Mrk 501 [9] while they were in a high state, which permitted one to measure their spectrum with good precision because of the high statistics.

Such spectra are often described by a simple power-law, as is the case for spectra from observations of γ rays of lesser energy. Sometimes however, a power-law with

[9] Mrk 421 and Mrk 501 were the first two TeV blazars to be discovered, in 1992 and 1996, respectively, both by the Whipple collaboration [11], [12].

exponential cut-off fits the data better:

$$\frac{dN}{dE} \propto e^{-E/E_{\text{cut}}} E^{-\alpha}, \tag{2.7}$$

where E_{cut} is the cut-off energy and α is the spectral index.

The presence or absence of a cut-off energy is interesting because it may indicate a feature of the acceleration mechanism producing the radiation, or it may indicate an absorption feature from the extragalactic background light for example. This is discussed further in chapter 3.

2.2.2 Variability

Having seen that the main descriptor of blazars, their SED, has the property of varying, it is natural to ask on what timescales these changes occur? TeV light curves have shown variability on timescales as long as years and as short as a few minutes [14] [15] [16]. Figure 2.8 shows the time development of a typical **flare**, from Mrk 501, that lasted for about ten days. Often, as was the case here, the optical, X-ray and γ-ray variabilities are correlated. However, this is not always the case; complex correlations do occur. For example, orphan flares have been observed, where a γ-ray outburst is not accompanied by a X-ray high state. This poses challenges for some emission models.

Again concentrating on the TeV regime, figure 2.9 shows an example of an exceptional flare with well-resolved substructure on the incredibly short timescale of about 200 s. Such rapid variability has implications regarding the size of the emitting region. If this region of radius R is to remain causally connected, then

$$\boxed{R \leq \frac{\delta}{1+z} c t_{\text{var}}}, \tag{2.8}$$

where t_{var} is the timescale of the variation and z is the cosmological redshift of the source. Note the presence of the Doppler factor in this equation. It comes from equation 2.4 and expresses the fact that, in the presence of beaming, observed time intervals may be much shorter than those occurring in the rest frame of the source, which alleviates the constraint put on the size of the emission region. Even so, this

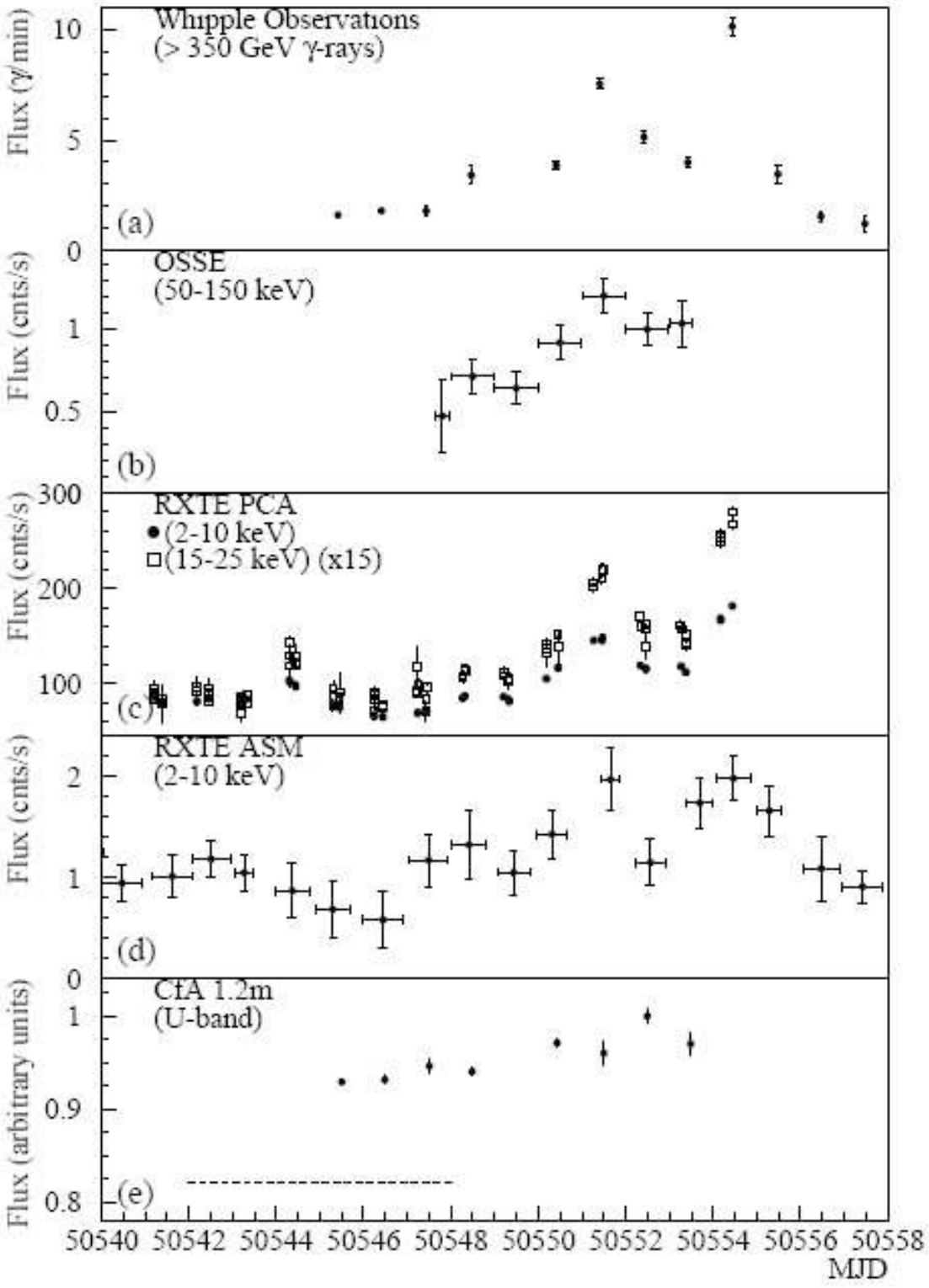

Figure 2.8: Multi-wavelength light curve for Mrk 501 in April 1997. a) very-high-energy γ rays, b) hard X rays, c) and d) X rays, e) optical U-band. Figure taken from [10].

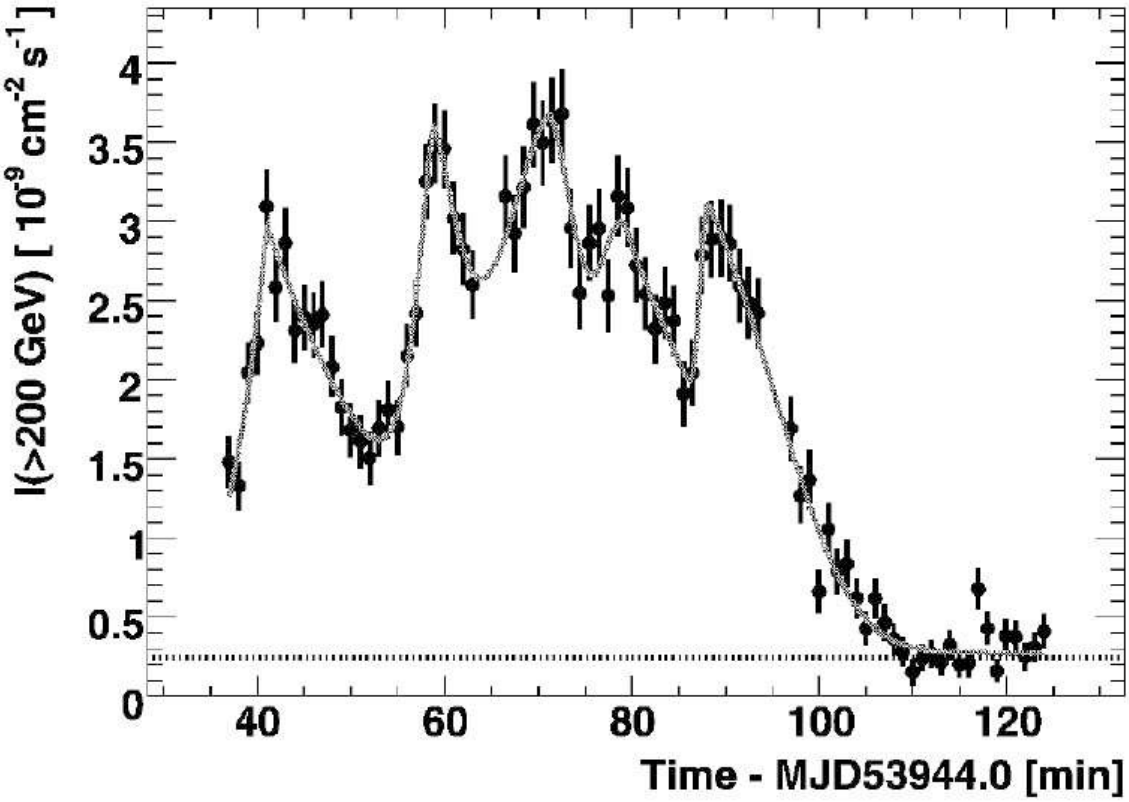

Figure 2.9: Light curve of PKS 2155-304 (integral flux above 200 GeV) for the flare of July 28, 2006. Data are binned in 1 min intervals. The dashed line shows the integral flux under the same condition for the Crab Nebula. The curve is a fit of a flaring model. Figure taken from [15], observations from the H.E.S.S. collaboration.

recently observed extremely short variability implies a more compact (smaller than the central black hole size) or more violent ($\delta \gg 10$, $\Gamma \gtrsim 50$) emission region for the TeV radiation than was previously considered [17] [18].

2.2.3 Sequence

Up to now, it was shown that blazars have in common a characteristic double humped SED and that they are capable of variations on many different timescales. However, not all blazars are the same; there exists further subclassifications in this class. A first division comes from the presence or absence of strong emission lines. Those that have such lines are called **Flat-Spectrum Radio Quasars (FSRQs)** and those that do not have them are called **BL Lacertae objects (BL Lacs)**, based on the name of an object that was originally mistaken for a variable star. Furthermore, within the BL Lac class, there is an historical division that grouped objects with a high value for the frequency of the first peak in the SED (in the UV to X-ray band) *vs* objects that had this peak at lower frequencies (in the infrared to optical band). These subdivisions are logically called **high frequency peaked BL Lac objects (HBLs)** and **low-frequency peaked BL Lac objects (LBLs)**, respectively. Nowadays, these subclasses no longer appear as disjoint as was the case when they were created. BL Lacs with intermediate frequency peak positions have been found and HBLs and LBLs now merely represent the extremes possibilities within the BL Lac class.

In an attempt to understand blazars more fully, it was proposed that there be a sequence along which the different classes could be ordered [19] [20]. According to this sequence, there exists an anti-correlation between the frequency of the first peak of the SED and the luminosity of the source. Thus, since FSRQs are typically more powerful than BL Lacs, the sequence implies that FSRQs→LBLs→HBLs goes in decreasing order of luminosity and increasing order of synchrotron peak frequency. Moreover, it was observed that as the peak frequency of the first hump decreases, the high-energy peak of the SED becomes more dominant compared to the low-energy peak. Hence FSRQs are dominated by their γ-ray radiation, LBLs have their low- and high-energy components roughly equal and HBLs emit more power at low energies.

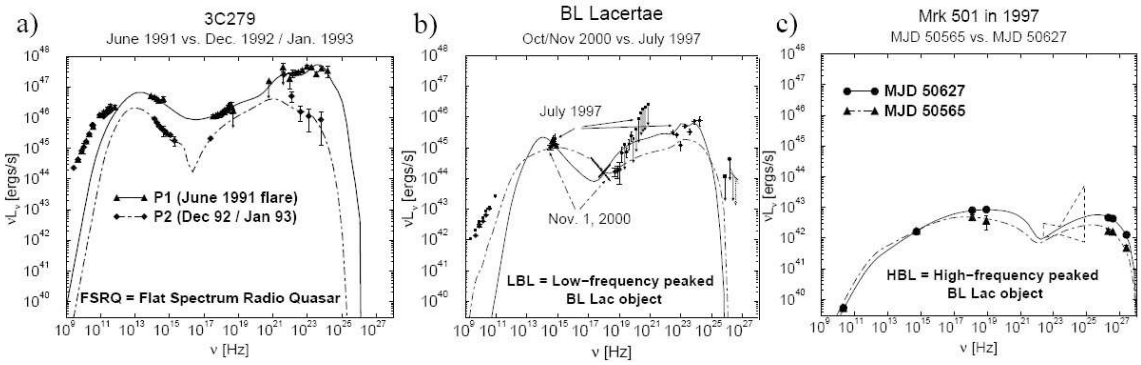

Figure 2.10: SEDs illustrating the blazar sequence. a) FSRQs have higher luminosity, lower synchrotron peak frequency and dominant high-energy peak, b) LBLs have intermediate synchrotron peak frequency and luminosity and the two SED humps are of similar importance, c) HBLs have higher synchrotron peak frequency, lower luminosity and the low-energy peak is dominant. The curves are obtained from a fit of a leptonic jet model and two different epochs are shown. Figure taken from [21].

As a final observation, the peak frequency of the high-energy hump is correlated with the peak frequency of the low-energy hump. Figure 2.10 shows examples of the SED of different types of blazars, which illustrate the points just presented.

It was shown recently that the luminosity/synchrotron peak frequency anti-correlation does not hold and was the result of selection effects [22]. FSRQs with low-energy peak frequency as high as those of LBLs have been found and HBLs are a minority among BL Lacs, which is contrary to what could be expected if the sequence was true. Still, this probably does not affect the correlation between low- and high-energy peak frequencies, which implies that HBLs have the highest high-energy hump peak frequencies and makes them more likely to be TeV emitters. This explains why, of the 19 blazars observed at TeV energies, only one is a FSRQ and only two are LBLs; all the others are HBLs. Figure 2.11 shows a map of the TeV sky at the moment of writing, while the VERITAS sky survey is not yet complete. The dominance of blazars as extra-galactic sources is obvious.

2.3 Models

How can blazars emit radiation that will produce such SEDs, with so much power at so high energies, and how can they exhibit such variability? A key element to the

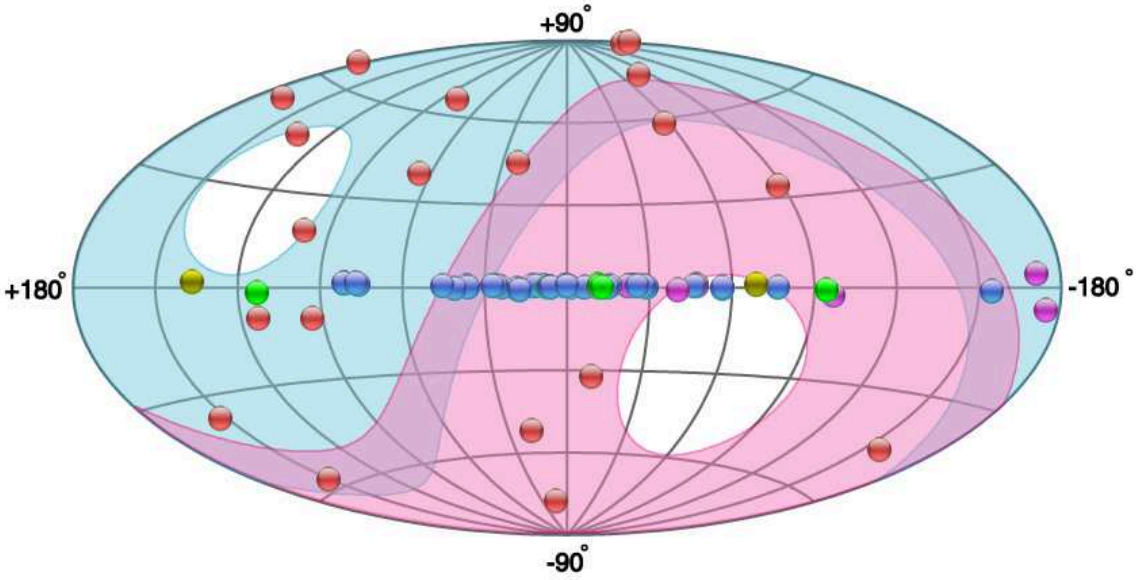

Figure 2.11: Catalog of TeV sources, in galactic coordinates. The blue shaded area represents the part of the sky observable from observatories located in the northern hemisphere, while pink shading indicates the southern sky. Blazars (HBLs, LBLs or FSRQs), are red and away from the galactic plane, where most unidentified, Wolf-Rayet and binary objects lie, colored in blue. Green objects are shell-type supernova remnants, purple is for pulsar wind nebulea and yellow is for X-ray binaries. This catalog is changing rapidly with the recent advent of new observatories; see chapter 4. Figure taken from [2].

answer resides in the beaming that was discussed earlier and which was shown to alleviate the problems of explaining the short timescale variations, high luminosity and high energies (by blue shifting). In all probabilities then, the γ rays seem to be produced inside the jets. But what are the mechanisms by which the γ rays are generated? The complete answer is complex and still being debated. There are a few classes of models which are mainly successful, but currently none of them is a definite favorite among the community [23]. What is generally accepted though, is the origin of the low-energy component of the SED. This hump exhibits strong linear polarization and only **synchrotron radiation**, the radiation that is emitted when ultra-relativistic electrons spiral in magnetic fields, is able to explain it properly along with the non-thermal nature of the low-energy spectrum [3]. There are many proposed mechanisms for the injection and acceleration of electrons in the jet [21]. These will not concern us here and it will suffice to recognize the existence of these ultra-relativistic electrons, which can give a hint for explaining the more complex

high-energy component of the SED. Here, the principal models are briefly outlined without going in the computational details, which can be quite involved.

2.3.1 Leptonic Model

Given that there are very energetic electrons in the jet, one way that γ rays can be produced is if the electrons upscatter soft photons through inverse Compton scattering; a fast electron collides with a soft photon, giving it some of its energy (figure 4.1 illustrates Compton scattering, just reverse the process for inverse Compton scattering). To escape the emission region, the γ rays produced must survive $\gamma\gamma$ absorption, pair production and synchrotron self-absorption. This process, in which the electrons are the direct cause of the high-energy radiation, represents the first class of emission models called **leptonic models**. The question of which population of soft photon gets boosted to higher energies gives rise to two different scenarios.

Synchrotron Self-Compton (SSC)

In the first scenario, it is the synchrotron radiation itself that acts as the soft photon target. Since the electrons are responsible for both the synchrotron (low-energy hump of the SED) and inverse Compton (high-energy hump) radiation, this model is called **Synchrotron Self-Compton (SSC)**. This mechanism is mainly motivated by the desire to explain the correlations between X-ray and TeV flares. Since the observation of some instances of the orphan flare phenomenon, the SSC model is somewhat challenged [23]. Also, while SSC may be a good descriptor of TeV blazars, it is generally less satisfactory for the case of GeV blazars.

Synchrotron External Compton (SEC)

The soft target photons need not be generated in the jet itself. Observations of non-blazar AGNs reveal that there are plenty of other sources of soft photons in this environment. In the **Synchrotron External Compton (SEC)** model, the soft photons can be ambient radiation coming from the dusty torus (infrared), from the accretion disk (UV), from the disk corona (X-ray), from the clouds responsible for the broad emission lines (optical), or it can even be the synchrotron radiation that escapes

the jet and is reflected back in, reprocessed by the gas clouds that are in the vicinity. The possibilities are many and theoreticians must carefully examine the densities of photons that each component can contribute to single out the dominant one. SEC models perform generally better than SSC models in the case of GeV blazars, but not for TeV blazars.

2.3.2 Hadronic Model

Presumably, if electrons can be accelerated in the jet, then protons coming from the material close to the black hole may be accelerated too. If there are protons in the jet, then other ways of producing γ rays exist. **Hadronic models** is the name for this group of models that generate the high-energy emission from energetic protons. The key element here is that the protons be energetic enough for the pion production threshold to be attained [21] in processes such as

$$\mathrm{p} + \mathrm{p} \rightarrow \begin{cases} \pi^0 + \text{debris} \\ \pi^{\pm} + \text{debris} \end{cases}, \tag{2.9}$$

or such as

$$\mathrm{p} + \gamma_{\mathrm{soft}} \rightarrow \begin{cases} \mathrm{p} + \pi^0 \\ \mathrm{n} + \pi^+ \end{cases}, \tag{2.10}$$

where the soft photon can come from synchrotron or external radiation, as in the leptonic models. Once this threshold is attained, high-energy γ rays can be produced from pion decay

$$\pi^0 \rightarrow 2\gamma_{\mathrm{hard}}, \tag{2.11}$$

or from pion cascades such as

$$\begin{aligned} \pi^+ &\rightarrow \mu^+ + \nu_\mu \\ \mu^+ &\rightarrow \mathrm{e}^+ + \nu_\mathrm{e} + \overline{\nu}_\mu \\ \mathrm{e}^+ &\rightarrow \mathrm{e}^+ + \gamma_{\mathrm{hard}} \quad \text{(bremsstrahlung radiation).} \end{aligned} \tag{2.12}$$

The hard γ rays then initiate electromagnetic cascades through cycles of pair production followed by bremsstrahlung radiation or synchrotron radiation from the population of more energetic electrons, or even inverse Compton scattering of soft photons,

depending on the density of the different particle populations and magnetic fields present. This results in the emission of more γ rays, some of which escape the emission region.

Another possibility is that the very-high-energy γ rays are produced from synchrotron radiation from the protons having energies up to 10^{20} eV and traveling in high magnetic fields in the jet (tens of Gauss). Similarly, the muons and mesons produced can also contribute to the very-high-energy emission through synchrotron radiation.

The motivation for hadronic models comes from the desire to explain the origin of charged cosmic rays. These particles, which can be extremely energetic (sometimes more than 10^{20} eV), appear to arrive isotropically on Earth, but that is because their trajectories have been randomized by extra-galactic magnetic fields. Their origin is thus a mystery and a candidate source for their production could be AGNs because of their extreme properties[10]. Confirmation of the blazar hadronic model would support that theory. One of the by-products of this class of models are neutrinos; observations of these particles with the new neutrino telescopes being built would add support to the model. Currently, hadronic models have difficulty explaining the fast variations observed [6].

2.3.3 Hybrid Model

In view of the mixed successes of the different theories, and although it may be expected that one of the models should dominate, it is not impossible that the different models represent extreme possibilities for the conditions in the jet and that in realistic cases a mix of the models could be more satisfactory. In fact, there are even claims that if the blazar sequence is real, then it may be that a mix of SSC and SEC models would explain it by gradually increasing the importance of the external component along the progression HBL $\rightarrow$ LBL $\rightarrow$ FSRQ. A similar explanation for the sequence can also be given by a mixing of the different versions of the hadronic model [21].

[10] This hypothesis has recently received confirmation from Auger results [24], but discussions are still going on.

As for hybrid leptonic-hadronic models, these might more satisfactorily explain the observations of correlated flares at X-ray and TeV energies that are followed by orphan TeV flares.

Clearly, more studies need to be done to properly understand blazar emission. One thing that stands out is the importance of multi-wavelength campaigns; the broad-band shape of the SED is needed to compare models, the TeV band is not enough. Not only is the broad-band SED crucial, variability information is needed as well to understand how the high states of emission can occur and how they differ from the normal state. This may help in discriminating between models. However, given the limited observing time on different instruments and the short timescales on which variability is seen, it represents a considerable effort from the community to obtain simultaneous multi-wavelength data, but progress is being made. Figure 2.12 summarizes the different possible emission processes discussed above.

2.4 1ES 1218 + 30.4

Having described blazars in their main properties, it is now possible to properly introduce the object that forms the center of this study, the 1ES 1218 + 30.4 blazar.

2.4.1 Basic Properties

1ES 1218 + 30.4 is a blazar of type HBL. It is located, in equatorial coordinates, at

$$R.A. = 12\,\mathrm{h}\,21\,\mathrm{min}\,21.9\,\mathrm{s},\ Dec. = +30^\circ\,10\,\mathrm{min}\,37\,\mathrm{s} \tag{2.13}$$

or, in galactic coordinates, at

$$l = 186.36^\circ,\ b = 82.73^\circ. \tag{2.14}$$

In figure 2.11, it is the highest point on the graph. It is visible at night in the northern hemisphere roughly from December to March.

This source first appears in the literature in 1970, as part of the second Bologna catalog of radio sources at 408 MHz [26]. Since then, it has been mentioned in more

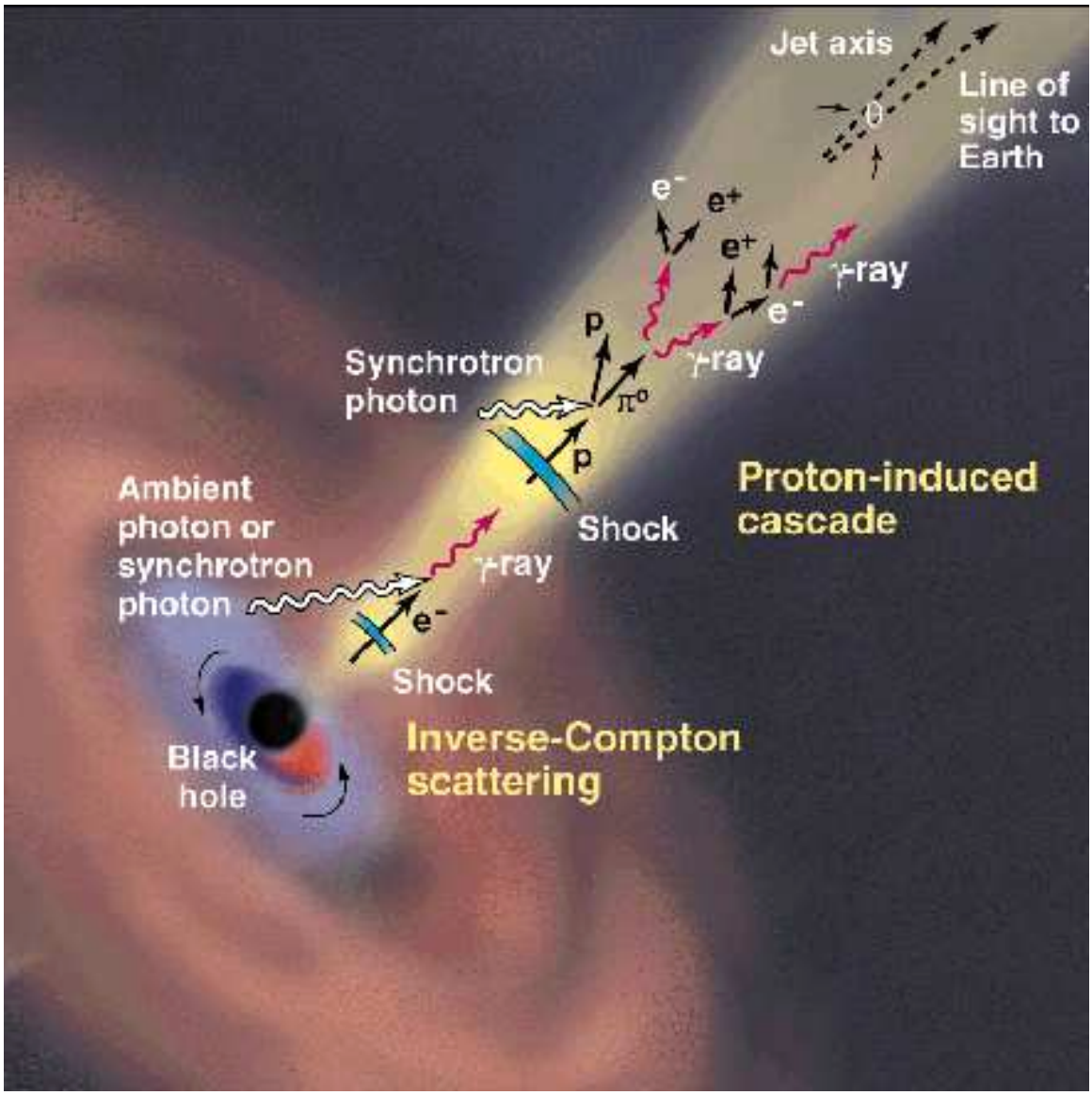

Figure 2.12: Main possibilities for emission processes in blazars: the SSC, SEC and hadronic models, or a hybrid of those. Figure taken from [25], illustration by K. Sutliff.

than 160 papers[11], many of which are survey results at different wavelengths or studies of blazar properties. One of those blazar studies looked at the SED patterns of known TeV blazars in order to derive a model that would allow prediction of TeV emission from other sources [27]. Based on the requirements imposed by this model, the authors of that paper selected a sample of sources that are bright in the radio and X-ray bands, with particular requirement on the position of the synchrotron peak. They then fitted the available SED data of their candidates to their SSC model to attempt a prediction of their very-high-energy flux. The result for 1ES 1218 + 30.4 was $\Phi_{\gamma,E>0.3\,\mathrm{TeV}} = 0.16\times10^{-11}\,\mathrm{photons/(cm^2\,s)}$ ($\sim$ 1.2% of the Crab Nebula's flux), with large uncertainties, since they show that another model yields $\Phi_{\gamma,E>0.3\,\mathrm{TeV}} = 0.67\times10^{-11}\,\mathrm{photons/(cm^2\,s)}$ ($\sim$ 5.1% of the Crab Nebula's flux). This made it a source that, although not expected to be exceptionally strong, is worth including in ground-based instruments TeV source searches, especially since several of the candidates listed in [27] have indeed been discovered in the very-high-energy regime.

Measuring the redshift of BL Lacs is usually not an easy task because of the weakness of spectral features. The redshift of 1ES 1218 + 30.4 is usually quoted as

$$z = 0.182, \tag{2.15}$$

with no uncertainty provided on the measurement. This value is reported from [28] or [29] for example. It is mentioned in those papers that this value was obtained on the basis of communications with the authors of a future paper (Perlman et al., 1998), but this paper does not seem to exist and so no solid information can be obtained regarding the quality of this redshift. The only available piece of information is that it was obtained spectroscopically. Another redshift estimate for this source is 0.130 $\pm$ 0.03 [30]. This one is older and obtained from photometry measurements using some assumptions regarding the emission of the host galaxy. Given that spectroscopic measurements of redshifts are usually more reliable than photometric ones, and that the one given here is also more recent, $z = 0.182$ will be the value adopted in this

[11] As listed by the SIMBAD (`http://simbad.u-strasbg.fr/simbad/`) and NED (`http://nedwww.ipac.caltech.edu/`) databases.

thesis. It would be good, though, to confirm this redshift to make sure no error is being propagated in the literature [31].

1ES 1218 + 30.4 has been observed with many different instruments, at different wavelengths and for different surveys. For this reason it has acquired many different names. The one used here, with the *1ES* prefix, comes from the X-ray observations of the *Einstein Slew Survey, version 1.* Other popular names include B2 1218+30, 1H 1219+301, H 1219+305, PG 1218+304, FIRST J122121.9+301037, QSO B1218+304, etc[12]... The recent TeV catalog [2] suggests the following name: TeV J1221+301, but the canonical 1ES 1218 + 30.4[13] will be used throughout this thesis because it is more widely known.

2.4.2 Multi-Wavelength Observations

As mentioned above, 1ES 1218 + 30.4 is an object well studied at many wavelengths. Here the most interesting features are reviewed.

Radio Observations

The radio observations, described in [32], made with the Very Large Array (VLA) confirm a compact source on the kpc scale, with maximum size 0.7 kpc. Those made with the Very Long Baseline Array (VLBA) are interesting in that they reveal the presence of a small jet 10 mas long, shown in figure 2.13. By examining the brightness of the jet and the dominance of the power emitted by the core, they deduce the following constraints on the physical parameters of the blazar:

$$15\,^\circ \leq \theta \leq 24\,^\circ \tag{2.16}$$

$$1.9 \leq \delta \leq 3.7. \tag{2.17}$$

Interestingly, the angle θ that the jet makes with the line of sight used in [27] for this object in the determination of TeV blazar candidates is $\theta = 2.9\,^\circ$, a value much smaller, probably obtained from constraints imposed by the SED and an SSC model.

[12] A complete listing comprising more than 33 names can be found in the SIMBAD and NED databases.

[13] Actually, this source's name is more often encountered written as 1ES 1218+304 and it is easier to find information about it when using this form.

It is explained in [32] that there is often disagreement between parameters extracted from radio data and data at higher energies, which could lead to the conclusion that the different radiations are produced in different parts of the jet or in different layers, moving with different bulk velocities or even with a different orientation to the line of sight.

Optical Observations

At optical wavelengths, Hubble Space Telescope (HST) observations resolve a source of apparent magnitude 15.68 $\pm$ 0.10 and an elliptical host galaxy of apparent magnitude 17.12 $\pm$ 0.03 [33]. The size estimated from these observations is (10.75 $\pm$ 1.24) kpc. HST observations have also permitted an estimation of the mass of the central black hole: $10^{8.58}\,M_\odot$ [34] [35].

As part of a blazar monitoring program, 1ES 1218 + 30.4 is routinely observed by the 1.03 m telescope at the Tuorla Observatory, Finland, and the 35 cm telescope at the KVA observatory on La Palma, Canary islands, Spain. Figure 2.14 shows the optical light curve obtained. Such monitoring may help in catching sources in high states.

X-ray Observations

X-ray monitoring is also particularly important because it is stressed in [27] that the X-ray flux measures, in their scenario, the number of TeV energy electrons. Such monitoring is currently being done by the Swift and RXTE satellites.

In the past, 1ES 1218 + 30.4 has been observed by the Einstein, ROSAT, BeppoSAX and XMM-Newton missions. Figure 2.15 shows the flux recordings obtained. Interestingly, one early mission showed evidence for an absorption feature in the X-ray spectrum [36]. This would be an important discovery since the spectrum of BL Lacs is generally featureless. It could give some insights on the environment surrounding the object. However, all recent observations do not show this behavior and the existence of this phenomenon has been ruled out at the 93% confidence level in general.

More recently, 1ES 1218 + 30.4 has been observed continuously for two days in

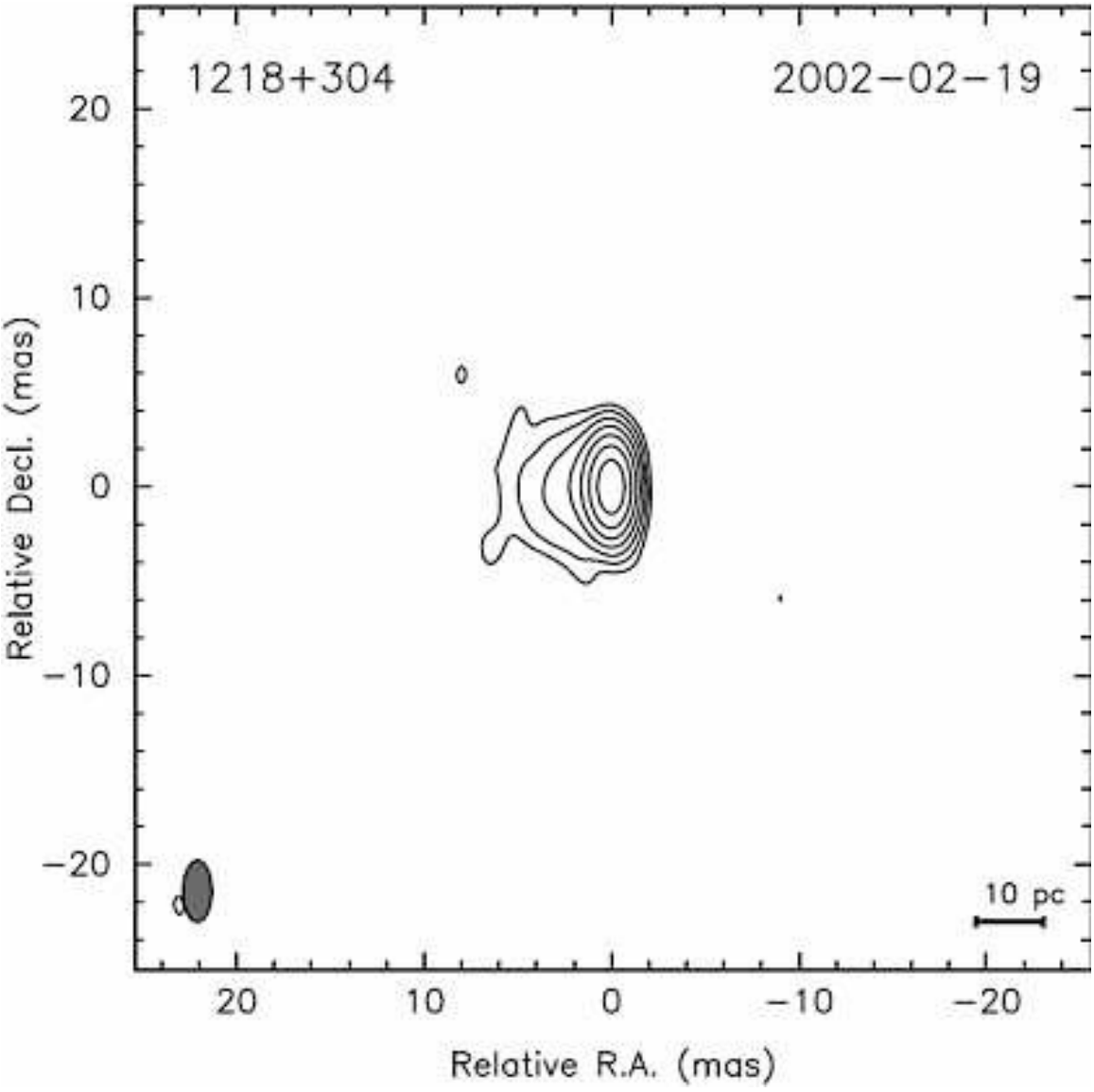

Figure 2.13: VLBA image of 1ES 1218 + 30.4 showing evidence for a small 10 mas jet with no visible counter jet. Total flux density at 325 MHz is 82 mJy, at 1.4 GHz is 71 mJy and at 5 GHz is 57 mJy. Figure taken from [32].

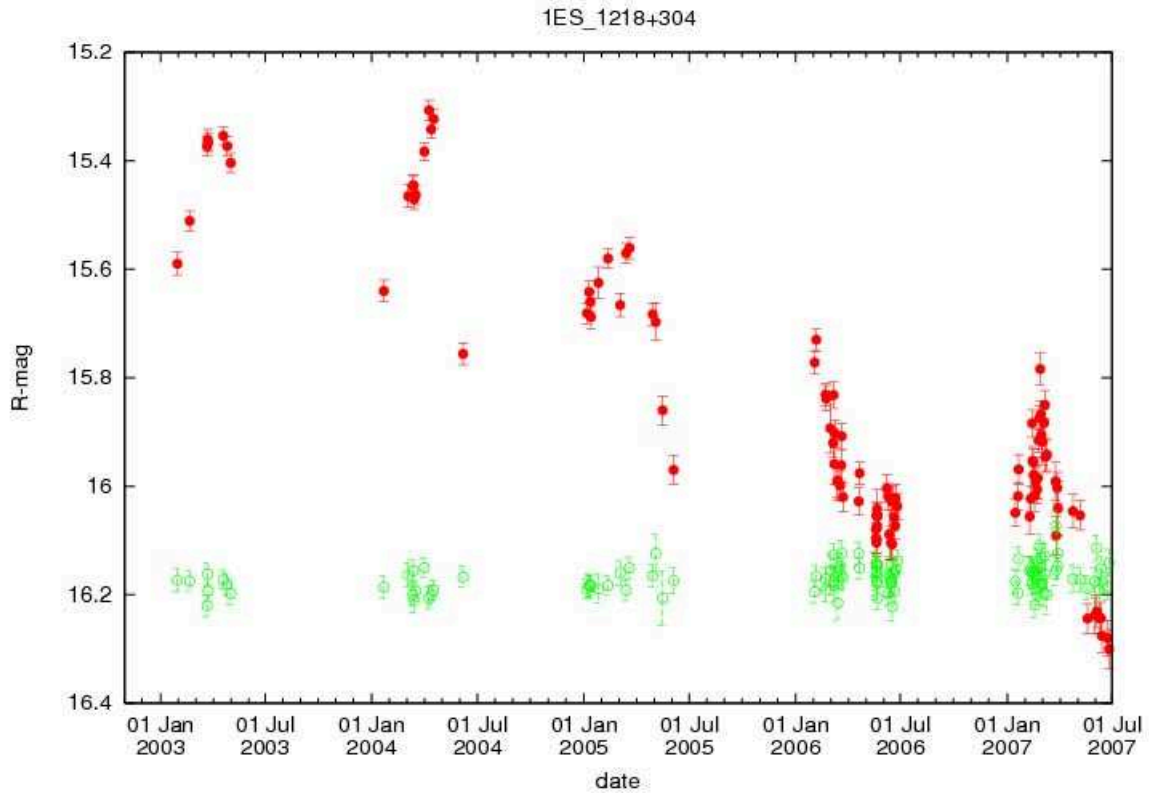

Figure 2.14: Optical observations of 1ES 1218 + 30.4 in one hour averages with the R-filter. The filled red markers are for the source, the empty green markers are for a control star. Figure taken from `http://users.utu.fi/kani/1m/1ES_1218+304.html`, preliminary data.

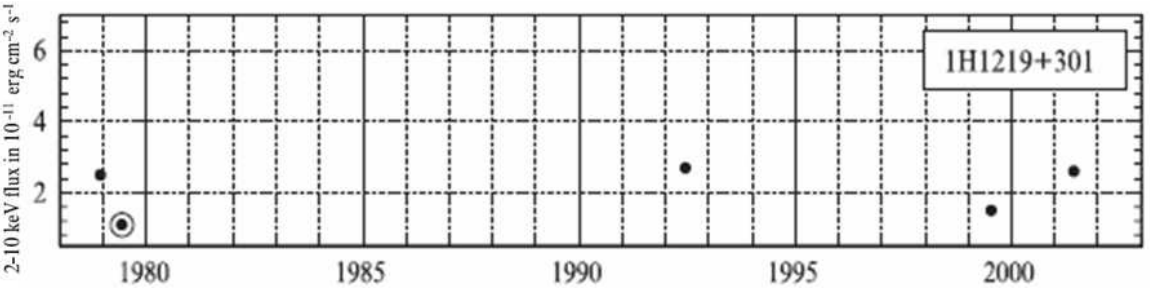

Figure 2.15: X-ray fluxes of 1ES 1218 + 30.4 as observed by various missions. The circled point represents an observation where intrinsic absorption was measured. This figure gives an idea of the X-ray flux variations of 1ES 1218 + 30.4; it can be added that the ROSAT satellite recorded fluxes at 1 keV varying in the larger range 0.8-4.5$\times 10^{-11}$ erg/(cm^2 s). Figure taken from [36].

May 2006 by the Suzaku X-ray satellite [37]. A large flare in the 5-10 keV band was detected with the flux changing by a factor ~ 2 on a time scale of $5{\times}10^4$ s. The time profile of the flare changed with energy and the increase of the flux in hard X-rays lagged behind that for soft X-rays, a behaviour rarely observed but expected to happen in theory [37].

γ-ray Observations

In the γ-ray range, 1ES 1218 + 30.4 was not detected until recently. Upper limits were calculated based on previous observations. The satellite-hosted instrument EGRET yielded $\Phi_{\gamma,E>100\,\mathrm{GeV}} < 10^{-11}\,\mathrm{erg/(cm^2\,s)}$, while the ground-based observatories yielded $\Phi_{\gamma,E>350\,\mathrm{GeV}} < 8.3{\times}10^{-8}\,\mathrm{photons/(m^2\,s)}$ (8% of the Crab Nebula flux) for Whipple [38] and $\Phi_{\gamma,E>840\,\mathrm{GeV}} < 2.67{\times}10^{-8}\,\mathrm{photons/(m^2\,s)}$ (12% of the Crab Nebula flux) for HEGRA [39]. The STACEE experiment also did not detect this source and an upper limit on the differential flux at 150 GeV was derived to be less than $5.2{\times}10^{-6}\,\mathrm{photons/(m^2\,s\,TeV)}$ [40].

In 2006, the MAGIC collaboration finally announced a detection of this object at TeV energies, at the 6.4σ level [41]. They found a flux above 100 GeV of $(8.7 \pm 1.4) \times 10^{-7}\mathrm{photons/(m^2\,s)}$ with no evidence for variability during their observations. They derived a spectra consistent with a simple power law:

$$\phi_\gamma(E) = (8.1 \pm 2.1) \times 10^{-7} \left(\frac{E}{250\,\mathrm{GeV}}\right)^{(-3.0\,\pm\,0.4)} \mathrm{m^{-2}\,s^{-1}\,TeV^{-1}}. \qquad (2.18)$$

The VERITAS group also performed observations of this source and preliminary results were presented in [42] (official results are in preparation for publication [43]).

In [44], a compilation of observations at many different wavelengths, including the MAGIC detection, is used to build the SED of 1ES 1218 + 30.4. The result is shown in figure 2.16.

2.4.3 *Theoretical Motivations for* TeV *Studies*

Studies of the TeV radiation from blazars are important in general to constrain the different models of emission, but in the case of 1ES 1218 + 30.4, what makes these

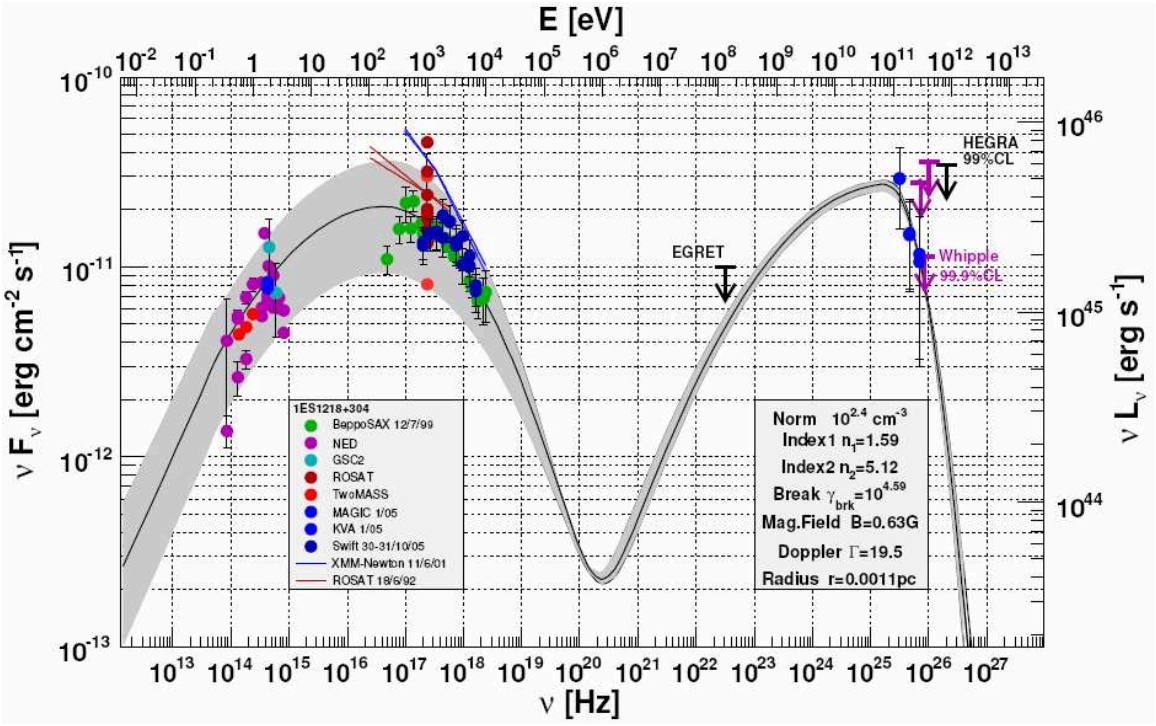

Figure 2.16: SED of 1ES 1218 + 30.4. A best fit SSC model is shown. TeV data have been corrected for the influence of the extragalactic background light absorption. Figure taken from [44].

studies interesting is primarily the distance of this source. At $z = 0.182$, it is the sixth farthest TeV blazar known and the farthest one seen by VERITAS. That means that the effect that the extragalactic background light absorption could have on TeV photons would be very pronounced in this case. This subject is treated in greater detail in chapter 3.

Another reason to pursue further observations of this object is that there are quantum theories of gravity that predict a breakdown of Lorentz invariance at high energies. While some of these theories predict an effect in the gravitational sector [45], others predict modifications in the electromagnetic sector. For example, it is argued in [46] that a quantum gravity modification of the dispersion relation such as that in equation 3.10 would lead to different speeds of propagation for photons of different energies. If, for an explosive event, a bunch of photons are all emitted at the same time, then their arrival time on Earth would be different, depending on their

energy. The time delay between the different photons would be

$$\Delta t \simeq \xi \frac{R}{c} \frac{E_{\gamma_2} - E_{\gamma_1}}{E_{\mathrm{QG}}}, \tag{2.19}$$

where R is the distance to the source, E_{QG} is the effective quantum gravity energy scale and ξ is a constant whose sign is still undetermined. Since the effect is magnified at high energy differences, it might be possible to assess the existence or not of such time delays and put limits on the energy scale at which quantum gravity effects become important by observing TeV γ-ray bursts or flares from blazars. The MAGIC collaboration might just have detected this phenomenon from the nearby blazar Mrk 501 [47]. Since the effect is also magnified by large distances, observation of fast flares from the more distant 1ES 1218 + 30.4 would be even more interesting.

In this thesis, emphasis is put on confirming the detection of 1ES 1218 + 30.4 claimed by the MAGIC group and on using those results to study the effect of the extragalactic background light absorption.

3

TeV γ rays and Extragalactic Background Light

Having introduced blazars in the previous chapter and seen that they can emit γ rays up to TeV energies, it must be realized that it is not immediately obvious that this radiation can reach us on Earth. In fact, there is a process by which TeV photons interact and which renders the Universe not entirely transparent to them; this is reviewed in this chapter.

3.1 Infrared Photons and TeV γ *rays: Pair Production*

When a high-energy photon collides with another photon of lower energy, they can transform into a positron/electron pair:

$$\gamma_{\text{TeV}} + \gamma_{\text{IR}} \rightarrow \text{e}^+ + \text{e}^-. \tag{3.1}$$

For this interaction to happen, though, some minimum energy condition is required for the photons. If the energy of the first photon is E, and that of the second photon is ϵ, then the **threshold condition** is summarized by this relation:

$$\boxed{E\epsilon_{\text{threshold}}(1-\cos\theta) \geq 2m_{\text{e}}^2c^4}, \tag{3.2}$$

where θ is the angle between the photons trajectories. Thus, for a 1 TeV photon to pair produce, it must at minimum collide head-on with a photon of 0.25 eV, *i.e.* an infrared photon, hence the subscripts in equation 3.1.

Not all such collisions above the threshold condition will be successful however. There is still a probability that the process will happen or not and this is quantified by

the cross-section of the interaction, $\sigma_{\gamma\gamma}(E, \epsilon, \theta)$, also called the **opacity per particle**. This interaction cross-section depends on the energy of the photons involved and on the angle of the collision. Its exact computation is rather complex, requiring methods from Quantum Electro-Dynamics (QED); exact and approximate solutions averaged over the directions for an isotropically distributed mono-energetic photon field target are given in [48], [49] and [50]. For the purposes of illustrating the γ ray absorption process, it suffices to know that this function has a peak of $\sim 1.4{\times}10^{-25}\,\mathrm{cm}^2$ situated at $E\epsilon = 3.72\, m_e^2 c^4$, or equivalently at $\lambda[\mu\mathrm{m}] = 1.33E[\mathrm{TeV}]$, and of width such that there is significant absorption of γ rays with photons of energies from $\epsilon/2$ to 4ϵ (a plot will be shown in chapter 7, figure 7.15). Hence a 1 TeV photon can pair produce with a variety of photons above the threshold mentioned earlier, but it is more likely to do so with a 0.875 eV near-infrared photon.

Given the opacity per particle, then, for a target **photon number density** $n(\epsilon, \delta\epsilon, r)$ of an **isotropic photon field** of photon energies between ϵ and $\epsilon + \delta\epsilon$ at location r, the **opacity per unit length** is $\sigma_{\gamma\gamma}(E, \epsilon)\, n(\epsilon, \delta\epsilon, r)$ [1]. The **mean free path**, at location r, of a photon of energy E traveling in this field is just the inverse of that:

$$\Lambda(E, \epsilon, \delta\epsilon, r) = \frac{1}{\sigma_{\gamma\gamma}(E, \epsilon)\, n(\epsilon, \delta\epsilon, r)}. \tag{3.3}$$

Since for a stream of photons $\phi_\gamma(E, r)$ traveling through absorbing material, the number of photons absorbed $(-)\, d\phi_\gamma(E, r)$ in an elemental path length dr is equal to $\Lambda(E, \epsilon, \delta\epsilon, r)^{-1}\, dr$, it follows that the observed flux at distance R from the source is modulated by a negative exponential:

$$\phi_\gamma(E, R) = \phi_\gamma(E, 0) e^{-\int_0^R \int_{\epsilon_{\mathrm{threshold}}}^{\epsilon_{\max}} \frac{1}{\Lambda_\epsilon(E,\epsilon,r)}\, d\epsilon\, dr}, \tag{3.4}$$

or

$$\boxed{\phi_\gamma(E, R) = \phi_\gamma(E, 0) e^{-\tau(E,R)}}, \tag{3.5}$$

where the quantity in the exponent is called the **optical thickness** for the photon of energy E. It is the number of mean free path lengths along the distance R and

[1] Here, $\sigma_{\gamma\gamma}(E, \epsilon)$ is $\sigma_{\gamma\gamma}(E, \epsilon, \theta)$ averaged over θ for an isotropic target photon field.

integrated over the different energies, encountered in the target photon field ($\epsilon \in [\epsilon_{\min}, \epsilon_{\max}]$), that permit pair production ($\epsilon \geq \epsilon_{\text{threshold}}$):

$$\boxed{\tau(E,R) := \int_0^R \int_{\epsilon_{\text{threshold}}}^{\epsilon_{\max}} \sigma_{\gamma\gamma}(E,\epsilon)\, n_\epsilon(\epsilon,r)\, d\epsilon\, dr}, \tag{3.6}$$

where $n(\epsilon, \delta\epsilon, r)$ has been replaced by its spectral counterpart $n_\epsilon(\epsilon, r)$ [2] to carry the integration over the energies.

To recapitulate, what these equations say concretely, in the context of TeV blazar observations, is that if very-high-energy γ rays travel in a medium where there are infrared photons present, then pair production is a process that can restrict the number of γ rays detected[3]. Thus, in order to study the emission mechanisms of such blazars, the observed spectra must be compensated for absorption to recover the true intrinsic spectrum. The question of how severe the attenuation at a given frequency is and therefore what correction factor must be applied, depends on the value of τ, and more precisely, since $\sigma_{\gamma\gamma}$ is a known function, the question really is: what is the value of $n_\epsilon(\epsilon, r)$? *i.e.* what are the properties of the absorbing photon field?

3.2 Extragalactic Background Light

A first soft photon field capable of producing absorption originates directly in the source environment of TeV blazar, being due to thermal emission from the dusty torus or accretion disk for example. However, this is not the photon field that is of interest here, since it is **already taken into account by the emission models** introduced

[2] $n_\epsilon(\epsilon, r) := \frac{\partial n(\epsilon, \delta\epsilon, r)}{\partial(\delta\epsilon)}$ has dimensions of number of photons per unit volume per unit energy and is normally expressed in units of photons/(cm^3 eV). For graphical representations, the related quantity $\nu I_\nu = \frac{c}{4\pi} u(\epsilon, r) := \frac{c}{4\pi} \epsilon^2 n_\epsilon(\epsilon, r)$ is often plotted instead. This usually has units of nW/(m^2 sr). The conversion equation from one quantity to the other in the units mentioned above is $\frac{\nu I_\nu [\text{nW/(m}^2\,\text{sr)}]}{\epsilon^2 n_\epsilon(\epsilon,r)[\text{photons/(cm}^3\,\text{eV)}]} = 3824\, \frac{\text{nW}}{\text{m}^2\,\text{sr}}\, \frac{\text{cm}^3}{\text{eV}}$.

[3] While pair production reduces the number of γ rays of a certain frequency, the pair created may induce inverse Compton scattering on a soft ambient photon, creating a new γ ray of lower frequency. Equation 3.5 can be used if **the production of second-generation γ rays from the absorption debris that re-enter the beam can be neglected**. This is discussed in [50] and is indeed expected to be a small effect in the context discussed in this chapter.

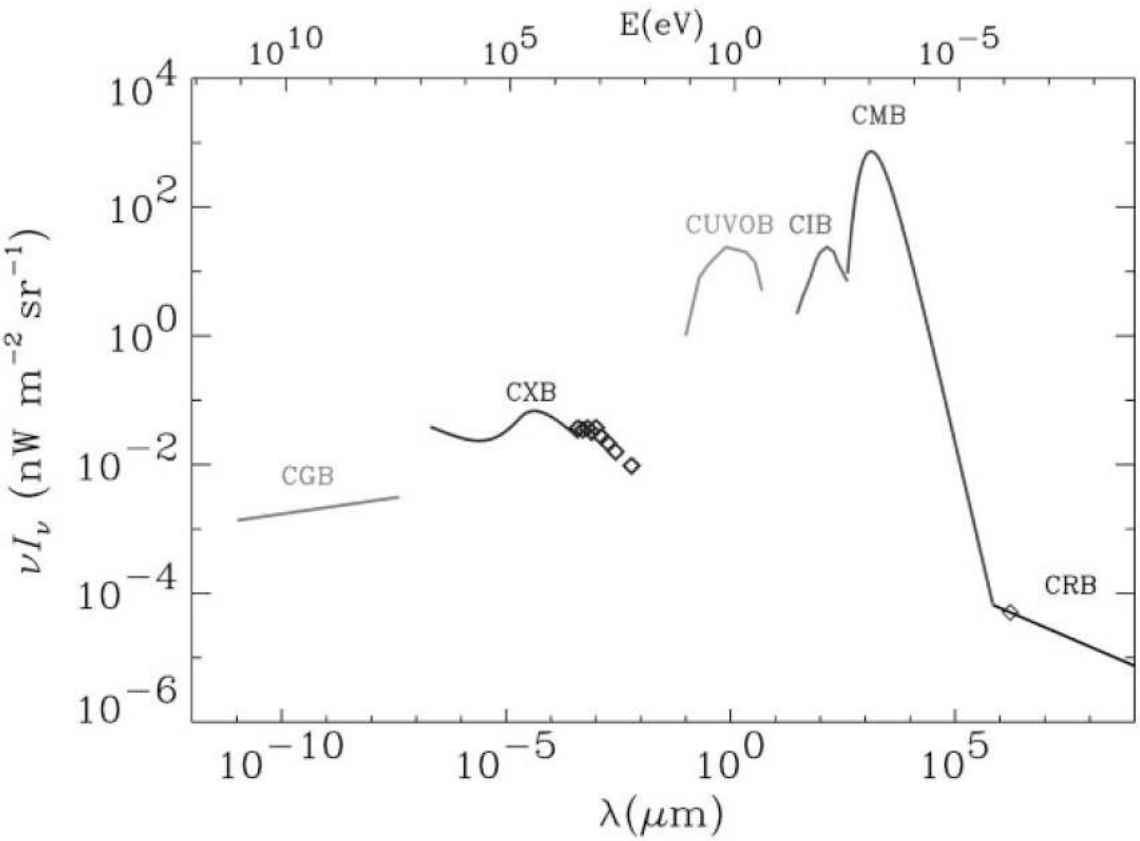

Figure 3.1: SED of the broadband cosmic background radiation. Figure taken from [54].

in the previous chapter, which must include this effect if they are to describe the radiation properly. What is of interest here is the effect of **Cosmic Background Radiation (CBR)** fields on the propagation of γ rays on extragalactic distance scales. The first person to think about the importance of this was Nikishov in 1962 [51], even before the discovery of the Cosmic Microwave Background (**CMB**) in 1965, after which Gould and Schréder in 1966 [52], and Jelley in 1966 [53] showed that the Universe would be opaque to γ rays of energy greater than 100 TeV.

In fact the Universe is permeated by many background fields as figure 3.1 shows. There is of course the well known CMB, which is the most important one in terms of power, but there are also backgrounds at all other wavelengths: the **CRB** (radio), the **CIB** (infrared), the **CUVOB** (UV and optical), the **CXB** (X-ray) and the **CGB** (γ-ray). These fields originate from important events in the evolution of the Universe and as such they carry information about its history. Since it was shown

that near-infrared photons are the most likely ones to interact with TeV radiation, the CIB is of greater concern here, but also the CUVOB since photons of higher energy can contribute to absorption too. The CIB, also referred to in the literature as the InfraRed Background (IRB), and the CUVOB are part of the **Extragalactic Background Light (EBL)** (a.k.a the Intergalactic Background Light (IBL) or the Diffuse Extragalactic Background RAdiation (DEBRA)), which embeds information about the structure formation ($z \sim 10^2$), reionisation ($z \sim 10$) and star formation peak ($z \sim 1$) epochs. More specifically, the EBL is mainly composed of two components. The first one is light from stellar emission and the second one comes from dust absorption and re-emission of the stellar emission. Assuming, then, that the **EBL light comes from galaxies**, where both of these processes occur, and that **the SED, the distribution, and the evolution of galaxies is known to sufficient accuracy as a function of their luminosity**, it is possible to estimate what the EBL should be[4]. This is what the authors of [56] have done and their result for the density of the extragalactic background light is shown in figure 3.2. This gives a first trial answer to the question of what is $n_\epsilon(\epsilon, r)$? Using that result, they go on and compute the optical thickness, which is plotted in figure 3.3.

The conclusions are clear from this graph; if the extragalactic background light density is as expected from the estimate, then very-high-energy radiation will suffer significant absorption in traveling through the Universe, and that even for relatively nearby objects. There thus exists a limit to how far TeV sources can be if their emission is to reach us in detectable amounts. This horizon seems to restrict sources to be within much less than a redshift of 0.5, unless the source has a fantastically high flux to start with. This may explain why all of the TeV blazars detected so far have $z \leq 0.35$ [2], why much fewer blazars are seen in this regime than at other wavelengths and why γ-ray bursts remain undetected at these energies.

Note: in computing the optical thickness to γ rays from models of the photon

[4]This is only one way of proceeding, other methods of predicting the EBL exist and are reviewed in [54]. Another one of the most popular models is that of Primack et al. [55], it is often used in deriving limits on the EBL from TeV observations.

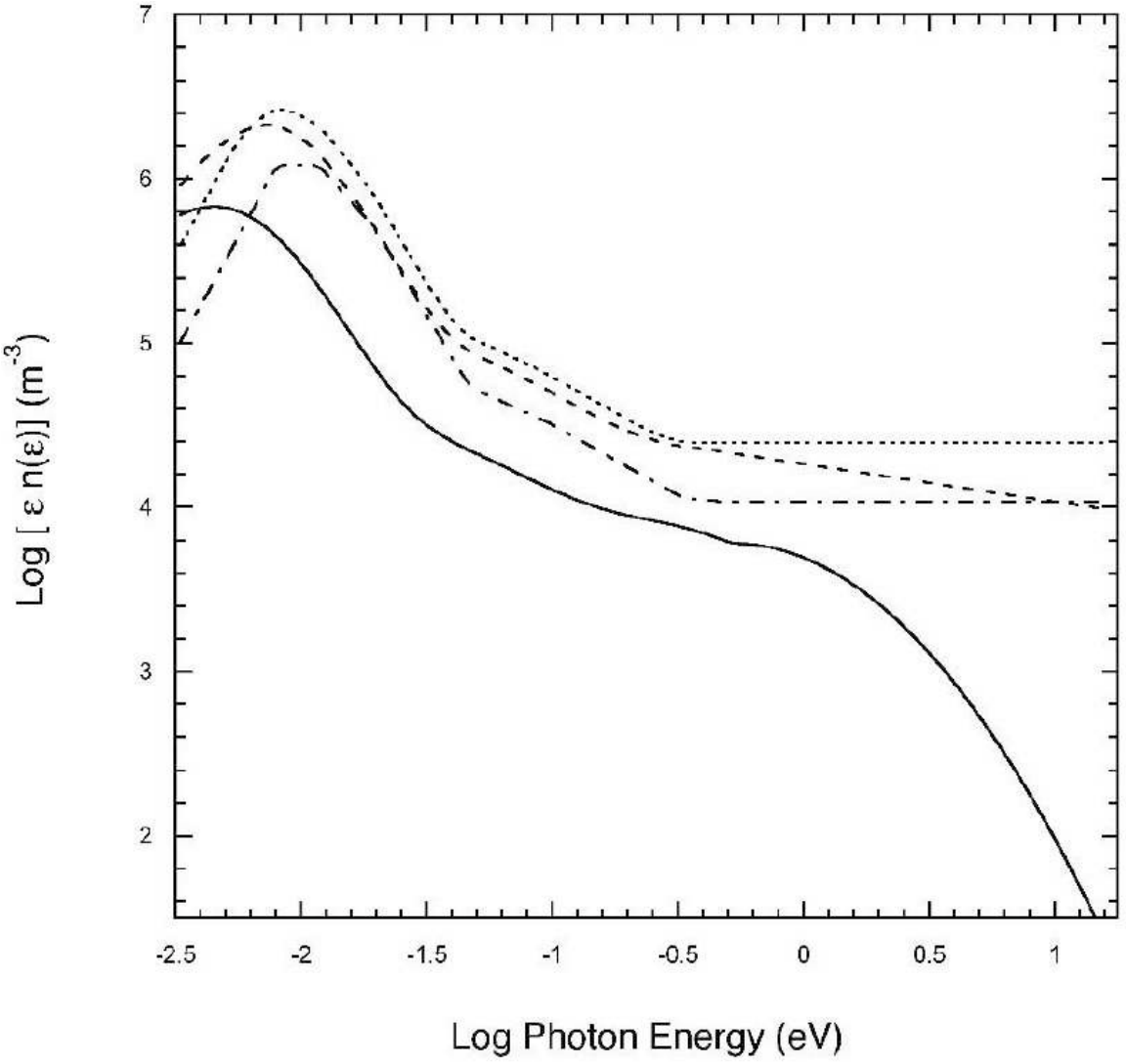

Figure 3.2: Photon density of the extragalactic background light estimated from galaxy SEDs, distributions and evolution (fast evolution model assumed here for the IR). The solid line is the result for $z = 0$ while the other ones are for redshifts of 1 (dashed), 3 (dotted) and 5 (dot-dashed). The x-axis corresponds to the energy ϵ in the text, it goes from the far-infrared to the UV. Figure taken from [56].

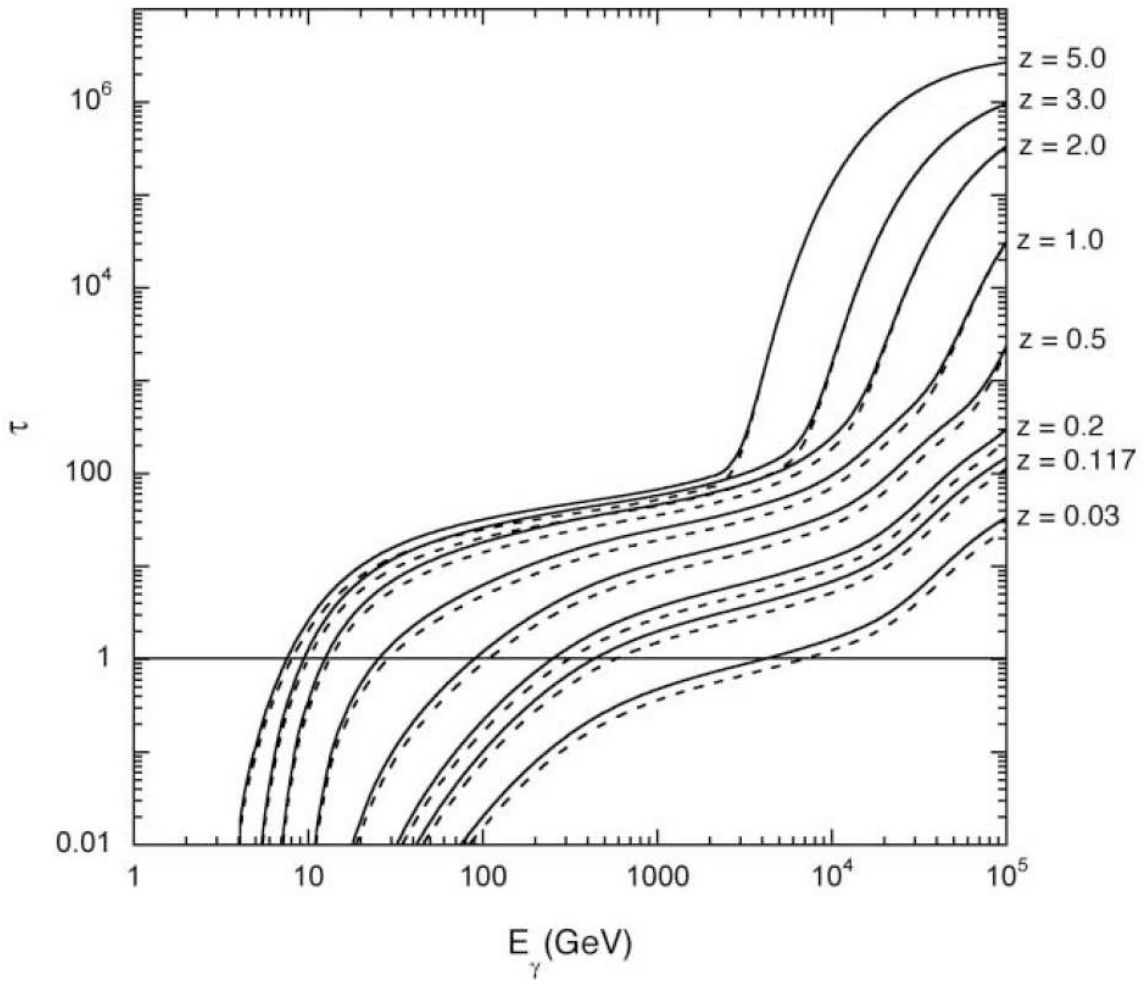

Figure 3.3: Optical thickness of the extragalactic background light to γ rays for different source redshifts and different evolution models (fast evolution = solid curves, baseline evolution = dashed curves). When $\tau < 1$, the region of space traveled by the γ rays of the corresponding energy is optically thin, whereas when $\tau > 1$ it is optically thick, *i.e.* the γ rays will most likely be significantly absorbed before reaching the observer. The quick rise at lower energies reflects the effect of interactions with the CUVOB bump in the EBL SED. The almost plateau-like behavior in the middle of the curves is due to the near to mid-infrared descent into the EBL SED valley (see figure 3.4). The quick rise at higher energies is mainly due to interactions with the far-infrared and CMB. The x-axis corresponds to the energy E in the text. Figure taken from [56].

density, the redshift dependence of $n_\epsilon(\epsilon, r(z))$ is not always given. Since all known TeV blazars have relatively low redshifts ($z \ll 1$), the simplifying assumption that one can **neglect the evolution of the EBL with redshift**, *i.e.* the assumption that $n_\epsilon(\epsilon, r) \approx n_\epsilon(\epsilon, R) =: n_\epsilon(\epsilon)$, where $R = r(z = 0)$, is usually done. This allows one to perform the r integration in equation 3.6 and to factor it out. This will be implicitly understood in the following[5].

3.3 Extragalactic Background Light Observations

Based on the estimate of the extragalactic background light given above, it appears clear that the EBL will have an effect on the spectrum of TeV blazars. However, it would be nice to know how reliable this estimate is and to compare it to experiment. In fact the best way to answer the "what is $n_\epsilon(\epsilon)$?" question would be to measure it directly. Unfortunately, measuring the EBL is notoriously difficult because of the strong foregrounds from the atmosphere, from zodiacal and galactic light, and from the instruments themselves. Some measurements could nevertheless be achieved and are reviewed in [54]. The first attempts were made with instruments on board rockets and then with the Infrared Astronomical Satellite (IRAS), but it was not until the advent of the COsmic Background Explorer (COBE) satellite, launched in 1989, that believable detections were attained. To date, the COBE results remain the best available direct data on the EBL and are confirmed by the more recent (1995) results from the Near InfraRed Spectrometer, another satellite-based experiment. Other types of measurements can yield limits on the amount of EBL. Among these are studies of the fluctuations in the EBL. These are a little easier to perform because they do not require absolute calibration of the instrument. Some results were derived from ground-based as well as from space-based observations, but they might be model dependent because they depend on the distribution of sources contributing to the

[5] Since for $z \ll 1$, $R \approx cz_{\text{source}}/H_0$, where H_0 is the Hubble constant, this also implies that $\tau \propto H_0^{-1}$. Also, upper limits on the photon spectral density derived in other works from TeV observations, *i.e.* from techniques that used observations of τ, can be scaled for different assumptions on the Hubble constants according to $\nu I_\nu \propto H_0$.

EBL. Other limits are derived from galaxy number counts. Since the EBL comes mostly from galaxies, their integrated light yields a strict lower limit on its value.

A comparison of the most reliable experimental results with the predicted SED of the model given in [56] is plotted in figure 3.4. Although the general shape of the spectrum is relatively well described, which argues in favor of a good understanding of the physical processes, this particular model seems to underestimate the EBL power at lower frequencies and to overestimate it at mid frequencies. At higher frequencies, the agreement is good, but the error bars are larger in that region. The overall moderate agreement casts some doubts about the ability of models to properly describe the absorption of TeV γ rays.

It appears, then, that even with measurements and limits, the situation remains somewhat uncertain because 1) the entire frequency range spanned by the EBL could not be successfully covered by experiment (at some frequencies, the EBL is too faint and was undetectable above the foreground); 2) the uncertainty associated with some measurements is relatively large due to the difficulty in subtracting the foreground; 3) some measurements at the same frequencies, but using different methods *e.g.* space-based *vs* ground-based, disagree, again plausibly because of difficulties in identifying correctly the foreground (see [57] for an example). Closer study of the data from Spitzer, the latest space-based infrared telescope will help resolve some of these problems. In the mean time, while it may seem difficult to predict accurately the amount of absorption suffered by very-high-energy γ rays[6] and from there extract a correct intrinsic spectrum, some people have turned the table around and started using TeV observations and our current understanding of emission processes as a tool to help constrain the EBL density; if our knowledge of the EBL is too poor to let us study the heart of blazars, maybe what we already know of them is good enough to help cosmologists understand better the structure and star formation history of the Universe? Equation 3.5 really is a case of one equation and two unknowns. Here, however, it

[6]It should be noted that [56] correctly reproduced the spectrum of the TeV blazar PKS 2155 -304 using their model and a generic blazar intrinsic spectrum, which supports the accuracy of their result.

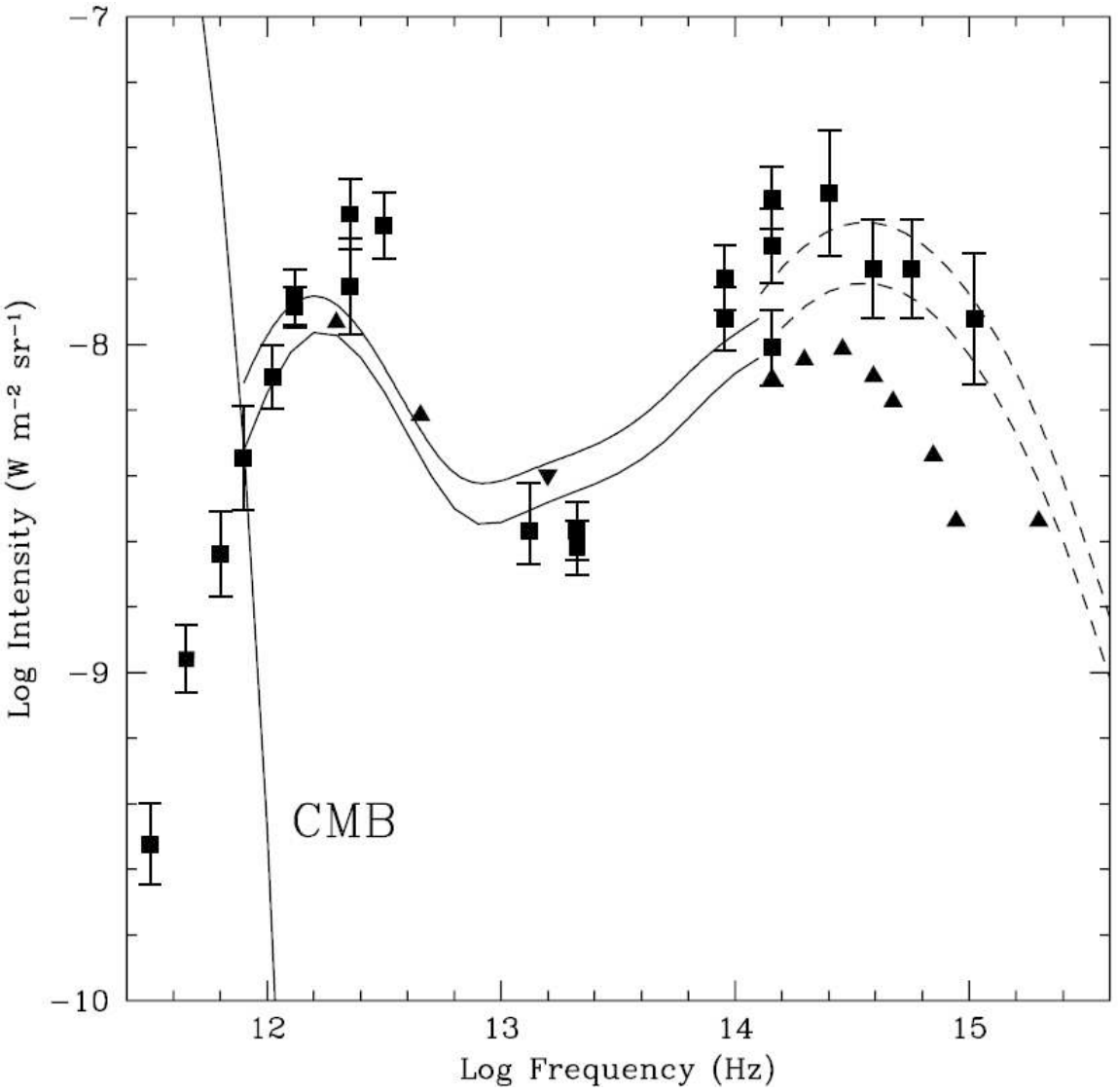

Figure 3.4: SED of the extragalactic background light; the two components of the EBL, star light and dust reemission, are clearly visible. The curves are obtained from the estimated EBL density of [56] for their fast (upper) and baseline (lower) evolution models. The data points are shown with error bars, the triangles pointing up with no error bar are lower limits from galaxy number counts and the triangle pointing down is an upper limit from TeV observations. The almost vertical line on the left represents the CMB spectrum. Figure taken from [56].

is believed that reasonable assumptions on the **intrinsic spectrum** $\phi_\gamma(E, 0)$ can already be made that impose limits on $\tau(E, R)$ and hence on $n_\epsilon(\epsilon)$.

The first attempts at doing so are reviewed in [54]. These searches concentrated on the spectral examination of Mrk 421 and Mrk 501, which were the only well studied TeV blazars at the time. At redshifts of $z = 0.031$ and $z = 0.034$, respectively, these objects are relatively close by and so it was not obvious that absorption features would be significantly detected. Since absorption generally increases with energy, a steepening of the spectrum past a certain energy was one of the expected signatures. However, it was difficult to show that such changes of shapes were not intrinsic to the source. In fact, models with no absorption at all have been as successful in fitting the early data as models that included absorption effects. In 2000-2001, Mrk 421 exhibited an exceptional flaring episode that allowed the spectrum to be measured at different flux levels. The results, displayed in figure 3.5, show that while the spectrum hardens with higher flux state, which can be interpreted as the peak of the high-energy spectrum shifting toward higher energies, the cut-off point remains at the same energy [58]. This suggested that the cut-off in the spectrum was not an intrinsic property of the source and was therefore indeed due to the absorption. However, the cut-off point in the spectrum of the equally distant Mrk 501 was found to be slightly incompatible with that of Mrk 421, implying that the steepening might not entirely be due to extragalactic background light absorption [59].

Whether the cut-offs in the Mrk 421 and Mrk 501 spectra are indeed due to absorption effects or not, the fact that γ rays of energies up to about 10 TeV have been detected suggests at least that $\tau(10\,\mathrm{TeV}, z = 0.03)$ is not too high. From this observation, limits were obtained on the normalization of the early EBL models. Other estimates of τ, and thus other limits, were obtained from considerations on the intrinsic spectrum of the sources based on modeling of their emission processes within the SSC framework [54].

The astute reader will have noticed that a constraint on $\tau(E, R)$ does not yield a definite constraint on $n_\epsilon(\epsilon)$. This is because the shape of the function $n_\epsilon(\epsilon)$ is

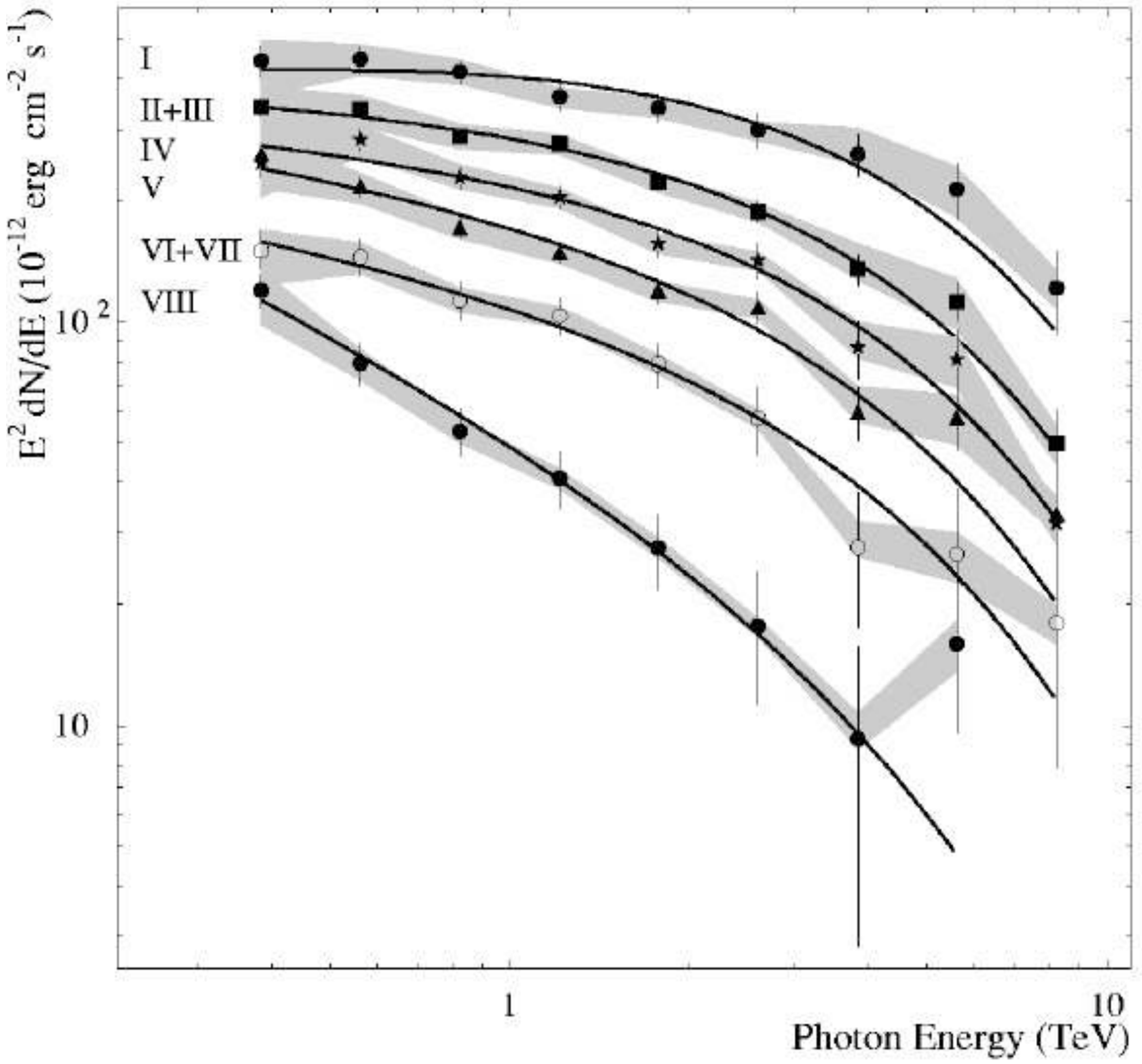

Figure 3.5: Spectral variability of Mrk 421. The spectrum hardens with higher flux states, but the cut-off point stays around 4 TeV, suggesting that the cut-off might be due to absorption effects external to the source. Curves represent a power-law fit to the data, with exponential cut-off. Figure taken from [58].

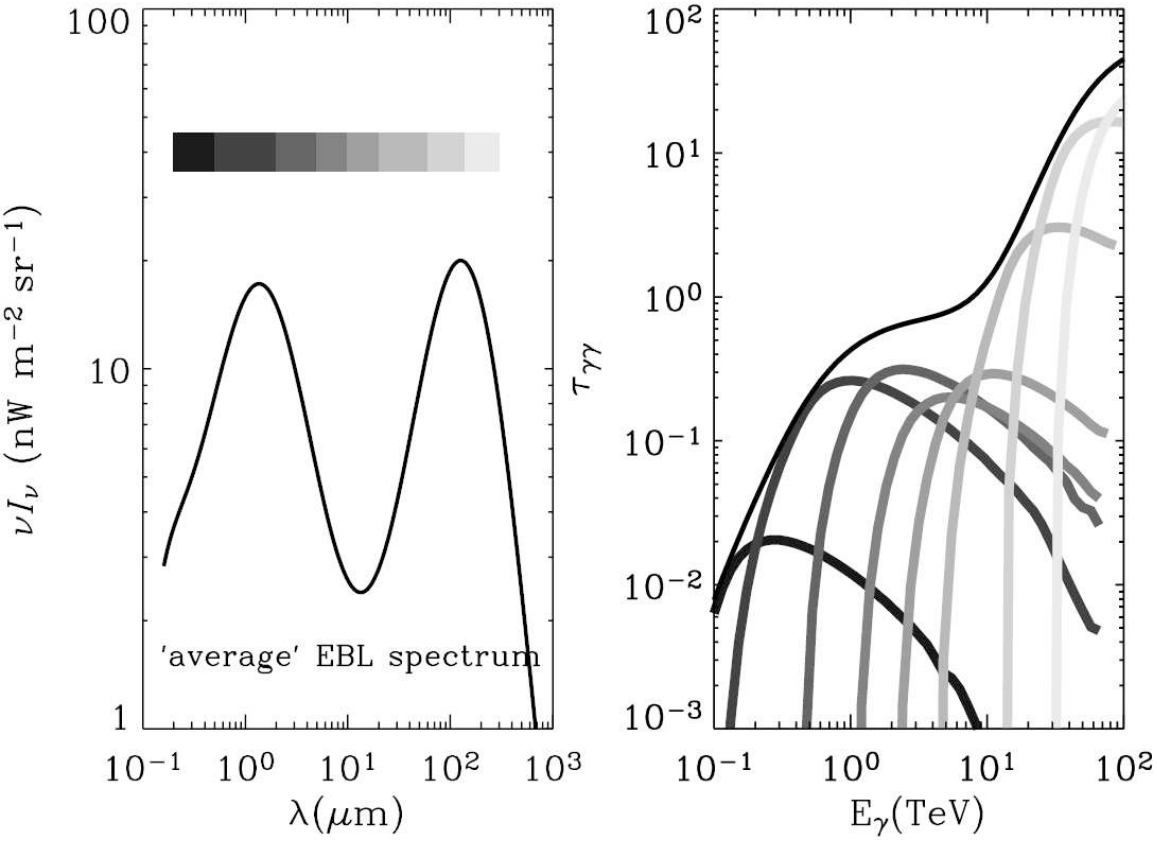

Figure 3.6: An average EBL density shape (CMB contribution omitted) accompanied by the associated optical thickness curve that it generates. The scale of shadings in the left panel defines ranges of wavelengths for the photons constituting the EBL. The right panel shows the contribution to the optical depth of each of these ranges. Figure taken from [60].

integrated over in equation 3.6. If $\sigma_{\gamma\gamma}$ was a *very* narrow peak, then one could constrain $n_\epsilon(\epsilon)$ at a single energy ϵ. But it has some significant width as mentioned previously and this means that a high-energy photon can interact with any from a variety of low-energy ones to pair produce. The constraint is thus globally on that part of the $n_\epsilon(\epsilon)$ curve that is enhanced by the interaction cross-section $\sigma_{\gamma\gamma}$; it is not a constraint at a particular ϵ. To illustrate this, figure 3.6 shows the contributions of different EBL wavelengths to the attenuation of high-energy photons of energy E. The shape of the EBL density curve is therefore seen as having a complex influence on the propagation of γ rays, making it difficult to relate a given opacity to a particular curve; different curves could in principle result in the same opacity at least for a partial range of energies. That is why in deriving limits on $n_\epsilon(\epsilon)$, one usually needs

to make an assumption on the **spectral *shape* of the EBL**. Once the shape is integrated over together with the cross-section, the limit really is on its normalization factor.

The complex role of the shape of the EBL density curve also renders searches for cut-offs in the spectra of TeV blazars as evidence for absorption by the extragalactic background light a little tricky. The reason for this is that not only can a cut-off be due to a feature of the source's acceleration mechanism rather than to absorption, a cut-off is not always a predicted consequence of a given EBL scenario. For example, [50] shows that if the EBL density falls as λ^{-1} in the near to mid-infrared range, then τ is flat in the region going from 1 to several TeV. This results in all frequencies in that range being attenuated equally and no cut-off appears in the TeV observations. Hence, the presence of a cut-off may be linked to absorption if effects intrinsic to the source can be discarded, but its absence does not indicate that absorption is not taking place. A recent study using a collection of allowable EBL scenarios confirms this possibility of having marginal steepening of the spectra in the range of interest to ground-based γ-ray observatories [61]. However, this study emphasizes that it is the ratio of the near to mid-infrared density of the EBL that governs the presence or absence of a spectral break around 1 TeV; under a given scenario, a spectral cut-off is expected (spectral softening), under another one, a decrease in the spectral index is foreseen (spectral hardening), and under yet another one, no spectral change is seen. If there is a break though, its magnitude is expected to be relatively small for nearby sources, but to be amplified with redshift. Also, this has a weak dependence on the intrinsic spectral index, which could help in constraining the EBL without assuming too much on the sources properties.

Since blazars at higher redshifts will suffer more absorption, especially at higher energies, another possible effect is that even if no spectral break is visible in the data, the spectrum of blazars could nevertheless get increasingly steeper with distance. Such a correlation was indeed claimed to have been observed in 2005 using the data from six TeV blazars [62]. However, the number of detected blazars has

more than doubled since then, mostly due to the start of operations of the H.E.S.S. collaboration's detectors, and a more recent study does not confirm the trend [63]. Instead, a plot of spectral index *vs* redshift, figure 3.7, shows a lot of scatter with no convincing evidence for increased spectral steepening at higher redshift. The authors of this paper explain that this could be due to a selection effect: at higher redshifts, it is easier to detect sources that are in increasingly more active state, which seems supported by the data, and have thus a harder spectrum according to the SSC emission model. This effectively cancels the steepening effect of the increased absorption at larger distances. [63]

Even though the redshift correlation observed in [62] does not seem to hold in view of the new data, this paper nevertheless introduced a new way of deriving upper limits on the EBL density, a method that can actually free us from making an assumption on the overall EBL spectral shape. As mentioned before, the width of the cross-section $\sigma_{\gamma\gamma}$ has the effect that it is not only a single point, but a whole *segment* of the $n_\epsilon(\epsilon)$ curve that effectively participates in the absorption of γ rays of a given energy. However, at a particular ϵ', there is a fundamental limit to how large $n_\epsilon(\epsilon')$ can be in a small interval $\delta\epsilon$ in order not to imply an attenuation greater than the observed one, no matter what the rest of the $n_\epsilon(\epsilon)$ curve looks like at $\epsilon \neq \epsilon'$. This limit turns out to be

$$n_\epsilon(\epsilon')\delta\epsilon \leq \frac{\tau_{\mathrm{m}}(E' := \frac{0.93\times10^{12}\,\mathrm{eV}^2}{\epsilon'}, R)}{R\sigma_{\gamma\gamma\mathrm{max}}}, \tag{3.7}$$

where $\tau_{\mathrm{m}}(E', R)$ is the measured opacity at the energy E' most absorbed by the background photons of energy ϵ', *i.e.* at the energy where the cross-section function is at its peak value $\sigma_{\gamma\gamma\mathrm{max}}$.

In 2005, the authors of [60] developed yet another interesting approach for constraining the density of the extragalactic background light without assuming one of the available theoretical models for computing $\tau(E)$ up to a normalization factor and constraining this factor based on assumptions about the intrinsic spectrum of sources. Instead, they created a series of 12 empirical scenarios consistent with the available

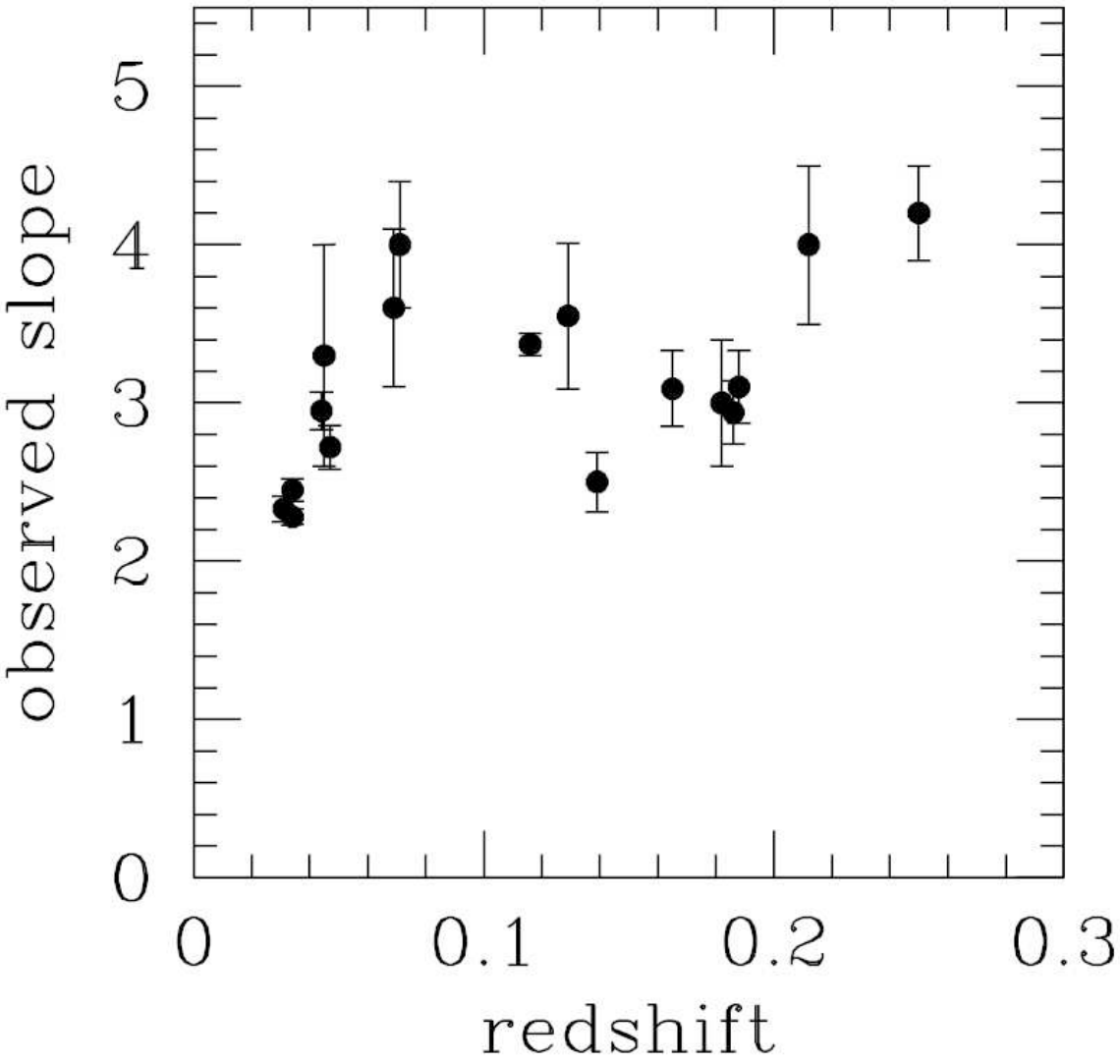

Figure 3.7: Spectral index *vs* redshift for 15 TeV blazars. No solid trend is apparent. Figure taken from [63].

direct measurements and limits of the EBL. With these scenarios, they computed the intrinsic spectrum of Mrk 421 and Mrk 501 and rejected the scenarios that produced intrinsic spectra that resulted in an exponential rise at high energies. Such intrinsic spectra are not expected by theory, except in very exotic models built to explain such features, and are considered to be unphysical. Only 5 of the 12 general possibilities were rejected, but the approach was interesting in that it relied very weakly on assumptions about the intrinsic source spectrum and did not use the shape of theoretical EBL models at all. Instead, the correct shape of the EBL is effectively left as a free parameter to be constrained by the data.

A similar approach[7] was applied in [64], which can be thought of as an extension of the previous idea. Rather than building a collection of plausible scenarios by hand, they divided the $n_\epsilon(\epsilon) - \epsilon$ plane into a grid and kept only the grid points that are consistent with current direct data and limits. They then formed a collection of more than 8 million possible curves by joining the remaining grid points with weighted spline functions. These curves are then constrained as before by keeping only those that result in plausible intrinsic spectra, except that now the data from eleven TeV blazars were used. The spectra that were used are shown in figure 3.8. The upper limits on the EBL spectral photon density were computed for two cases, a *realistic* one where the intrinsic spectral index derived is not expected to be lower than 1.5 according to mainstream theory [65], and an *extreme* case where the intrinsic spectral index is allowed to be as low as 2/3, as hypothesized to be possible in some situations[8]. The most constraining blazars were found to be Mrk 501, H 1426 + 428 and especially the more distant ($z = 0.186$) 1ES 1101 - 232, for the near to mid-infrared wavelengths. The results are shown in figure 3.9, which summarizes well the situation as it displays what are arguably the best combined limits obtained so far from TeV blazars studies (with minimal assumptions about the intrinsic sources spectra and the EBL spectral

[7] This approach will be explored in more detail in section 7.2.

[8] The rationale behind these assumptions relies on theoretical modeling of the processes occurring in the jets and goes beyond the scope of this thesis; some of the considerations involved are explained in [64].

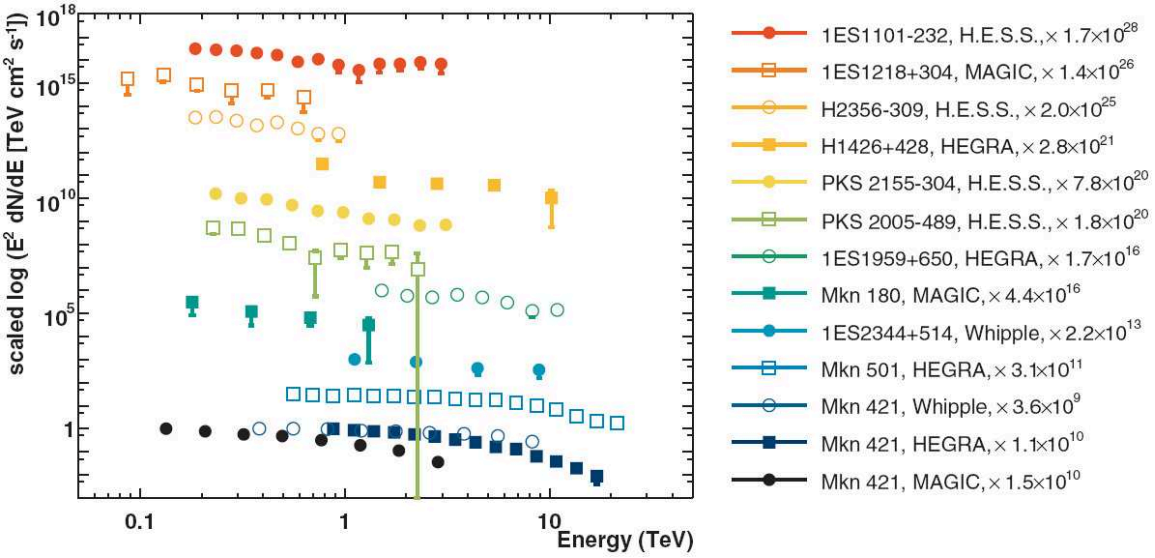

Figure 3.8: Spectra of eleven TeV blazars used to constrain the EBL spectral photon density. The spectra are scaled to avoid cluttering and are arranged in order of increasing redshift, with the lowest redshift at the bottom of the plot. Figure taken from [64].

density shape) together with the detections and limits from direct measurements, and the predictions from theoretical and semi-empirical EBL models. What stands out is that these new limits are in conflict with some of the direct measurements in the near-infrared, which supports the hypothesis that zodiacal light residuals were badly subtracted from the measurements. Also, in the mid-infrared range, where direct measurements are particularly difficult to achieve, the limits from blazars are the most constraining ones, which shows the importance of pursuing TeV observations. Although none of the theoretical models is seriously constrained by the TeV results, the graph suggests that this could change soon with the observations of more blazars. Note that some of the models are however already in danger from galaxy count lower limits.

During the course of 2007, the situation continued to evolve rapidly thanks to new detections from ground-based γ-ray observatories. The object 1ES 1101 - 232 is at a redshift $z = 0.186$ and has a very hard spectrum making it particularly interesting. It has been included in the study mentioned above as well as in other, less sophisticated, EBL investigations that arrived at similar conclusions [66] [67] [65]. The BL Lac 1ES 0347 - 121 was also discovered at a similar redshift $z = 0.188$ and observed with

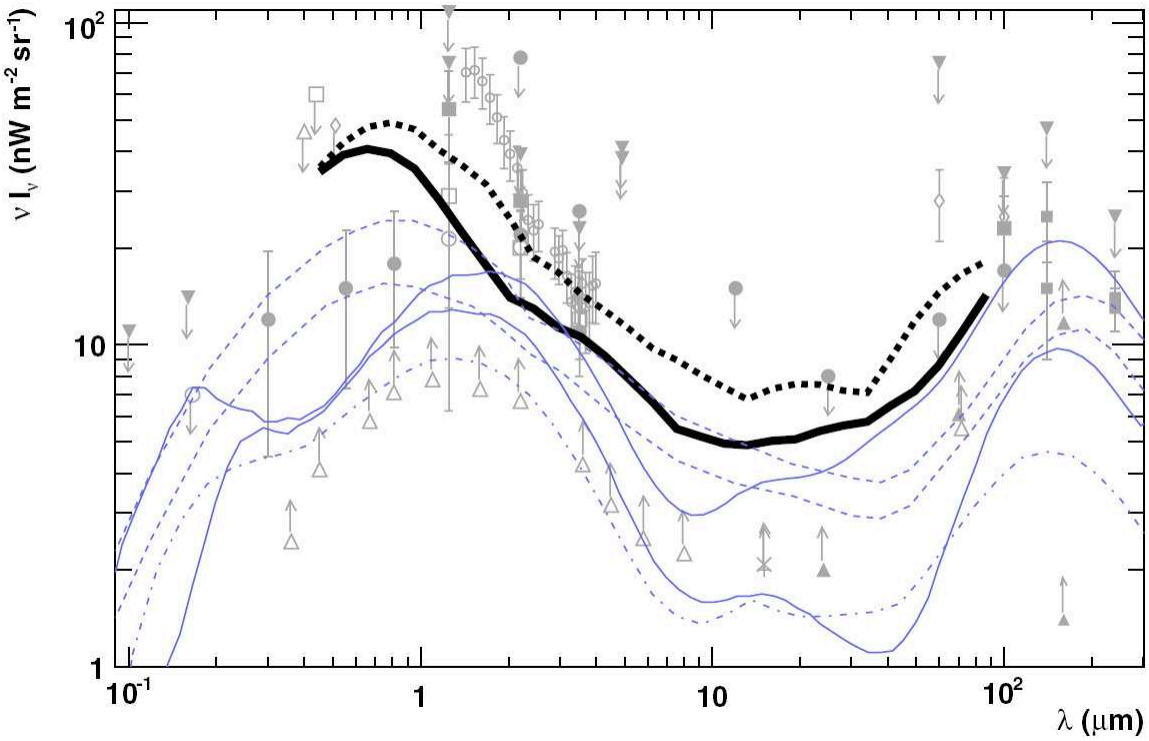

Figure 3.9: Limits on the EBL spectral photon density. Thick solid black curve: combined limits from eleven TeV blazars, realistic case. Thick dashed black curve: same as previous, but extreme case. Thin solid blue curves: updated Kneiske et al. model, high and low. Thin dashed blue curves: Stecker et al. models, fast and baseline evolution. Thin dashed dotted curve: Primack et al. model. Grey markers: direct measurements and limits. Figure taken from [64].

a similar spectral index [68]. The constraints derived for this case are also similar to those obtained from the previous object. Then, the blazar 1ES 0229 + 200 was detected at TeV energies [69]. At an intermediate redshift of $z = 0.1396$, it is closer than the other ones discussed here, but it is a much harder source, with an observed spectral index of about 2.50 and observable from 500 GeV up to 15 TeV. This source is thus able to constrain the mid-infrared part of the EBL spectrum more effectively than other ones and analysis with a predefined EBL model confirms that the EBL SED in this region is only slightly above the source counts lower limits. However, a reanalysis in [70] suggests that the limit should be loosened a bit, arguing that intrinsic spectral indices between 1.0 and 1.5 are obtainable in theory [71].

In summary, TeV observations of blazars are a useful tool in studying the extragalactic background light spectrum, especially since they can give a handle to tackle the problem in a range of energies where direct measurements are difficult to perform. Various methods have been used in the past. All of them require an assumption about the intrinsic source spectrum, either by modeling the source or by setting a limit on the intrinsic spectral index, and most of them require an assumption about the EBL shape too, but some clever analyses manage to escape that one. This is particularly important because any error in the EBL shape is amplified by the exponential function in equation 3.5. The fewer assumptions there are, the more robust the limit will be. Also, the energy calibration of the TeV instruments is important because a systematic shift of energies of $\sim 15\%$ can change the conclusion of EBL studies as shown in [60].

A result that seems to emerge is that the EBL density is close to the lower limits set by the galaxy count observations, leaving little room for components from other sources. Consequently, the Universe appears to be more transparent to TeV γ rays than previously thought. This could translate into a greater number of TeV blazars being detected at even greater distances, *e.g.* the recently observed PG 1553 + 113 might set a record for the farthest observed blazar. Its redshift is not yet confirmed, but is expected to be $0.30 < z < 0.56$ [72]. This finding that blazars are observable

from farther away may be the result of a low EBL density as suggested here, and this is the simplest explanation, but if it eventually comes to contradict other more direct measurements it could also lead to the reconsideration of other assumptions. An explanation could be that the emission processes of blazars are not well understood and that one is not evaluating the intrinsic spectrum correctly, underestimating the power at very-high energy. Another one would be that the physics of the absorption process is not as expected. This possibility is discussed next.

3.4 Pair Production and Lorentz Invariance Violation

In light of the MAGIC result that a quantum gravity effect might have been observed for the first time in the light curve of a TeV blazar (previously mentioned in section 2.4.3), it becomes interesting to note that a breakdown of Lorentz invariance could have consequences on the absorption process of γ rays by the extragalactic background light.

This idea emerged in 1999 in [73], and it built on a proposal from [46] that the energy-momentum relation of special relativity could need modification due to quantum gravity effects. Not only would this lead to dispersion in the arrival times of photons of different energies, it would also modify the threshold condition of pair production. In such a framework, the **dispersion relation of particle species i is modified by quantum gravity** in a way that the ordinary momentum $\vec{p}_i^{\,2}$ is altered by a function f_i of energy that parametrizes an effect suppressed by the quantum gravity scale $E_{\rm QG}$ [9]. The resulting modified momentum is given by

$$c^2\vec{q}_i^{\,2} = c^2\vec{p}_i^{\,2}\left[1 + f_i\left(\frac{E_i}{E_{\rm QG}}\right)\right] \tag{3.8}$$

$$= (E_i^2 - m_i^2c^4)\left[1 + \xi_i\frac{E_i}{E_{\rm QG}} + \mathcal{O}\left(\frac{E_i^2}{E_{\rm QG}^2}\right)\right] \tag{3.9}$$

$$\approx E_i^2 - m_i^2c^4 + \xi_i\frac{E_i^3}{E_{\rm QG}}, \tag{3.10}$$

[9] $E_{\rm QG}$ is usually taken to be the Planck mass $M_{\rm Planck}c^2 = 1.22\times10^{19}$ GeV, but some theories predict it could be much less than that.

where only the leading term that grows with energy has been kept, and where ξ_i quantifies the strength of the correction (can be positive or negative depending on the quantum gravity scenario) and is usually taken of order 1.

With the assumptions that **the laws of energy and momentum conservation are unmodified in the new physics**, it can be shown that with such dispersion relations for the photon and the electron, the equation 3.2 for the threshold condition of pair production becomes

$$\epsilon_{\text{threshold}} = \frac{m_e^2 c^4}{E} + \frac{E^2}{4E_{\text{QG}}}\left(\xi_\gamma - \frac{\xi_e}{2}\right), \tag{3.11}$$

for head-on collisions [73].

Under the modified dispersion relations scheme, it can also be shown that the speed of particles is now given by

$$v_i(E_i) := \frac{\partial E_i}{\partial q_i} \approx c\left(1 - \frac{m_i^2 c^4}{2E_i^2} - \xi_i \frac{E_i}{E_{\text{QG}}}\right). \tag{3.12}$$

Note that this is not the limiting speed of the particle, it is its speed at energy E_i with $m_i c^2 \ll E_i \ll E_{\text{QG}}$. The limit speed c_i, when $E_i \to \infty$, is not dictated by the second term, which goes to zero in this case, it is dictated by the quantum gravity term. However, $E_i \to \infty$ cannot be taken in this equation because the quantum gravity corrections were only kept to first order and are linear in E_i. It can be hypothesized, though, that the combined effect of the full corrections may lead to $c_i \neq c$ and one could write the difference as $c_i =: c(1 - \delta_i)$. While the exact δ_i is not known here, we may define an energy dependent correction $\delta_i(E_i) := \xi_i \frac{E_i}{E_{\text{QG}}}$ that can be used in the context of our approximate calculations ($m^2c^4 \ll E_i \ll E_{\text{QG}}$). With this definition, and recalling that at threshold, the energy of the electron and positron is approximately half that of the γ ray, one gets that $\frac{E}{E_{\text{QG}}}\left(\xi_\gamma - \frac{\xi_e}{2}\right) = \delta_\gamma(E) - \delta_e(E/2)$, such that equation 3.11 can be rewritten as

$$\epsilon_{\text{threshold}} = \frac{m_e^2 c^4}{E} + \frac{E}{4}\delta_{e\gamma}(E), \tag{3.13}$$

where $\delta_{e\gamma}(E) := \delta_\gamma(E) - \delta_e(E/2)$ is the speed difference, between the γ ray and the electron in this interaction, that is due to a quantum gravity correction. This

form emphasizes the fact that this effect is due to differences between the very-high-energy speeds of photons and electrons. This is different from the effect described in section 2.4.3, where only the speed of photons is at play. Therefore, whether the MAGIC finding is confirmed or not does not rule out the possibility outlined here, they are independent phenomena, even though they have the same cause.

To explore the consequences of this result, figure 3.10 illustrates the effect of the additional term in the threshold condition. Depending on the sign of $\delta_{e\gamma}(E)$, the energy of the low-energy photon that is required to pair produce can follow two trends. It can either start decreasing at a higher rate past a certain energy ($\delta_{e\gamma}(E) < 0$), which implies that massive pair production with the CMB, which is the densest part of the EBL, will start affecting γ rays of lower energy[10]. Or it can stop decreasing and start increasing ($\delta_{e\gamma}(E) > 0$), which implies that the highest energy γ rays could possibly not find a dense enough photon field of high enough energy to pair produce[11]. This means that the Universe could become effectively transparent to radiation of ultra-high energy.

The interest[12] in the latter possibility was initially stirred up as a potential way of avoiding the "γ-ray crisis" that plagued the analysis of Mrk 501 [76]. When the TeV spectrum of this source was measured to go above 10 TeV, computation of the intrinsic spectrum by deconvolving the absorption effects with the EBL models of the time led to an intrinsic spectrum that grew exponentially at the highest energies. This was recognized as a major problem as none of the emission models could account for such a possibility. In fact this is now regarded as an indication that the

[10] The $\delta_{e\gamma}(E) < 0$ case has the further implication that the decay of photons to an electron positron pair becomes kinematically allowed. This is further discussed in [74] and [75].

[11] The $\delta_{e\gamma}(E) > 0$ case has also the implication that energetic electrons could Čerenkov radiate in vacuum, which would set a limit to the energy that these can have in cosmic rays. This is explored in [75] and turns out to be a lesser constraint than the one that can be derived from pair production.

[12] Another thing that may have increased the interest in Lorentz invariance violation theories is that they provide a way of escaping the GZK cut-off in the cosmic-ray spectrum. The existence of this cut-off was debated for a while, so explanations were searched for, Lorentz invariance violation being one possibility [74].

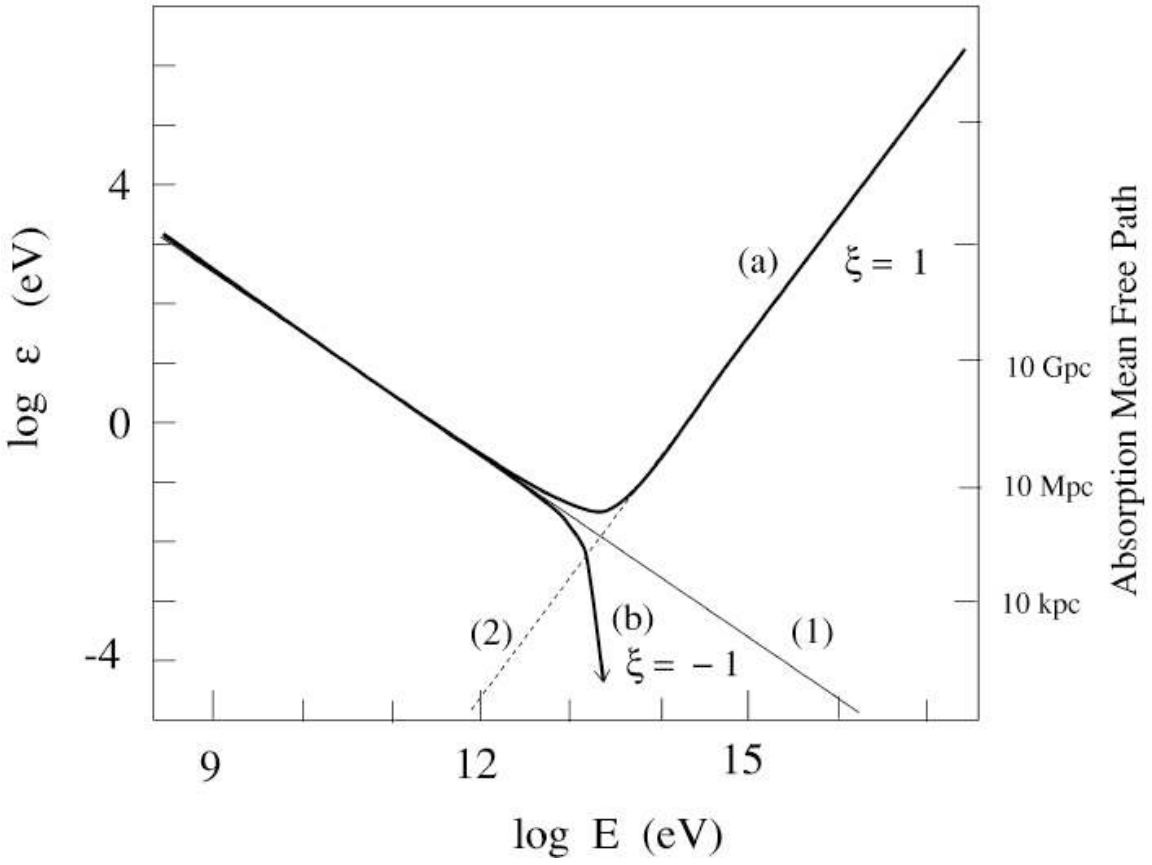

Figure 3.10: Modified energy threshold for pair production by Lorentz invariance violation effects. The line (1) shows the unmodified energy threshold. The line (2) shows the effect of the quantum gravity term in equation 3.13 for $1 \equiv \xi := 2\xi_\gamma - \xi_e = \frac{2E_{QG}}{E}\delta_{e\gamma}(E)$. Curve (a) shows the superposition for $\xi \equiv 1$ and curve (b), for $\xi \equiv -1$. The right vertical axis shows the mean free path of γ rays of energy E corresponding to these scenarios. Figure taken from [73].

EBL models producing this are wrong and it has grown into a criterion for rejecting them, as seen above. But at the time, other solutions were explored to explain the lower absorption than expected and breakdown of Lorentz invariance was included as one of the possibilities. Although it has never been taken too seriously because the other solutions required less exotic physics, it is good to keep the Lorentz invariance violation possibility in mind, especially because of the implications that the MAGIC discovery could have. If these results are confirmed, it might be interesting to revisit the consequences for pair production in more detail. The picture given here, which is also the one found in the literature, is probably oversimplified. For one thing, it implicitly assumes that **although the threshold condition is modified, the cross-section is not significantly modified**, this certainly could necessitate a verification. Also, it is not clear how the effect would manifest itself in the TeV regime, because of the double humped nature of the EBL SED. This could turn out to be complex, with lower attenuations than expected at some energies and higher ones at others. It is possibly akin to the perverse effects that a systematic error in energy calibration of TeV detectors can have.

Since the general consensus seems to be that the EBL density has to be lower than originally expected, no more "γ-ray crisis" phenomenon is seen in the de-absorbed spectra of blazars. From this point of view, one can argue that absorption effects are properly explained by the theory and that no significant deviation from predictions are seen. This allows one to place limits on $\delta_{e\gamma}(E)$ as was done, for example, in [77], [78] and [79]. According to these papers, no absorption anomaly due to Lorentz invariance violation is present in the Mrk 501 spectrum up to at least 20 TeV. This implies $\delta_{e\gamma} < 1{\times}10^{-15}$, or in a quantum gravity context, $E_{QG} \geq 0.3 M_{Planck} c^2$, which already discards some models of that theory [79]. Since the limit is derived from equation 3.13, there is unfortunately no explicit dependence on the distance from the source. However, it can be expected that if there is a deviation from classical theory, it would be more apparent in the spectra of distant sources, since these are more affected by the attenuation.

As a final note, let us mention that since the γ-ray detection techniques rely on the pair production interaction, Lorentz invariance violation could have a subtle effect on those [73]. These techniques will be discussed in the next chapter, but it will be assumed that **Lorentz invariance violation is not interfering** with them.

Part II

EXPERIMENT

4

Brief History of γ-Ray Experiments

Having described some interest for studying astrophysical γ rays in the previous chapters, it is now appropriate to discuss the means by which they are detected. Since photons of these energies are very penetrating, it is not possible to focus them and generate images in the way that a classical telescope would do. Instead, astrophysicists wanting to explore the very high energies have been forced to borrow some techniques from the particle physicists and adapt them to their needs. Over the years, the two groups have mixed creating the field now known as **astro-particle physics**. In this chapter, some of the ways in which γ rays interact are described and it is shown how these interactions are taken advantage of in the design of detectors that can achieve the triple goal of measuring the direction of propagation of the rays, their energy and the variation of their flux over time.

4.1 Satellite Experiments

Depending on their energy, γ rays interact with matter in different predominant ways. Typically, below a few hundred keV, the photoelectric effect is dominant. Above that, and up to tens of MeV, Compton scattering is the most important process. Beyond that, pair production dominates [6]. Figure 4.1 illustrates the different interactions.

The way to detect γ rays thus relies on building devices that exploit these interactions in their respective most efficient energy range. However, as mentioned in the introduction, cosmic γ rays are blocked by the atmosphere. The obvious, but not-so-technically-easy, way to access them, then, is to place a detector in orbit around the Earth; and that is indeed where the field of γ-ray astronomy evolved most rapidly in

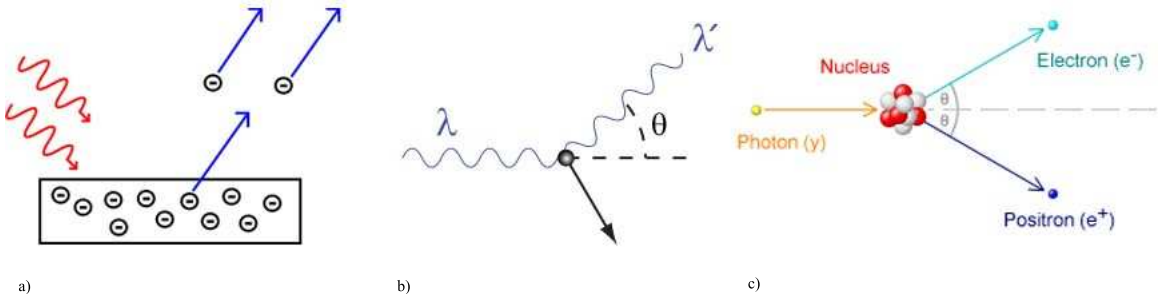

Figure 4.1: γ-ray interactions with matter. Panel a) shows the **photoelectric effect** by which electrons are ejected from a material receiving radiation of high enough energy (greater than the work function of the material). This is the dominant interaction at energies less than a few hundred keV. Panel b) shows the **Compton scattering** process in which a photon loses energy (increases wavelength, $\lambda' > \lambda$) to an electron. The electron recoils and the photon is scattered at an angle that conserves the momentum of the system. This interaction is important between a few hundred keV and tens of MeV. Panel c) illustrates **pair production**, which is the principal interaction above $\sim$10 MeV. A photon passing nearby a nucleus is transformed into an electron/positron pair. The photon must have energy greater than the rest mass of the particles created. The presence of the nucleus is required to conserve momentum and energy. Figures taken from `http://en.wikipedia.org/`.

its early days.

In order to achieve the goal of measuring the source location of the rays, some sort of telescope must be built. This could be achieved by forming a collimator with dense material that would restrict the γ rays to coming only from a predetermined direction or could be achieved by constructing some kind of pinhole camera. However, both of these solutions have the defect that the entrance aperture necessarily needs to be small, relative to the rest of the apparatus, to provide good spatial resolution. This is clearly a difficulty for γ-ray astronomy since the fluxes involved are quite small as seen in chapter 2. Therefore, the collection area needing to be as large as possible, other ways of determining the rays direction of propagation need to be used. Coded aperture telescopes, in which a mask formed from random patterns of open and closed apertures sits at the entrance of the telescope (essentially forming multiple overlapping pin-hole cameras), help increase the collection area while preserving the ability to reconstruct the source location from the mask's shadow position on the detector [80]. However, this technique remains useful only for soft γ rays and high intensity events like γ-ray bursts because a decent flux is still needed to cast appropriate shadows. Also, the detector needs to be pixelated, which is better accomplished with solid state detectors working using the photoelectric effect. Most space γ-ray telescopes

functioning at energies closer to those of interest in this thesis are instead usually built on the basis of the Compton scattering or the pair production interactions, which are described in more detail below.

4.1.1 Compton Scattering Telescope

In the Compton scattering type of telescope [81] [82], a first stage made up of cells of scintillator material, a material that emits light when traversed by a charged particle, acts as a target for an incident γ ray to Compton scatter off some electron. For each cell, some photomultiplier tubes, playing the role of pixels, record the light emitted by the recoil electron as this interaction takes place. This permits location of the position of the interaction. The scattered γ ray travels further down the telescope to a second stage where a denser scintillator induces pair production or multiple Compton scatters followed by photo-absorption, until the γ ray is completely absorbed. More photomultiplier tubes measure the light produced by the charged particles created or accelerated during the absorption in the scintillator. With the intensity of the measured light levels at both stages, the energy of the recoil electron and scattered γ ray can be deduced. From the location of the interactions in both scintillators, the direction of the scattered photon is measured. Using the Compton scattering equation

$$\lambda' - \lambda = \frac{h}{m_e c}(1 - \cos\theta), \tag{4.1}$$

the angle of the scatter can be deduced. This does not give the exact origin for the source of the γ ray, but rather a ring of possible source origins. This evidently complicates the analysis, but after the observation of many events, it is possible to deduce a source location from intersection of the rings. Figure 4.2 illustrates such a telescope, COMPTEL from the CGRO mission.

4.1.2 Pair Production Telescope

At energies higher than about 30 MeV, the Compton process becomes less efficient and it becomes more advantageous to exploit the pair production phenomenon. Telescopes built on this principle alternate layers of dense material, where the pair production can

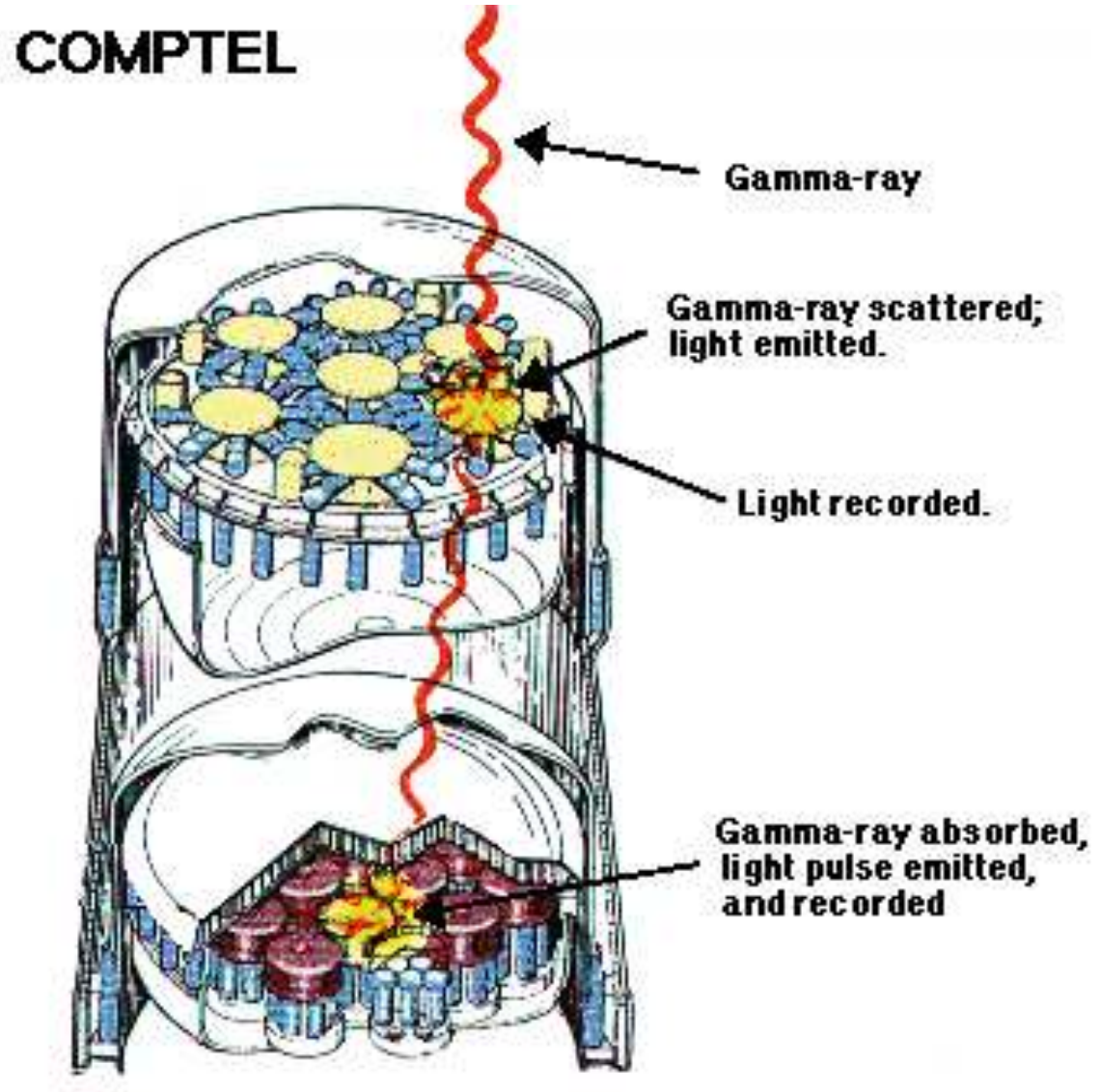

Figure 4.2: Working principle of Compton scattering telescopes. A γ ray Compton scatters in the first scintillator stage and is later absorbed in a second scintillator stage. The light emitted by the scintillators permits the measurement of the energy of the γ ray and its angle of scatter. Figure taken from `http://imagine.gsfc.nasa.gov`.

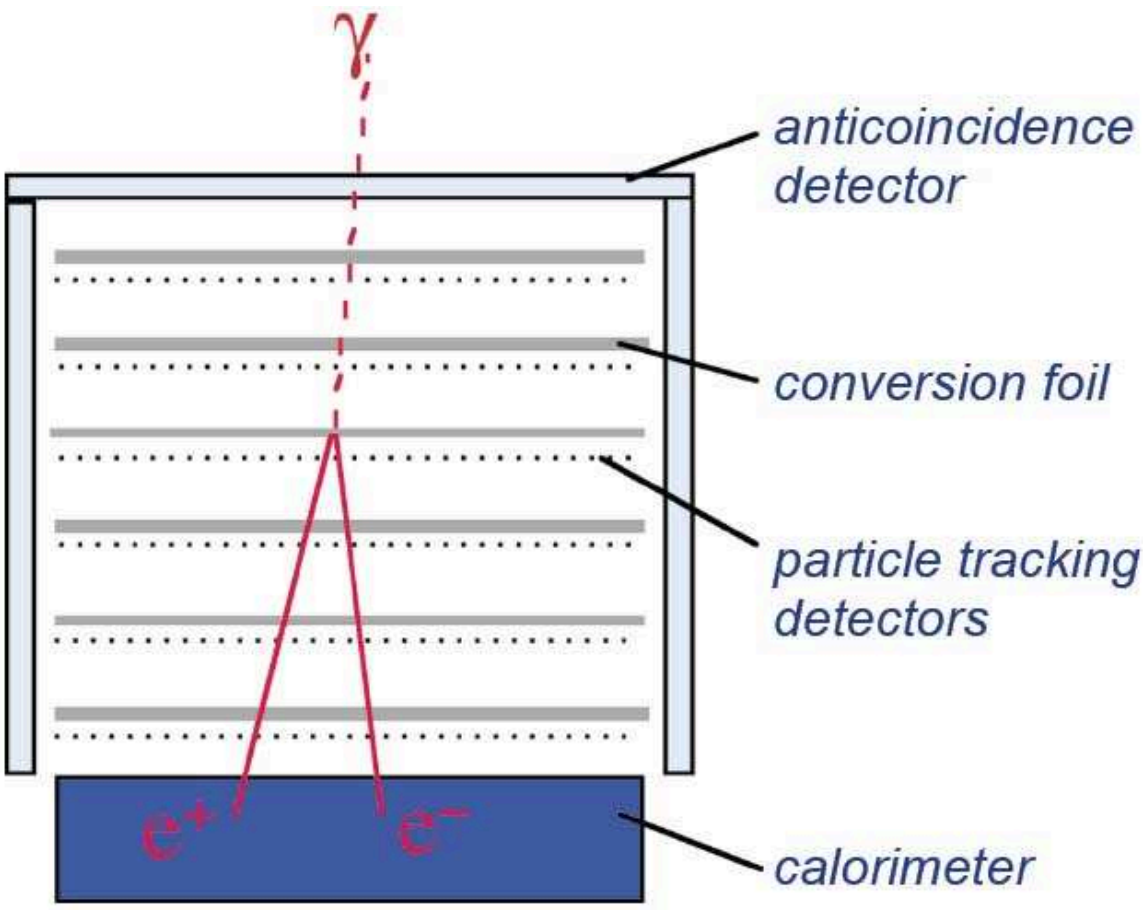

Figure 4.3: Working principle of pair production telescopes. The γ ray pair produces in a conversion layer while the electron and positron paths are measured by the tracking layers. The calorimeter measures the energy of the particle pair. Figure taken from `http://glast.gsfc.nasa.gov/`.

take place, with layers of tracking detectors, which are meant to track the trajectories of the interaction products [81] [82]. The last layer of the detector is a calorimeter which absorbs the particles and measures their energy. The sum of the energies of the products is an estimation of the energy of the primary γ ray. The tracks left by the pair are used to reconstruct the arrival direction of the photon. Figure 4.3 shows the main elements of a pair production telescope.

Of course, since charged cosmic rays can mimic the effect of γ rays passing through the detector and therefore constitute a huge background, being so much more numerous than the latter, a means of identifying those is required. For this reason γ-ray telescopes are generally enclosed within an **anti-coincidence shield**. This is made from a layer of scintillator material that, as mentioned above, emits light when

traversed by a charged particle. Detection of light generated by the shield forbids activation of the data acquisition system of the telescopes so that only γ-ray events are recorded.

4.1.3 Brief History of Satellite Experiments

Since the 1960s, many satellite missions have detected non-solar γ rays. It is not the place here to list them all[1], but it is appropriate to highlight the major historic developments in γ-ray astronomy so that the reader can better appreciate the current status of the field. Most of the information listed here can be found in [83] and [84].

1961 Explorer XI, the first high-energy astrophysics satellite is launched. It is a mission dedicated to γ-ray observations above 50 MeV. The cylindrical instrument is small, measuring only 20 inches high and having a 10-inch diameter. It consists of a sandwich of crystal scintillators with a Čerenkov[2] counter, surrounded by an anti-coincidence shield. Over its less than five month lifetime, it detected 22 γ rays, opening the era of γ-ray astronomy space missions.

1967 The third Orbiting Solar Observatory, OSO-3, contains a γ-ray detector similar to the one of Explorer XI, but slightly more sophisticated, with an energy detector. It established more firmly the beginning of γ-ray astronomy by detecting 621 events over a 16 months period. It also revealed the anisotropy of γ-ray radiation over the sky, with a higher concentration along the galactic equator.

1969 The Vela satellites, launched by the U.S. military to detect clandestine nuclear tests around the globe, each had six γ-ray detectors on board that worked in the 150-750 keV range. These detectors accidentally discovered the unexpected phenomenon of γ-ray bursts. 73 such events were recorded during the ten years of operations of these satellites.

[1] A comprehensive list can be found here:
`http://imagine.gsfc.nasa.gov/docs/sats_n_data/gamma_missions.html`.

[2] See section 4.3 for an explanation of the Čerenkov effect.

1972 Launch of the Small Astronomy Satellite 2 (SAS-2) mission (NASA). This satellite was dedicated to γ-ray astronomy in the 20 MeV-1 GeV range and hosted a pair production telescope. The tracker was a gas filled spark-chamber. Even though it operated only for six months due to power failure, it managed to map the galactic plane, demonstrating a correlation between the γ-ray radiation and galactic features. It also discovered emission from discrete sources like the Crab and Vela pulsars, and measured the high-energy component of the diffuse γ-ray background.

1975 Launch of COS-B (European Space Agency), a satellite similar in design to SAS-2. It confirmed and extended its results. The mission was planned to last two years, but in reality lasted more than six and a half years. The energy range was 30 MeV-5 GeV and the effective area was of the order of 50 cm^2 at 400 MeV.

1991 NASA's second great observatory[3], the Compton Gamma Ray Observatory (CGRO) shown in figure 4.4, is put in orbit for a mission that will last almost nine years [85]. On board are four instruments dedicated to the γ-ray energy regime:

BATSE, the Burst And Transient Source Experiment, is a group of eight large field-of-view detectors forming an all sky monitor for the energy range 20-1000 keV;

OSSE, the Oriented Scintillation Spectrometer Experiment, is a group of four orientable collimated instruments with scintillator detectors covering the range 0.05-10 MeV;

COMPTEL, the imaging Compton Telescope shown in figure 4.2, has a field of view of 1 sr with a few degrees resolution and functions in the the 0.8-30 MeV range;

EGRET, the Energetic Gamma-Ray Experiment Telescope, is a pair production

[3]The other NASA great observatories were 1) the Hubble Space Telescope working in the optical regime, 3) the Chandra X-ray observatory and 4) the Spitzer infrared telescope.

telescope with a spark chamber stack for tracker. It was designed to study the 20 MeV-30 GeV range.

CGRO was a big satellite weighting 17 tons. Each of its instruments gained an order of magnitude in sensitivity over previous generations. Among its accomplishments, it provided a sky map of the distribution of the radioactive isotope ^{26}Al, performed the most complete survey of the galactic center, and recorded more than 2700 γ-ray bursts, which were found to be separated into short and long bursts depending on their time profile. The most important instrument for what concerns high-energy astronomy was EGRET, which was 10 to 20 times bigger than its predecessors and so had a much larger effective area ($\sim$1500 cm^2 between 200-1000 MeV). It reached sub-degree angular resolution and 20 % energy resolution. It generated the first all sky survey above 100 MeV and discovered 271 sources, many of which have still unidentified counterparts at other frequencies. Blazars were identified among those sources and found to be a primary source of γ-ray emission. A map of the third EGRET catalog is shown in figure 4.5.

Since CGRO was taken out of orbit in 2000, there has been a gap in the coverage of the high-energy γ-ray sky. There are still some satellites in operation capable of observing hard X rays and soft γ rays, the Rossi X-ray Timing Explorer (RXTE), the High Energy Transient Explorer (HETE-2) and Swift are examples, but Compton and pair production telescopes have been missing for some years to cover the higher energies attainable by satellite experiments. It is true that ESA's INTEGRAL, the INTErnational Gamma-Ray Astrophysics Laboratory, helped fill the gap left by Compton-type telescopes when it started operating in 2002, but it remains insensitive to energies above 10 MeV [86]. Instead of operating with a Compton telescope, this satellite benefited from advances in detector technology and works with a coded mask aperture. The gap was recently further reduced by the successful launch, in spring 2007, of AGILE, the Italian satellite Astro-rivelatore Gamma a Immagini LEggero [87]. Its main instrument is a compact pair production telescope with a silicon tracker

replacing the usual spark chambers. Smaller than EGRET, but having a wider field of view, better tracking material, faster electronics and better resolution, it operates in the 30 MeV-50 GeV and has sensitivity similar to its predecessor.

But now, the γ-ray community is awaiting the first results from GLAST[4], NASA's Gamma-ray Large Area Space Telescope that launched in June 2008 [88]. This satellite hosts two instruments, the Large Area Telescope (LAT) and the GLAST Burst Monitor (GBM). The LAT is a pair production telescope, a successor to EGRET, but with improved technology and wider field of view ($\sim$2.5 sr). Like AGILE, the tracker is made of silicon strips, which lead to better spatial and energy resolutions ($\sim$0.5-5$'$ and $\sim$10 %, respectively). The LAT is also bigger, which will permit one to attain unprecedented sensitivity, 50 times better than EGRET, in the range 20 MeV-300 GeV. With this increased range at higher energies, overlap with the low-energy limit of ground based detectors becomes possible for the first time, see section 4.3.2. The GBM will permit observations of the 8 keV-25 MeV complementary range [89]. This will allow the detailed study of γ-ray bursts.

Overall, γ-ray detection from satellites offers many advantages like direct interaction with the photons, which permits easy discrimination against background cosmic-ray particles, large fields of view, and long duty cycles. However, due to the constraints on the payload that spacecrafts can carry, these size-limited satellites can only detect γ rays in a regime where the flux is high enough for them to register a significant amount of counts. As it turns out, the flux of cosmic rays is steeply falling with increasing energy, following a power law, from which it follows that these kinds of detectors are useful only up to a certain energy (pushed to a few hundred GeV by the GLAST mission). Still, γ rays exist above those energies, and important astrophysical phenomena are expected to occur at those higher energies. So how can those rare γ rays of highest frequency possibly be detected? The answer has to do with expanding on the idea of the pair production telescope.

[4]On August 26, 2008, GLAST was renamed the Fermi Gamma-ray Space Telescope.

Figure 4.4: The CGRO satellite. It hosts four instruments: COMPTEL, BATSE, EGRET and OSSE. Figure taken from `http://cossc.gsfc.nasa.gov/docs/cgro/`.

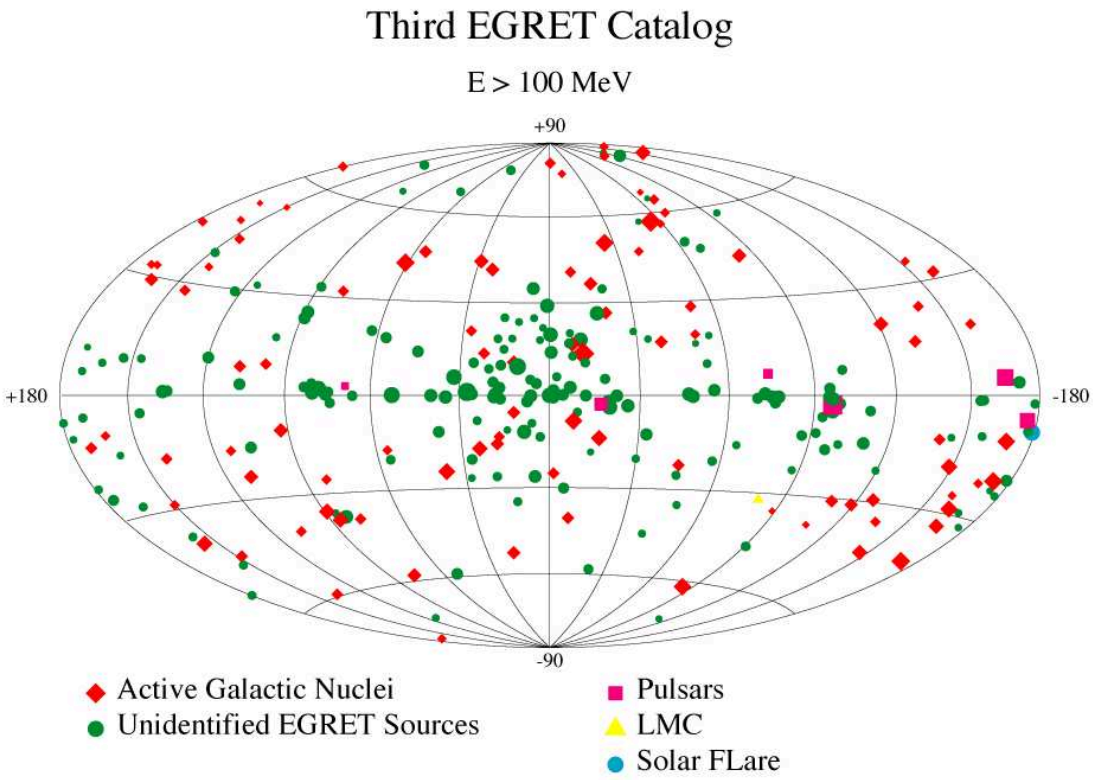

Figure 4.5: The third EGRET catalog. The majority of identified objects are LBL blazars. Compare to the TeV catalog in figure 2.11. Figure taken from `http://cossc.gsfc.nasa.gov/docs/cgro/`.

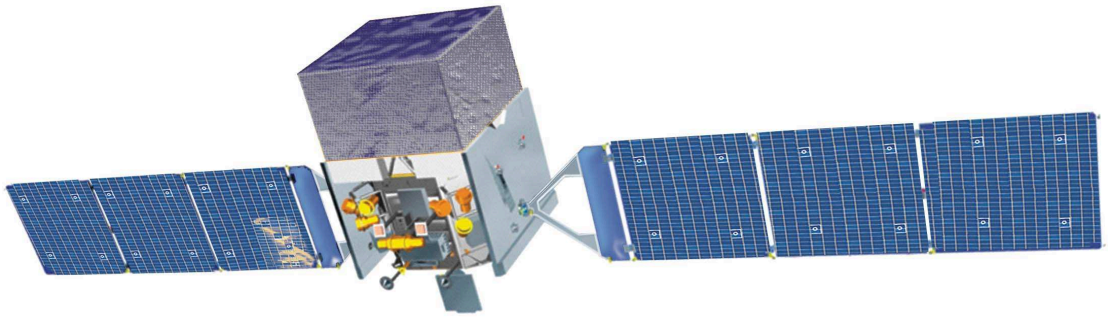

Figure 4.6: The GLAST satellite. Its main instrument is the Large Area Telescope (LAT), a pair production telescope with silicon-strip trackers. It also hosts the GLAST Burst Monitor (GBM), which extends the energy coverage to the X-ray and soft γ-ray regimes. It launched on June 11, 2008. Figure taken from `http://glast.gsfc.nasa.gov/`.

4.2 Air-Shower Arrays

When it was said earlier that γ rays are blocked by the atmosphere, one can understand this as the process of the γ rays interacting with it. In fact, at higher energies than the satellites can detect, the interaction involved is pair production induced from the γ rays passing close to the nucleus of one of the atmosphere's atoms. So why not take advantage of this interaction and make the atmosphere be a part of the detector, in some kind of giant pair production telescope? This is exactly the idea behind the air-shower array type of telescope. However, the concept of pair production telescope needs to be modified somehow because the products of the pair interaction will themselves interact further with the atmosphere and are therefore not directly detectable. In fact, in passing close to more atmospheric nuclei, the high-energy electron and positron produced in the interaction of the primary γ ray with the atmosphere will suffer **bremsstrahlung radiation**, a radiation emitted when a charged particle is accelerated or decelerated by an electric field. This radiation takes the form of secondary γ rays being emitted. Those secondary γ rays can, in turn, pair produce. The newly formed pairs radiate more γ rays and the cycle repeats itself. Thousands of particles are created in this way, leading to what is called an **Extensive Air Shower (EAS)** of particles, hence the name of the detectors to be described below: air-shower arrays.

EASs induced by γ rays typically start at an altitude of about 20 km, *i.e.* when the γ rays have traveled for a distance equal to one radiation length ($\sim$37.7 g/cm^2) in the atmosphere (the atmosphere has a thickness of about 27 radiation lengths $\sim$1000 g/cm^2). The shower grows and eventually attains a maximum number of particles when the electrons and positrons energy losses due to ionization of the surrounding medium becomes more important than losses due to the radiation process, and Compton scattering of the γ rays becomes more effective than pair production. From then on the cascading effect decreases in importance until the particles are no longer energetic enough to radiate or pair produce at all. The longitudinal extent of the shower thus depends on the energy of the primary, but is generally of the order

Figure 4.7: The Tibet AS-gamma Experiment. Detectors of particles are deployed over a large field at mountain altitude (4300 m above sea level). Figure taken from `http://www.icrr.u-tokyo.ac.jp/em/index.html`.

of 10 km. The width of the shower is not large in comparison, being only of a few tens of meters. The width is mainly due to the electrons Coulomb scattering from the atmosphere's molecules and the longitudinal extent is due to the pair production and bremsstrahlung radiation being highly beamed in the forward direction at high energies. Because of this important beaming effect, the main axis along which the shower develops is a good indication of the arrival direction of the primary γ ray. Figure 4.8 shows the results of a simulated extensive air shower.

In an **air-shower array**, many detectors are used to record the passage of the particles forming the showers, with scintillator materials for example. Since the showers normally die well above sea level, those arrays must be placed at high altitude if they are to catch any cascading particles. Even at mountain altitudes, only the very highest energy cosmic rays ($\gtrsim 100$ TeV) will produce showers of long enough extent to be detectable in this manner[5]. The flux of γ rays at those energies is evidently tiny, but because air-shower arrays are ground-based instruments, it is possible to deploy them in large fields of hundreds of km^2, producing extremely large collection areas which make detections possible. An example is shown in figure 4.7.

However, not only γ rays produce extensive air showers, cosmic rays do too.

[5]Actually, the air-shower array shown in figure 4.7 has a peak sensitivity around 100 TeV, but it can still detect showers of energies as low as a few TeV [90].

Cosmic-ray hadrons may undergo several collisions with atmospheric nuclei, expelling nucleons from local atoms and thus generating a nucleonic component to the forming shower. In these nuclear collisions involving the primary or the fragments produced, mesons may be formed, and in particular, the π meson or pion. The neutral pions quickly decay to photons: $\pi^0 \rightarrow 2\gamma$. These γ rays then initiate electromagnetic subshowers in the way described before. Meanwhile, the charged pions decay to muons and neutrinos: $\pi^+ \rightarrow \mu^+ + \nu_\mu$ and $\pi^- \rightarrow \mu^- + \bar{\nu}_\mu$, forming a muonic part to the shower. The muons may decay to electrons and neutrinos or even reach the ground due to their Lorentz time-dilated lifetime. The right panel of figure 4.8 shows what happens to a 1 TeV proton entering the atmosphere. Note that the width of the proton induced shower is larger than the purely electromagnetic one. This is a general feature of hadronic showers and is due to the transverse momentum that the pions are produced with. Because of the many different particles involved in hadronic showers, these also tend to be less uniform than electromagnetic showers.

Cosmic electrons also produce purely electromagnetic extensive air showers, and so they look exactly the same as those of γ rays. However, the fraction of cosmic rays that is made up of electrons is negligible, being suppressed by a factor 100-1000 [6], and so this component does not constitute an important background.

Overall, then, charged cosmic rays are responsible for the vast majority of extensive air showers. In fact, air-shower arrays are primarily designed to study any cosmic rays, not just γ rays. That is because their spectrum at ultra high energies permits the study of exotic physics, plus, at those incredibly high energies, the cosmic rays incoming directions are less prone to have been randomized by deflections due to interstellar magnetic fields, making cosmic rays interesting by themselves since they may point back to their original production site. Still, it is possible to do γ-ray astronomy with air-shower arrays by examining the nature of the particles that have been intercepted by the detectors; showers that are exempt of nucleonic and muonic components are likely to be due to γ rays. The energy deposited in the detectors can be linked to the energy of the primary and the arrival time of the particles in different

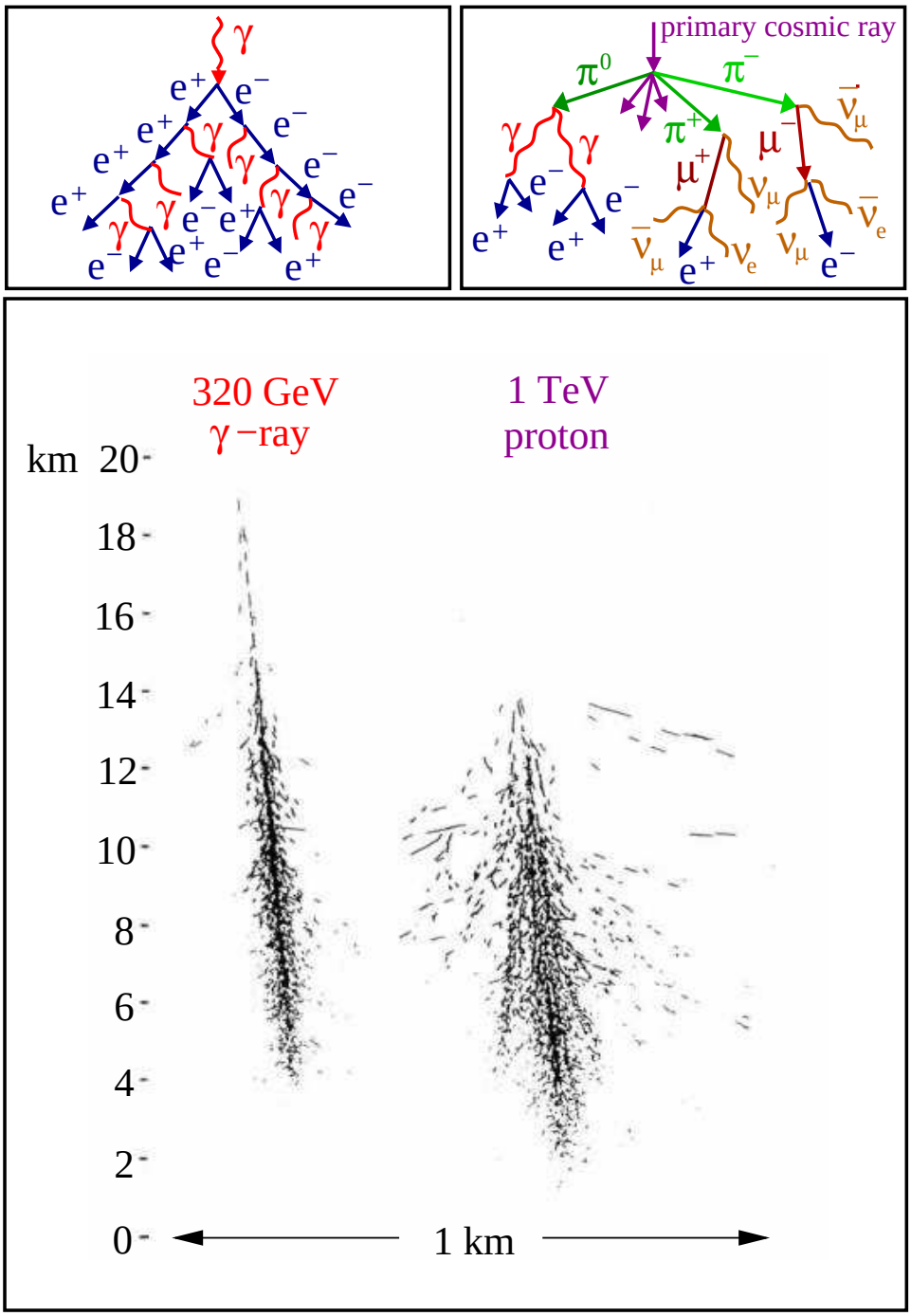

Figure 4.8: Simulated extensive air showers and interactions diagrams. The left part of the panel shows a 320 GeV photon interacting high in the atmosphere. The resulting shower is purely electromagnetic and is rather narrow. The right part illustrates the development of an hadronic shower involving nuclear collisions and production of pions, which decay to form an electromagnetic and a muonic component to the shower. Due to their diverse contents and greater transverse momentum that the pions can carry, the hadronic showers are less homogeneous and are more spread laterally. Figure taken from [6].

detectors gives an indication about the incoming direction.

4.2.1 Brief History of Air-Shower Arrays

The main historical developments concerning air-shower arrays are as follow:

1912 Victor Hess studies the discharge rate of electroscopes in balloon experiments. From the observation that the electroscope discharges faster at higher altitudes, he deduces that there must be some kind of radiation coming from space that ionizes the atmosphere: the cosmic rays. He received the 1936 Nobel prize for this discovery.

1938 The French physicist Pierre Victor Auger notices that detectors located many meters apart record simultaneously the arrival of particles. He concludes that the particles originate from a single event, the interaction of a cosmic ray with the atmosphere. He thus discovers the extensive air showers.

1946 The first air-shower detectors are built by Bruno Rossi in the USA, and by Georgi Zatsepin in Russia. They aim to study the structure of the Auger showers.

1962 The first cosmic ray with energy of $1{\times}10^{20}$ eV is measured. The discovery is made at the Volcano Ranch array in New Mexico by John Linsley and his team [91].

1989 The Chicago Air-Shower Array in combination with the MIchigan muon Array (CASA-MIA), located in Utah, searches for γ-ray sources with energies above $1{\times}10^{14}$ eV and finds none [92].

1999 First observation of a γ-ray signal above TeV energies from a point source, the Crab Nebula, made by an air-shower array, the Tibet Air-Shower - gamma experiment [90]. In the following years, they will also detect γ rays from Mrk501 and Mrk421 in flaring state.

Other important arrays include the German KASCADE (KArlsruhe Shower Core and Array DEtector) and its extension KASCADE-Grande [93], and Japanese AGASA (Akeno Giant Air-Shower Array) experiments [94]. However, the new Pierre Auger Observatory will supersede any other air-shower array [95]. It will comprise a southern site in Argentina and a northern site, probably in Colorado, USA. The southern site is nearly completed and has already started taking data. More than 1600 water tank type detectors are spread over thousands of km^2 making this the largest air-shower array ever built. The northern site will be even bigger.

Obviously, air-shower arrays have the advantage of extremely large collection areas and wide fields of view because they are a non-pointed type of instrument (arrival directions come from timing information). Their disadvantage comes from the fact that the cosmic rays are observed indirectly, through the shower particles that they generate and they are also only effective at much higher energies than satellites can reach, since the particles from low-energy showers do not penetrate to the detectors. Of course, a technique does exist to access the energies in the gap left between satellite and air-shower methods, being of central importance to this thesis, but it relies on yet another level of sophistication: the indirect observation of the extensive air showers.

4.3 Atmospheric Čerenkov Experiments

For extensive air showers of lesser energy, that do not make it to ground level, the detection strategy is to look closely at the atmosphere and search for clues that something changed due to the passage of the shower. The particles of the shower are highly energetic after all and it is not unreasonable to think that they could have a measurable effect in interacting with the atmosphere. Indeed this happens to be the case and a method for detecting γ rays can be built on these grounds. It cannot, however, be properly described without first setting the stage with a review of the interaction process between the particles and the atmosphere, the Čerenkov radiation.

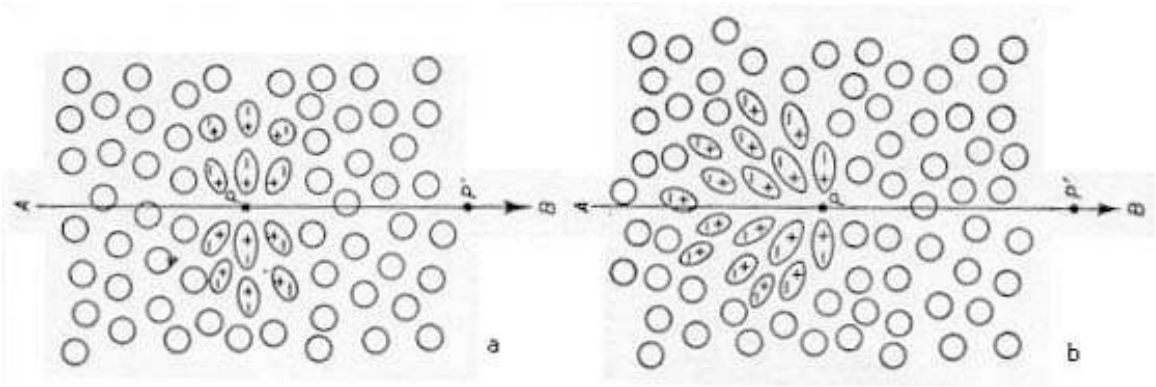

Figure 4.9: Deformation of atoms near the incident charged particle creates small dipoles that relax once the charged particle travels further away. a) slow moving particle, the situation is symmetric b) fast moving particle, the asymmetry of the situation creates an effective dipole. Figure taken from [96].

4.3.1 Čerenkov Radiation

The faint blue light that is often seen in pools containing radioactive material, and which was observed by some scientists like Marie Curie as early as 1910, is called **Čerenkov radiation**, after Pavel Alekseyevich Čerenkov, who studied it extensively, starting in 1934. It is due to a charged particle traveling in a medium and moving faster than the local speed of light, *i.e.* $c/n < v < c$, where c/n is the speed of light in a medium of index of refraction n, and v is the speed of the charged particle. To see this, and in order to keep things intuitive and more transparent, let us adopt a qualitative treatment valid in the far radiation zone. The full theoretical explanation is complex and yields the same result.

When a charged particle traverses a transparent medium, the atoms of the dielectric are polarized as the particle passes by, creating lots of little dipoles that relax once the particle has traveled farther. This sets off a brief electromagnetic pulse. If the particle is moving slowly, the situation is symmetric along the axis and there is no radiation at large distances, the dipole radiation interferes destructively (see figure 4.9a). However, if the particle goes faster, then the situation becomes asymmetric along the axis, creating a resulting dipole field where a coherent effect allows radiation to be observed at large distances (see figure 4.9b).

The angular distribution of the radiation can be deduced by looking at the Huygens

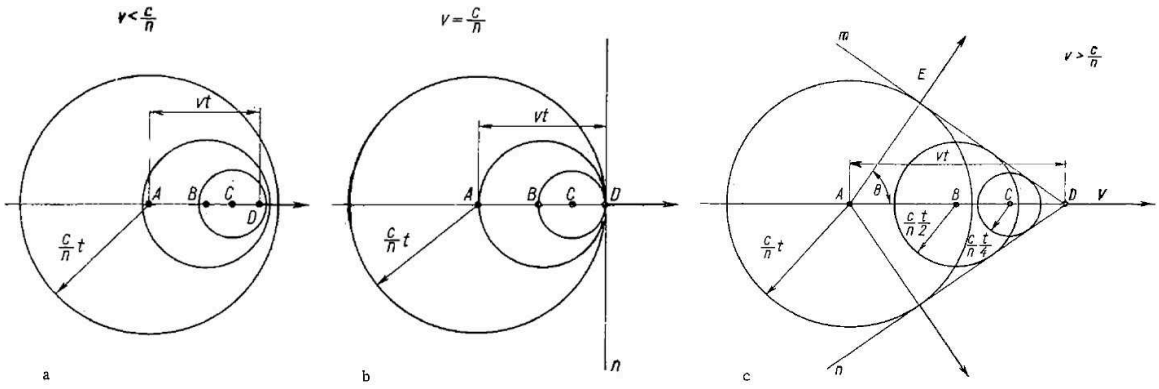

Figure 4.10: Wavelets construction of Čerenkov radiation. Wavelets from relaxing dipoles interfere constructively when the charged particle travels faster than the local speed of light in the medium of propagation. Here the circles of different diameters represent the wavelets traveling at speed c/n when the particle, traveling at speed v, was at points A, B, C and D.
a) $v < c/n$, there is no constructive interference, hence no radiation.
b) $v = c/n$, a coherent plane is created, but theory predicts zero intensity in that case.
c) $v > c/n$, a wavefront is created at angle $\theta_{\check{C}}$ from the particle's trajectory.
Figure taken from [97].

wavelet construction of the effect. Figure 4.10a shows the case $v < c/n$ where it can be seen that the wavelets cannot add coherently because the phase velocity of the wave always leads the particle. In figure 4.10b, the threshold case $v = c/n$ is illustrated, where a coherent plane is created, but the complete theory predicts that the intensity is zero in this case. The interesting case $v > c/n$ is shown in figure 4.10c. Here, a wavefront traveling at the Čerenkov angle $\theta_{\check{C}}$ with respect to the particle's direction is created by the coherent superposition of the wavelets generated along the track. This is analogous to the bow wave from a boat.

From simple geometrical reasoning, it is easy to relate the angle of emission of the radiation to the distance traveled by the wavelet and the distance traveled by the particle in time t. The famous Čerenkov relation follows:

$$\boxed{\cos\theta_{\check{C}} = \frac{1}{n\beta},} \tag{4.2}$$

where $\beta := v/c$. The angle of emission thus grows with the particle's velocity and is independent of its mass.

As for the color of the radiation, it cannot be simply inferred from these diagrams. The classical theoretical treatment yields the following equation for the radiated en-

ergy per unit path length:

$$\frac{dE}{dl} = 4\pi^2 e^2 \int_{\beta n>1} \left(1 - \frac{1}{\beta^2 n^2(\lambda)}\right) \frac{d\lambda}{\lambda^3}. \tag{4.3}$$

It is readily seen that the major contribution to the integral comes from the short-wavelength region of the spectrum, because of the $1/\lambda^3$ dependence. Hence the Čerenkov light appears bluish to the human eye, but also has some near UV component. Note that the integration must stop at higher frequencies than the near UV because the index of refraction becomes less than 1 in that case and it is no longer possible for the particle to respect the Čerenkov condition for radiation.

4.3.2 Detecting Atmospheric Čerenkov Radiation

Now that the basics of Čerenkov radiation have been explained, it is interesting to see what consequences it has for the detection of extensive air showers. In that case, the medium is evidently the atmosphere, which has index of refraction $n \approx 1.000\,096$ at an altitude of 10 km [98] (also see figure 4.11), where showers of hundreds of GeV attain their maximum number of particles [6]. Since the shower particles have been generated from a very energetic primary, it can be assumed that their energy is much greater than their rest mass and that $\beta \approx 1$, at least for the major part of the shower, prior to its decline. Equation 4.2 then implies that the particles will radiate Čerenkov light at an angle of about 0.8 °. Since the particles are highly beamed in the forward direction, it means that the shower itself radiates approximatively at this angle. So, for the part of the shower close to maximum, the Čerenkov light pool will form a circular area on the ground that extends up to a radius of $\sim$ 140 m. It is possible to estimate the density of photons in this light pool. From equation 4.3, it is easy to show that the number of Čerenkov photons radiated by a particle along a path l, taken here to be the radiation length at this altitude ($\sim$ 930 m), is

$$N = 2\pi\alpha l \sin^2\theta \left(\frac{1}{\lambda_1} - \frac{1}{\lambda_2}\right), \tag{4.4}$$

where $\alpha \approx 1/137$ is the fine structure constant. Taking $\lambda_1 \approx 200$ nm and $\lambda_2 \approx 600$ nm as the range over which photons are emitted yields $N \approx 28\,000$ photons. Multiplying

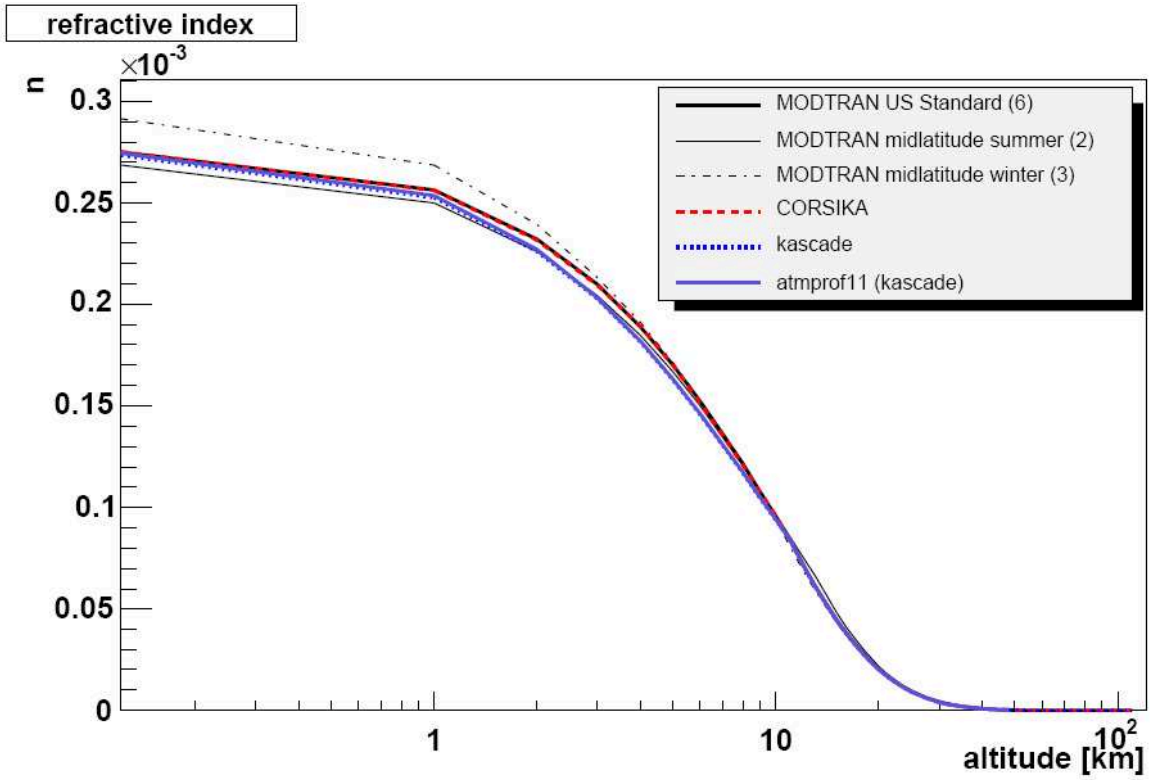

Figure 4.11: Refractive index *vs* altitude. The y-axis is actually $n - 1$. The different curves show the values used in different simulation programs. Figure obtained from [99].

this by the thousands of particles constituting the shower and dividing by the area of the light pool yields a photon density of $\sim 500\,\text{photons/m}^2$.

Of course the calculation shown above is extremely crude and does not include many considerations like the facts that the changes in index of refraction with altitude affect the Čerenkov angle by about an order of magnitude along the shower extent, there are many more particles near shower maximum than at the beginning of the shower, the approximation that $\beta \approx 1$ to high accuracy loses strength as the shower progresses and thus modifies the correct Čerenkov angle and number of emitted photons, the shower has a width, etc. The proper way to do the calculation is to perform Monte Carlo simulations. Results of such simulations [100] show that the Čerenkov light pool formed on the ground is quite uniform in density up to a radius of about 125 m (at mountain altitude $\sim$ 2300 m), where the photon density starts to decrease steadily (see figure 4.12). In the circle of near uniformity, the photon

density is of the order of 10-100 photons/m^2 for showers of 100 GeV to 1 TeV [6]. The simplified calculation presented here, useful for illustration purposes, was thus not too far off from reality. Its main objective is to motivate the idea that if an optical instrument is cleverly designed, then γ-ray extensive air showers may be detectable through their Čerenkov emission. Moreover, since a detector placed anywhere within the Čerenkov light pool could yield a successful measurement (see figure 4.13), or, inversely and more appropriately, since any shower falling within a radius of ~ 120 m of a detector could be detected, the effective area of the instrument has the potential to be huge, of the order of 4×10^4 m^2, which can give sensitivity to relatively low γ-ray fluxes.

Part of the challenge in using this technique is that the detector must be sensitive enough to discern the feeble Čerenkov blue light over the night-sky background light. Measurements made by the author, and presented in appendix C, indicate that the night-sky background flux is around 3×10^{12} photons/(s sr m^2) at high elevation and in the wavelength region corresponding to Čerenkov light observations. This seems like a huge number compared to the 10-100 photons/m^2 Čerenkov light yield of air showers. However, because light and the particles in the shower travel nearly at the same speed (actually the particles are going a little faster than the local speed of light), Čerenkov photons emitted at the top of the shower reach the bottom of the shower at almost the time when the last Čerenkov photons are emitted. This means that the whole Čerenkov light yield arrives almost simultaneously on the ground. In fact, it turns out that the Čerenkov light pulse has a width of only a few ns. By choosing an integration time just wide enough to encompass the Čerenkov pulse, one can therefore reduce the effect of the night-sky background, since within 5 ns, say, its integrated flux is 15×10^3 photons/(sr m^2).

The other key point to reduce the amount of background photons is to restrict the solid angle subtended by the instrument to accept only photons arriving from directions of potentially observable showers. If one is to keep the advantage of the large effective area, this means reducing the acceptance angle up to about $2\times1.3\,^\circ$,

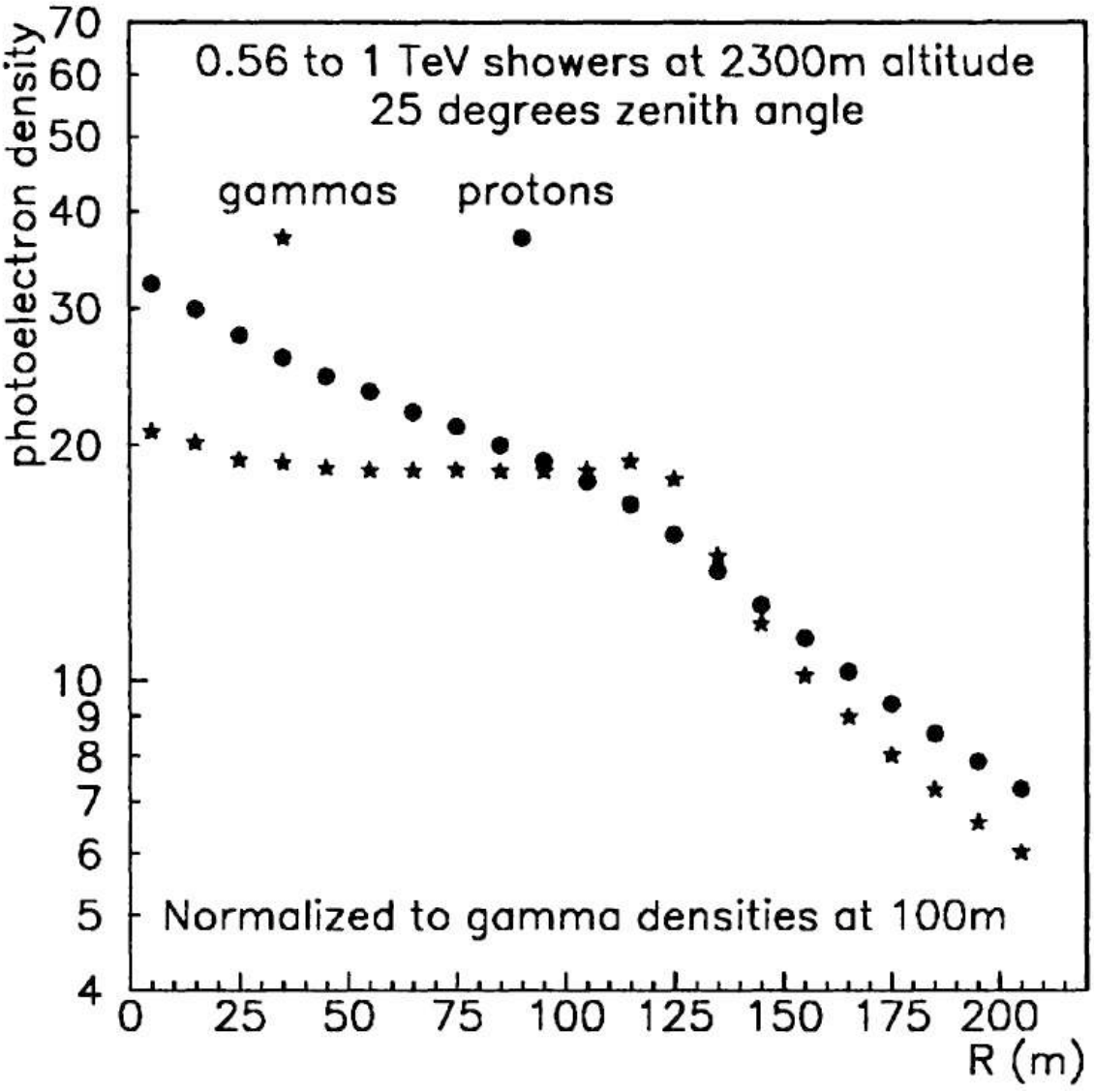

Figure 4.12: Photon density of the Čerenkov light pool for γ rays and protons induced showers. Figure taken from [100].

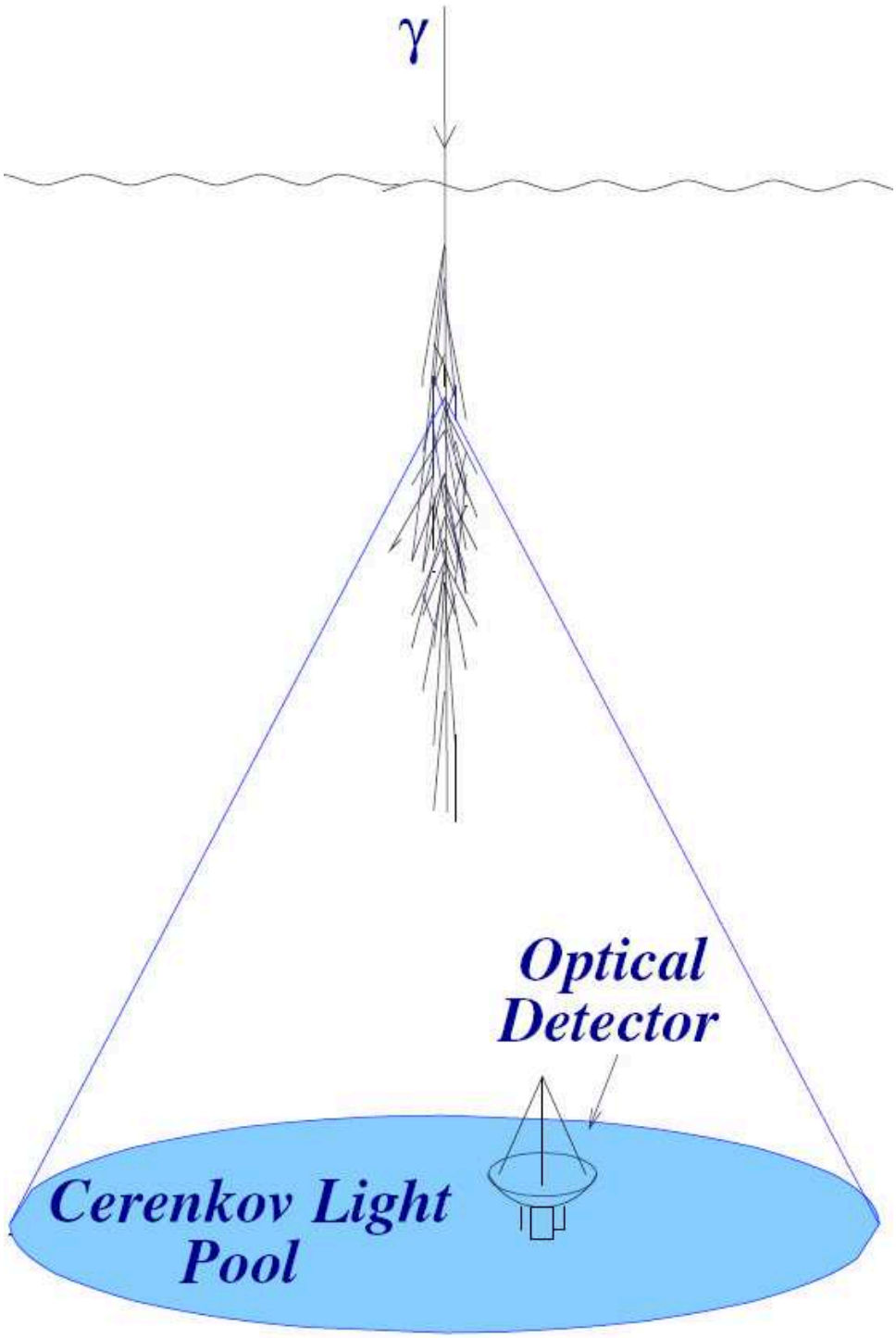

Figure 4.13: The effective area of the atmospheric Čerenkov technique is huge, being of the order of the Čerenkov light pool on the ground. Any shower falling within a radius of $\sim 120\,\mathrm{m}$ of a detector has a potential to be detected. Figure taken from [101].

corresponding to twice the maximum Čerenkov angle the extensive air showers could sustain (a smaller acceptance angle implies loss of effective area). This amounts to a solid angle[6] of 1.6×10^{-3} sr and implies that an instrument built with these characteristics would detect ~ 25 photons/m^2 from the night-sky background light. It thus becomes apparent that a technique based on detecting the Čerenkov light from extensive air showers is feasible, the signal being no longer buried in an overwhelming background.

More rigorously, and putting things in equations [6], if S is the signal (number of detected photons) due to the Čerenkov light yield C (photons/(nm m^2)) being collected by a detector of area A [7], which has efficiency η depending on wavelength λ (nm),

$$S = \int_{\lambda_2}^{\lambda_1} C(\lambda)\eta(\lambda)A\, d\lambda, \tag{4.5}$$

and if B is the night-sky background number of detected photons in integration time τ inside the solid angle Ω [8] subtended by the instrument,

$$B = \int_{\lambda_2}^{\lambda_1} B(\lambda)\eta(\lambda)\tau A\Omega\, d\lambda, \tag{4.6}$$

then the signal to noise ratio, where the noise is taken to be the random Poisson fluctuations in the background counts, is

$$\frac{S}{N} := \frac{S}{\sqrt{B}} = \sqrt{\frac{A}{\tau\Omega}}\frac{\int_{\lambda_2}^{\lambda_1} C(\lambda)\eta(\lambda)\, d\lambda}{\sqrt{\int_{\lambda_2}^{\lambda_1} B(\lambda)\eta(\lambda)\, d\lambda}}. \tag{4.7}$$

From this expression, it becomes obvious that the significance of signals over noise is going to be enhanced if the collecting power of the detector is augmented, while the integration time and subtended solid angle are minimized (but not to arbitrarily small values, see footnote 8). Interestingly, since the night-sky background is more

[6] The solid angle subtended by a cone of apex angle α is $2\pi(1-\cos(\alpha/2))$.

[7] This A is the collection area of the detector for the Čerenkov photons, not to be confused with the effective area for γ ray detection, which is much larger, being of the order of the area of the Čerenkov light pool on the ground.

[8] Both τ and Ω are assumed to be large enough to detect the Čerenkov photons from the whole shower, and they are implicitly already integrated over in $C(\lambda)$.

important at longer wavelengths, as shown in appendix C, and the Čerenkov light peaks at shorter wavelengths, it is also more advantageous to choose a detector that is more efficient in the blue-UV part of the spectrum.

The above calculations show that it is possible, and relatively easy, to detect extensive air showers and measure their arrival rate with a simple detector consisting of a mirror focusing light onto a photomultiplier tube for example. The energy of the primary can be estimated by the amount of Čerenkov light recorded; the atmosphere effectively acts as a calorimeter. However, because charged cosmic rays also produce extensive air showers with particles that will also generate Čerenkov light, a simple detector will not be able to discriminate between these and the γ-ray induced showers. Additionally, the arrival direction of the primary cannot be reconstructed from the output of such a modest instrument. To take full advantage of the air Čerenkov technique, more sophisticated apparatus is needed.

One such type of instrument is the **Čerenkov wavefront sampling detectors**, of which STACEE[9] (Solar Tower Atmospheric Čerenkov Effect Experiment) is an example [102]. In this type of instrument, a large field of heliostats, usually shared with day-time solar power experiments, reflects the Čerenkov light to an array of photomultiplier tubes placed on an observing tower (see figure 4.14). Each photomultiplier tube sees only one heliostat, such that each photomultiplier tube records a sample of the Čerenkov wavefront, at the position of the corresponding heliostat, as it reaches the ground. Similarly as for air-shower arrays, it is by studying the arrival time of the signals in each detector that the arrival direction of the primary is determined; **the wavefront is assumed to be spherical in shape and to land on the ground as a "pancake"**. Unlike air-shower arrays, the identification of charged cosmic rays is not done from the detection of particles produced only in hadronic showers, but relies instead on differences in the arrival patterns of the Čerenkov light from an electromagnetic shower from those of a hadronic shower, a technique that remains challenging.

[9] Members of the STACEE collaboration included a large group from McGill University.

Figure 4.14: The STACEE experiment. A large field of heliostats reflects the Čerenkov light to an array of photomultiplier tubes placed on an observing tower. Figure taken from [1].

A more successful technique is the **imaging atmospheric Čerenkov telescope** (IACT) systems [103]. Here, a large reflecting dish redirects the Čerenkov light to a "camera" - a pixelated detector made up of photomultiplier tubes, such that an actual image of the extensive air shower can be recorded, *i.e.* the angle of emission of the Čerenkov photons is preserved. From the image of the shower, it becomes easy to reconstruct the arrival direction of the primary, it is given by the axis along which the shower develops. Also, hadronic extensive air shower images look quite different from those due to γ rays, so this technique allows for good discrimination against the cosmic-ray background (more on this in chapter 6). By combining several IACTs in an array, one obtains different views of the same extensive air shower (see figure 1.2). This allows for better reconstruction of the event, which leads to better energy and angular resolution and better discrimination power against the background events. This is the type of instrument that the VERITAS experiment uses. Its apparatus is described in detail in chapter 5.

4.3.3 Brief History of Imaging Atmospheric Čerenkov Telescopes

To complete this portrait of the main ideas that lead to the design of today's imaging atmospheric Čerenkov telescopes, let us finish this section by placing the major advances that made such instruments possible into their historical context. In particular, the developments in the completion of the VERITAS array, to which the author participated, will be highlighted.

1926 L. Mallet realizes the first experimental studies about Čerenkov radiation, but his work was forgotten. The same is true about the first theoretical prediction of the effect by Heaviside around 1888 [104].

1934 P. A. Čerenkov extensively studies the radiation that now bears his name and for which he wins the Nobel prize in 1958. I. M. Frank and I. Y. Tamm develop the classical theory of this radiation in 1937 and V. Ginsburg, the quantum theory in 1940.

1948 P. M. Blackett proposes the idea that Čerenkov light from high-energy charged particles traveling in the atmosphere make up 0.01% of the light from the night sky, but he concluded that this would be too faint to be observable [103].

1952 W. Galbraith and J. V. Jelley discover flashes of light in the night sky. These were shown, a few years later, to be due, in some cases, to the Čerenkov light emitted by extensive air showers [105].

1960 A. E. Chudakov, in the Crimea, builds the first real atmospheric Čerenkov γ-ray telescope. It comprises many detectors made from search lights, each with a photomultiplier tube at its focal point. No detection of sources of cosmic γ rays could be made, the main problem being the large background of cosmic-ray nuclei. The situation will not improve significantly for many years.

1985 A. M. Hillas proposes a new method based on the shape of the extensive air showers images to discriminate between γ-ray and cosmic-ray nuclei primaries [106].

1989 Implementing the scheme proposed by A. M. Hillas, T. C. Weekes and his group obtain the first TeV γ-ray detection of the Crab Nebula with the Fred Lawrence Whipple Observatory (FLWO) 10-m atmospheric Čerenkov telescope [107], which was built in 1968 and was converted to an imaging instrument in 1982 [108]. The Crab Nebula becomes the standard candle for TeV astronomy.

1996 The first array of IACTs is built by the HEGRA collaboration. They demonstrate the power of stereoscopic observations of extensive air showers [109]. Their system comprises five telescopes with $8.5\,\mathrm{m}^2$ reflectors. Stereoscopic observations will also be investigated, in 1998, at the FLWO with the 10-m telescope and a 8 m companion [110].

2000 The arrays of four IACTs CANGAROO-III [111] and H.E.S.S. [112] are under construction. The MAGIC collaboration also makes plans to build a giant IACT [113].

2003 The VERITAS collaboration obtains approval and funding to build an array of four 12 m telescopes to be constructed at the Horseshoe Canyon site on Kitt Peak in Arizona. A year later, the first telescope prototype, with one third of the mirrors that the full telescopes will have and with a half-instrumented camera, is built at the base of Mount Hopkins at the base camp of the FLWO. The prototype demonstrates the viability of the project.

2005 The VERITAS prototype is upgraded to a fully operational telescope. After experiencing some site problems on Kitt Peak, it is decided to build the second telescope next to the first one, on the temporary site of the FLWO. Stereo observations begin the following year, as does the construction of the third and fourth telescopes, still on the same site, due to the ongoing problems with the Kitt Peak site.

2007 In February, the fourth VERITAS telescope sees first light. Array operations with the full system begin in March of that year [114]. Observations of TeV

γ-ray sources are already being confirmed by the array [115, 116, 117, 118, 119], which suggests a bright future for the experiment.

Today, there are basically four recent TeV IACT experiments, spread rather uniformly around the world, that are changing the face of γ-ray astronomy: VERITAS with its array of four 12 m telescopes in Arizona, CANGAROO-III (Collaboration of Australia and Nippon for a Gamma-Ray Observatory in the Outback) in Australia with an array of four 10 m telescopes, H.E.S.S. (High Energy Stereoscopic System) in Namibia with an array of four 12 m telescopes and MAGIC with a huge 17 m telescope. All have successfully integrated the techniques learned in the past and operate with a threshold near 100 GeV, which complements the coverage of lower energies provided by the GLAST satellite (GLAST has very little sensitivity above 100 GeV).

As for the future, the MAGIC and H.E.S.S. are already increasing the size of their experiments. MAGIC is entering its phase II with the construction of a second 17 m telescope [120] and so is H.E.S.S. with the construction of a rectangular 32 m by 24 m dish at the center of their existing array [121]. The goal of these improvements is to lower the energy threshold further and to be more sensitive to weak sources.

There are also many ideas for the design of future observatories. On the camera side, finer pixel size and larger fields of view would provide for better angular resolution, increased effective area, improved proton rejection and additional imaging parameters that would permit better sensitivity above 1 TeV [122, 123]. Other concerns about the camera include the lowering of its construction cost while improving the electronics [124] and the type of pixels used, with the possibility of using Multi-Anode Photo Multiplier Tubes (MAPMTs) [125] or new solid state devices with better quantum efficiency, which would be good to decrease the energy threshold. On the reflector side, there is a natural tendency to go to larger dishes for improved collection area of Čerenkov photons at lower energies [126], and there are studies for alternatives to the standard Davies-Cotton design (see chapter 5), which would perform better for wide fields of view [127]. There even is a research and development experiment that will attempt using refractive optics [125]. Overall, the main line of thought is a desire

to expand the energy range both below and above the current limits and increase the sensitivity. To arrive at such goals, people have started studying large arrays of IACTs [128], with possibilities of combined arrays composed of slightly different types of telescopes featuring some of the improvements mentioned above. This could result in a multi-purpose ground-based observatory that extends over $\sim 1\,\mathrm{km}^2$ and that could operate in the 30 GeV-300 TeV range [129, 130, 131, 132].

4.4 Summary of γ-Ray Experiments

Starting with the three basic γ-ray interactions with matter, introduced at the beginning of this chapter, it was shown, by following the processes involved in the absorption of γ rays, how this cosmic radiation could be detected with different techniques. Although they may have been presented here in some kind of logical order, from direct to more indirect methods, until the IACT instruments of interest here could be introduced, it must be realized that their evolution was interleaved in time with different techniques being developed simultaneously and influencing each other. The diversity of instruments produced shows how imaginative the physicists have had to be in order to detect astrophysical γ-ray sources. Their success is even more remarkable given that the γ-ray range in the electromagnetic spectrum spans over 15 orders of magnitude ($\sim 100\,\mathrm{keV} - 100\,\mathrm{EeV}$), that the fluxes diminish quite rapidly with increasing energy and that there are numerous backgrounds which make the detections non obvious. It is also quite astonishing to see how the diverse techniques developed complement each other nicely, leaving no gap in the energy coverage, even permitting some overlap, which is important for cross-correlating results. Because the γ-ray range designates such a large energy band, it is useful to subdivide it. Perhaps not surprisingly, the limits of the sub-bands correspond more or less with the limits of the detection techniques introduced above. Table 4.1 defines the different γ-ray bands, which are also shown schematically in figure 1.1.

Even though the entire γ-ray energy range is covered, there are still some advantages and drawbacks for each detection method. Satellite missions are risky, expen-

Band	Range	Detection technique
low-energy (LE)	100 - 1000 keV	Coded aperture space telescopes
medium-energy (ME)	1 - 30 MeV	Compton space telescopes
high-energy (HE)	30 MeV - 100 GeV	Pair production space telescopes
very-high-energy (VHE)	100 GeV - 100 TeV	Atmospheric Čerenkov telescopes
ultra-high-energy (UHE)	$>$ 100 TeV	Air-shower arrays

Table 4.1: Definition of the sub-bands of the γ-ray regime. This classification may vary between different authors. The one presented here is inspired from [6].

sive, limited in size and have poor angular resolution. However, they have excellent duty cycles, since they are above the weather. Atmospheric Čerenkov experiments are cheaper to build and have large effective areas, but they have small fields of view and can only operate during moonless nights, a rather small amount of time in comparison. Air-shower arrays have huge effective areas and they can operate all the time, but they can only access the very highest energies. Adding to this the fact that the number of detectors in operation is relatively small, whatever their type, these drawbacks may prohibit full time coverage of interesting sources at some wavelengths. Therefore, it is important to continue being inventive and think of other ways of detecting γ rays, which could extend the present possibilities. Other techniques already exist, that were not discussed in this short review and that allow for the study of cosmic rays in general or even of γ rays in particular. One of them is to make use of the air fluorescence, or more exactly the luminescence, that the showers produce in ionizing and exciting the air molecules (the HiRes [133] and Auger [134] experiments have ground-based detectors for this purpose, OWL [135] and EUSO [136] are proposed space detectors looking down on Earth for this luminescence). Another one is to make use of the radio signature of air-shower particles interacting with Earth's magnetic field (the LOPES [137] experiment investigates this aspect). Other techniques are to make use of a large water pool to provoke greater output of Čerenkov radiation from particles in air showers (Milagro [138] employs this strategy, as will HAWC [139]), or to make use of the Čerenkov light produced by the primary itself to

identify it (the TrICE [140] experiment attempts to see this direct Čerenkov light). Ideas are not missing, but, for the remaining of this thesis, let us concentrate on the IACT technique and its application in the very-high-energy regime. The VERITAS instrument is described in more detail in the following chapter.

5

VERITAS Array

The VERITAS experiment, located 70 km south of Tucson, at the base of Mount Hopkins, at the base camp of the Fred Lawrence Whipple Observatory in southern Arizona, consists of a recently completed array of 4 imaging atmospheric Čerenkov telescopes (IACTs), figure 5.1. Because of its stereo imaging capabilities and its fast cameras, it constitutes a new generation instrument playing an important role in the ongoing revolution in the field of ground-based γ-ray astrophysics. This chapter will highlight the main hardware components of the array as well as describe the workings of the data acquisition system and the strategies developed to take advantage of such an apparatus.

5.1 Davies-Cotton Design

When designing the reflector for the telescopes, different constraints have to be taken into account. Amongst these are the cost and the ease of fabrication and maintenance.

Figure 5.1: Photograph of the completed VERITAS array, located at the base camp of the Fred Lawrence Whipple Observatory. Joining the location of the telescopes with lines forms a four-sided shape with sides of lengths 85 m, 35 m, 85 m and 109 m [141].

The cost factor dictates the use of several facet mirrors instead of a single huge mirror, while the ease of fabrication and maintenance factor suggests that each facet be of the exact same shape. The facets are placed such that they all have their individual focus point superposing, this imposes a spherical shape for the reflector. Choosing the use of spherical mirror facets is simpler and cheaper to make than parabolic ones. Hence results a telescope design named after its inventors, the **Davies-Cotton** design[1] [142]. Specifically, if the facets have radius of curvature c, then they have focal length $f = c/2$ (from elementary geometric optics of spherical mirrors), which becomes the focal length $F \equiv f$ of the whole reflector. The radius of curvature C of the reflector is then not equal to c or $2F$, but simply $C = F$ (contrary to what geometric optics intuition would suggest, *i.e.* the reflector, although spherical in shape and made of smaller spherical mirrors, cannot be treated as a huge spherical mirror), see figure 5.2.

For the VERITAS telescopes, the collaboration opted for a diameter of $D = 12\,\mathrm{m}$ for each reflector. This offers greater collection surface than the existing Whipple γ-ray telescope ($D = 10\,\mathrm{m}$) [108], which is the previous telescope used by the collaboration, and is similar in size to the H.E.S.S. telescopes [143]. Only the MAGIC telescope was larger ($D = 17\,\mathrm{m}$) at the time of writing. As another improvement, the f-number ($f/\# := F/D$) was chosen to be $f/1.0$, *i.e.* $F = 12\,\mathrm{m}$, *vs* $f/0.7$ for the Whipple 10-m. Simulations showed that a larger $f/\#$ reduces the aberration due to mirrors that are off-axis [144]. Very large $f/\#$ are more difficult and costly to build, so the chosen size was a good compromise. The main draw back of the Davies-Cotton design is that it is not isochronous; due to the way the facets are placed, a planar wavefront impinging perpendicularly on the telescope acquires a time spread when received at the focus point. For the VERITAS telescopes, this is around 4 ns and does not constitute too much of a problem because the Čerenkov wavefront itself has a similar spread in time.

The 345 mirror facets per telescope are hexagonal in shape, which permits close tiling of the reflector surface. They measure 61 cm from side to opposite side and

[1] This design evolved from a suggestion made by R. Gardon [142].

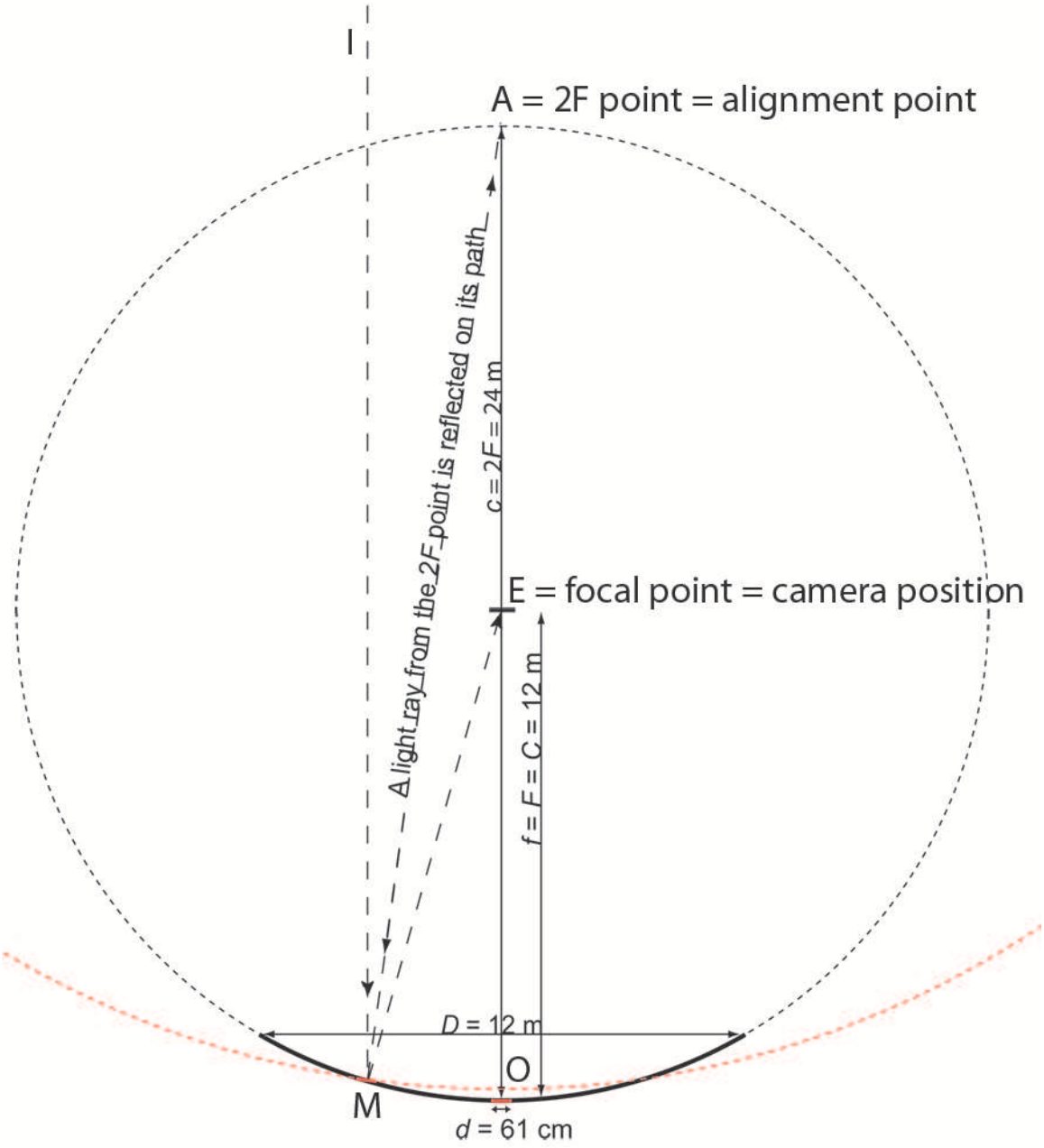

Figure 5.2: Davies-Cotton telescope design. The reflector (solid black arc of circle) is spherical in shape and has a 12 m diameter. The spherical mirror facets (two are shown as solid red line segments) are hexagonal, measure 61 cm across, and have a radius of curvature of 24 m, as is illustrated by the red dotted arc of circle. A light ray coming from point I, and parallel to the optical axis, is reflected by facet M to the focal point E where the camera is positioned. A light ray coming from point A, at twice the focal distance on the optical axis, bounces back on itself after reflection at point M. The same holds for the facet at point O, or at any other point on the dish. Note that the triangle AEM is isosceles with two sides equal to the focal distance and that the point A is not the center of curvature of the facet at point M.

are 11.5 mm thick, with a 24 m radius of curvature [145]. The area of each facet is 0.322 m^2, which yields a total area for the reflector of $\sim 110\,m^2$. They are shaped from glass by a company[2], but are aluminized and anodized directly on site. The aluminum is deposited in a 180 nm thick layer on the front side of the facet to avoid absorption of the UV light by the glass. Anodizing then hardens the aluminum, making it more resistant to degradation due to the Arizona desert conditions (there is no protective dome around the telescopes). The reflectivity of the facets is $\geq 85\,\%$ in the 280-450 nm range, and in particular is kept $\geq 90\,\%$ at 320 nm, which is more important since this corresponds to the UV part of the spectrum where most Čerenkov emission takes place. This is achieved by controlling the thickness of the anodized layer and making it equal to 80 nm. The degradation of the mirrors' reflectivity with time and position on the optical support structure (OSS) is currently under investigation, but early results seem to indicate a 3 % effect per year, which is acceptable. A plan has been established to schedule progressive recoating of the mirrors such that the array always remains in optimal conditions.

A commercial[3] altitude-over-azimuth positioner mount supports the OSS. Custom software controls the motion of the telescope and tracking errors are less than 0.01 °. Maximum slew speed is 1 °/s [146].

5.2 Mirror Alignment

With the question of the design comes the question of the alignment method. For the case of the Davies-Cotton telescope type, this turns out to be relatively simple due to the property that each facet is spherical in shape and with radius of curvature equal to $2F$. It can be shown that, for this kind of design, a properly aligned facet will reflect, back on their original path, the rays of light emanating from a source located at the $2F$ point, see figure 5.3. This is precisely the idea used by the alignment system. A laser beam is fired at a mobile beam splitter mounted at the $2F$ point. The beam

[2]Displays & Optical Technologies Inc. `http://www.doti-optics.com/`.
[3]Rotating Precision Mechanisms Inc. `http://www.rpm-psi.com/`.

splitter position is controlled by a computer to redirect the laser beam to one of the facets of the reflector. The return beam is spotted and the facet is reoriented such that the return beam overlaps with the original beam. The procedure is repeated for all facets. Each mirror is supported from the back by three mounts of different heights that attach to the OSS. The different heights for the mounts allow for correct inclination of the facets with respect to the optical axis of the telescope. Each mount needs to be carefully pre-positioned at the correct angle prior to the mounting of the mirrors themselves, a lengthy process. This ensures that any possible error that would result in colliding mirrors can be corrected before it is too late; the mounts become inaccessible once the mirrors are installed. Correct positioning of the mounts also eases the alignment process and minimizes physical stress on the mirrors that could change their shape. The facets have three holes in them which serve as anchor points to attach to the mounts (figure 5.4). The anchors are gimbals that gently squeeze the mirror in place and which can slide up and down a threaded rod that is fixed to the mount, see figure 5.5. A nut accessible from the front of the mirror allows control of the position of the gimbal along the threaded rod. It is by turning these nuts that the facets are reoriented into correct alignment. Alignment is stable enough that it only needs to be done once a year.

5.2.1 Point Spread Function and Bias Alignment

A measure of the success of the alignment process is the size of the point spread function (**PSF**) of the telescope, the full width half maximum of a 2D Gaussian fit to the image of a bright star on the focal plane. Since the telescope is aligned in horizontal position, the PSF is good at low elevations. However, as the telescope is tilted up to normal observation elevations, the weight of the support structure is redistributed differently, which makes the OSS flex slightly and consequently degrades the quality of the alignment. To counteract this effect, a procedure called **bias alignment** was established [147]. It consists of measuring the displacement of the mirrors between stow position and observation elevation, and then intentionally misaligning the mirrors by minus this amount during alignment at stow position, such that they come

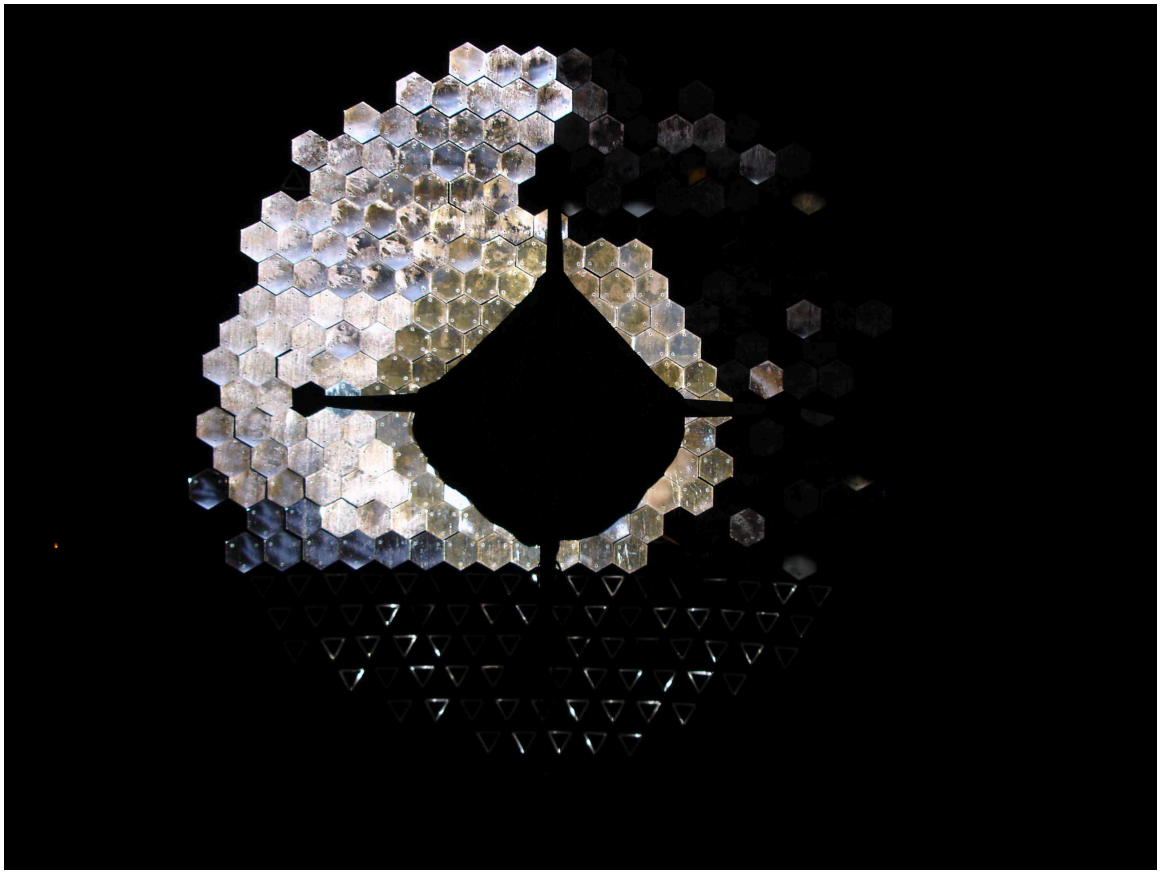

Figure 5.3: When the mirrors are properly aligned, a light beam coming from the alignment point is reflected back on itself. In this night photograph, the camera was held at the alignment point. The light from the flash is returned to the camera only from the mirrors that have been aligned (left side). Mirrors that are not aligned remain dark in the picture (right side). This trick provides a fast check of the alignment. The bottom rows were not populated with mirrors when this picture was taken.

Figure 5.4: Photograph of mirror mounts. The metal triangles keep the supporting threaded rods of a mirror facet at the desired distance and parallel to each other.

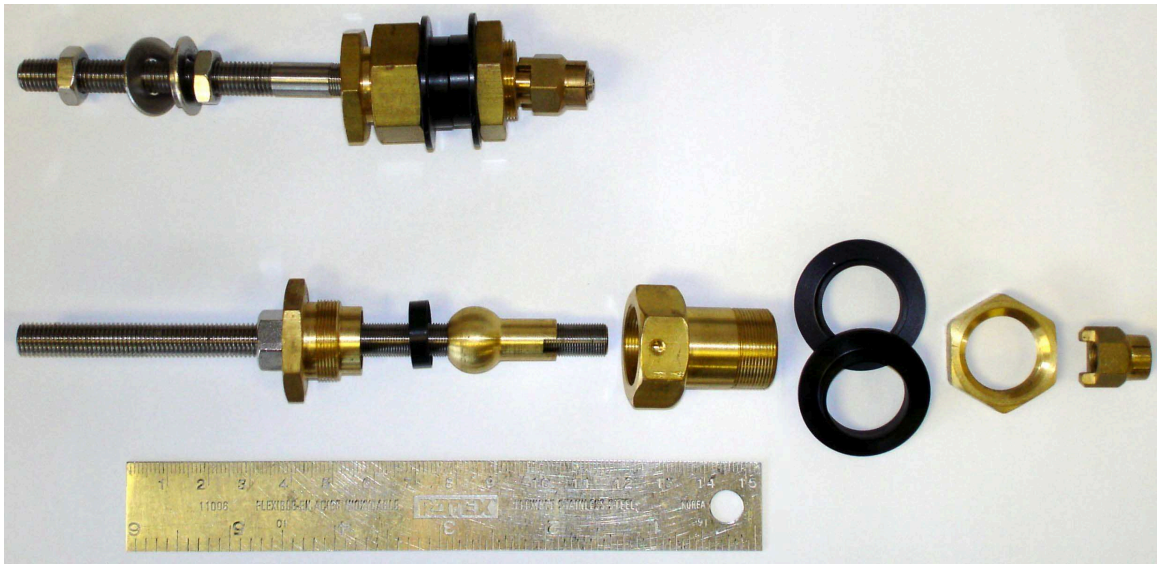

Figure 5.5: Assembled and exploded views of a gimbal assembly. The mirrors are gently squeezed between the two black rings on each gimbal. The alignment is adjusted by turning the front nuts, which makes the gimbal assembly slide up and down the threaded rod.

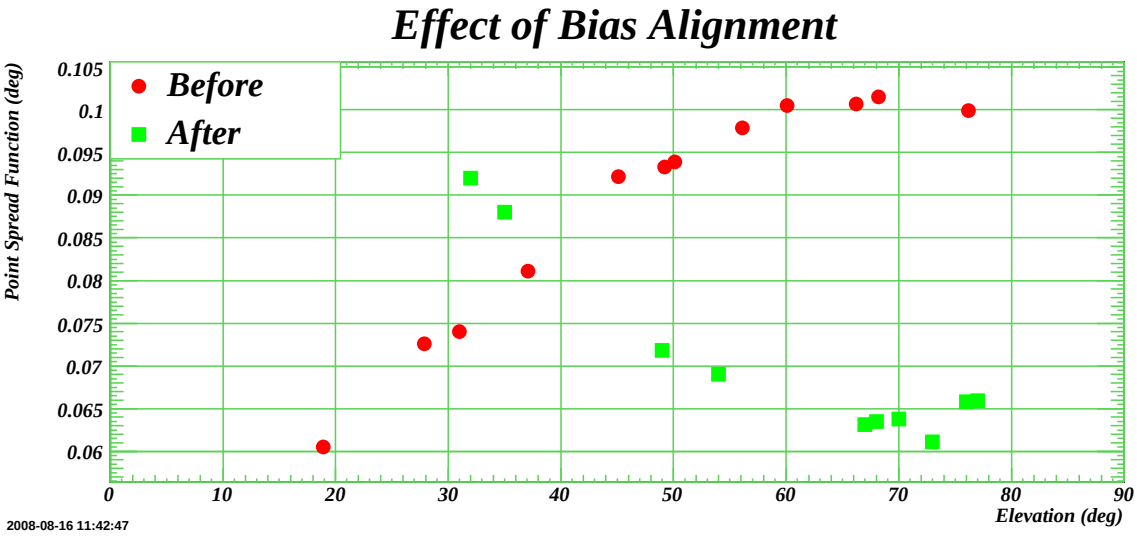

Figure 5.6: As a result of applying a bias alignment, the point spread function of telescope 1 of the array improved substantially at higher elevations. Circles and squares are the symbols for the data taken before and after the bias alignment, respectively. Figure replotted from [147].

back into the desired position when flexing occurs at higher elevations. The measurement of the displacements is done by placing small laser pointers on the mirror facets and orienting them such that they produce a spot on a screen placed at the camera plane. A ccd camera takes a picture of the spot at stow position and at 65° elevation. The displacement of the laser spot on the screen can be correlated to the amount of misalignment needed. Figure 5.6 shows how the PSF varies with elevation before and after bias alignment. After bias alignment, the PSF is $< 0.075°$ between 55° and 85° elevation. This is about half the pixel size (see section 5.3).

5.3 Camera

After the Čerenkov photons from the extensive air showers have bounced off the properly focused reflector, they are collected by a camera that converts the light image into electrical pulses. The Čerenkov photon yield being relatively low (recall section 4.3.2) and limiting background due to the night-sky background being present over all of the optical band, the detector must be fairly sensitive (see appendix C for more details on the night-sky background). Fortunately this background is minimum at bluer frequencies, where the Čerenkov emission is peaked. Thus, under appropriately

dark conditions, photomultiplier tubes with peak sensitivity in the blue region can detect the Čerenkov light from extensive air showers over the night-sky background light[4]. Each camera, which is hosted in a protective box equipped with a shutter and attached to the dish by a giant quadrupod, consists of an array of 499 Photonis XP2970/02, 29 mm diameter, 10-stage photomultiplier tubes (see figure 5.7). This yields a field of view of 0.15 ° per pixel and a total field of view of 3.5 ° for the entire camera, which are appropriate dimensions to see the structure of the extensive air shower images. The photomultiplier tubes have a quantum efficiency around 25 % at 320 nm and provide a gain $\sim 2 \times 10^5$ when held at a high voltage of 850 V. A low-noise pre-amplifier is included at the base of each photomultiplier tube to boost the signal by a factor of 6.6 so that the noise acquired during transmission through the 45 m cables is reduced in relative importance, see figure 5.8. Integrated on the pre-amplifiers is also an output that permits monitoring of the anode current. This allows a computer to automatically turn off a pixel that would risk being damaged by too high a current *e.g.* generated by a bright star in the field of view or from human activity near the observatory. Studying the currents over long-term periods can also reveal pixel health issues. When pixels malfunction, they are progressively replaced by new ones. Currently 97 % of the pixels are functional, but the goal is to have > 99 %. The pre-amplifiers heat the camera, threrefore temperature and humidity sensors have been installed in the camera box and are monitored by the same program that monitors the anode currents. The observer can then decide when it is safe to operate the camera without risk of arcing or overheating.

5.3.1 Light Cones

The pixels described above are round in shape. This implies that their close-packed hexagonal tiling is inefficient, as many gaps exist between the circular sections. To increase the collection efficiency, light concentrators, or **light cones**, are placed in

[4]Modern photodiodes could eventually be considered for the pixels if progress is made in their construction, but at the time of design the venerable photomultiplier tube still had a superior signal to noise ratio [148] and so were chosen for this experiment.

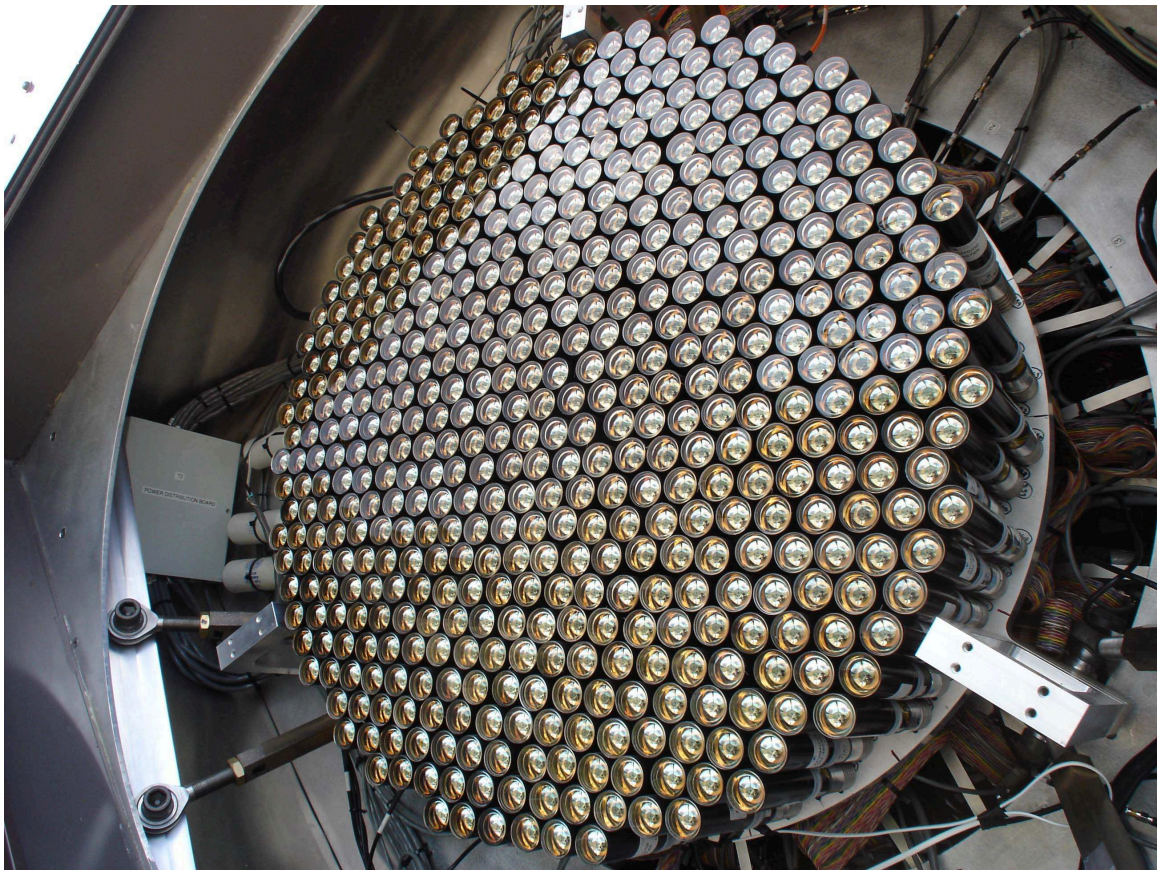

Figure 5.7: Photograph of a VERITAS camera. The light cones are not installed in this picture.

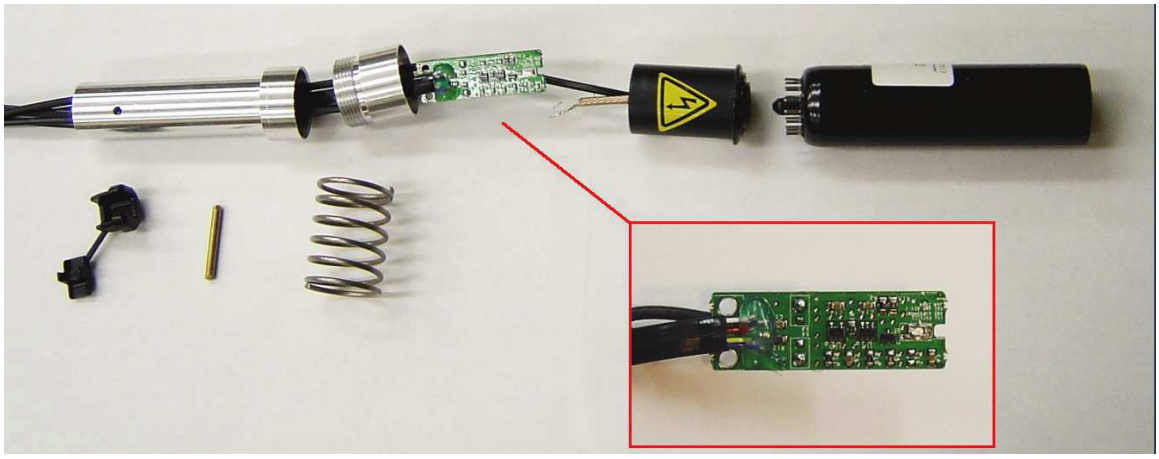

Figure 5.8: Photograph of a photomultiplier tube. The inset shows the pre-amplifier board. Picture taken from [149].

front of each pixel, see figure 5.9. These are shaped with a hexagonal entrance linear cone and evolve to Winston-type cones[5] [151] that fit the photomultiplier tubes' photocathode sensitive area. The cones are hollow and light bounces off the inner faces until it reaches the photocathode. They are coated with an aluminum layer providing $> 85\,\%$ reflectivity above 260 nm. The collection efficiency of the camera is increased from $55\,\%$ to $75\,\%$ with the presence of the cones. Not only do they reduce dead space between the pixels, they also limit their field of view; each pixel sees little more than the entire reflector when the cones are installed. This helps reduce the amount of night-sky background light that reaches the detector. Their optimal shape is a compromise between good collection efficiency and good shielding efficiency. It has been studied in numerical simulations [150] and two designs were tested in the field with the result that the hybrid Winston cone offered the best compromise. The hope is that the light cones will help lower the threshold of the experiment and improve the sensitivity.

It is expected that the cones need to be changed every two years. However, it was demonstrated by the author and a colleague, using the tools described in 5.6, that dust accumulates non uniformly on the inner surfaces of the cones and that this could introduce small gradients in the camera response (a $< 5\,\%$ effect [152]). Following this discovery, a procedure has been established to clean the light cones with CO_2 snow every month .

5.4 Electronics (Data Acquisition)

The VERITAS cameras are equipped with photomultiplier tubes, as mentioned previously. These photomultiplier tubes generate an analog electrical signal in response to an exposition to light (next chapter's figure 6.1 shows what this signal looks like). In order for this signal to be conveniently handled by computers for analysis, it must

[5] A pure Winston cone has a very sharply defined aperture with high acceptance of photons within a certain solid angle and very low acceptance of photons outside this solid angle. However, they do not tile exactly, leaving some dead-space on the detector [150].

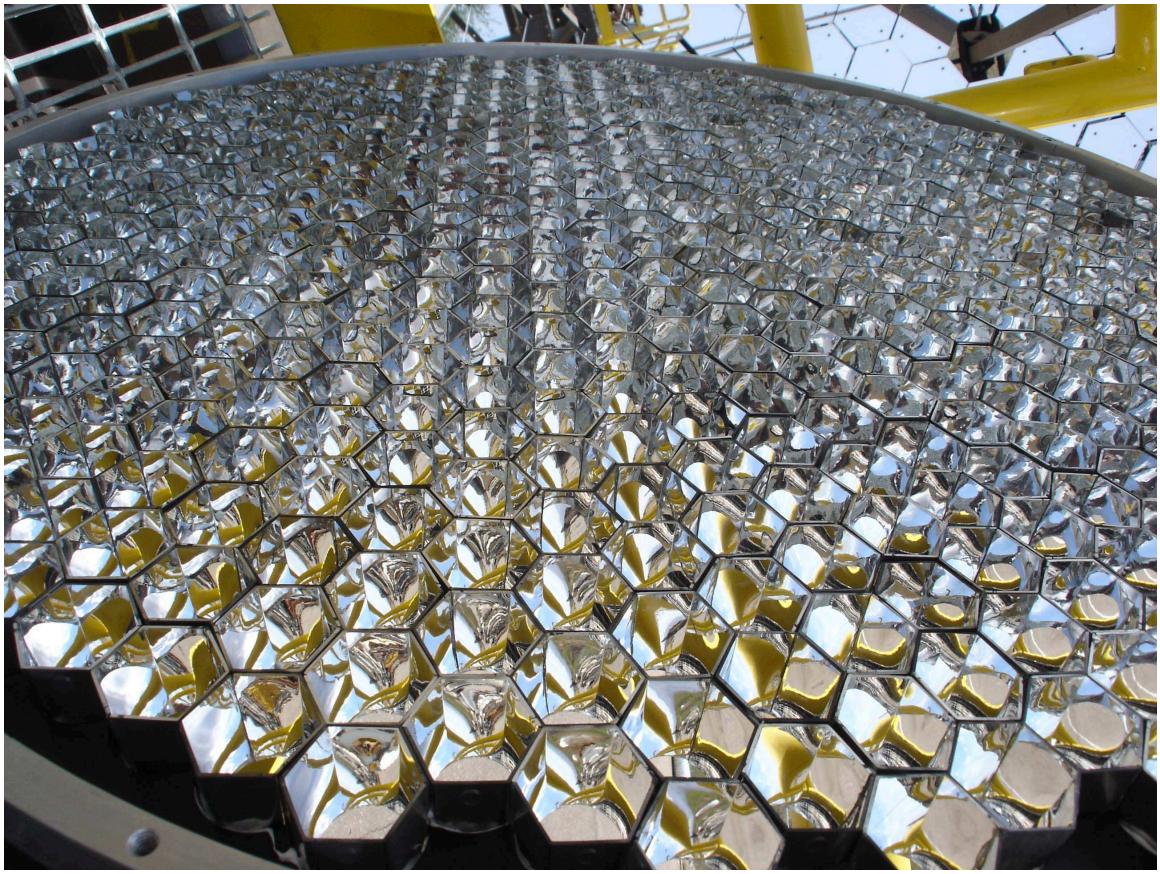

Figure 5.9: Photograph of the light cones plate.

be digitized. This is the role of the Flash Analog-to-Digital Converters (**FADCs**). These are input boards that measure time-varying voltages, much like oscilloscopes do. Each board has 10 input channels (see figure 5.10) and each telescope has enough boards to handle 500 channels, one for every pixel of the camera and one extra for other purposes. Each channel receives a photomultiplier tube waveform, that has decreased in amplitude by a factor of about 0.75 due to cable losses, and samples it with 8-bit resolution at a rate of 500 MHz, *i.e.* each 2 ns the waveform's amplitude is given a number between 0 and 255. The conversion factor is 256 digital counts (d.c.) for 2 V after the pulse has been amplified by a factor 7.26 by the input stage of the board[6]. The justification of the use of the fast FADC compared to the more common and slower Analog-to-Digital Converter (ADC) is given by the realization that when one is able to digitize the details of the photomultiplier tube pulses (the length of the Čerenkov pulses are of the order of a few ns), one can select more appropriately the integration window and therefore have better control on the signal to noise ratio. Also, by having the full trace, one can imagine applying digital signal processing techniques to it so as to modify or enhance the signal. The better timing resolution offered by the FADCs might also permit the study of arrival time gradients in the images of extensive air showers, which could eventually serve as a discrimination parameter between different types of showers [146].

For a single 20-minute run, with 499 channels and 4 telescopes, the amount of data recorded at those rates (continuous digitization, *i.e.* no trigger) would correspond to a file size of about 12 TB. Given that the flux of the Crab Nebula, the standard candle in TeV astronomy, is only of 2.35×10^{-7} photons/(m^2 s) above a TeV, and that a VERITAS three telescope system detects only 7 γ rays per minute from this source [153], a file of this size would be completely dominated by background events from cosmic-ray extensive air showers and night-sky background fluctuations. This is clearly intractable and a means of reducing the amount of irrelevantly recorded data

[6]For large voltage deviations, when the digitization would saturate at the value 255 d.c., the board actually switches to a lower gain path (reduces the input gain to a factor of 1.21) that allows digitization of larger pulses. The total raw pulse (unamplified) input range is thus 0 V to −1.65 V

Figure 5.10: Photograph of a FADC board. One can see the 10 input channels receiving pulses from 10 pixels. Sitting on the board are also the CFD modules, one for each channel.

must be used. Therefore, a set of conditions must be defined such that when they are met by the 500 waveforms of the different telescopes, a command is issued to the data acquisition system to start recording, *i.e.* the FADCs are stopped and their buffers are read in. This set of conditions is what is called the **trigger** of the experiment.

5.4.1 Trigger

Without a trigger mechanism, the system would save to disk mostly uninteresting information. How does one reduce the rate of background events while preserving the interesting γ-ray images? The obvious thing to start with is to look only for the interesting parts of the waveforms, that is, search for deviations of the waveforms from their baseline. This is what is called the level 1 trigger. Then, as these may happen randomly due to night-sky background fluctuations or simply noise in the channels, the thing to look for at a second level is clusters of such pixels in the camera that got lit up; these constitute an **event**. Finally, at a third level, with an array of telescopes, it is required that the events be seen by a certain number of telescopes participating in the observation. These trigger conditions are described in more detail below (and in more technical detail in [154]).

L1: Pixel Trigger

The level 1 trigger, or L1, consists of having some pixels lit up in the camera. What defines a pixel as 'lit up' is that the pulse that its photomultiplier tube emits when receiving light must be 'bigger' than some predetermined threshold value; explicitly the pulse waveform must intersect with the threshold waveform, which is just a constant DC voltage. When such a comparison is achieved, a trigger signal of level 1 is sent. However, the exact time of release of this trigger signal is subject to debate because pulses starting at the same time, but having different amplitudes will cross the threshold voltage at different times, resulting in jitter in the trigger signals. To solve this, Constant Fraction Discriminators (**CFDs**) are used to perform the comparison [155]. These modules sit on the FADC boards (see figure 5.10). They split the input signal in three copies. One copy is sent to a threshold discriminator that works in the

way described above. Of the other two copies, one is delayed and inverted, and the other one is attenuated by some factor. These two modified copies are then added and sent to a zero crossing discriminator that will consequently fire when the attenuated copy equals the delayed one. It can be shown that the zero crossing discriminator fed with that signal will always trigger at some constant amount of time after the start of the pulse, see figure 5.11. This amount is user-configurable and depends on the attenuation factor and the delay time. If all the pulses have the same rise time, then this translates in the trigger being issued at a constant fraction of the pulse height, hence the name CFD. The outputs of the threshold discriminator and of the zero crossing discriminators are thus combined in the CFD circuit to output the level 1 trigger for input signals that are large enough, and the triggers will be synchronous for pulses arriving at the same time, even if they have different amplitudes.

The question of what is 'large enough' for a photomultiplier tube signal to pass the level 1 trigger depends on the rate at which one desires to take data, and as such depends on the complete trigger chain. Therefore, this question will be addressed later in this section.

L2: Pattern Trigger

To have some pixels lit up is not a sufficiently powerful condition to reduce the data rate when one wants to operate at lower energy thresholds. Such hot pixels happen all the time due to fluctuations in the night-sky background light and appear randomly on the camera. They do not form any particular kind of image, they just look like noise and do not constitute something of interest for recording. Therefore, the next step in the trigger chain, L2, is to examine the spatial and temporal distribution of the L1 signals from a camera to find some patterns that may have been due to γ-ray induced showers. In other words, the pattern trigger looks for images that may represent more than simply random noise. For each telescope, a dedicated computer receives the L1 signals. It divides the camera into overlapping patches of 19 pixels and searches each patch for a predetermined number of adjacent L1 triggers within a predetermined time window. The usual settings are 3 adjacent pixels firing within a

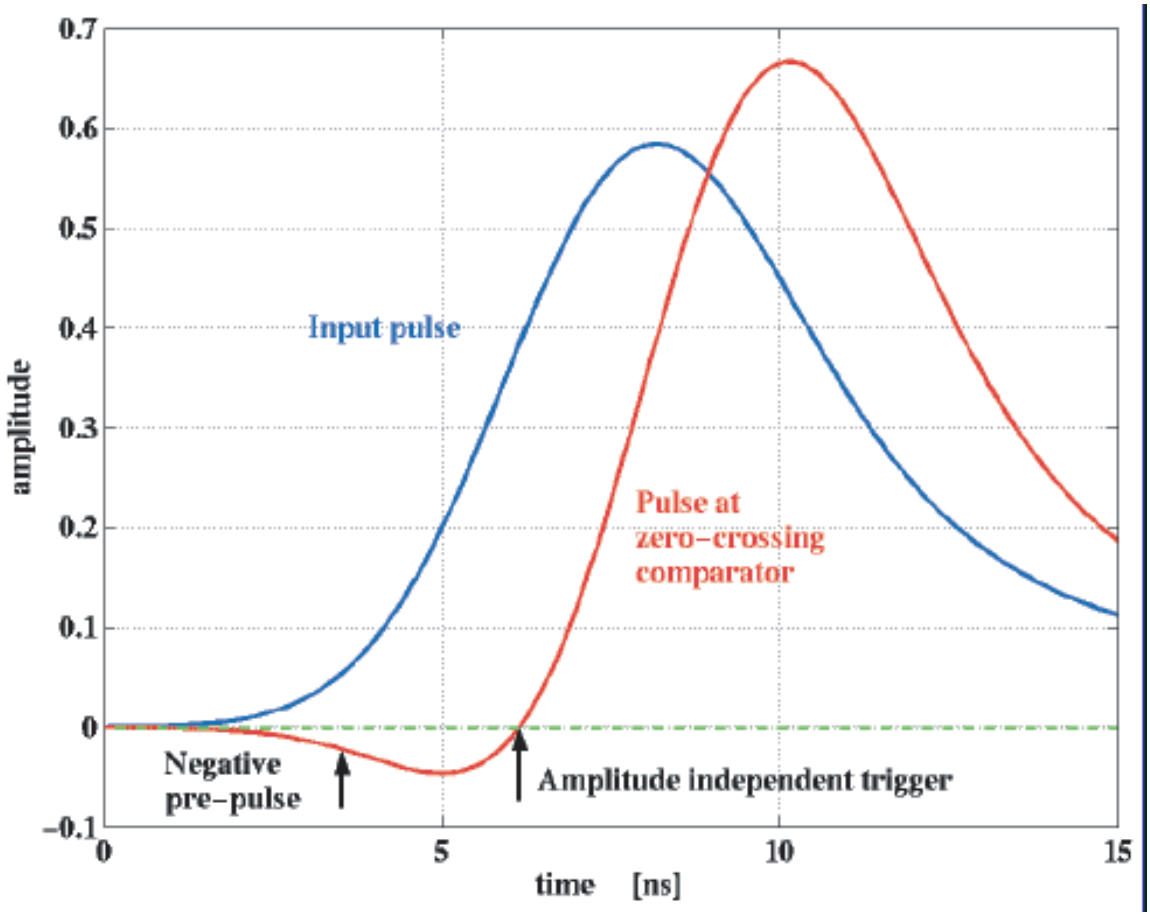

Figure 5.11: CFD working principle: the input pulse is attenuated and added to an inverted and delayed copy. This creates a pulse which has a negative part followed by a positive part. The trigger time corresponds to the zero crossing time of that pulse and is independent of the amplitude of the input pulse. Here the blue curve shows the absolute value of the input pulse, which is conventionally taken to be negative for a photomultiplier tube, and the red curve shows a magnified version of the combined pulses, so that one can clearly see the negative pre-pulse. Figure taken from `http://astro.ucla.edu/~veritas/docs/sub_proj8/cfd.pdf`

6 ns window, corresponding approximately to the time spread of the Čerenkov light front arriving on the detector plus some allowance for electronic jitter. By having this time window as narrow as possible a large proportion of false triggers are avoided and this helps reduce the energy threshold of the experiment. One therefore sees the importance of the CFDs' ability to assert the L1 signal at a time independent of the pulse amplitudes.

L3: Array Trigger

With the trigger system defined so far, all types of showers will have a chance of being recorded, not just γ-ray induced showers. This is not a problem for most cosmic rays because they usually produce images that look different from the images that γ rays produce. They can therefore be discriminated against during the analysis. However, there still exists a subset of cosmic rays which produces images that look like those of γ rays. For these, the stereoscopic capabilities of an array become a great asset. By seeing a shower image from more than one location, it may be possible to infer the nature of the primary particle with more precision; a cosmic-ray-induced shower may look like a γ-ray one from one view point, but look undeniably cosmic-ray like from another one. Furthermore, single muons are capable of producing Čerenkov images that, when viewed only partially, look identical to low-energy γ-ray ones. However, this phenomenon is very local and these images are seen by only one telescope at a time. It becomes apparent that by asking that a shower image be seen by more than one telescope, the single muon background is eliminated and the shower analysis is improved. This is the level 3 trigger. In more detail, the L2 signals from each telescope are sent to the L3 computer. Delays are applied to the L2 signals to compensate for propagation time in the cables and for Čerenkov light front arrival time at each telescope (approximatively calculated from the pointing direction of the array). The L3 modules then search for a coincidence in the L2 signals between a predetermined number of telescopes within a predetermined time window. The usual required number of telescopes is 2 (for observations with a 3-telescope array, as was the case for the results presented in this thesis) and the usual time window is 100 ns. This

time window was conservatively chosen to allow for different widths and curvatures in the Čerenkov light fronts, and for some electronic jitter, but a study shows that the rates remain stable if the window is narrowed down to around 25 ns [154]; therefore, the coincidence window may eventually be reduced to this value, when the system is better understood, so as to reduce the rate of accidental triggers. The L3 system is also in charge of giving the event numbers and of monitoring the dead-time. Dead-time in the system is dominated by the reading time of the telescopes, which is around 400 µs, and it scales with the array rate. It is about 7% for an L3 rate of 150 Hz.

Bias Curve

Now that the three trigger levels have been explained, one can go back to the question of what the threshold of the CFDs should be set at. Ideally this should be set as low as possible to catch low-energy events, but as the CFD threshold is lowered, the rate of L1 triggers will grow because of night-sky background fluctuations being large enough to cross the diminished threshold value. Since more and more pixels will pass the L1 trigger, which has become more accessible, the probability of L2 triggers due to night-sky background fluctuations also grows. Similarly, with more L2 triggers, the number of accidental L3 triggers also grows due to this background. Eventually, these false triggers become so numerous that it will be unreasonable to take data at such high rates. The CFD threshold is thus determined by taking what is called a **bias curve**. This is a graph of the L2 or L3 trigger rates as a function of the L1 CFDs' threshold. Figure 5.12 shows a typical example. There are two regions to the curve. The steep descent is the region dominated by night-sky background fluctuation triggers. The flatter part represents the triggers due to cosmic-ray showers. The CFDs' threshold is set at a value where the night-sky background fluctuations stop dominating the trigger rate, this will ensure stable running conditions. Note how the trigger rate due to cosmic rays drops when the telescope multiplicity requirement is changed from 1 to 2, and to 3 telescopes. Also note how the night-sky background dominated part of the curve shrinks with higher telescope multiplicity requirements, allowing to set the L1 threshold lower. The observations discussed later in this thesis were taken

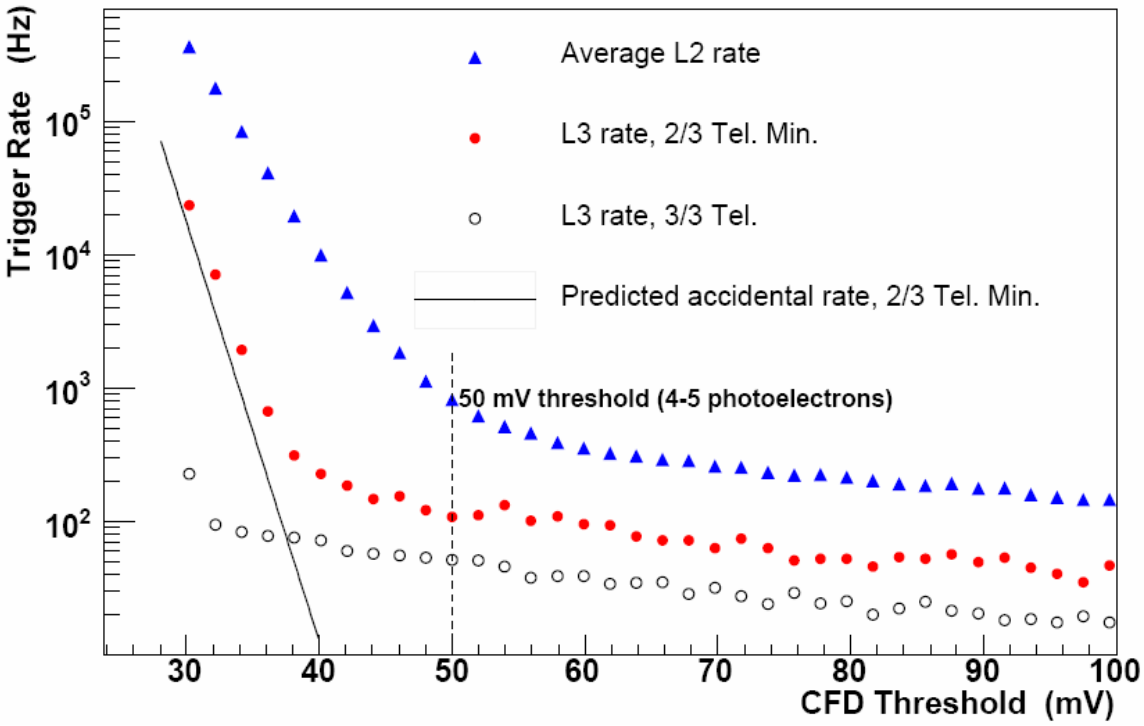

Figure 5.12: Bias curves for the L2 and L3 rates for an array of 3 telescopes. The average L2 rate curve should be multiplied by about a factor 3 to be compared with the other two curves, resulting in the curve corresponding to the L3 rate for the 1/3 telescope configuration. The L3 coincidence window was set for 50 ns, the telescope readout was disabled to avoid dead-time issues and the array was pointing to a dark region near zenith. The dashed line indicates normal operating threshold for the CFDs. The error bars are of the order of the marker sizes. Figure taken from [154].

with the 2 out of 3 telescopes configuration. The CFD threshold was conservatively chosen to be 50 mV, which corresponds to 4-5 photoelectrons [154]. This allows for observations being taken in a wide range of conditions.

Pedestal Trigger

Other types of triggers can be handled by the L3 system for calibration purposes. Such are the pedestal triggers, also called random triggers because they are not initiated by a physical event like an extensive air shower, but are simply artificial triggers forced by the system and so appear random in the sense that they could record a shower event by accident, but that is unlikely. The **pedestal** is the output value of a photomultiplier tube when there is no Čerenkov light input. This base value is adjustable and is usually set to around 16 digital counts so that small negative

fluctuations due to the night-sky background do not result in negative values that the FADCs could not deal with. The pedestal triggers occur at a rate of 1 Hz and are used to monitor the background light levels and stars in the field of view.

Laser Trigger

Another calibration trigger is the laser trigger (uniform laser shots illuminate the cameras to measure the relative gain and relative timing of the pixels; see section 5.6 for details on the laser system). The trigger is directly activated by a photodiode monitoring the laser shots. This is useful to investigate low laser light levels to perform single photoelectron analyses for example. Before the trigger was upgraded to be able to identify precisely the laser events, laser shots were found in the data by looking for a high multiplicity of hit channels. The scheme to make this procedure more reliable was then to point the telescopes at different dark patches of the sky to suppress triggers due to cosmic rays and then use the normal triggering scheme, but with the delays adjusted for laser runs with the flashes arriving simultaneously at all cameras.

5.4.2 Data Flow

Once a L3 trigger is issued, the acquisition system [156] is ordered to start recording. For each telescope, there are four Virtual Machine Environment (VME) crates that hold the FADC boards, plus another, auxiliary, one that holds the clock trigger module and the Global Positioning System (GPS) clock. Upon receipt of the trigger signal, the VME acquisition asks the FADC boards to look back in their 64 µs circular memory buffer to extract a 48 ns (24 samples) segment that contains the pulses that caused the system to trigger. The lookback time corresponds to the time that was needed to generate the trigger. The VME system stores the information it reads into 8 MB buffers that, once full, are transfered by a Scalable Coherent Interface (SCI) link (50 MB/s [7]) to a computer called the **event builder**. The event builder thus

[7] This is more than enough since the main limitation is the VME rate of reading for the FADC boards, around 780 kB/s per crate, resulting in about 3 MB/s to be sent to the event builder. The VME

receives fragments of events from the four crates reading the FADCs, and trigger, and time stamp information, from the auxiliary crate. It assembles these data to form a telescope event file and writes it to disk. This readout happens for all telescopes at the same time.

Another computer, the **harvester**, is in charge of receiving the telescope event files from each event builder, which are sent into 160 kB buffers over Gb ethernet. The harvester assembles the telescope files into a single array file that follows a custom-made format called the VERITAS Bank Format (**VBF**). It also compresses this file using a compression algorithm developed specifically for VERITAS data[8]. Using this scheme, the data for a run take up a few GB of disk space compared to the TB that would be needed without a trigger system. This scheme also has the advantage that the telescope events are already matched within the file; no analysis time is required to find the correspondence of events between telescopes. At the end of the night, the harvester data are transfered to an archive where members of VERITAS can access them for off-line analysis.

At the same time that the data acquisition is happening, a database logs the conditions of observations. It holds the configuration of many hardware components: high voltage values, CFD settings, patterns for the L2 system , lookback times, etc. These are read when initiating the hardware at the beginning of the night. If a change of configuration is made by the observers, the database records the time of change and new values implemented. Other than configuration informations, the database also records acquisition information such as the type of run, the source name, the trigger type, and diagnostic information such as weather conditions, currents in the photomultiplier tubes, telescope tracking, observer comments, etc.

The whole data acquisition system is ultimately controlled by the array control process, with which the observer interacts. Figures 5.13 and 5.14 show the details of the flow of trigger signals and data.

---

reading time is the source of the dead-time in the system.

[8]This algorithm compresses to levels comparable to commercial compressors, but its main advantage is that it speeds up the reading process of the files.

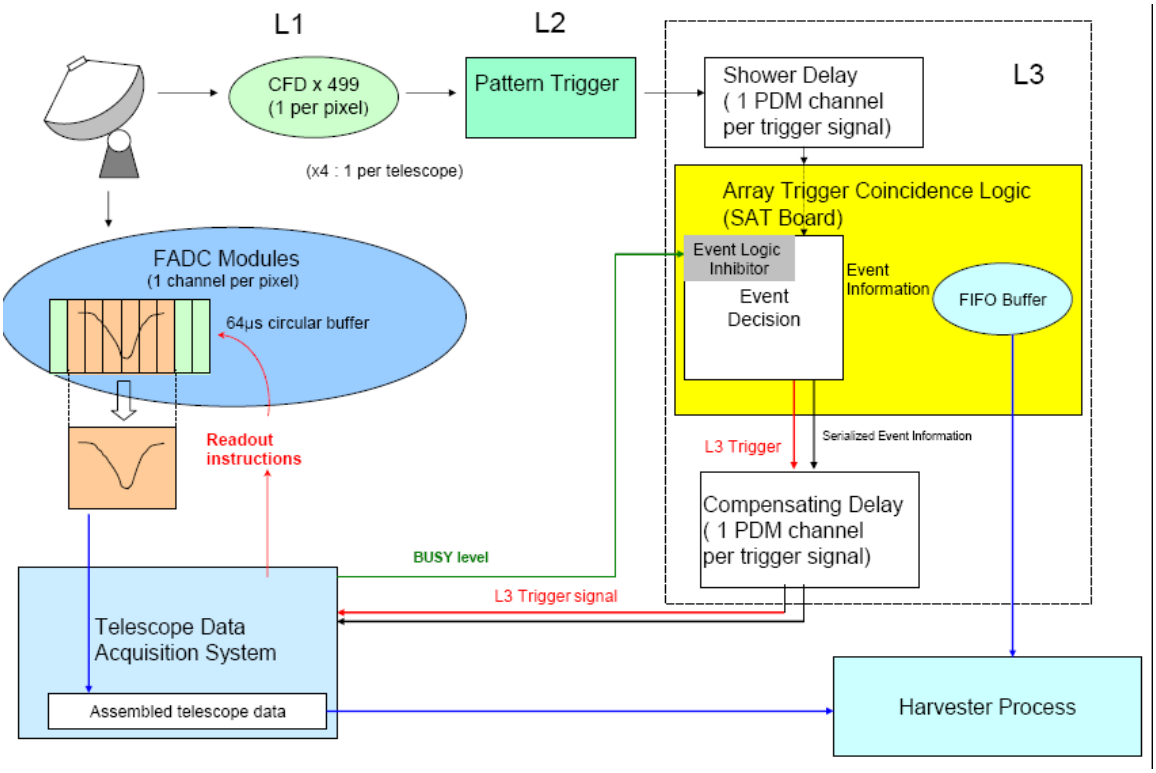

Figure 5.13: Propagation of the trigger system signals and basic data flow. Refer to text for explanation. Figure taken from [154]

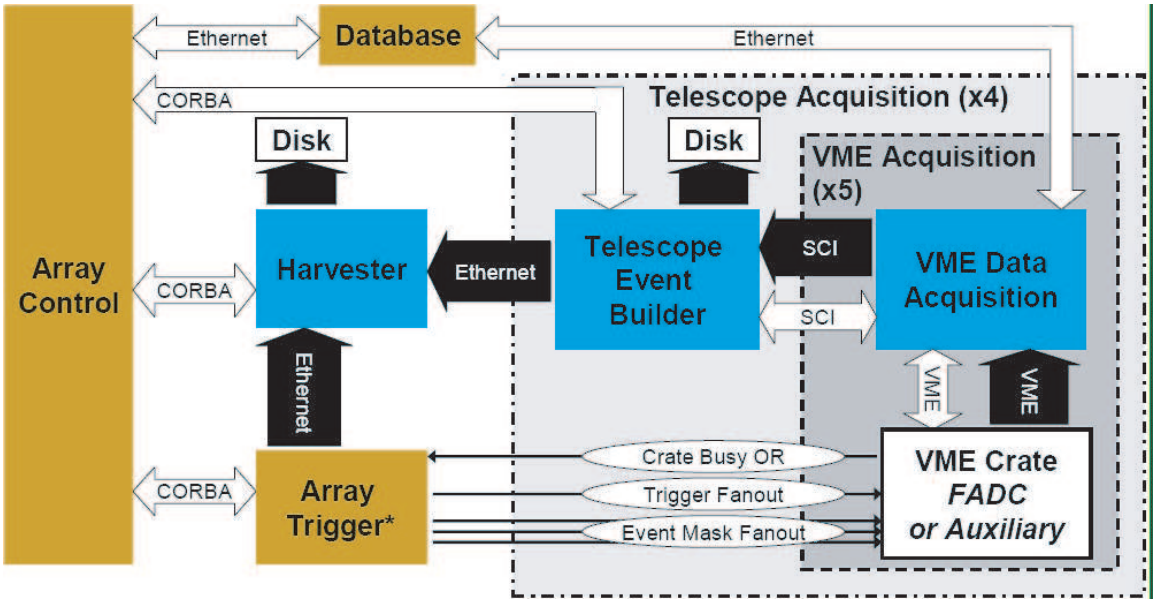

Figure 5.14: Details of the data acquisition system. Refer to text for explanation. Figure taken from [156]

Charge Injection

To test that the data flow is behaving as expected, a **charge injection system** has been implemented. This is basically a sophisticated programmable pulse generator that injects pulses, of shape, frequency and amplitude selected by the observer, into the pre-amplifier of every pixel [149]. The observer can choose to pulse every pixel of the camera or just a specified subset. This mimics the pulses that would normally be generated by the photomultiplier tubes and allows one to test the complete data acquisition chain. The charge injection system is particularly useful to diagnose problems, since it can also be used during the day.

5.5 Observing Strategies

Having a working detector is not sufficient to undertake quality measurements. Good observing conditions are limited in time, so a strategy must be developed to make the most of them.

First, since the Čerenkov light of extensive air showers is very faint, it is a natural strategy to minimize the amount of background light by observing only during the very darkest times[9], *i.e.* those nights when the moon is below the horizon. This means that observing is done during **dark runs**, periods of two to three consecutive weeks during which each night has at least two hours of moonless, observable, sky. Typically, dark runs start with nights of a few hours of moonless time, from sunset to moon rise, and grow into longer nights until the moon is completely absent from sunset to sunrise, after which the moonless time starts decreasing again and observing becomes limited by moon set and sunrise. After a week or so of unobservable nights during which the moon is present all night, a new dark run cycle starts again. Seasonal variations obviously affect the duration of the nights, and the length of the different parts of the cycle, but the main disruption from the cycle is due to a complete stop of observing activities during the months of July and August, because this is monsoon season in Arizona and all the sensitive electronic components are shut down and

[9]The subject of how dark is the night sky is further discussed in appendix C.

disconnected to protect them from lightning storms.

Next, weather conditions must be good too. The presence of clouds, even if not directly overhead, can change the detector's response. The clouds can block light coming from one direction and reflect light coming from another one. This is true for light coming from the extensive air showers themselves and from other sources too, like undesired city lights that can make the sky brighter than it should be. To help in the run selection during analysis, observers give a letter grade rating for the sky conditions at the moment of observations. This can be a little arbitrary because clouds are hard to see at night. To palliate to this, a (far) infrared radiation pyrometer (FIR) was installed on the OSS of one of the telescopes. It measures the temperature of the sky, and clouds in its field of view of 2.9 ° are easily detectable as a significant rise in temperature. A conventional weather station is also used to monitor wind strength and humidity conditions, which can prevent data taking in extreme cases. Weather satellite maps and information from nearby telescopes is also taken into account when verifying observing conditions.

Depending on the quality of the sky, primary or secondary sources are observed, or, if conditions prohibit observing, engineering work may be undertaken. The decision of what sources should be considered as primary or secondary is made by a time allocation committee (TAC) that receives observing proposals and selects the ones having the most chances of success or representing interesting physics to be investigated. The TAC also decides how much time should be spent on each source, which guides the observers in defining a schedule for data taking. Also important in designing this schedule are the times when a source is observable during the night. For quality observations, the sources should be at an elevation of about 60 ° or higher, otherwise the shower images degrade, the threshold goes up due to lower photon density on the ground and the sky is also brighter at lower elevations. Elevation charts for each source are therefore produced and observations times are optimized based on these.

At run time, it is also important to acquire some background observations against

which to compare the observations of the source. This can be done in ON/OFF or in wobble mode. In **ON/OFF mode** (also called **pair mode**), the source is centered in the field of view and tracked for a given period of time; this defines the ON portion of the observations. Then, the telescope is slewed back to the starting position (same declination, but offset in right ascension equal to the duration of the run) and tracking resumed, so as to observe the same portion of sky for the same duration of time, but with the source off the field of view; this is the OFF portion of the observation. The ON/OFF observations were regularly used with the Whipple 10-m telescope, and were used still with the VERITAS array to allow analysis with an established method. But with the larger field of view of VERITAS and its improved event reconstruction, the preferred way of taking background observations is with the **wobble mode**. In this mode, the source is offset from the camera center by some amount (usually, 0.5 °) and the background can be extracted from regions in the camera with the same offset, but located away from the source. This has the advantage that no OFF observations are required and thus maximizes the observing time, but the analysis is not as straightforward as with the pair mode (see section 6.6 for details on the analysis). Typical runs last for 20 min and the wobble direction (North, South, East or West) is changed between runs to avoid possible biases.

Also of importance at run time is the number of telescopes to use and the multiplicity required for the array trigger. With four telescopes, it could be advantageous to divide the array in sub-arrays and increase the number of sources observed at the same time, even if that could mean longer observation times for each source. With higher array trigger multiplicities, one can obtain higher quality data (from the multiple views) and also lower the CFD threshold while still operating at reasonable rates, but the higher multiplicity is done at the expense of a lower effective area. There clearly are some trade-offs to be made while configuring the observations. The different possibilities are still under study and at the time of writing the maximum number of telescopes available has always been used, both for simplicity reasons while the array was being built and understood, and because of the weakness of the sources

we observed. For example, most of the data presented in this thesis were taken with 3 telescopes and an array multiplicity requirement of 2 (see section 7.1.1 for more details).

Finally, during observations, events can happen that require a change from the established schedule. These events may be the result, for example, of looking at the quicklook analysis, a real-time monitor that runs on the harvester where data is being accumulated. This monitor does a fast, but fairly complete, analysis of the ongoing run, giving significances of γ-ray excesses, detection rates and diagnostic informations. This allows observers to tell right away if something is wrong in the data acquisition, or on the contrary, if the source under investigation is highly active, which would prompt for extended time being spent on this source. At all times, a γ-ray burst monitor is also concurrently running. This monitor receives alerts from the γ-ray burst coordinate network (GCN), a network of satellites that can quickly detect and give information about γ-ray burst events[10], and notifies the observers about the time and location of the bursts so that they can slew the telescopes to their position as fast as possible and try to catch some of their activity. Be it for diagnosing problems or for triggering extended observations, the strategy implemented by these systems is to give quick information to the observers to optimize the response time and increase the chances of observing interesting phenomena.

5.6 Hardware Monitoring

In order for the observing strategies to be useful, the array must be in top operating condition. The charge injection system mentioned in 5.4.2 is part of the routine checks that are made to verify the data flow. However, since this injects pulses in the pixel pre-amplifiers, it does not directly test the pixels themselves. Ideally, the pixels should also be flat-fielded, *i.e.* equalized in gains, to ensure a uniform camera response.

To accomplish the task of testing and flat-fielding the pixels, a system was designed

[10] See `http://gcn.gsfc.nasa.gov/` for more information about the GCN.

to **illuminate the camera uniformly**. It consists of a UV laser whose output is split in four and directed by optical fiber to diffusers mounted 4 m directly in front of the cameras (the system is similar to the one described in [157]). Each observing night, a 5 min laser run, where the laser is pulsed at 10 Hz, is taken. As mentioned in 5.4.1, another copy of the laser signal can be used to trigger the acquisition system externally, or the multiplicity of hit channels could be used too. The laser runs provide calibration information for the analysis, but they also allow the health of pixels to be monitored over long periods of time. To this effect, a small suite of software was written by the author and colleagues at McGill University to quantitatively compare pixel responses and log the results in an interactive web page[11] that can easily be consulted by people on site in charge of maintaining the cameras or by analysts wanting to verify the state of the system on a particular night. The basic components of this data quality monitoring (DQM) software suite are outlined in what follows[12].

5.6.1 Pixel Diagnosis

The first step in the DQM processing is to integrate the (pedestal subtracted) FADC traces over time so as to extract the charge output by each pixel for each laser event ($Q = \int I dt = \frac{1}{R} \int V dt$). Then a diagnosis is performed to flag pixels whose properties (mean charge over the laser run, charge variance, mean pedestal, pedestal variance, etc.) are statistically different from that of the rest of the camera or are outside predefined fixed bounds. The misbehaving pixels are then labeled, based on the nature of the misbehaving, as dead, carrying L2 synchronization signals to the FADC crates, monitoring the laser photodiode channel or simply non-standard with respect to the other ones, see figure 5.15.

[11] The data quality monitoring web site can be found at `http://veritas.sao.arizona.edu/DQM/index.html`.

[12] Note: the DQM software developed at McGill University is mainly preoccupied about pixel health monitoring. Another kind of DQM suite, that examines more closely the quality of the data acquisition exists and has been developed by another collaboration member, see `http://gamma1.astro.ucla.edu/diagnostics/`.

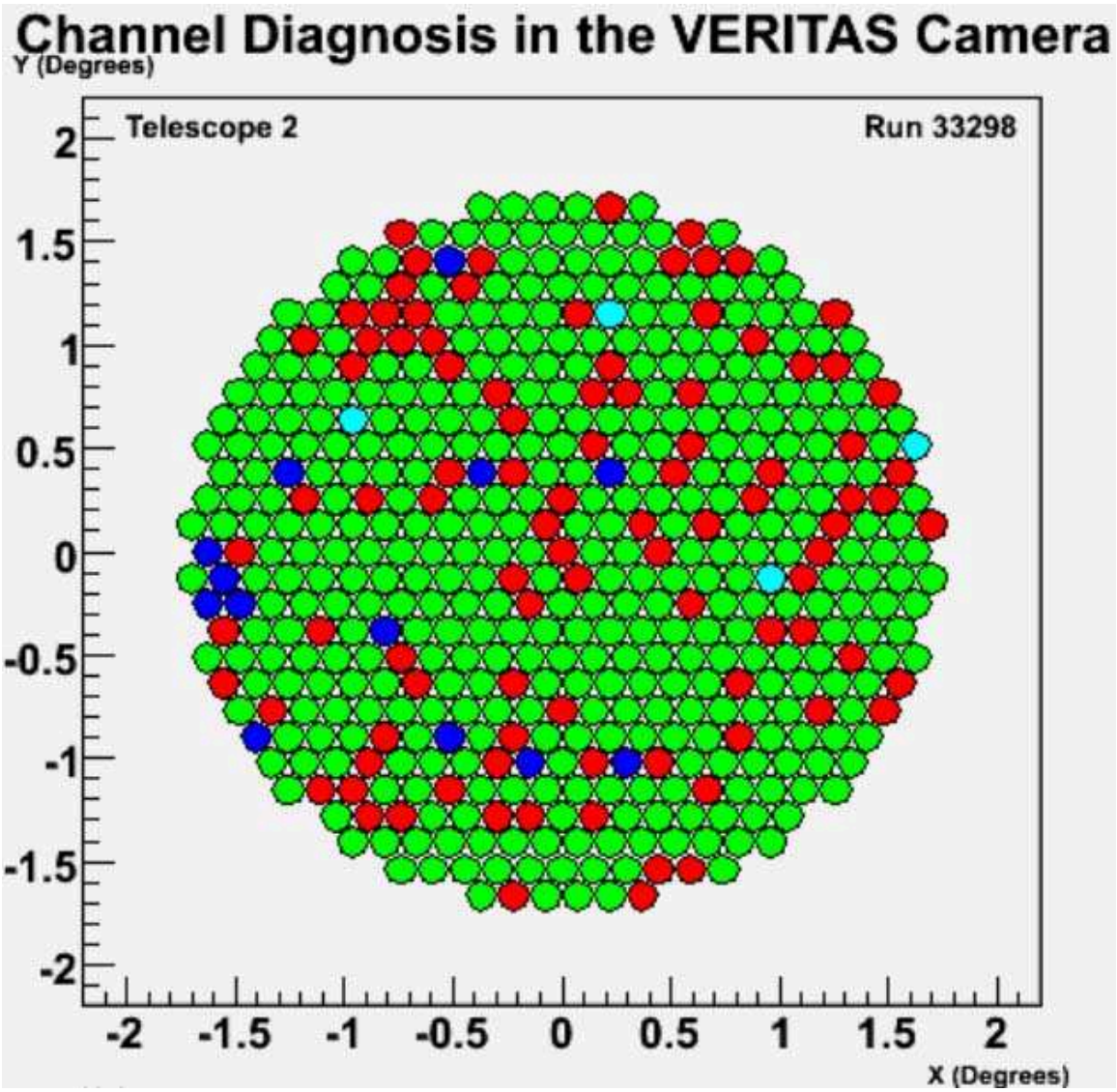

Figure 5.15: Diagnosis of the pixels' health. Green pixels are good, blue pixels are dead, cyan pixels are carrying L2 synchronization signals and red pixels are not necessarily bad, but are non-standard in some aspect of their response (it could be an abnormal mean charge value or variance, or it could be its pedestal level, or some other property that is verified by the diagnosis program).

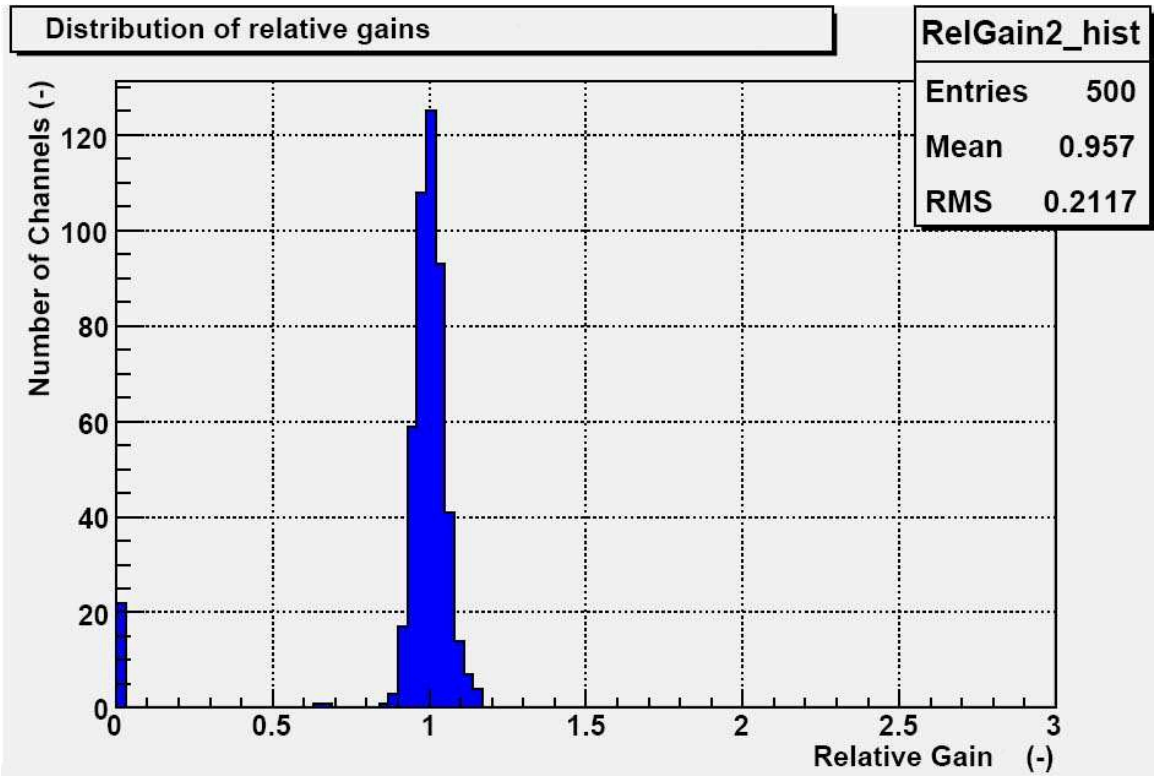

Figure 5.16: Distribution of the relative gain of the pixels for telescope 2 of the array. When a camera is properly flat-fielded, the distribution has a small width as is the case here. The small concentration of tubes with 0 relative gain correspond to dead tubes or channels carrying the L2 synchronization signals.

5.6.2 Relative Gains

Once the diagnosis has been performed, it becomes possible to define meaningful average quantities over the camera pixels by using only the good channels that have been identified. To verify the flat-fielding of the camera for example, the mean charge over the good pixels is found for each event and the ratio of every pixel's charge to this mean charge is computed. This yields the relative gain for each pixel. The relative gains from each event are then averaged to reduce the uncertainty. Figure 5.16 shows the distribution of the relative gains for a camera that has been properly flat-fielded.

It is important to note that the flat-fielding of the camera, based on the relative gains, relies heavily on the assumption that the **laser intensity is uniform over the camera**. The diffuser is supposed to make this happen, but there was an instance during the building of the array where the diffuser was not doing a perfect job. As

a result of flat-fielding with a bad diffuser, a gain gradient was subtly encoded for a relatively long time in the camera response, and it could not be easily unveiled [158]. Only by looking at pedestal variance distributions or absolute gain distributions could the uneven response be understood. Since then, the diffusers have been replaced by better quality ones and the flat-fielding is inspected more closely, in part with the tool described in section 5.6.4.

5.6.3 Absolute Gains

Other than relative gain data for flat-fielding the camera response in the analysis, absolute gain calibration information is also needed for understanding the response of the detector and being able to model it appropriately in simulation studies.

The **gain** of a photomultiplier tube is defined as the ratio of the number of electrons collected at the anode to the number of photoelectrons generated at the photocathode. This definition, as formulated here, is however inapplicable in practice since the number of photoelectrons generated due to a pulse of light is not directly measurable or deducible when a calibrated light source is unavailable, as is the case in this experiment. Hence, it is a tricky challenge to compute the needed gain from the sole output of the anode; another input seems to be missing. What saves us here is the recognition that the photoelectrons are generated randomly following a **Poisson distribution**. In fact, as photons hit the photocathode, photoelectrons are produced with a given probability (the quantum efficiency). The number of photoelectrons generated by light pulses of equal intensity will vary from pulse to pulse, but their distribution will follow the binomial distribution. Since the quantum efficiency is relatively small, it can be expected that **the Poisson distribution is a good approximation** for the binomial distribution in this case. Now, using the property that the variance of the Poisson distribution equals its mean, and using the fact that μ/σ **is scale invariant** as the population of photoelectrons is amplified by the gain of the photomultiplier tube, allows one to finally relate the unmeasurable number of photoelectrons to the measurable number of electrons collected at the anode and the spread of this number over many tries. Thus, the other handle on the problem of the gain measurement

is the repeatability of the experiment. By repeating the experiment a great number of times, the variance of the population becomes measurable and this knowledge is used in place of the knowledge of the initial number of photoelectrons. This method for the gain calculation, dubbed the **statistical method**, was successfully used at McGill to measure the gain of the STACEE photomultiplier tubes; results and details can be found in [159].

In equations, let G be the gain of the photomultiplier tube, μ_i be the mean total charge of the photoelectrons, σ_i be the standard deviation on the total charge of the photoelectrons[13], μ_f be the mean total charge of the population of electrons measured at the anode end of the photomultiplier tube, and σ_f be its standard deviation. Then,

$$\begin{aligned} G &:= \frac{\#_f(e^-)}{\#_i(e^-)}, && \text{by definition of gain;} \\ &= \frac{\mu_f/e^-}{\mu_i/e^-}, && \text{using the charge values;} \\ &= \frac{\mu_f/e^-}{\frac{(\mu_i/e^-)^2}{(\sigma_i/e^-)^2}}, && \text{since } \tfrac{\mu_i}{e^-} = (\tfrac{\sigma_i}{e^-})^2, \text{ according to Poisson statistics;} \\ &= \frac{\mu_f/e^-}{\frac{(\mu_f/e^-)^2}{(\sigma_f/e^-)^2}}, && \text{from a scale invariant of the population;} \end{aligned} \tag{5.1}$$

that is,

$$\boxed{G = \frac{\sigma_f^2}{\mu_f}\frac{1}{e^-}} \quad \text{in term of measurable properties.} \tag{5.2}$$

A program in the DQM suite applies this method to the VERITAS cameras[14]. The laser used for illuminating the camera is not outputting the same exact pulse at every shot. To correct for this, a laser monitor is built in the program as the mean

[13] What should be used for the Poisson distribution parameters are not μ_i and σ_i, which have units of charge, but μ_i/e^- and σ_i/e^-, which are unitless numbers of photoelectrons.

[14] To be correct, this method should really also include a correction factor for the dynode's statistics. Fluctuations in the number of generated electrons at each dynode tend to broaden the final distribution of electrons collected at the anode. It can be shown that the correction factor is $\frac{1}{(1+\alpha^2)}$, where α is the width of the single photoelectron distribution and depends on the applied voltage [148]. Simulations tend to show that α has a value around $0.4 - 0.5$, but experimental verification at nominal voltages could not be obtained yet and is still under study. Therefore, the correction factor is not yet included in the output of this DQM program.

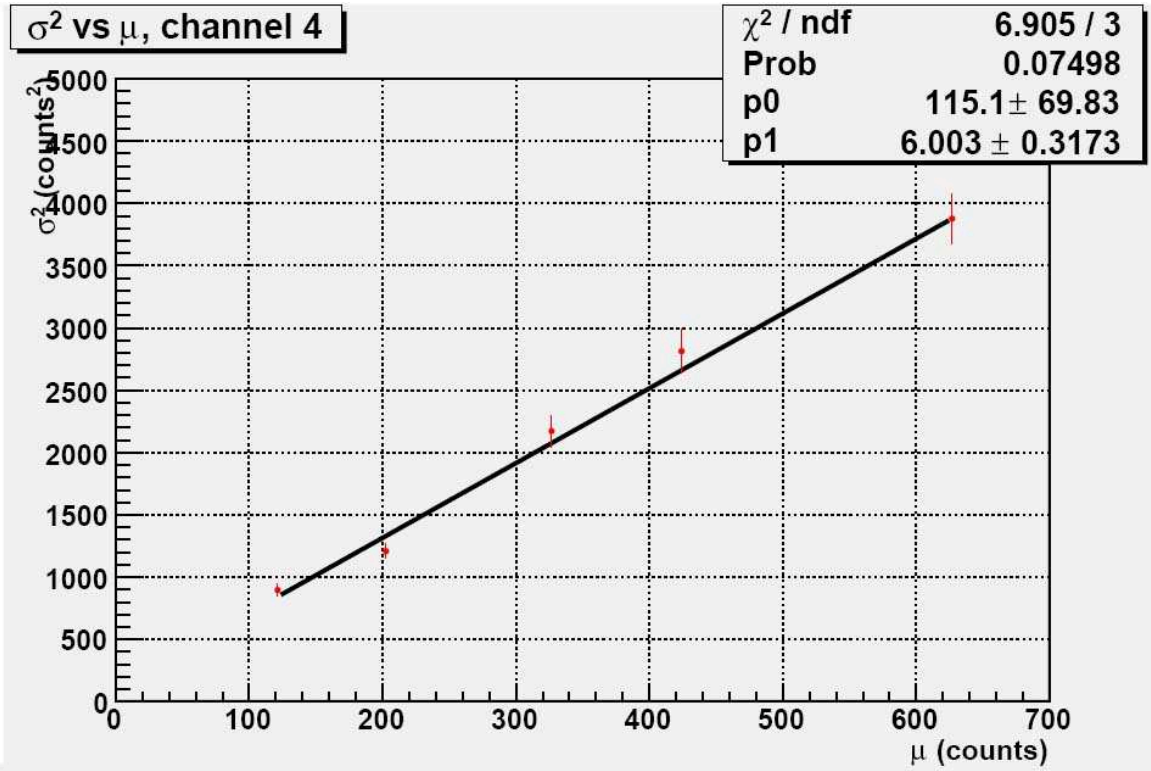

Figure 5.17: Absolute gain computation using the statistical method for a pixel in the telescope 2 camera. Using different attenuations for the laser, the relation between σ_f^2 and μ_f can be verified to be linear. The slope is related to the absolute gain of the tube. The non-zero intercept is due to electronic noise.

charge of the good channels of the camera, and correction factors are subsequently applied to each pixel's measured charge for every laser shot. Figure 5.17 shows an example of gain calculation using this technique.

It can be noted that the distributions shown in figures 5.16 and 5.18 are different in shape. The difference between them is believed to be due to the quantum efficiency of the photocathode of the tubes (in the large sense of the term, *i.e.* including collection efficiency and electron input system efficiency). In effect, the relative gains method described above uses the output of the tubes, which convolves the photocathode and electron multiplier, whereas the absolute gain method described here measures only the electron multiplier part. Not enough data concerning the quantum efficiencies could be found to ascertain this hypothesis, but the fact that the absolute gains computed here do correlate with other methods of finding the absolute gains suggests that at least no errors were done in the computations. If it can be shown that the

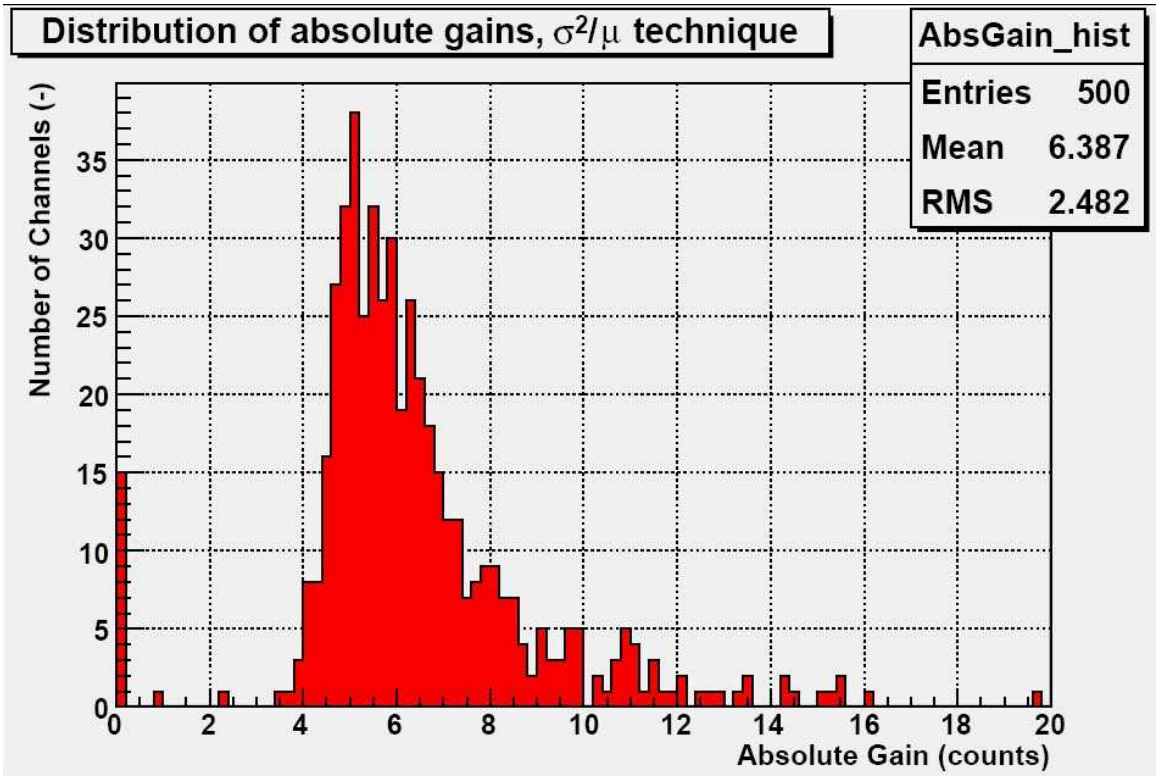

Figure 5.18: Distribution of the absolute gain of the pixels for telescope 2 of the array. The x-axis units are actually FADC counts per photoelectron. The small concentration of tubes with 0 absolute gain correspond to dead tubes or channels carrying the L2 synchronization signals. The data was taken on the same night as for that shown in figure 5.16. The two distributions have different shapes because the two methods do not measure the same thing. When computing the relative gains as specified in the previous section, the quantum efficiency of the tubes is included in the result. When computing with the statistical method, only the contribution from the electron multiplier is measured.

difference is indeed due to the quantum efficiency, then the ratio of the absolute gains, as computed here, to the relative gains, as computed above, could be used as a monitor of the quantum efficiency degradation over time.

5.6.4 Camera Uniformity

Sometimes, problems with non uniformity in the camera are not obvious to spot by eye. For this reason, a final program in the suite of the McGill DQM software was written to examine the distributions, over the camera face, of all the quantities it computes (over a hundred different quantities). The program attempts to find statistical evidence for the presence of gradients. It works in a very simple manner by dividing the camera face in pairs of pixel sets, *e.g.* inner and outer halves of the camera

or left and right halves, etc., and it computes the probability that the mean of the quantity being compared is compatible within uncertainty across the two members of each pair of pixel sets. The probability output is compared to a user-defined ridiculous probability criterion and the quantities that are judged improbably compatible with respect to this criterion are flagged and displayed to the user for closer inspection. Such a program will hopefully help quickly find and diagnose gradient problems that have been long to unveil in the past. A suite of monitoring programs like the DQM one is indispensable to the good functioning of such a large project as the VERITAS experiment.

Part III

ANALYSIS

6

Analysis Technique

In the previous chapters, different types of apparatus able to detect γ rays were discussed. The one involving the array of imaging telescopes used by the VERITAS collaboration was described at greater length because arrays of this type prove to be the most useful tools at very high energies, which are the energies of interest in this thesis, and of course because this array was the one used for the observations which are reported on here.

As was seen earlier, the signal recorded by this apparatus, for an incident γ-ray flux $\phi_\gamma(E) := \frac{dN_\gamma}{dt\,dA\,dE}$, is a set of FADC traces which represent a sequence of images of the extensive air showers formed by the absorption of γ rays by the atmosphere. Symbolically, one could write this as

$$\begin{aligned}&\{V_i(t)\}_n = \\ &\left\{ \int \left[\int \int \phi_{\text{Čerenkov}} \left(\text{EAS}(\gamma_n\left(\phi_\gamma(E)\right))\right) T(\theta_{\text{Zn}}, \theta_{\text{Az}}, x_i, y_i) d\theta_{\text{Zn}}\, d\theta_{\text{Az}} \right] \varepsilon_i(\lambda) d\lambda \right. \\ &\left. \times \text{e}^{-}\, G_i^{\text{PMT}}\, R_i\, L_i\, G_i^{\text{FADC}}\, C_i^{\text{V}\rightarrow\text{d.c.}} \right\},\end{aligned} \tag{6.1}$$

where

$\{V_i(t)\}_n$ is the set of FADC traces in digital counts. i runs over the number of channels connected to a photomultiplier tube in the detector and n represents the n^{th} γ ray seen by the detector placed in the flux $\phi_\gamma(E)$.

γ_n is an artificial function that discretizes $\phi_\gamma(E)$, which we think of idealized as a *continuous* flux. The "function" γ_n here is just a device to generate the n^{th} photon in a stream of random photons of energy E. The γ ray has a random impact parameter b.

EAS is a function that generates an extensive air shower from γ_n. It has a general shape that can be grossly linked to the energy of the primary γ ray and it is oriented along this latter's direction. Fluctuations in the shape are possible even for γ rays of identical energy.

$\phi_{\textbf{Čerenkov}}(\theta_{\mathrm{Zn}}, \theta_{\mathrm{Az}}, \lambda, t)$ is a function that describes the Čerenkov light distribution coming from the showers. It is the number of Čerenkov photons per unit time, of wavelength λ, that reach the telescope at time t and from zenith angle θ_{Zn}, and azimuth θ_{Az}. The total number of photons produced over the different wavelengths is related to the primary's energy.

$T(\theta_{\mathrm{Zn}}, \theta_{\mathrm{Az}}, x_i, y_i)$ represents the action of the telescope forming an image at the focal plane from the shower object and includes mirror reflectivity, point-spread function, lightcones, pointing direction and other acceptance effects. Integration of $\phi_{\mathrm{Čerenkov}}(\theta_{\mathrm{Zn}}, \theta_{\mathrm{Az}}, \lambda, t)$ with this function gives the number of photons that reach the photomultiplier tube i with coordinates (x_i, y_i) in the camera plane. Only Čerenkov photons emitted along a certain direction and coming from showers having impact point within an effective area A_{eff} will reach the camera.

$\varepsilon_i(\lambda)$ is the wavelength-dependent quantum efficiency of photomultiplier tube i;.

e^- is the electronic charge (in Coulombs) to convert the number of photons per second into a number of photoelectrons per second, *i.e.* a current.

G_i^{PMT} is the gain of photomultiplier tube i.

R_i is the resistance that acts as a current to voltage converter in the photomultiplier tube.

L_i are the cable losses in channel i.

G_i^{FADC} is the electronic gain factor going into FADC.

$C_i^{\mathrm{V}\rightarrow\mathrm{d.c.}}$ is the Volts to FADC counts conversion factor.

The job of the analysis is to solve the inverse problem of deducing $\phi_\gamma(E)$ in equation 6.1 from the measurement of these traces $\{V_i(t)\}_n$. This is a mathematical beast that cannot be tackled analytically as could be done for example for the night-sky background instrument, see appendix C. Obviously, direct substitution in the above "equation" is not possible, even if all the characteristics of the detector are known. What limits the approach here is that there are some *a priori* unknowns concerning the details of what a particular shower will look like: shape, position, orientation and energy. Each extensive air shower is different and results from a series of random processes, starting by its very location. Therefore, clever alternate ways of relating the showers to the properties of their γ-ray primary are needed; these will be explained later.

If one cannot *directly* link a set of FADC traces to the initial energy-dependent flux, one can however fairly easily recognize the signature of shower images in the traces. This, at least, gives a way of counting γ-ray photons and of establishing the existence of a ϕ_γ in the first place. But even this simple counting analysis is complicated by the fact that imaging atmospheric Čerenkov telescopes not only record images of γ rays, but also of other background processes due to night-sky background fluctuations and cosmic rays. These pollute the $\{V_i(t)\}_n$ by adding noise to the traces and by increasing the number of events far beyond what could be expected solely from the γ-ray flux. As has been seen, the hardware used allows very fast recording of images. A typical run might contain something of the order of 3×10^5 events, the vast majority of which (more than 99.5%) are only background due to cosmic-ray events. Therefore, very potent **cuts** are needed, *i.e.* means of distinguishing the γ-ray images of interest from the background images. Then, since one wishes to prove the existence of sources of γ rays, it is necessary to evaluate the significance of the γ-ray image counts by comparing them to the counts obtained from control regions where no sources are expected.

An analysis scheme capable of performing these tasks has been implemented in software written by a subgroup of the VERITAS collaboration [160]. The particu-

lar package used in this thesis is called *VEGAS*, an acronym standing for VEritas Gamma-ray Analysis Suite [161]. This is the collaboration's standard offline analysis package that accomplishes the processing of the data in six stages. It reads the data in the VERITAS VBF format (section 5.4.2) and processes it under the object-oriented data analysis framework ROOT. The tasks performed by these stages to extract useful information from the FADC traces are described in this chapter, as is an optimization of the main cut parameters, which was performed by the author.

6.1 Camera Calibration

The first task to be performed by the analysis is the calibration of the data received in each of the pixels of the cameras. Without this, a uniform lightfront impinging on the camera would look distorted when recorded because of the different gains for each of the pixels. Although the pixels are set to approximately the same gains, as mentioned in the previous chapter, so that the L2 trigger does a sensible job, the cameras are not perfectly flat-fielded. Moreover, the length of cable used to connect the pixels to the FADCs is also only approximately equal for all the pixels, resulting in delays in the responses for different channels. These effects thus need to be deconvoluted from the image recordings. Stages 1 and 2 of the *VEGAS* package perform these tasks.

6.1.1 Calibration Calculation

Stage 1 of the analysis is responsible for collecting all necessary hardware quantities from the data itself and from the database. From the laser run of the night the program calculates the relative gains and relative timing corrections to be applied to the data.

The relative timing corrections are necessary for the correct positioning of the integration window. They rely on the assumption that **the laser lightfront reaches all the pixels in the cameras at the same time**. The leading edge position of the pulses recorded in each channel, **T-Zeros**, are found in a more or less sophisticated way, depending on the particular algorithm chosen for this stage. Figure 6.1 shows a

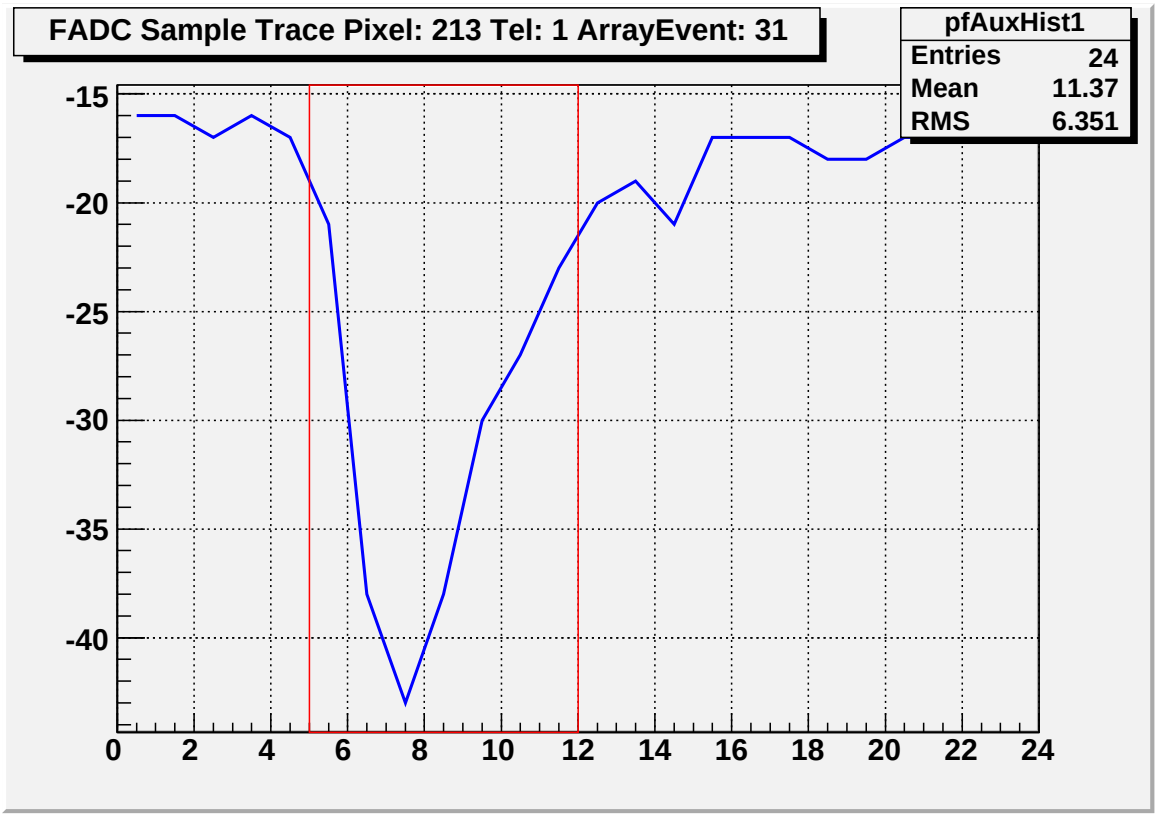

Figure 6.1: Example of a typical FADC trace. The integration region is between the two vertical lines. The x-axis is the FADC sample number (each sample is taken at a 2 ns interval) and the y-axis is the digitization of the pulse shape, in FADC units.

typical FADC trace. For the purposes of this thesis, the default algorithm was used, *i.e.* the T-Zeros are found by spotting the time position of the 50% height point on the rising edge of good pulses (the pulse is actually negative, as shown in the figure, but it is customary to work with its absolute value, hence the rising edge is what is looked for). This is done by linear interpolation on the trace. These times are averaged over many events and compared to their mean over the good pixels in the camera to finally yield a set of relative timing offsets with which one can reposition the integration window to overlap with the interesting part of the trace.

The relative gain calculation is done in a similar fashion as that described in section 5.6.2 and relies on the assumption that **the laser intensity that each pixel in the cameras sees is the same**. A difference is that the method used here does not, in the computation of the mean over the camera, remove channels which

are a little far from the average behavior, along with the dead and L2 channels.

From the data to be analyzed itself, the program again computes a set of T-Zeros. The ones from the laser run gave reliable relative timing offsets between pixels, but no absolute mean positioning for Čerenkov pulses because the trigger settings for laser data and observing data are different, and therefore result in different delays for the absolute positioning of the pulses. These new T-Zeros provide the required mean position of the pulses in the observing data. The integration window is then set so that 30% of its width is in front of the determined starting times of the pulses. This ensures that the rising edge below the 50% point of the trace is also included in the window. The width of the window is fixed to 7 samples, this value being chosen as a compromise to maximize the signal to noise ratio [162].

Also from the observing data, the program analyzes the pedestal triggers (see section 5.4.1) over different time slices of the run and computes the average baseline level and noise over which the Čerenkov light pulses sit. Each slice is 3 minutes long, the typical timescale over which stars travel the distance of a photomultiplier tube's diameter in the focal plane, although this depends somewhat on the particular pointing and tracking mode used.

From the database, other hardware quantities are collected, *e.g.* telescope positions, pointing information, tracking model, high voltage settings and pixel status, camera configuration, digital counts / photoelectron ratios, inter-telescope calibration constants[1], etc.

6.1.2 Calibration Application

Once the necessary hardware-dependent quantities have been collected the analysis proceeds to the calculation of the charge deposited in each pixel for each event. This is the job of stage 2 in the *VEGAS* analysis chain. The outputs of the calibration calculations for the laser run and the data run are both used to correct the raw data.

The traces in the different FADC crates are corrected for jitter in their reading time by shifting the data of each crate in time such that the L2 pulses, of which a

[1] Inter-telescope calibration is not yet fully understood and is currently the subject of investigation.

copy is sent to each crate, become aligned. The start of the integration window is then adjusted for the relative time offsets calculated previously. The result of the integration step can be visualized in figure 6.2.

The pedestal data for the given integration width is subtracted from the integrated trace and the relative gain corrections computed from the laser data are applied to these data to obtain a collection of calibrated images. Each such image, of which figure 6.3 is an example, is also accompanied by the pointing of the telescope, which is linearly interpolated from the database recorded tracking positions, which were extracted during the previous stage.

The pedestal and laser data are further used to identify misbehaving pixels. The gain of each pixel is compared to the mean over the camera and pixels with gains judged too far from the average are removed from the analysis. Similar comparisons are made for the gain variances and pedestal variances. A pixel identified as bad due to a non-acceptable pedestal variance may be excluded from the analysis only for that particular time slice when it was misbehaving as could be the case, for example, for a changing star field in the camera view. Pixels identified as bad based on their gain properties are excluded for the whole run.

During this stage one could also apply any desired trace modification, *e.g.* for noise padding, or pixel smoothing algorithm to account for the suppressed pixels, but none of this was done in this thesis because these options were not fully implemented or tested at the time of writing.

6.2 Image Cleaning

Now that the data have been calibrated and freed of hardware dependencies, the software image analysis can proceed. In figure 6.3, one can see that there seems to be a blob of hotter pixels surrounded by a sea of much colder ones forming a mostly random pattern, which can be associated with noise coming from the night-sky background fluctuations. So the first step in image processing is to remove such noise to keep only the interesting hot blob, which contains the extensive air shower

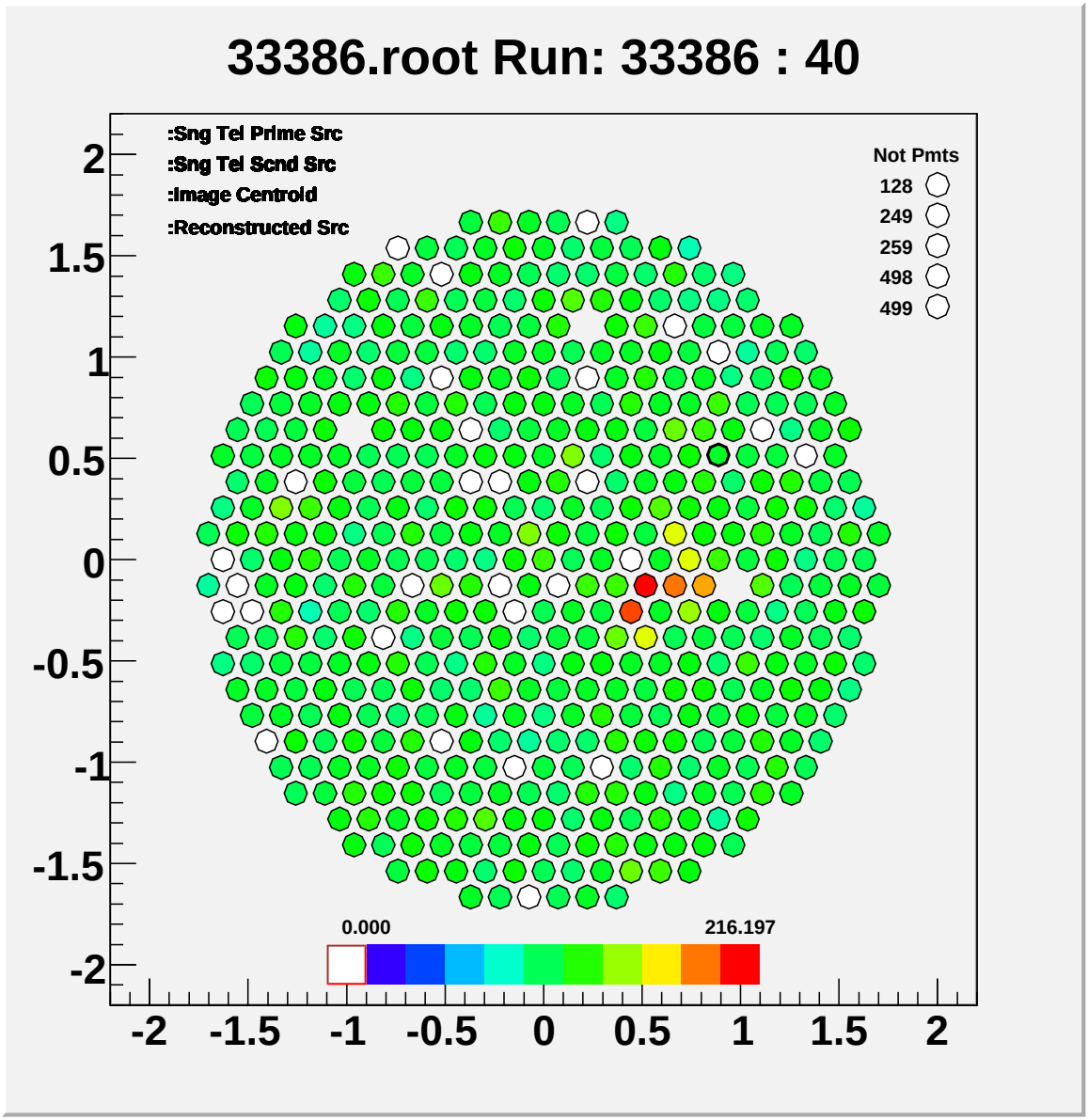

Figure 6.2: Example of a T2 image prior to gain equalization and pedestal subtraction. The color coding of the pixels correspond to their raw integrated charge. Note that, since the camera is already pretty well flat-fielded, gain equalization produces only imperceptible changes to the eye in this picture.

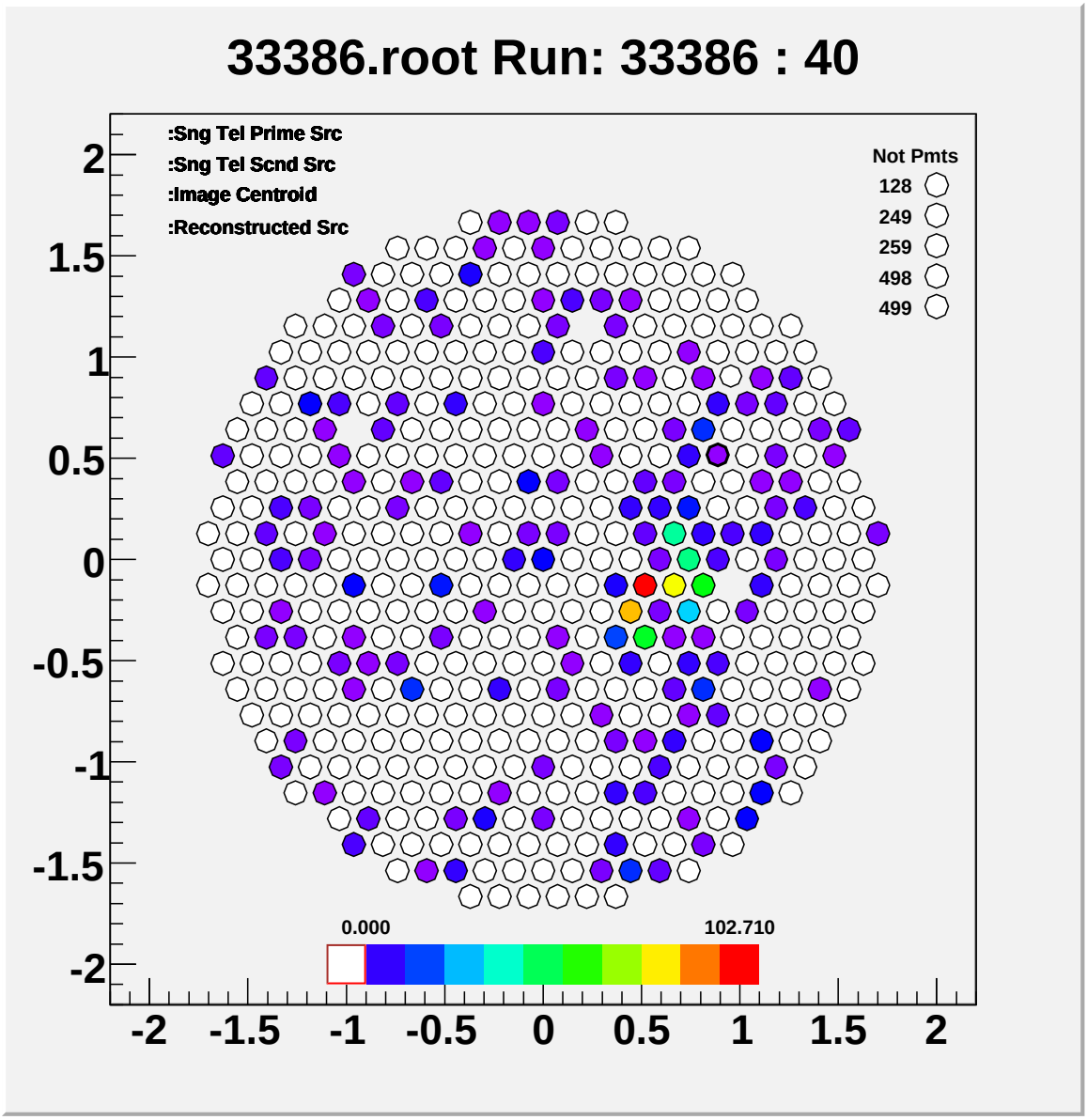

Figure 6.3: Example of a T2 image after gain equalization and pedestal subtraction, but prior to cleaning. The color coding of the pixels correspond to their integrated charge residual after the applied corrections.

information. This is performed by stage 3 of the analysis chain[2].

Different cleaning algorithms can be thought of. Many are defined in terms of a comparison between the signal in a given pixel and its pedestal variance[3]. If the signal exceeds the pedestal variance by more than a certain threshold factor, then the pixel is retained in the image, otherwise, it is discarded. The comparison of the signal to its pedestal variance means that the criterion is not based on a fixed parameter. For brighter skies, the pedestal variance will be higher, and for darker skies, it will be lower, resulting in different criteria for the strength that the signal must have to be counted as statistically improbable to be due to night-sky fluctuations.

Examples of cleaning algorithms include a *"simple cleaning"*, which was used by the Whipple collaboration [163] and which made use of two thresholds: a picture threshold and a boundary, lower, threshold. Pixels passing the picture threshold criterion are called picture pixels. Pixels passing the boundary threshold criterion with the additional requirement that they sit next to a picture pixel are then obviously called boundary pixels. Both picture and boundary pixels that survive the algorithm are then deemed image pixels and kept for further analysis.

A second example of a cleaning algorithm is the *"single isolated pixel cleaning"*[4], which builds on the previous algorithm by adding the extra requirement that a picture pixel cannot be isolated, it needs a neighbor boundary or picture pixel. This was judged necessary for the VERITAS data because the simple cleaning described above produced too many image pixels that are not necessarily tied to the main image and distort the results of the successive analysis. The removal of isolated picture pixels helps cure this problem. The method is illustrated in figures 6.4 and 6.5.

Ideally, one would want the thresholds that define the picture and boundary pixels to be as low as possible such that low-energy events, that produce dimmer images,

[2]The stage 3 tasks are now being executed by the stage 2 *VEGAS* program for increased processing speed, but they remain a conceptually different step.

[3]In the *VEGAS* package, the term pedestal variance really is an abuse of language as it truly refers to the pedestal standard deviation.

[4]The *single isolated pixel cleaning* is also called the *Event Display cleaning* because it is the default cleaning used in the *Event Display* analysis chain, where it was first introduced.

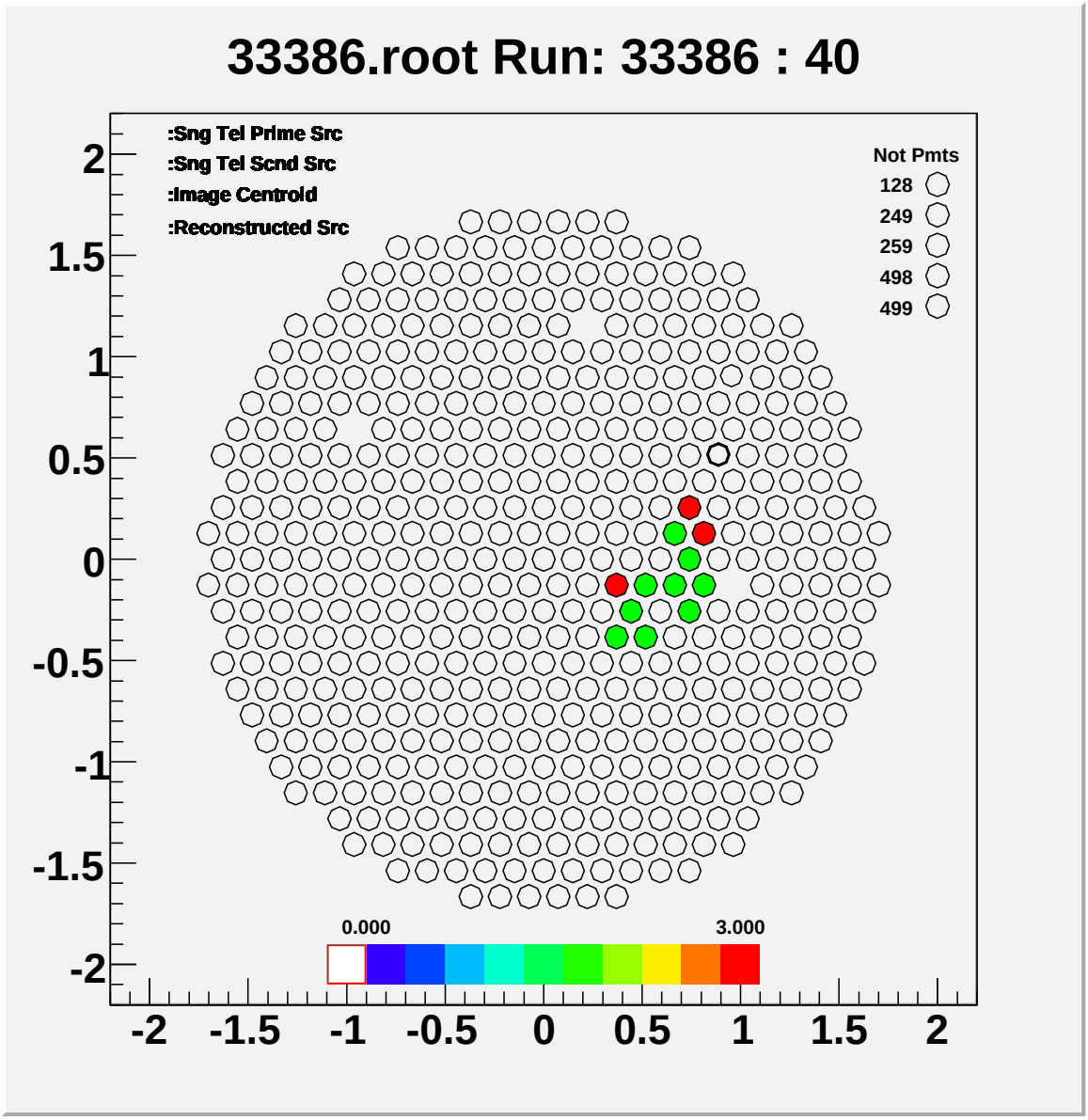

Figure 6.4: Example of a T2 image with picture (green) and boundary (red) pixels identified. Both green and red pixels become image pixels to be used in the Hillas parameterization (section 6.3). The method used is the *single isolated pixel cleaning* with a picture threshold of 5 and a boundary threshold of 2.5.

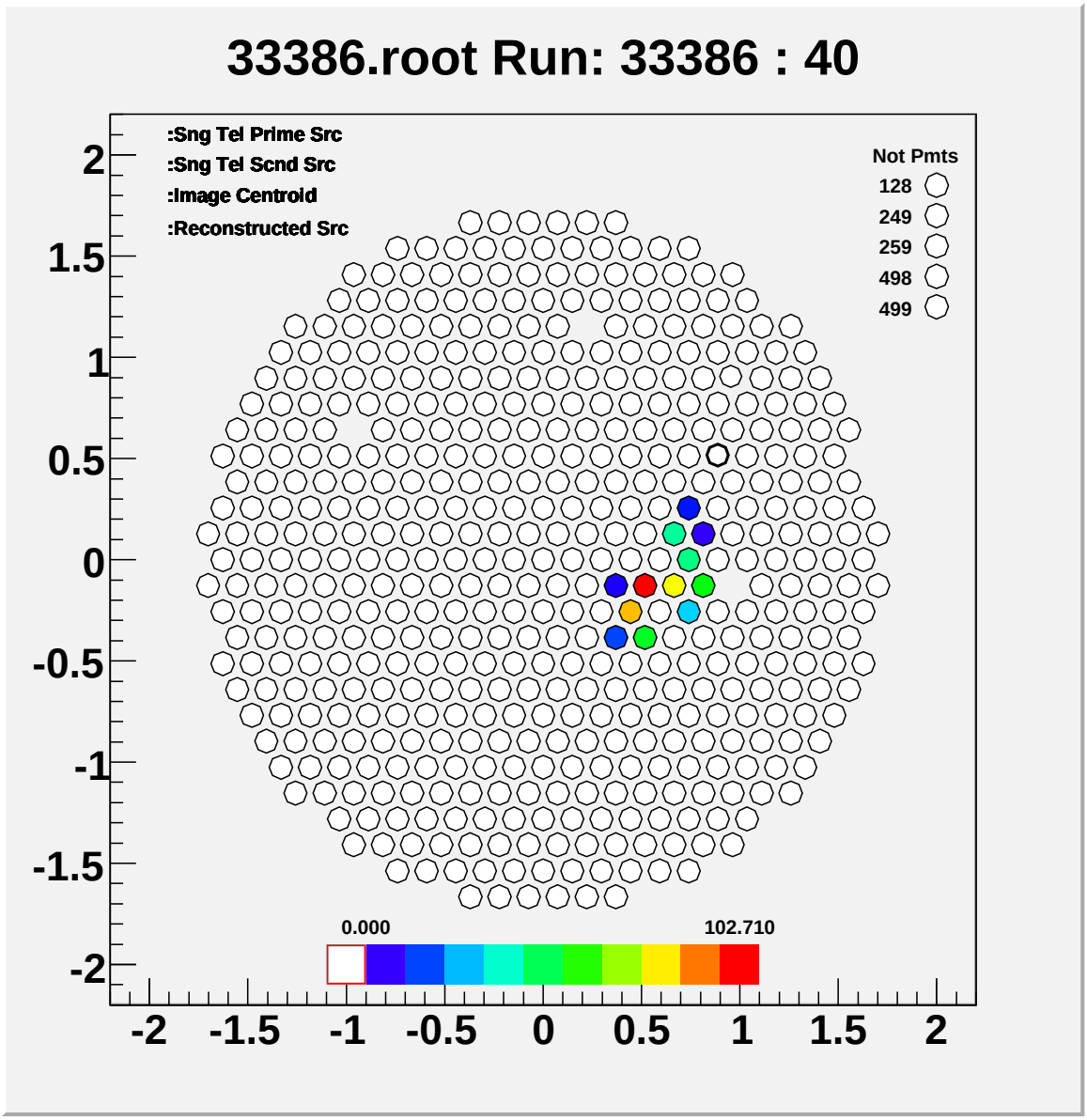

Figure 6.5: Example of a T2 image after cleaning. The color coding of the pixels correspond to their integrated charge residual, *i.e.* it reflects how much Čerenkov light they received. The cleaning method used is the *single isolated pixel cleaning* with a picture threshold of 5 and a boundary threshold of 2.5.

are kept in the analysis with enough pixels to faithfully reconstruct them. However, lowering these thresholds increases the number of pixels that can wrongly pass the cut because of random fluctuations of the night-sky background. This is what justified the evolution of the original simple cleaning algorithm to the *single isolated pixel cleaning*. Further evolutions, and new additions to the *VEGAS* chain, are the *"double isolated pixel cleaning"*, which is the same as the previous algorithm, but asks that every picture pixel has at least two neighbor pixels; and the *"cluster pixel cleaning"*, which also builds on the above and keeps only the most significant contiguous cluster of picture and boundary pixels. All those algorithms are discussed at greater length in [164] where it is shown that the *double isolated pixel cleaning*, and the *cluster pixel cleaning* are each performing better than their respective predecessors at lower thresholds. Although the cluster pixel cleaning seems the most promising of the methods, it has not been sufficiently tested yet and the results presented later in this thesis make use of the well-accepted *single isolated pixel cleaning* method. With the standard cleaning thresholds factors of 5 for picture pixels and 2.5 for boundary pixels, this yields relatively few images with apparent noise and in fact this method is practically equivalent to the double isolated pixel cleaning and cluster pixel cleaning at the same thresholds.

Other related techniques exist to prepare images for parameterization. For example one can imagine some kind of low-pass filter applied on a Fourier transform of the image to smooth out the high frequency noise. Such a technique was investigated using simulations in [165] and looked promising, but an internal qualitative investigation using some real VERITAS data revealed that there is most probably little gain in implementing this technique compared to the standard method discussed above and which works reasonably well [166] [5]. More noise removing techniques inspired

[5]The author of this thesis would, however, like to see this investigation pushed further before a negative conclusion be drawn, and suggests that quantitative comparisons of the reconstructed Hillas parameters with and without filtering on the Fourier transform of the images be performed, as was originally done in [165]. The author believes that application of the Fourier transform low-pass filtering could be useful in removing night-sky noise contributions from within the shower image itself,

from image processing software are probably worth investigating as well.

6.3 Hillas Parameters

Another task performed by stage 3 of the analysis is the parameterization of the event's image on a single-telescope basis. As was mentioned in section 4.3.2, the sought-after γ-ray images appear grossly as compact elliptical shapes in the camera plane. This is in contrast to some of the background images that look like rings (muons) or large, not-so-well-defined, blobs (cosmic rays), see figures 6.6 and 6.7 for examples of these. It thus makes sense to fit an ellipse to the images and use the parameters of the ellipse to discriminate between the different types of images. This is the approach pioneered by Hillas in 1985 [106], hence the name **Hillas Parameters** for the parameters of the fitted ellipse and some related quantities. Figure 6.8 shows an ellipse fitted, by a moments analysis, to a candidate cleaned image.

Explicitly, the main Hillas parameters[6] are:

xc x coordinate, in degrees, of the centroid of the image, weighted by the signal strength in the image pixels (black cross in figure 6.8).

yc y coordinate, in degrees, of the centroid of the image, weighted by the signal strength in the image pixels (black cross in figure 6.8).

width transversal angular extent, in degrees, of the fitted Hillas ellipse (semi-minor axis length). Corresponds to the spread of image pixel positions perpendicular to the main axis, weighted by the signal strengths.

which the standard cleaning cannot do. The filtered image could then be further cleaned with the standard or newer methods, with possibly lower cleaning thresholds and yield images reconstructed with higher accuracy. This could result in improved source direction determination, improved energy estimation and lower energy threshold. It is unclear whether the increased computing time would be a major burden, but it may also be possible to preselect images for which the Fourier transform techniques would be the most beneficial and apply it only to those.

[6] It can be noted that the Hillas parameters are not all independent. For example, α is derived from a combination of the *miss* and *distance* parameters. The way to compute the Hillas Parameters is given explicitly in [167].

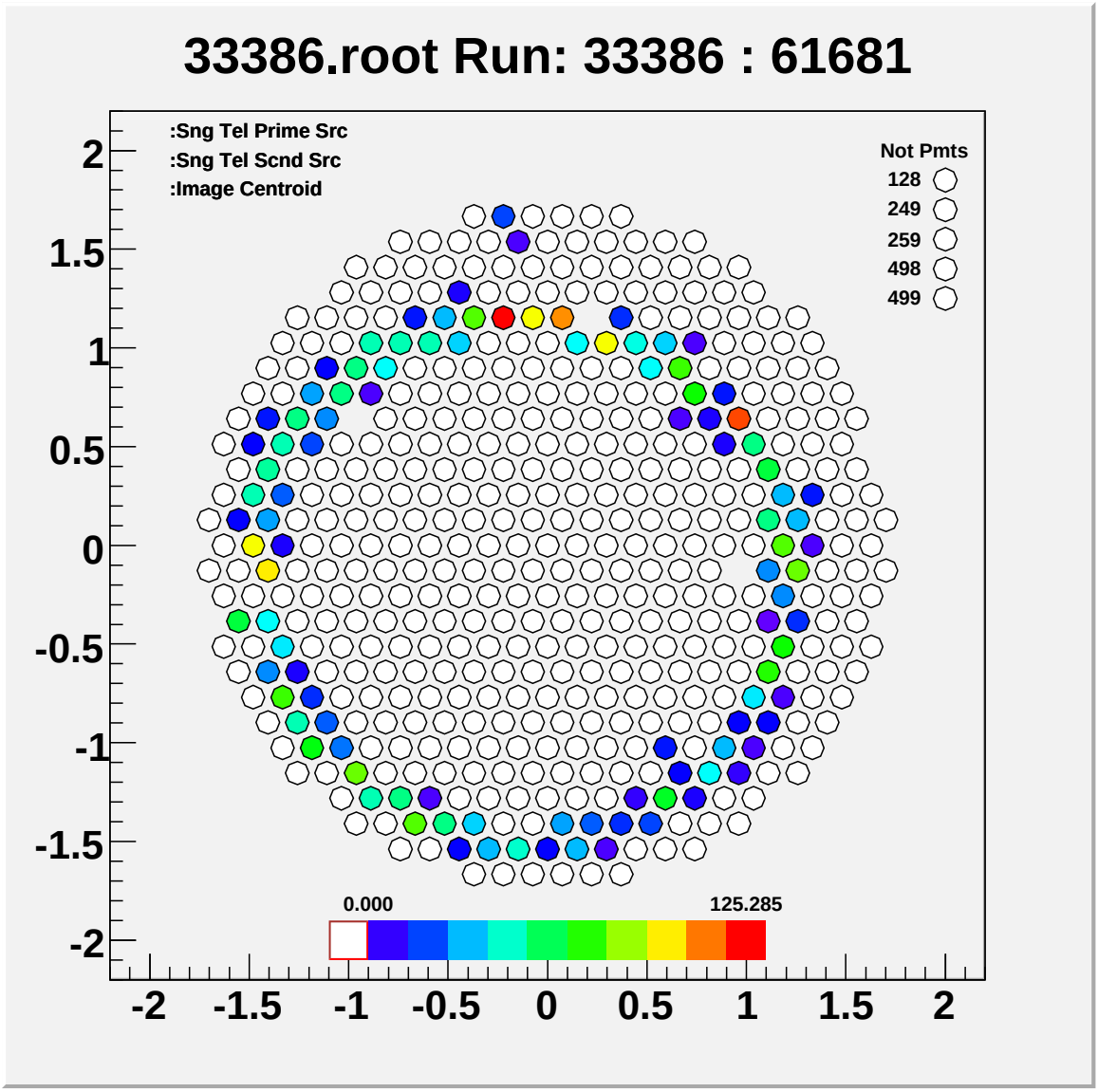

Figure 6.6: Example of a muon ring image in T2.

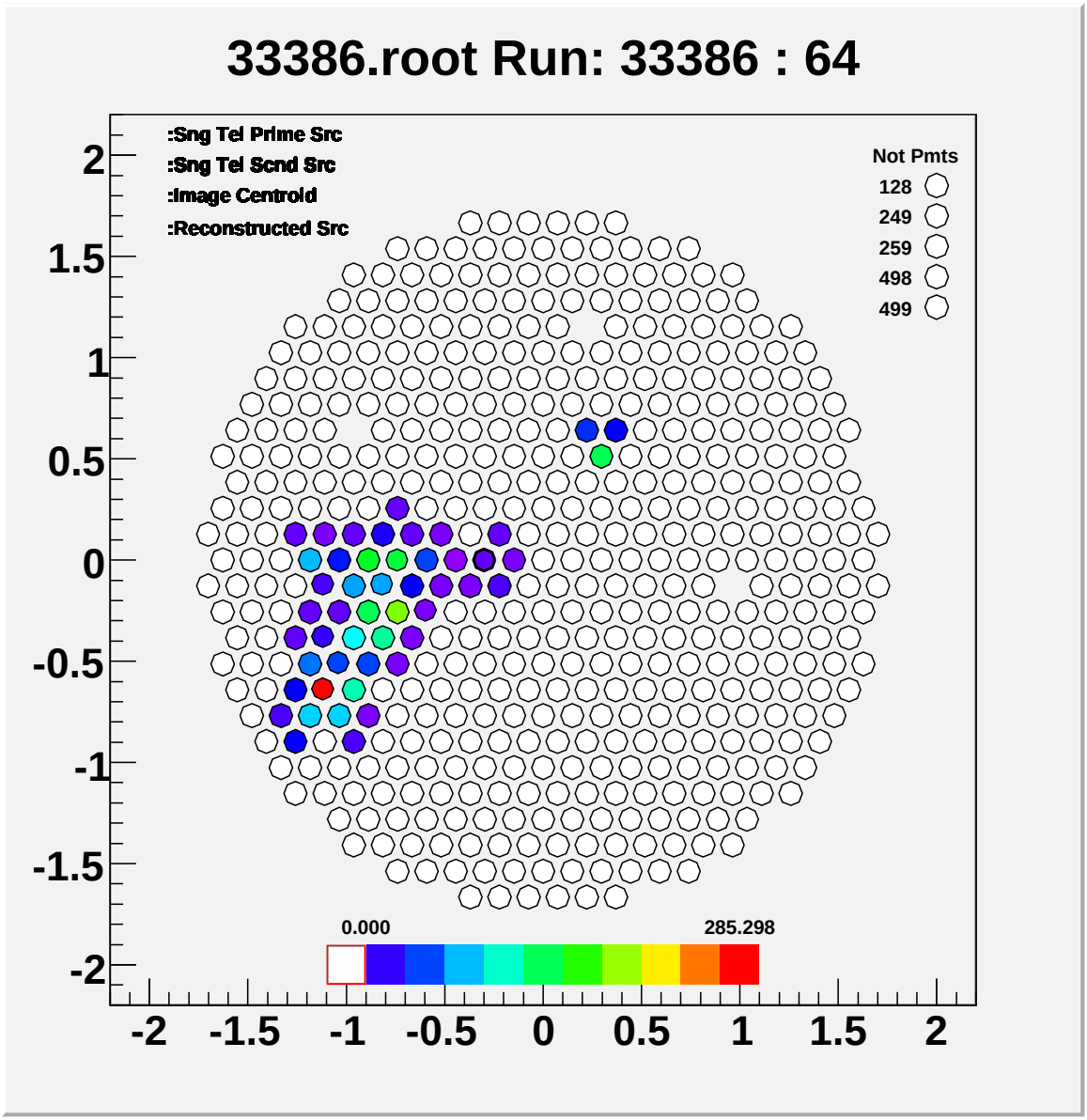

Figure 6.7: Example of a cosmic ray image in T3.

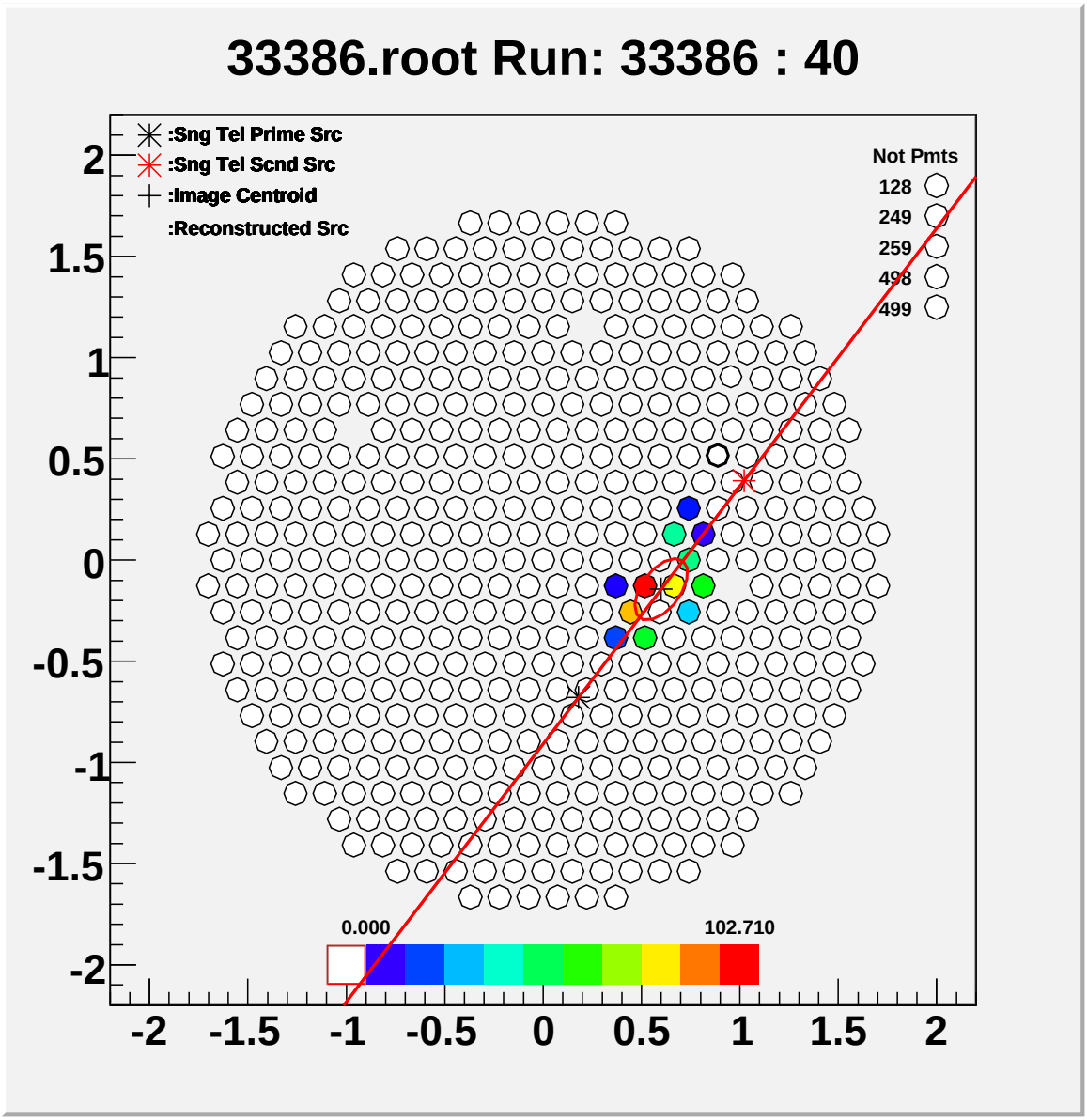

Figure 6.8: Example of an image in T2 that was successfully Hillas-parameterized.

length longitudinal angular extent, in degrees, of the fitted Hillas ellipse (semi-major axis length). Corresponds to the spread of image pixel positions parallel to the main axis, weighted by the signal strengths.

miss perpendicular angular distance from the center of the field of view to the image axis, in degrees.

azimuthal-width same as *width*, but with respect to an axis that would pass through the center of the field of view and the image centroid.

distance angular distance, in degrees, between the center of the field of view and the image centroid.

α angle, in degrees, between the major axis of the fitted Hillas ellipse and an axis that would pass through the center of the field of view and the image centroid.

size Sum, in digital counts, of the signals in the image pixels.

asymmetry skewness of the signal distribution along the major axis.

Figure 6.9 shows pictorially the meaning of these parameters.

Some analyses that involve only one telescope assume that **the source is point-like and its location is at the center of the field of view**. This is the case for analyses that make use, for example, of the α parameter defined above, since it involves the center of the field of view in its definition. The motivation for this parameter comes from the observation that images of extensive air showers due to γ rays coming from a point source should have their main axis pointing to the source location, much like meteor trails in a meteor shower all seem to come from the same point in the sky. Hence, images of γ rays from the source are expected to have low values of α. This α turned out to be the most powerful parameter in single-telescope analyses and was extensively used by the Whipple collaboration. The fact that such analyses assumed the position of the source in the field of view constrained the number of unknowns in the analysis and the previous set of parameters came to be known as

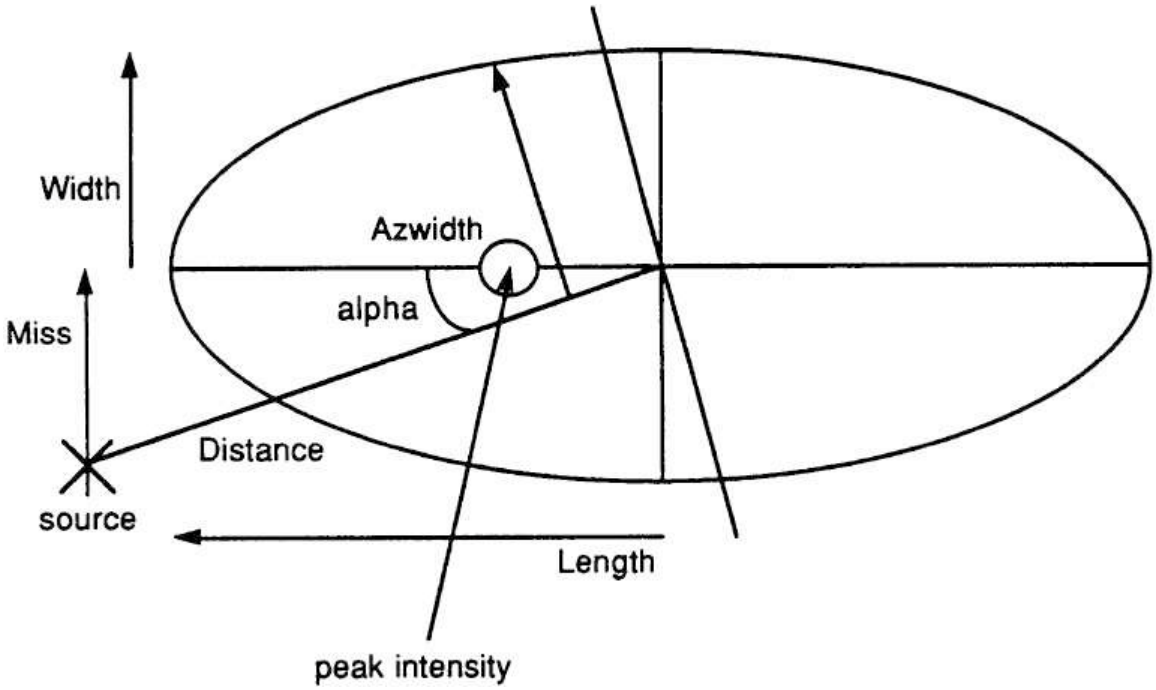

Figure 6.9: Schematic representation of the Hillas parameters. Note that here the center of the field of view and the location of the source are assumed to be coincident. Figure taken from [167].

the **1-D Hillas parameters** to distinguish it from the following set of parameters that are used when **no source location is assumed or the source is extended** and the problem becomes a two-dimensional search for a signal in the field of view. The **2-D Hillas parameters** add the following parameters to the previous ones:

disp angular displacement, in degrees, between the image centroid and the reconstructed, most probable, source position in the image plane.

x1 x coordinate, in degrees, of the reconstructed, most probable, source position, in degrees (black star in figure 6.8).

y1 y coordinate, in degrees, of the reconstructed, most probable, source position, in degrees (black star in figure 6.8).

x2 x coordinate, in degrees, of the reconstructed, less probable, source position, in degrees (red star in figure 6.8).

y2 y coordinate, in degrees, of the reconstructed, less probable, source position, in

degrees (red star in figure 6.8).

To understand how these parameters are deduced, observe that the prolongation of the major axis of a shower image should intersect with the location of the source in the image plane, since the axis indicates the direction of propagation of the original γ ray. From the asymmetry of the image one can deduce which part corresponds to the top of the shower, since the viewing angle (from below the shower) makes it *appear* brighter near its top; hence one can deduce which part of the image is closer to the source location. Now, also observe that images become more and more elongated as the impact parameter of the showers on the ground increases. Showers impacting close to the telescope look more circular in the image plane because they offer a more head-on view to the telescope, and showers impacting further away offer a more lateral view, resulting in a more elongated image. It can then be seen that the more elongated an image is, the further away it is from the source in the image plane. Lessard et al. recognized that fact in [168] and managed to relate the elongation of an image to the distance it should lie from the source location along the prolongation of the major axis in the direction of the asymmetry (this direction is sometimes ambiguous, which explains why there is a set of more probable and a set of less probable coordinates for the location of the source). The relationship is given by

$$disp = \xi \left(1 - \frac{width}{length}\right), \tag{6.2}$$

where ξ is a scaling parameter that depends on many things (height of the shower, model of the atmosphere, etc.) but can be quite successfully experimentally calibrated from observations of a known source.

Although the *VEGAS* package is able to compute both the 1-D and 2-D Hillas parameters, the analysis presented in chapter 7 only makes use, indirectly, of the 1-D parameters because, as will be shown in section 6.4, when there are multiple telescopes involved in the observations, the analysis need not rely on the 1-D or 2-D Hillas parameters alone. Instead, the parameters measured from all telescopes can be combined to yield an improved set of parameters. In particular, the arrival direction

of the shower can be established by other means than that described above, and so the 2-D Hillas parameters are not strictly needed.

6.4 Reconstruction

In single-telescope mode, selection of γ-ray images is based solely on the Hillas parameters. When observations are made with more than one telescope, one can combine the measurements of these parameters from the different telescopes and derive a new set of improved, more potent, parameters that represent the shower characteristics better. Also, the stereoscopic views of the showers make it possible to deduce their trajectories in the atmosphere with greater accuracy. Calculation of the trajectories and improved parameters are what is referred to as the **reconstruction** of the events. This is performed by stage 4 of the analysis.

Before any reconstruction is attempted however, the cleaned Hillas-parameterized images need to pass further tests that will ensure that the reconstruction will yield reliable results. These tests are known as **quality cuts** and are as follows:

- The images must be sufficiently luminous that they cannot be due to a night-sky background fluctuation.
- The image must not lie too close to the edge of the camera, otherwise it could be truncated, which would certainly affect the Hillas parameterization. For example, an image which would normally have its main axis passing through the center of the camera could, if truncated along its length, appear as having its main axis perpendicular to the original direction.
- The images must contain a minimum number of useful pixels to ensure that the image axis fitting was robust.

In terms of requirements on the parameters, they translate respectively to what is shown in table 6.1 [7].

[7] Note that alternative or additional quality cuts are possible. The ones listed here are the standard used by the VERITAS collaboration in its preliminary phase and are the ones used in this thesis.

Quality Cuts
$size \geq 400$ d.c.
$distance < 1.3\,^{\circ}$
$N_{\text{tubes}} \geq 5$

Table 6.1: Quality cuts

6.4.1 Geometrical Reconstruction

With the assurance that the remaining images are of good quality and that the main axis of their fitted Hillas ellipses are correctly oriented, one can proceed to the geometrical reconstruction. Since a shower develops along the initial trajectory of its primary γ ray, its axis points back to the source location. In the views of the sky as seen by the different cameras, this source location is a common, but still unknown, point. The shower, being physically much closer to the telescopes than the source is, is however imaged at different places in the cameras, but the images axes still point to the source location. Thus, by superimposing the views of the sky from the different cameras, the intersection of the main axes of the different ellipses obtained for an event indicates the arrival direction of the primary in the sky. This is illustrated in figure 6.10. Most of the time it is unlikely that there is a single intersection point when there are more than two cameras involved. In this case, the perpendicular distance squared from a point to each image axis is minimized. The distances are weighted by the *size* parameter following the idea that a more luminous image probably has a better defined main axis than a less luminous one. Accurate reconstruction of the source position is important because better angular resolution allows one to decrease the size of the signal region in the statistical analysis and thus to reduce the amount of background noise in the measurement (see section 6.6). It would also improve morphological studies of extended sources. Currently the **angular resolution** of VERITAS, defined as the 68 % containment radius of reconstructed source positions

There is ongoing work within the collaboration to optimize these cuts and possibly reduce these requirements that effectively impose a threshold on the energy that a shower must have in order to pass the cuts.

for simulated showers, is around 0.15°, but studies are underway to improve this by using alternative reconstruction algorithms [169].

Similarly one can follow the main axis of the shower in the other direction, up to where it hits the ground. This point is referred to as the **core location**. To find it, one again intersects the axes from the image ellipses, but this time the cameras are not superimposed. Instead they are projected from their respective telescope location to a common plane perpendicular to the telescopes pointing direction. The intersection of the axes in this plane yields the point where the primary particle would have hit it and this can be propagated further to the ground [170]. Figure 6.11 illustrates the procedure. To improve the accuracy it is customary to refine the axes of the ellipse by not using the result of the Hillas fitting procedure, but to use lines that pass through the centroid of the ellipses and the source location in the cameras, obtained as described above. These new axes are more likely to represent the true shower axis because of the use of the "averaged" source location. The core location resolution is around 7.5 m for VERITAS [171].

6.4.2 Shower Parameters Reconstruction

Up to now the trajectory of the primary particle has been reconstructed. However, this is not sufficient to extract a useful signal since this does not tell us which showers originate from a γ-ray primary or from a cosmic-ray one. As has been mentioned previously, the morphology of the showers changes between the different types. The Hillas parameters already provide some information regarding their shape, and in a stereoscopic system the different cameras provide different views, hence different sets of Hillas parameters. Therefore a way to combine the information from the different cameras regarding the shape of the showers is highly desirable as it would provide an improved overall picture of what the shower really looked like and from which primary particle it originated. Other means of finding the nature of the primary particle have been suggested in [171] and include examination of the temporal information of the images (γ-ray images should be narrower in time), examination of the homogeneity of the Čerenkov light pool (energy estimates from individual telescopes should agree

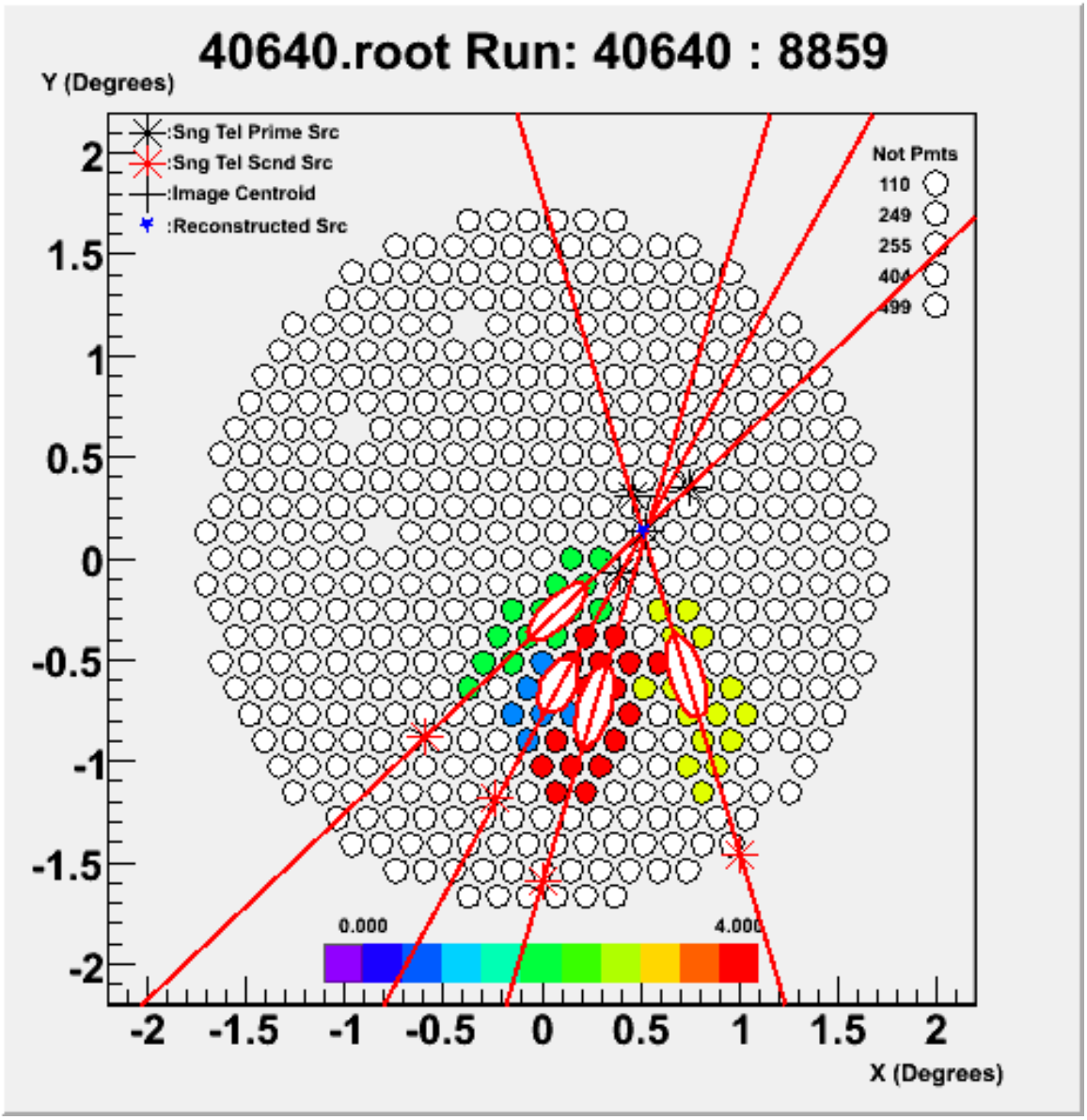

Figure 6.10: Example of a reconstructed shower's arrival direction by superposition of the shower images from the different cameras. The intersection of the main axes indicates the arrival direction in the sky. The color coding represents the telescope numbers. In reality the cameras do not superimpose perfectly as shown here. The small rotations that they may have with respect to each other are taken into account by the analysis program. Also, the example here is rather an ideal one in that there is a single intersection point. Usually there is more than one intersection point and the perpendicular distance to a point from each ellipse axis must be minimized.

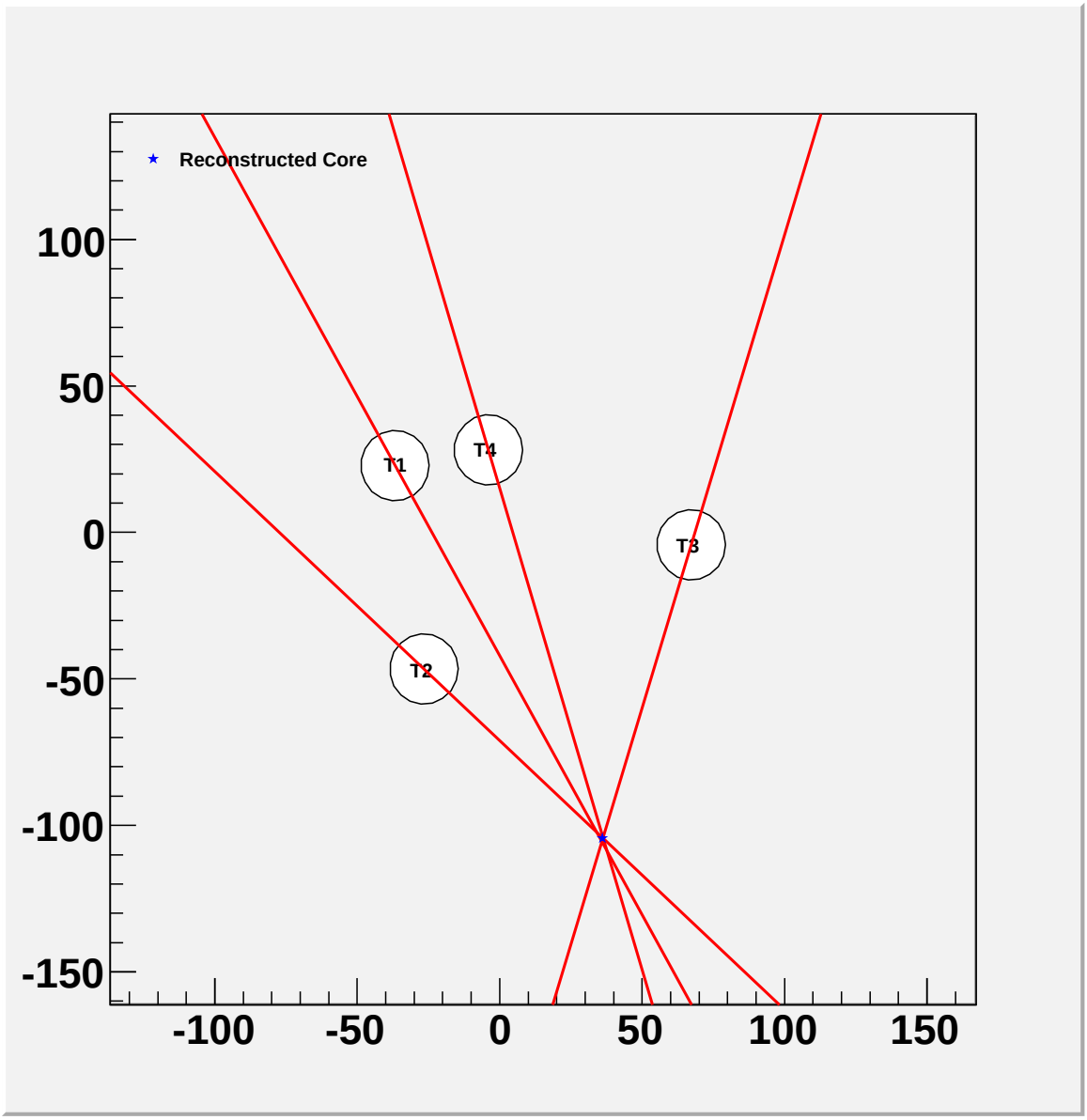

Figure 6.11: Example of a reconstructed shower's core location. The intersection of the main axes of the ellipses (ellipses not shown here), back-propagated from the telescopes locations indicates the core location in the plane of the telescopes dishes. Units of the axes are meters.

more closely for γ rays), and examination of shower axis as seen from individual telescopes (axes should intersect more closely for γ rays than for cosmic rays). Here we concentrate on γ/hadron separation based on the shape parameters.

To combine the images from a shower, a simple averaging procedure for the parameters will not do. The reason for this is that the image dimensions are different between the cameras because the shower is seen from different distances from each telescope and are therefore not directly comparable. Also, observable showers originating from a source at some angle pass through different layers of the atmosphere and interact differently with the Earth's magnetic field than showers originating from another source at a different angle. This affects the development of the showers and implies that the typical dimensions of a γ-ray-initiated shower are dependent on the observing angle. Equally affecting the typical dimensions of such a shower is obviously the energy of the primary, which also needs to be taken into account. All this complicates the problem of arriving at a small set of combined parameters that can easily be used for all observations to distinguish the "γ-ray shower shape" from that of the other images.

To resolve these difficulties, it was first suggested in [172] to try to predict, based on the observing conditions (distance and angle from the shower) and the observed luminosity of the image seen by a telescope, what dimensions the image should have had if it was indeed due to a γ ray interacting with the atmosphere. This prediction can then be compared to what is actually observed and the results of the comparisons for each camera averaged. If the image compares well to what is expected from a γ-ray induced shower for a majority of the cameras, then it is very likely to be due to such a primary particle.

In equations, what is actually being computed by *VEGAS*[8] is [160]:

$$MSP := \frac{1}{N_{\mathrm{tel}}} \sum_{k=1}^{N_{\mathrm{tel}}} \frac{p_k}{< p_{\mathrm{sim}}(\theta_k, b_k, size_k) >}, \tag{6.3}$$

where MSP stands for Mean Scaled Parameter, and the parameters to be used are

[8]Other analysis packages may have different combined parameters. They are similar to those presented here in that they are based on the same idea, but are the result of a different implementation.

the dimensions of the Hillas ellipses, *i.e.* their *width* and *length*. Hence the combined parameters that permit distinguishing the different classes of images are MSW and MSL. Here, p_k is the value of the parameter that is measured in camera k. It is being compared to $< p_{\rm sim}(\theta_k, b_k, size_k) >$, which is the prediction for the value of the parameter under investigation based on the angle of observation θ_k, the **impact distance** b of the shower from the telescope k (distance to core location obtained as mentioned above), and the energy of the shower evaluated indirectly by the luminous content of the image, *i.e.* its *size* parameter. The prediction comes from averaging the results of many simulated γ-ray-induced showers of different energies whose Čerenkov light is propagated through a model of the detector and whose images pass the quality cuts discussed above, to avoid any biases. In fact, the ingenious way to get around using equation 6.1 in reverse is to use brute force calculations to compute that equation in the forward direction for many simulated cases and compare the results to the actual observations to identify what they corresponded to. The simulations are obviously made in advance of the analysis computations since they can be used in many different analyses and take long to generate[9]. Their averaged results are stored in two-dimensional lookup tables which are accessed at analysis time by impact distance b and *size* variables. There are different tables for different zenith angles, different observation wobble offsets, different noise levels (to be able to analyze data taken while the moon was up for example) and other tables that differ in azimuth angle to take into account effects due to the geomagnetic field which can widen extensive air shower coming from certain directions [174]. Examples of lookup tables for *width* and *length* are shown in figures 6.12 and 6.13. Interpolation is used to access information between two bins of the lookup tables or between different lookup tables. The averaged comparison in equation 6.3 is close to 1 when the images are

[9]Simulations for VERITAS can use the KASCADE or CORSIKA shower generators and the ChiLa, KASCADE or GrISUDet detector models. The correctness of the simulations is verified by comparing standard analysis parameters (number of triggers, mean scaled parameters, etc..) between a simulated set and real data. Simulated cosmic rays are compared to background data and simulated γ rays are compared to data from the Crab Nebula. For more details see [173] and references within.

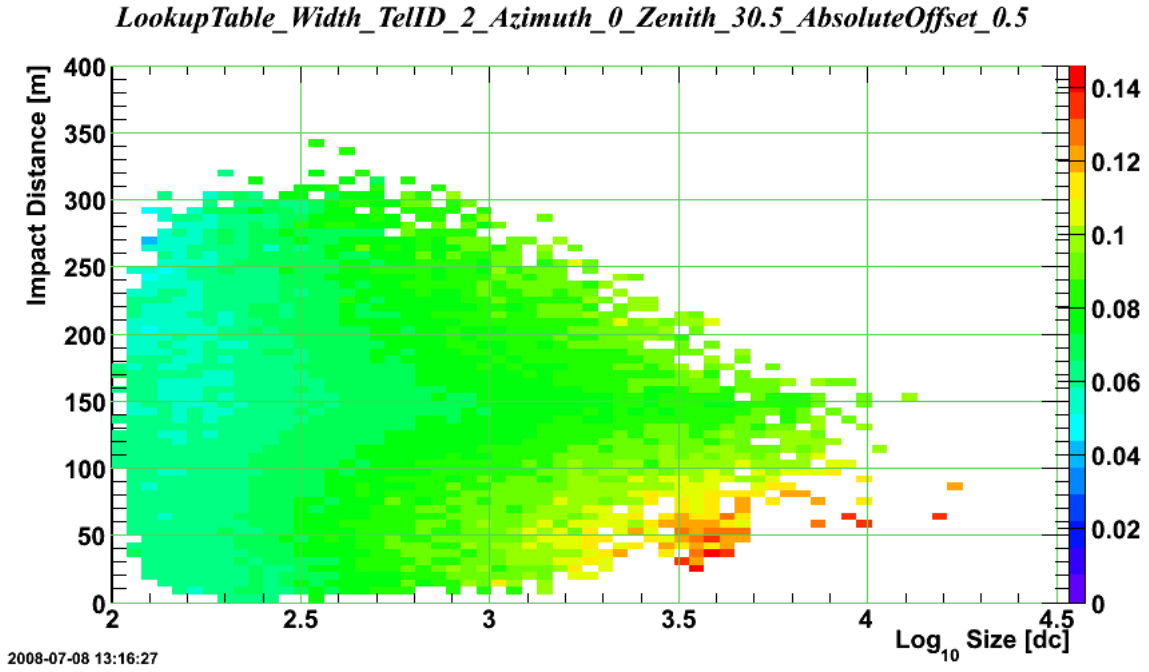

Figure 6.12: Lookup table for *width*. From the *size* and impact parameters of an event, an expected *width* is extracted from this table generated from simulations of γ rays. This expectation value is compared to the measured one to see if the recorded image has the characteristics of a typical γ ray. This is done for all the telescopes participating in the observation. The color scale represents *width* values in degrees.

really γ-ray-like.

Another shower parameter that is evaluated at this stage is its energy. This is not a geometrical parameter that will help distinguish the type of primary particle, but it is useful in another obvious way: it will permit spectral studies to be undertaken. The energy of the primary will affect the dimensions of a shower as was just discussed, but it is not evaluated from the *width* and *length* parameters. Rather, it was shown in [175], that the energy scales well with the *size* parameter, *i.e.* the intensity of the detected Čerenkov light. To correct for distance effects, an additional dependency on the impact parameter improves the relation. This then provides a way of estimating the energy. Just like before, lookup tables based on *size* and impact parameter b can be used. Only this time, the aim is not to predict what the value of energy should have been if the primary was indeed a γ ray and compare it to what is actually measured, but to use the energy value extracted from the lookup table as a genuine estimate. The

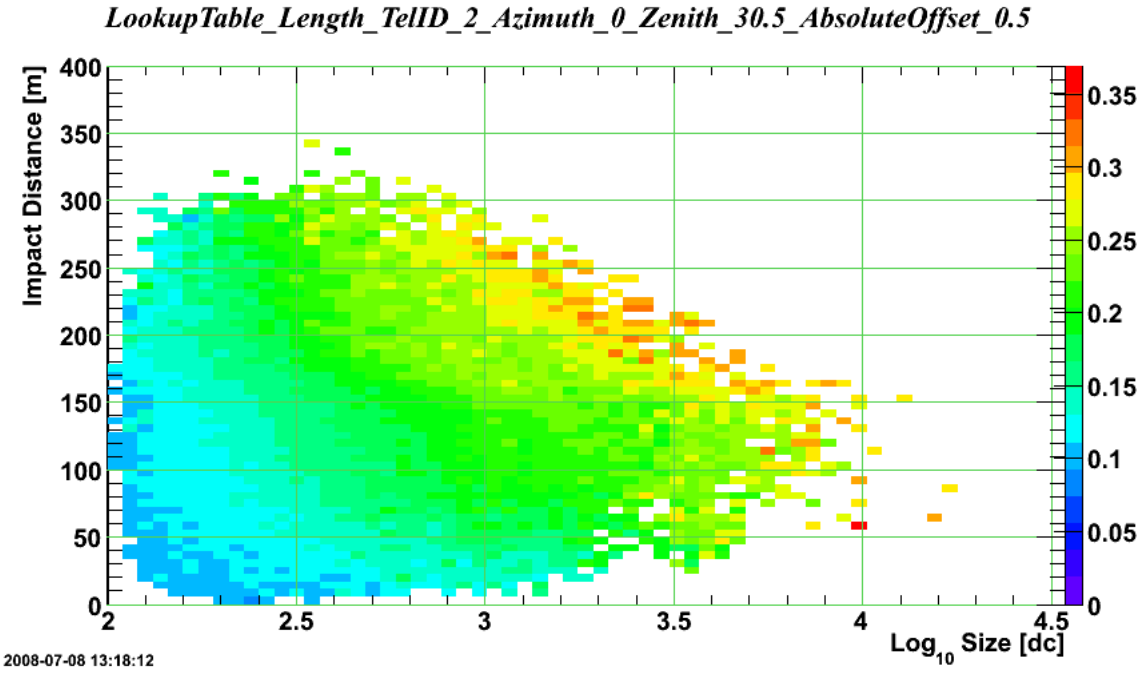

Figure 6.13: Lookup table for *length*. From the *size* and impact parameters of an event, an expected *length* is extracted from this table generated from simulations of γ rays. This expectation value is compared to the measured one to see if the recorded image has the characteristics of a typical γ ray. This is done for all the telescopes participating in the observation. The color scale represents *length* values in degrees.

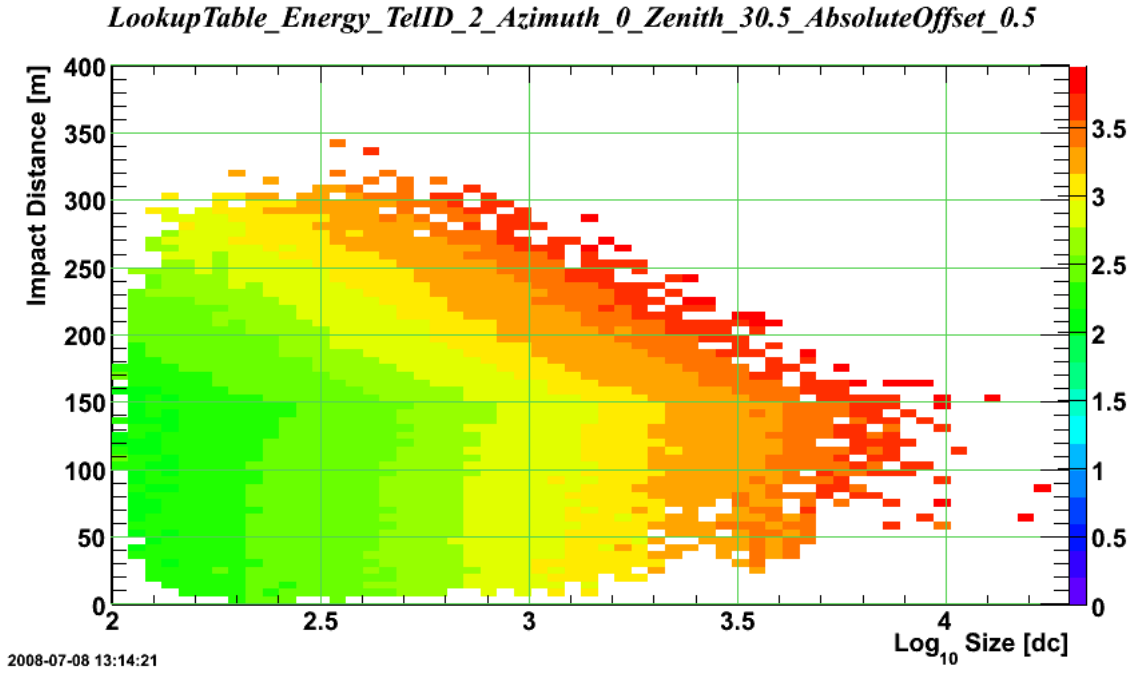

Figure 6.14: Lookup table for energy. From the *size* and impact parameters of an event, an energy value is extracted from this table generated from simulations of γ rays. This is done for all the telescopes participating in the observation and the results are averaged to improve the energy estimation. The color scale is log(E/GeV).

estimates from the different telescopes are then averaged (can be weighted by *size*) to improve the results. An example lookup table for energy is shown in figure 6.14.

6.5 Selection Criteria

Stage 4 of the analysis provided useful combined parameters to compare shower images. The use of these combined parameters, MSW and MSL in particular, is done in stage 5, which is a "cutting" stage where images that resemble γ-ray induced showers are kept and the ones that do not are thrown away. This obviously leads to the question of how far away from 1.0 are MSW and MSL allowed to be? What are the criteria that these parameters must respect for the shower to be identified as being caused by a γ-ray primary? Unfortunately, there is no clear answer to that. There is not a magic value for those cuts that will result in a perfect selection of γ rays simultaneously with a perfect rejection of cosmic rays. The reason for that is illustrated in figures 6.15 and 6.16, which show the distributions of the MSW and MSL

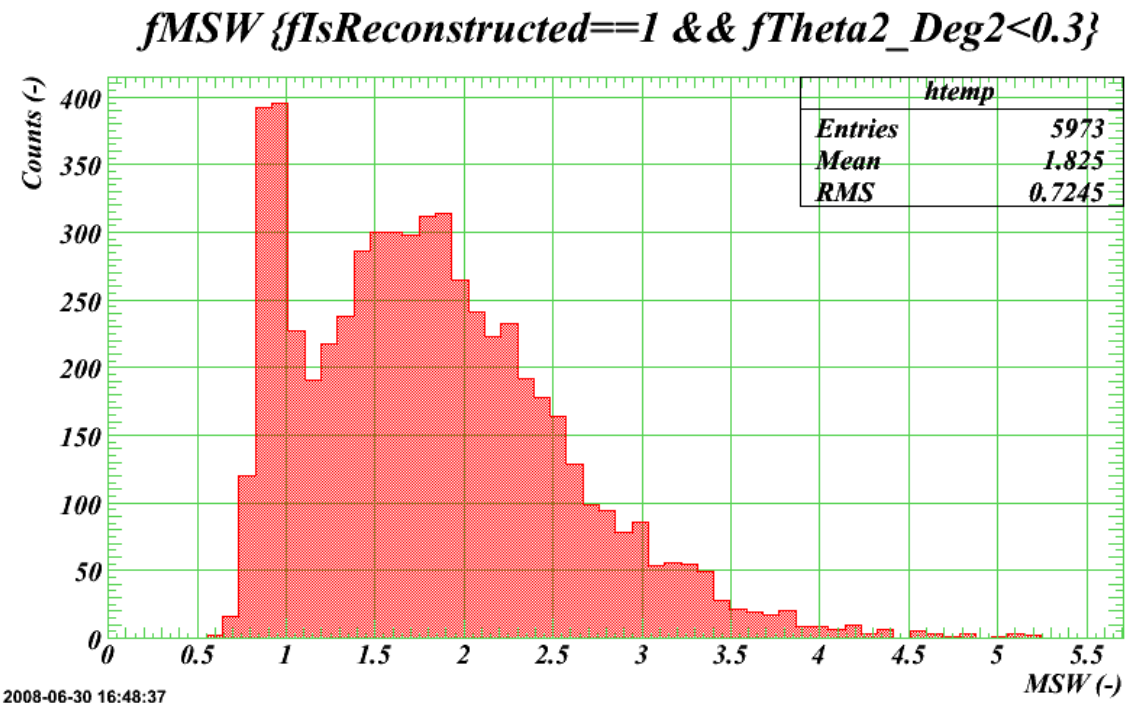

Figure 6.15: MSW distribution for a strong source, Mrk 421 during a flaring episode on May 2nd, 2008 (run 40640). A loose cut ($\Theta^2 < 0.3$, see later for explanation) has been applied to select shower images that have been reconstructed with an arrival direction within a large portion of the field of view, which includes the source. The peak at $MSW \sim 1$ indicates that many showers had a reconstructed *width* similar to what can be expected from simulated γ rays. The other component of the distribution, the large hump that peaks around 1.7 indicates showers that did not resemble those due to γ rays; they constitute background events. This can be confirmed by plotting the same graph but for a region of the field of view that does not include the source. In that case, the large hump remains, but the γ-ray peak vanishes.

parameters for a strong source, such that a γ-ray signal is easily identified. It can be seen that there is a subset of cosmic rays whose showers look very much like those of γ rays. Cuts are like a semi-transparent medium (or a filter) with a transmission coefficient. We try to select the medium that lets the signal pass while blocking the background as much as possible. So, clearly, a compromise needs to be made. How this compromise is reached cannot be answered right now because it depends on the contents of the next section. This discussion will therefore be deferred until section 6.7, where it will be shown that cut values can be optimized based on signal to noise arguments. For the time being, let us simply assume that an efficient value for these cuts has been found (from the figures, this is likely to be around $MSW < 1.1$ and $MSL < 1.3$) and proceed to the evaluation of the significance of the signal.

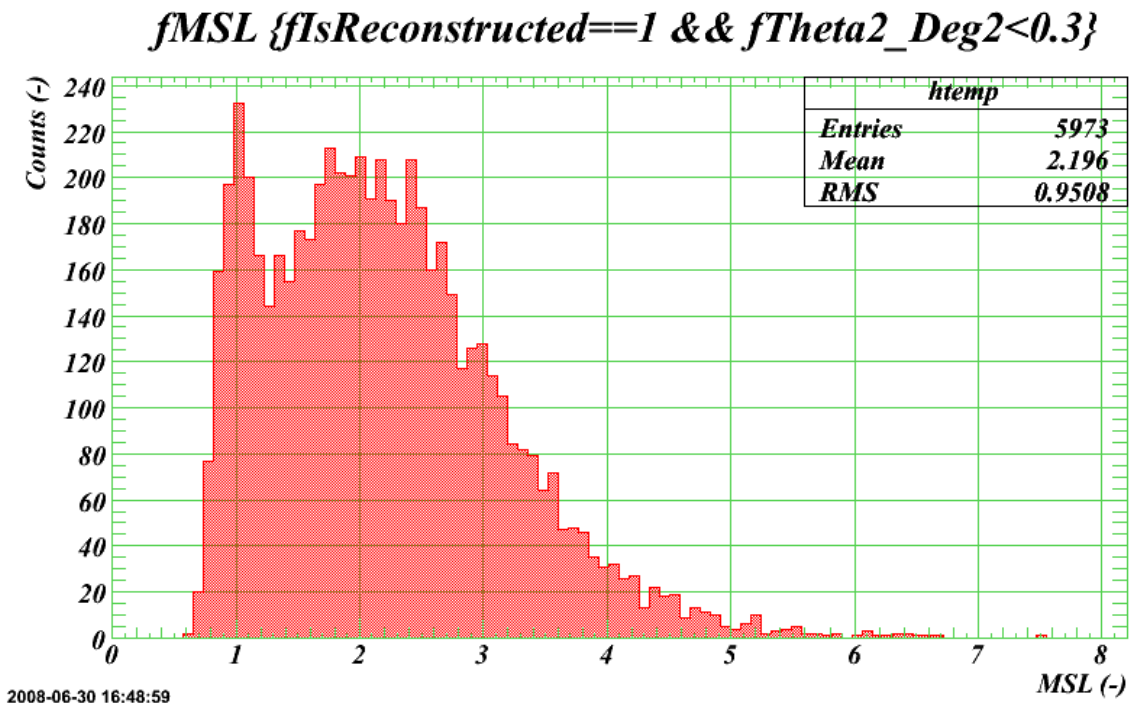

Figure 6.16: MSL distribution for a strong source, Mrk 421 during a flaring episode on May 2nd, 2008 (run 40640). A loose cut ($\Theta^2 < 0.3$, see later for explanation) has been applied to select shower images that have been reconstructed with an arrival direction within a large portion of the field of view, which includes the source. The peak at $MSL \sim 1$ indicates that many showers had a reconstructed *length* similar to what can be expected from simulated γ rays. The other component of the distribution, the large hump that peaks around 2 indicates showers that did not resemble those due to γ rays; they constitute background events. This can be confirmed by plotting the same graph but for a region of the field of view that does not include the source. In that case, the large hump remains, but the γ-ray peak vanishes.

6.6 Signal Background and Significance

Now that the images are classified as being due to a γ-ray primary or not, it is possible to count them and use statistical tools to make claims about the significance of these counts. The final stage of the analysis, stage 6, takes care of this accounting. Two points are of importance when making the counts.

First, which of the γ-ray-like events should be counted? Presumably, not all of the observed γ rays within the field of view come from the putative source under investigation. This can actually be quantified by using the reconstructed source location from each event. If an event's direction of arrival is found to be within a certain angular distance from the putative source's location, then it is worth counting it. If the event's arrival direction is far from the source, then it is not counted. The distance from the reconstructed arrival direction to the putative source location is symbolized by Θ and is measured as an angle in the field of view. Actually, Θ^2 is the variable commonly plotted because the area of a circular region scales with it; an example plot is shown in figure 6.17. Again, the criteria on Θ^2 used to distinguish the γ rays due to the source from the other ones is subject to debate and it will be addressed in the next section. For the moment, let us just recognize that it should not be too far from our ability in reconstructing the showers' arrival directions, *i.e.* our angular resolution $\sim 0.15\,^\circ (\Rightarrow \Theta^2 \lesssim 0.023\,^{\circ 2})$.

Secondly, of the events that seem to come from the direction of the source, what proportion can be attributed to background events due to random γ rays or cosmic rays having showers really resembling those of γ rays? This second point renders necessary the use of a background model. There are different ways of implementing this, and different background models each have their advantages and disadvantages making them more or less suitable for a particular analysis; see [176] for a detailed account. The two more widely-used models are described in the next subsections.

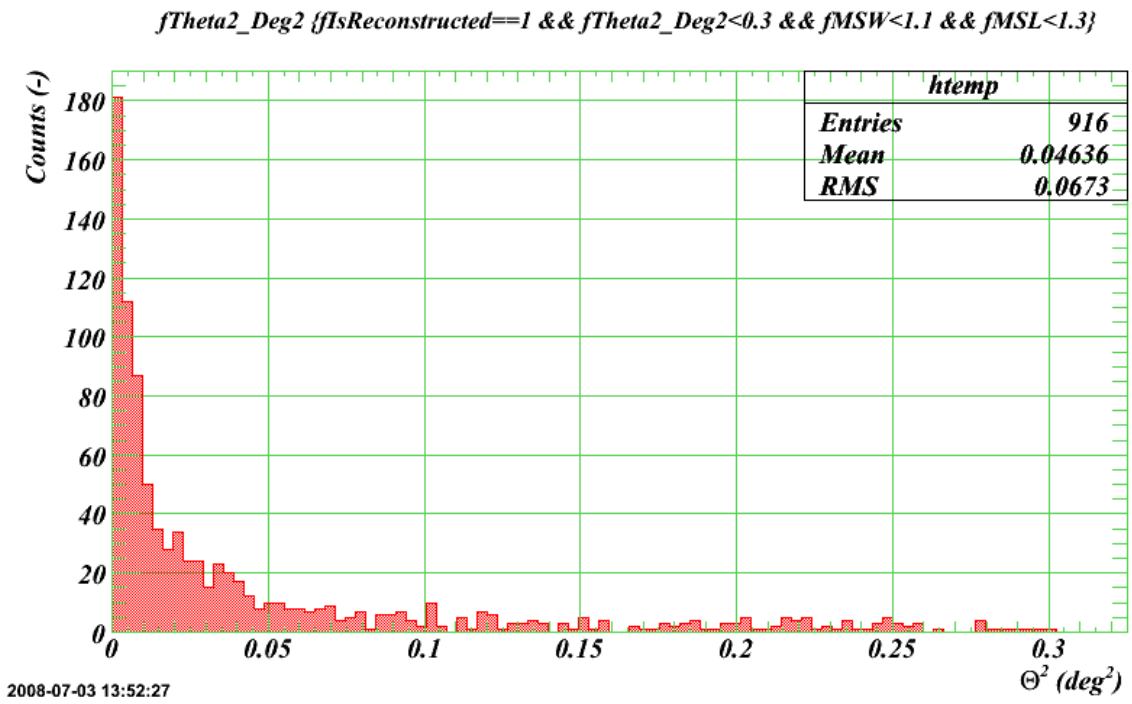

Figure 6.17: Θ^2 plot of a strong source, Mrk 421 during a flaring episode on May 2nd, 2008 (run 40640). The cuts $MSW < 1.1$ and $MSL < 1.3$ have been applied to select shower images that have the γ-ray-like appearance. The peak at small values of Θ^2 indicates that many showers had a reconstructed arrival direction near the Mrk 421 nominal position in the sky. The non-zero bin contents at greater values of Θ^2 indicate that γ-ray-like showers are arriving from all directions (this is not particularly strong here because only one run was used, but for weaker sources where many runs are required to see a signal this becomes more apparent); they constitute a background to be subtracted from the signal. For a weaker source, the peak is far less pronounced and can be difficult to distinguish from the background counts, thus the importance of using statistical tools to quantify the significance of any excess number of counts at low values of Θ^2.

6.6.1 Reflected-Regions Background Model

In the **Reflected-Regions Background Model**, illustrated in figure 6.18, the counts of γ-ray-like showers originating from the signal region (circular region of radius Θ around the location of the putative source coordinates) are compared to the counts of those originating from background regions of the same size as the signal region and located at the same radial distance from the center of the field of view, but at different azimuthal angles, as if the signal region had been reflected through the center of the field of view. This, of course, is only appropriate for observations taken in wobble mode, where the source is offset from the tracking position by a certain amount. The main advantage of this model is its simplicity: there is no need for dedicated "OFF" runs that use up valuable dark time (see section 5.5) since the background is extracted from the same observations as the signal, and the symmetry of the model means that there is no need to weight the counts of the background regions differently since it is assumed that **the acceptance is identical for all regions, signal and reflected ones**. This is especially useful for spectral analysis since it avoids the systematic uncertainties inherent to the use of acceptance curves. Shortcomings of this model are that it cannot handle parts of the field of view close to the tracking position (in which case it is not possible to define background regions) and it is likely to fail if there are extended or multiple sources in the field of view (which could contaminate the background regions with signal counts).

6.6.2 Ring-Background Model

An alternative to the reflected-regions model is the **Ring-Background Model** depicted in figure 6.19. In this case, the background events are counted from events whose arrival direction is inside an annulus region around the signal region. This kind of analysis is more suited for sky survey studies, since every point in the field of view can be used as the center of a putative signal region, even the points close to or at the tracking position. Like the reflected-regions model, the ring model is however not immune to contamination of the background by γ-ray signals if the source is extended

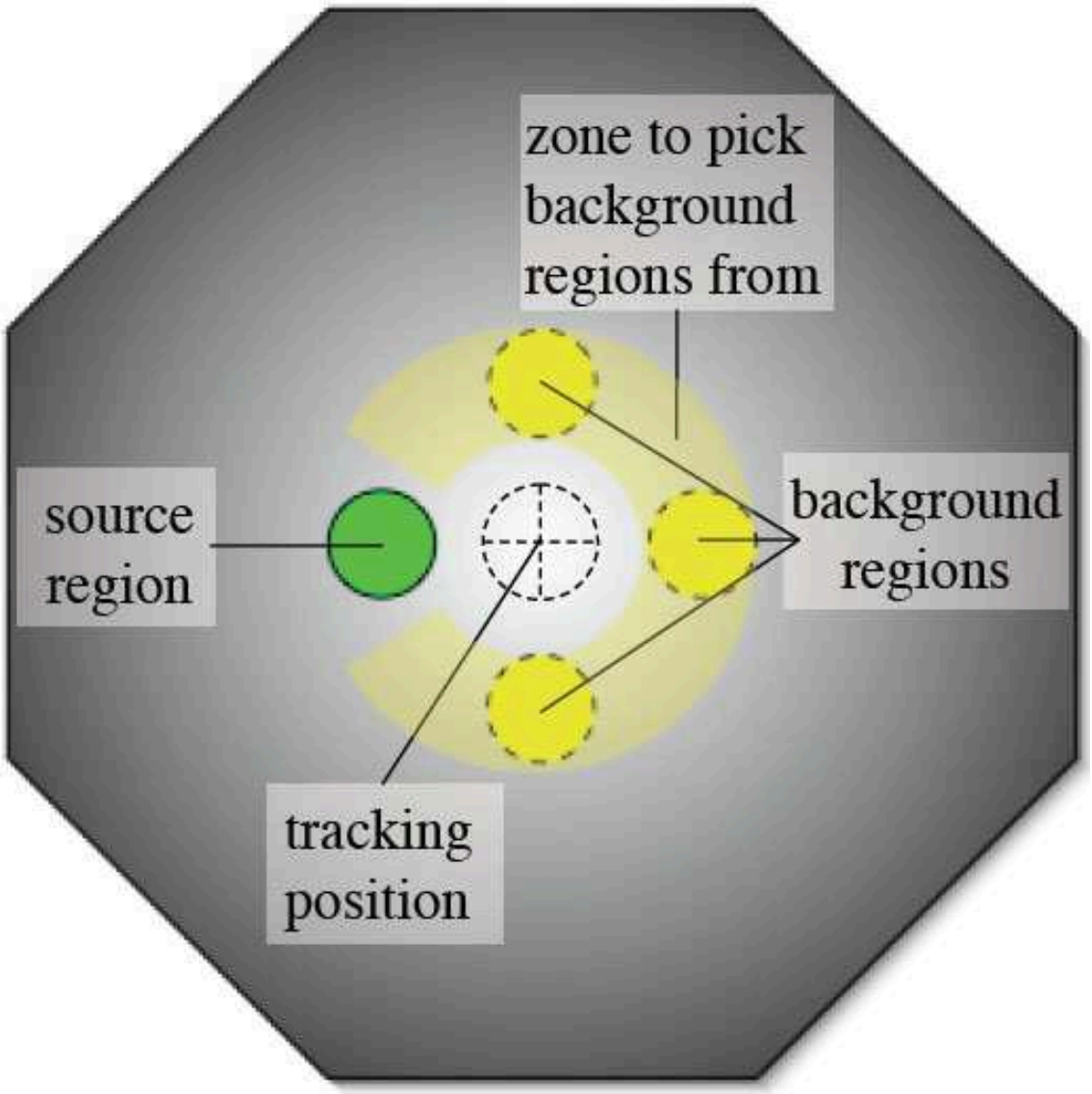

Figure 6.18: Reflected-region analysis. The background regions are taken from rotations of the signal region around the center of the field of view, which is the tracking position. In this way, the acceptance of the background regions is the same as that of the source region. No two regions should overlap and the zone from where background regions are allowed to be picked starts slightly away from the signal region. This ensures that no signal events are accidentally reconstructed in a background region; this would artificially increase the importance of the background. Figure taken from [160].

or if there are many sources in the field of view. Moreover, since the background region encompasses different radial distances from the center of the field of view than the signal region, it is necessary to weight the number of events in the different parts of the ring according to the acceptance of the system. The **acceptance** is the relative ease, or probability, with which a shower coming from a particular part in the field of view is detected. It varies mostly radially, being maximal at the center of the field of view and decaying toward the edges, but it also varies as a function of zenith angle and as a function of energy [176], [177]. Background γ-ray-like events are used to generate it, *i.e.* events that passed the shape cuts. Their number as a function of reconstructed direction offset from the pointing position yields the acceptance curve (an example is shown in figure 6.20). Although it can be obtained on a run-to-run basis, a set of dedicated "OFF" runs is required for studies needing good statistics. The fact that acceptance curves depend on energy makes the ring-background model less desirable for spectral studies, compared to the reflected-regions model, because it introduces additional uncertainties.

For extended or multiple sources, there exists the Field of View Model that avoids the possibility of a contaminated background, but this will not be discussed here as it is a relatively new implementation in one of the VERITAS analysis packages and it requires more testing. Details can nevertheless be found in [178]. The important thing is to have at least two background models to compare to check for systematic uncertainties. For 1ES 1218 + 30.4, the source of interest in this thesis, the reflected-regions and ring models will suffice since this source is not extended.

6.6.3 Significance

From counting the γ-ray-like events in the signal and background regions of the field of view, we get the numbers $N_{\gamma,\mathrm{s}}$ and $N_{\gamma,\mathrm{bg}}$, respectively. The subscript γ is there to remind us of the dependence of these numbers on the chosen cuts; these define what γ-ray-like events look like. Given these numbers, the question that is of interest now is to establish 1) if $N_{\gamma,\mathrm{s}}$ is a significant number, *i.e.* is there statistical evidence for a detection? and 2) if there is a significant signal, then what is the rate of detected

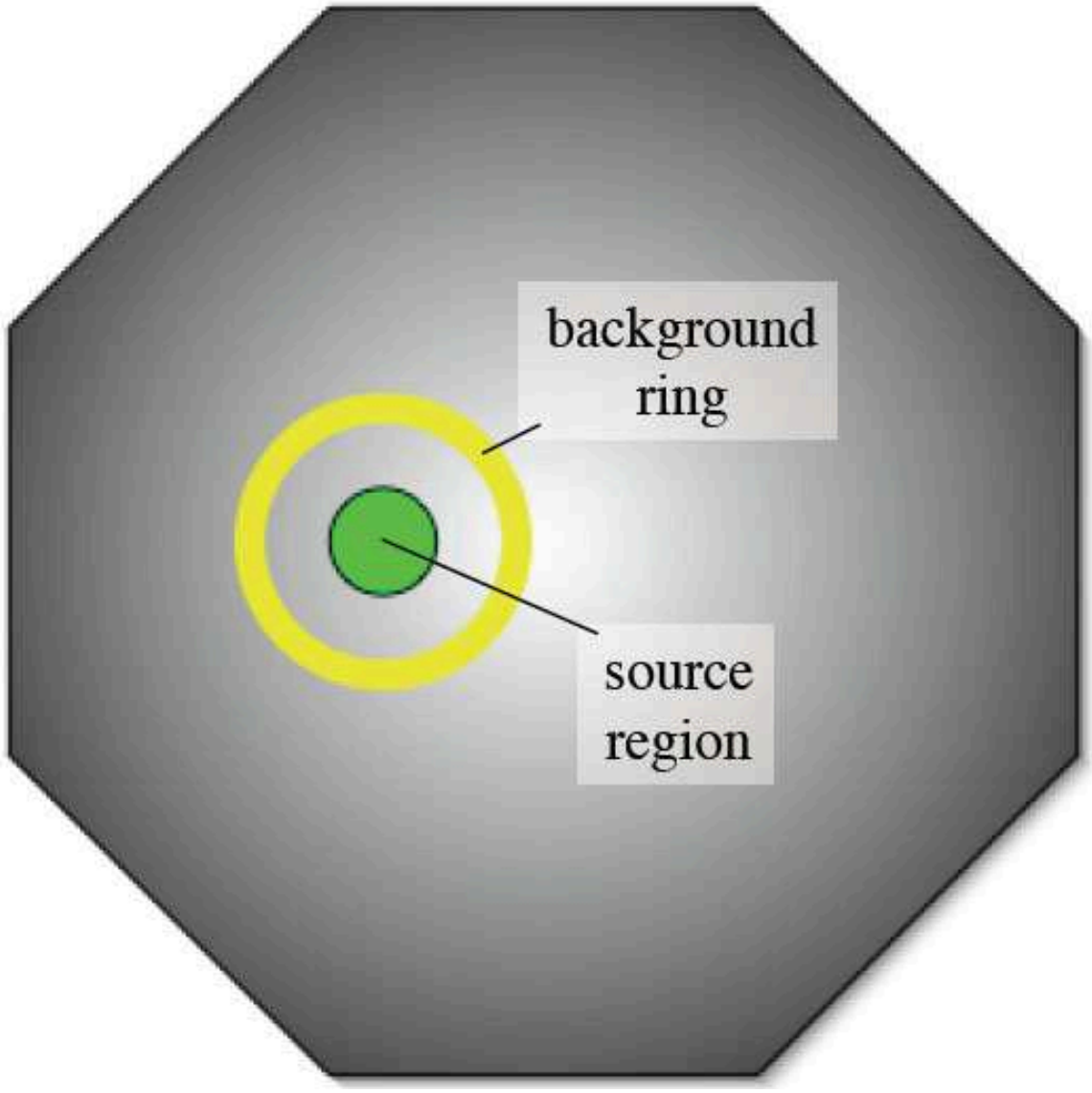

Figure 6.19: Ring-background analysis. Here the background events are counted from events whose arrival direction is inside an annulus region around the signal region. The background and signal regions have different acceptances, which must be taken into account. This is represented here by the radial gradient (the white to gray shading) in the background of the figure. Figure taken from [160].

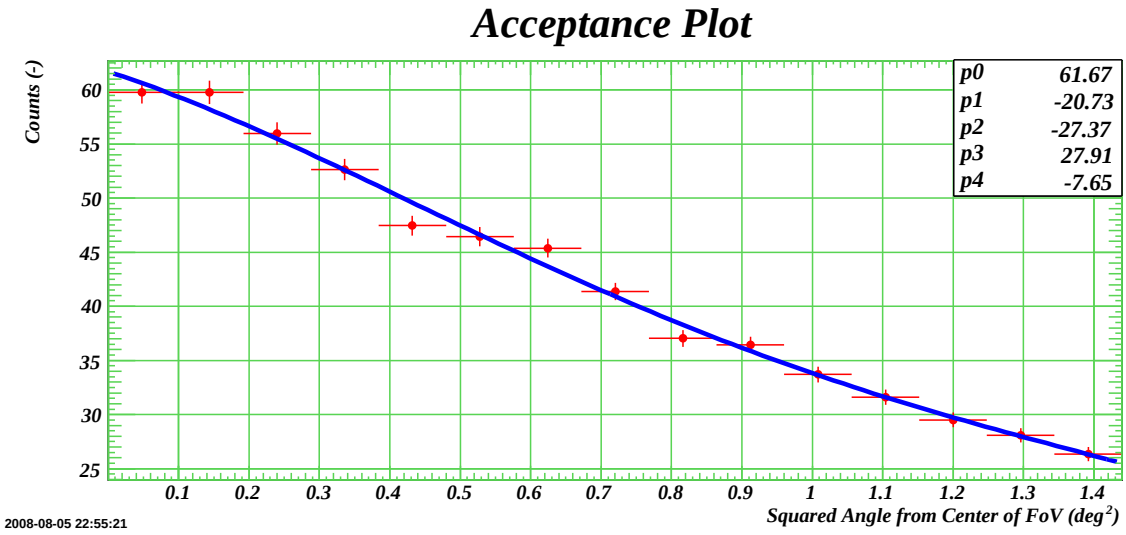

Figure 6.20: Example acceptance curve obtained from the complete set of files for the 1ES 1218 + 30.4 observations presented in chapter 7.

γ rays? Of course $N_{\gamma,\mathrm{s}}$ and $N_{\gamma,\mathrm{bg}}$ cannot be compared directly since the acceptances of the two types of regions may be different. To compare them the background counts must be normalized by a factor α [10] that takes this into account and can be computed as follows [176]:

$$\alpha := \frac{\int_{\mathrm{s}} \kappa_{\gamma,\mathrm{s}}(\psi_x, \psi_y, \theta_{\mathrm{Zn}}, E, t)\; d\psi_x\; d\psi_y\; d\theta_{\mathrm{Zn}}\; dE\; dt}{\int_{\mathrm{bg}} \kappa_{\gamma,\mathrm{bg}}(\psi_x, \psi_y, \theta_{\mathrm{Zn}}, E, t)\; d\psi_x\; d\psi_y\; d\theta_{\mathrm{Zn}}\; dE\; dt}, \tag{6.4}$$

where κ_γ is the acceptance for γ rays of energy E in the region covering coordinates ψ_x and ψ_y in the field of view at zenith angle θ_{Zn} during time t.

As an example for what the value of α might be, consider the reflected-regions model. In this case the expression 6.4 for α reduces simply to

$$\alpha = \frac{1}{n}, \tag{6.5}$$

where n is the number of background regions. This is so because the acceptance of all the regions is the same and all regions are observed for an equal amount of time, so the integrals cancel out, except for the fact that there is a factor of n more background regions than signal regions. Typically, there can be anywhere from 1 to

[10] The normalization factor used in this section is not to be confused with the Hillas parameter α used earlier to describe the orientation of shower image axes.

11 background regions, so α could be between 0.09 and 1. For the ring-background model, the acceptances of the signal and background regions do not cancel out. The computation is therefore more difficult and must be done numerically. This is where the acceptance curve discussed previously plays a role.

With the normalization factor defined as such, the excess of γ rays observed can be written as

$$N_{\gamma,\mathrm{Excess}} := N_{\gamma,\mathrm{s}} - \alpha N_{\gamma,\mathrm{bg}}. \tag{6.6}$$

If $N_{\gamma,\mathrm{Excess}}$ is negative, then there is obviously no evidence for a detection. If it is positive, then one must evaluate whether this result is far enough away from zero that it is reasonably unlikely due to random fluctuations in the signal and background counts.

Evaluation of the significance of the excess number of counts is not as simple and straightforward a problem as might first appear. Li and Ma [179] argue that the correct way to proceed is to compare the excess counts to their estimated standard deviation $\sigma_{N_{\gamma,\mathrm{Excess}}}$ under the assumption that **all recorded photons, $N_{\gamma,\mathrm{s}}$ and $N_{\gamma,\mathrm{bg}}$ are due to background (there is no source)**. The **significance** S_γ is thus defined as the number of standard deviations that separate $N_{\gamma,\mathrm{Excess}}$ from an expectation of zero signal, from which a probability for the observation can be computed. In equations, it can be shown that

$$S_\gamma := \frac{N_{\gamma,\mathrm{Excess}}}{\hat{\sigma}_{N_{\gamma,\mathrm{Excess}}}} = \frac{N_{\gamma,\mathrm{s}} - \alpha N_{\gamma,\mathrm{bg}}}{\sqrt{\alpha(N_{\gamma,\mathrm{s}} + N_{\gamma,\mathrm{bg}})}}, \tag{6.7}$$

where the caret on $\sigma_{N_{\gamma,\mathrm{Excess}}}$ indicates that this is an estimated value since the background is not known exactly.

If S_γ is small, then the observed excess is not that improbable; if it is large, then $N_{\gamma,\mathrm{Excess}}$ is not likely to be compatible with a random draw from a population centered on zero with standard deviation $\hat{\sigma}_{N_{\gamma,\mathrm{Excess}}}$ and may thus be due to the presence of a source. In the field of γ-ray astronomy "large enough" is defined as $S_\gamma \geq 5$ standard deviations (also written as $5\,\sigma$) in order to claim a detection. Once this has been achieved, other, independent, groups are encouraged to obtain similar results so as to confirm the discovery.

Even though formula 6.7 is correct, it still has some problems when the statistics are low or when α is not close to 1. Li and Ma [179] derive another significance formula that performs better in these cases. It comes from the method of hypotheses testing using the maximum likelihood ratio test. The result is more complicated, but can still be given in analytical form:

$$S_\gamma := \sqrt{2}\sqrt{\sum_i N^i_{\gamma,\mathrm{s}} \ln\left(\frac{\sum_i N^i_{\gamma,\mathrm{s}}}{\sum_i \frac{\alpha^i}{1+\alpha^i}(N^i_{\gamma,\mathrm{s}} + N^i_{\gamma,\mathrm{bg}})}\right) + \sum_i N^i_{\gamma,\mathrm{bg}} \ln\left(\frac{\sum_i N^i_{\gamma,\mathrm{bg}}}{\sum_i \frac{1}{(1+\alpha^i)}(N^i_{\gamma,\mathrm{s}} + N^i_{\gamma,\mathrm{bg}})}\right)}, \tag{6.8}$$

where the i's are indices representing the different observations made; they are not exponents. This formula, which is actually the generalized Li and Ma formula that can be used to combine the results of observations having different α values [39], has since become the standard to evaluate the significance of positive observations and is the one used in the *VEGAS* package[11].

One thing worth noting about the significance is that it scales like $\sqrt{t}$, where t is the observation time. This can be seen both in equations 6.7 and 6.8 with the understanding that the signal and background counts increase linearly with time for a steady source. $S_\gamma/\sqrt{t}$ then depends only on source strength and not on time. It can therefore be taken as a sensitivity measure. This is useful when comparing sets of cuts or the performance of different experiments that may have observed a source for different times or to estimate the required observation time to attain a given significance for a source of a given strength.

Typically, an uncertainty is not quoted together with a significance value. This may be because the uncertainty on $N_{\gamma,\mathrm{Excess}}$, $\hat{\sigma}_{N_{\gamma,\mathrm{Excess}}}$, is involved in the significance computation in the definition of equation 6.7. Therefore, computing the uncertainty on the significance feels like computing the uncertainty on an uncertainty. If the

[11] Recently an alternative to equation 6.8, based on Bayesian statistics, has been proposed in [180], but it is still not used within the VERITAS collaboration, possibly because it requires the implementation of numerical techniques and because these statistics are harder to interpret than conventional ones.

computation is nevertheless performed, it can be shown that[12]

$$\delta S_\gamma = \sqrt{1 + S_\gamma^2 \left(\frac{\delta \hat{\sigma}_{N_{\gamma,\mathrm{Excess}}}}{\hat{\sigma}_{N_{\gamma,\mathrm{Excess}}}} \right)^2}, \tag{6.9}$$

where $\delta \hat{\sigma}_{N_{\gamma,\mathrm{Excess}}}$ is the uncertainty on $\hat{\sigma}_{N_{\gamma,\mathrm{Excess}}}$. The first term is due uniquely to the statistical fluctuations on $N_{\gamma,\mathrm{Excess}}$. The second one is from the uncertainty on its standard deviation, since only an estimate of this latter quantity can be made. If the background is well estimated and the significance is not too high, the second term is probably not important with respect to the first one. This may be another reason why the uncertainty on the significance is usually not quoted; it may be that it is assumed to be 1. However, equation 6.9 only gives the statistical uncertainty due to the possible fluctuations in $N_{\gamma,\mathrm{Excess}}$ and $\hat{\sigma}_{N_{\gamma,\mathrm{Excess}}}$ due to limited statistics. This does not include systematic uncertainties associated with the particular choice of formula to implement the significance definition and which may perform more or less satisfactorily when statistics are low. In [181], many different ways of computing the significance are compared with the result that this systematic may be larger than 1 in some cases[13]. When comparing significances, it is therefore important to use the same formula. The significance also depends on the choice of background model. Depending on the chosen one, α and $N_{\gamma,\mathrm{bg}}$ will vary. This should theoretically not change $N_{\gamma,\mathrm{Excess}}$, but it will change its uncertainty $\hat{\sigma}_{N_{\gamma,\mathrm{Excess}}}$ because of a better or worse background estimation, hence S_γ will change too. This means that comparing the significances obtained from different background models is also a tricky business. What one may be measuring by doing that is the effect of a systematic associated with the choice of background model; an agreement in the significances from different models is not necessarily expected, unless the α's are comparable. Another thing

[12] This assumes uncorrelated contributions to the uncertainty, which may not be the case. Just remove the square root and the squares for the correlated case.

[13] In the views expressed in [181], our formula 6.8, that is used to produce the results of this thesis, is a reasonable choice, but not the best available one. Instead, it is suggested that one uses the less known *Uniform Most Powerful Unbiased Binomial ratio test*, which is easy to implement and may have more optimal properties when low counts are considered.

to consider is that the significance depends on the chosen cuts. As for the choice of background model, significances from analyses utilizing different cuts are not expected to agree; one simply uses a set of cuts that has been shown to give good results. The uncertainty derived in equation 6.9 is just the variations that can be expected in the significances if the observations are repeated, and analyzed, in the same way (and the emission from the source did not vary); on average, variations of a little more than $1\,\sigma$ are expected.

6.6.4 Rate and Flux

Having established the existence of a source, one can then proceed to the evaluation of the **detection rate**, R_γ. This is quite simply given by

$$\boxed{R_\gamma := \frac{N_{\gamma,\mathrm{s}} - \alpha N_{\gamma,\mathrm{bg}}}{t_{\mathrm{live}}}}, \tag{6.10}$$

where t_{live} is the **live time** of the run, *i.e.* the duration of the run minus the time where the system was busy and could not record new events (dead time). The detection rate is another measure of the strength of a source (it is typically about $7\,\gamma$/min for the Crab Nebula, depending on the choice of cuts) and it brings us a step closer to the wanted flux $\phi_\gamma(E)$ in equation 6.1 since the rate has units of numbers of γ rays per unit time. All that is left to do is to separate the observations into energy bands, which can be done using the parameterization discussed in section 6.4.2, and divide by the energy bin size and by the collection area of the system.

The collection area of the system is not so well defined because an extensive air shower is not certain to be detected if it falls within a certain radius of the array and not certain to be undetected if it falls outside; there is a transition region. Instead, one defines an **effective area** that folds in acceptance effects. It is a number that represents the collection area that an ideal detector, having a sharp transition between detection and non-detection regions and the same detection characteristics as the real detector, would have. It is computed from simulations of γ-ray events thrown over a region of known area A_0 (in the plane perpendicular to the optical axis) at the center of which lies the array. The detected showers are counted and the effective area is

deduced in the following way [175]:

$$A_{\gamma,\mathrm{eff}}(E) := A_0 \frac{N_\gamma(E)}{N_{\mathrm{sim}}(E)}, \tag{6.11}$$

where $N_\gamma(E)$ is the number of showers passing trigger and selection criteria at energy E, and $N_{\mathrm{sim}}(E)$ is the number of simulated γ-ray showers of energy E over area A_0. There is a dependence on energy because smaller showers are more difficult to detect than larger ones (they produce less light), so the effective area at low energies is smaller. At higher energies, the bigger shower images are more likely to have a lot of light at the edge of the camera and to be rejected by the quality *distance* cut. Figure 6.21 shows an example of an effective area curve. At energies above a few hundred GeV, the effective area of VERITAS is around or above $1\times10^5\,\mathrm{m}^2$.

In reality, one does not simply divide by the effective area to get the flux from the source. The reason is that the energy is reconstructed with only finite precision. Therefore, when binning the rates by energy, some events are going to end up in the wrong bin. Since the energy spectra of the type of sources we observe are typically described by rapidly decreasing power-laws, there will naturally be more events with a badly estimated energy that will be promoted to a higher energy bin than there are mis-reconstructed events demoted to a lower energy bin. This needs to be compensated for and one way to do it is to modify the effective area curve to take this effect into account. The procedure to do so is complicated and not in the scope of this thesis; details can be found in [175] and [182].

6.7 Cuts Optimization

As has been emphasized by the subscript γ in formulas like equation 6.8 for the significance and 6.10 for the rate, some of the results obtained are dependent on what exactly it is that is recognized as a γ-ray-like shower; these formulas implicitly depend on the value of the cuts applied since the counts of γ-ray and background events will vary according to this choice. It is thus possible to optimize the cuts to enhance a particular result. This is why in section 6.5 no definite cut values could be given, but only a rough estimate, based on visual inspection of some parameter distributions,

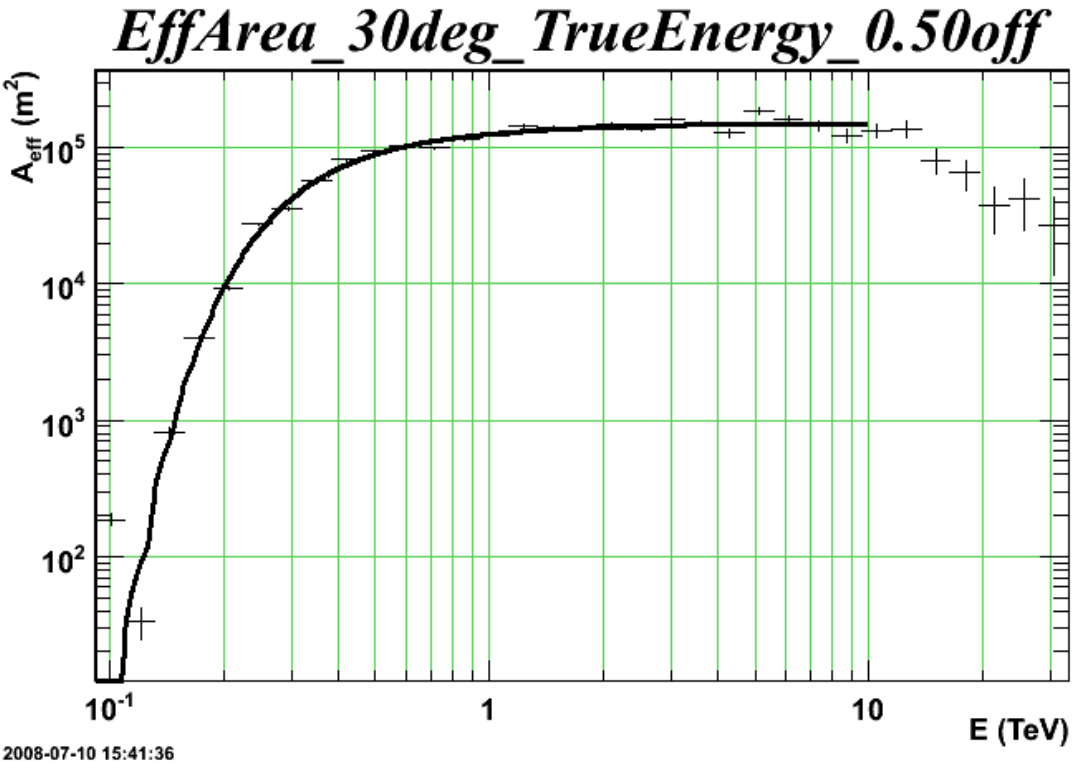

Figure 6.21: Effective area curve. The effective area increases quickly with energy as more luminous showers become easier to detect. At very high energies, quality cuts that ensure proper reconstruction of the events make the effective area decrease. Effective area curves are generated for different observing angles because different sections of the Čerenkov light pool are accessible at different angles; here the curve is generated for a zenith angle of 30 ° and a wobble offset of 0.5 °. The black curve is a high-order polynomial parameterization to the data points, which come from simulations. Here, the true simulated energies are used. In reality, when doing spectral reconstruction, this curve must be modified to take into account the finite energy resolution of the detector.

that would not be so bad in the majority of situations. Since different results use the number of γ-ray and background events in different ways, optimal cuts depend on the result that one wants to enhance. When emphasis is put on detection, then the significance is optimized. When spectral analysis is done, the number of excess counts in the different energy bins is optimized.

The problem of optimizing cuts is one in many variables; there are the MSW, MSL and Θ^2 cuts, the type and size of the background regions, but also the quality cuts prior to event reconstruction. Since the number of selected γ-ray and background events is a complicated function of the cuts, for which no analytical representation is available, the problem must be tackled numerically. Moreover there are some correlations between different cuts. For example, changing the size of the signal region (Θ^2 cuts) also changes the number of background regions that can be fitted in the reflected-regions background model; the smaller the signal region, the more background regions that can be used, but they too will be smaller. There is an equilibrium to be reached. This means that the cuts cannot be optimized one at a time, but that the global optimum is found by varying all the cuts together. The problem is thus a very difficult one, not just because of the number of parameters that can be adjusted, but because the computations themselves demand considerable time. What is usually done instead is to reduce the number of variables by optimizing only the most critical cuts that come at the end of the analysis and to assume that **other cuts are already near their optimal value, based on previous studies**. In this thesis, the confirmation of the MAGIC detection of 1ES 1218 + 30.4 was of primordial importance. Therefore, a maximization of the significance was of interest. The results of this study made by the author, with the release 1_0_10 of the *VEGAS* package, are presented here. Only the MSW, MSL upper limits[14] and Θ^2 cuts, and the number of background regions for the reflected-regions model[15] were investigated,

[14] There was a general consensus within the collaboration that little would be gained in optimizing the lower limit for the MSW and MSL cuts. These were left at their default value of 0.05. This could nevertheless be investigated more thoroughly.

[15] Optimization for the ring-background model was not possible because the α value was not readily

with the quality cuts left to the values given in table 6.1 (this avoided the need to generate new lookup tables every time a quality cut would change).

To optimize the cuts for a source, data are needed. Moreover, to yield an unbiased analysis, the optimization cannot be done on the data to be analyzed. A solution could be to split the 1ES 1218 + 30.4 data set in two and use one of the subsets for optimization and the other one for analysis, but that would mean a loss of statistics needed to claim a detection. Instead, one could use simulated data for the optimization, but the results are not likely to be as representative as if real data were used. Therefore, data from the Crab Nebula (the powerful source that serves as standard candle in γ-ray astronomy) were used. A set of 10 runs from October and November 2007 was selected by the collaboration to undertake this study, but problems with 2 of the runs were found during quality checks so these were rejected. Because 1ES 1218 + 30.4 is so much weaker than the Crab, it is necessary to dilute the Crab data. The reason is that, for 1ES 1218 + 30.4, the γ-ray peaks in histograms like those shown in figures 6.15, 6.16 and 6.17 are expected to be much closer to the noise level. Therefore it is possible that cuts optimized for the Crab at full strength (see table 6.2) are not appropriate to make the peaks stand out for a weaker source. To dilute the Crab data to 5% of its strength, about the flux expected from 1ES 1218 + 30.4, one could mix the Crab runs with a set of about 200 non-detection runs in similar elevation and azimuth bands, but this proves long to analyze and hard to find (there are only a finite number of suitable runs and in fact there were not enough at the time of this study). Instead, the following trick is used [183]. The selection of γ rays is done on the full Crab data set and the number of excess γ-ray-like event, $N_{\gamma,\mathrm{Excess}}$, is computed as normal. This number is then scaled-down to 5% of its value to yield $N'_{\gamma,\mathrm{Excess}}$. The number of signal counts is then modified to be $N'_{\gamma,\mathrm{s}} := N_{\gamma,\mathrm{s}} - N_{\gamma,\mathrm{Excess}} + N'_{\gamma,\mathrm{Excess}}$. The significance of the *fake* faint source is then computed with $N'_{\gamma,\mathrm{s}}$ and $N_{\gamma,\mathrm{bg}}$. In this way, the good statistics of the Crab are still preserved (no events are thrown away) so that statistical fluctuations of the excess

available as a stage 6 output at the time this study was performed.

Standard Selection Cuts
$MSW < 1.02$
$MSL < 1.15$
$\Theta^2 < (0.158\,^\circ)^2 = 0.0250\,^{\circ 2}$
Number of reflected background regions = 7

Table 6.2: Standard selection cuts

counts are reduced and the optimization can proceed on firm grounds.

The strategy employed to find the global maximum was first to vary all the cuts together, but on a sparse grid (otherwise this is too computationally demanding), to approach the region of interest in parameter space quickly. Then, once in a region where the different parameters are near their optimal value and correlation effects are reduced, the best parameter estimates are refined by varying only one parameter at a time, but over a finer grid. This way the different maxima are found with greater precision. A check is done by re-performing a multi-variable scan, still sparse but more tightly centered on the new maxima, and verifying that no improvements can be made. If improvements are found, then the single-variable scans are redone with the newer best estimates for the other parameters. This cycle is repeated until satisfactory convergence is attained. For the number of reflected background regions to use, one cannot proceed in this way, since this is a discontinuous parameter. The above procedure is then repeated for various choices of number of background regions and the optimal value is kept. Figure 6.22 shows the result of the final single-parameter scans, *i.e.* once the other parameters are a small step away from their optimal value. The MSW parameter shows a fairly sharp peak around 1.00 in the sensitivity curve, which demonstrate the necessity to have this parameter well tuned. The MSL cut is a little less critical as can be seen by the broader bump in its sensitivity curve; small differences in the value of this cut are not going to affect the resulting significance as much as similar differences in the MSW cut. The curve for the Θ cut also shows a fairly broad peak region. The final optimized selection cuts obtained are given in

Optimized Selection Cuts for a 5% Crab-like Source
$MSW < 1.00$
$MSL < 1.20$
$\Theta^2 < (0.116\,^\circ)^2 = 0.0135\,^{\circ 2}$
Number of reflected background regions = 10

Table 6.3: Optimized selection cuts for a 5% Crab-like source

table 6.3. These results are consistent with those of other collaboration members performing similar studies; comparisons can be found in [184]. Compared to the standard cuts given in table 6.2, which were optimized for the Crab Nebula at full strength while the array was in construction phase, one can see that the main difference is that a tighter cut on Θ^2 performs better for a weaker source (this also allows the use of more background regions), while the shape cuts do not make that much of a difference. With the optimized cuts the sensitivity to the scaled-down Crab source was $2.57\,\sigma/\sqrt{\mathrm{h}}$, an 11% improvement compared to the standard cuts, the γ-ray rate was $0.30\,\gamma$/min, and the background rate was $0.66\,\gamma$/min. However, the rate curves in figure 6.22 show that higher γ-ray rates can be attained by opening up the cuts, at the expense of a sensitivity drop. In fact, the standard cuts give a higher rate, with $0.37\,\gamma$/min. When applied to the full-strength Crab source, the optimized cuts for a weak source yielded a sensitivity of $30.1\,\sigma/\sqrt{\mathrm{h}}$, a 2% improvement compared to the standard cuts (meaning that the standard cuts were not perfectly optimized for the array configuration when the data were taken), a γ-ray rate of $6.09\,\gamma$/min, and a background rate of $0.66\,\gamma$/min (same as previously because the background event counts are not scaled down for the optimization procedure, only the signal counts are).

Now equipped with an analysis technique that relates the measured pulse sizes of the camera photomultiplier tubes to a γ-ray flux, and with a set of optimized cuts that enhances weak signals, the study of the case 1ES 1218 + 30.4 can be undertaken. This is the subject of the next chapter.

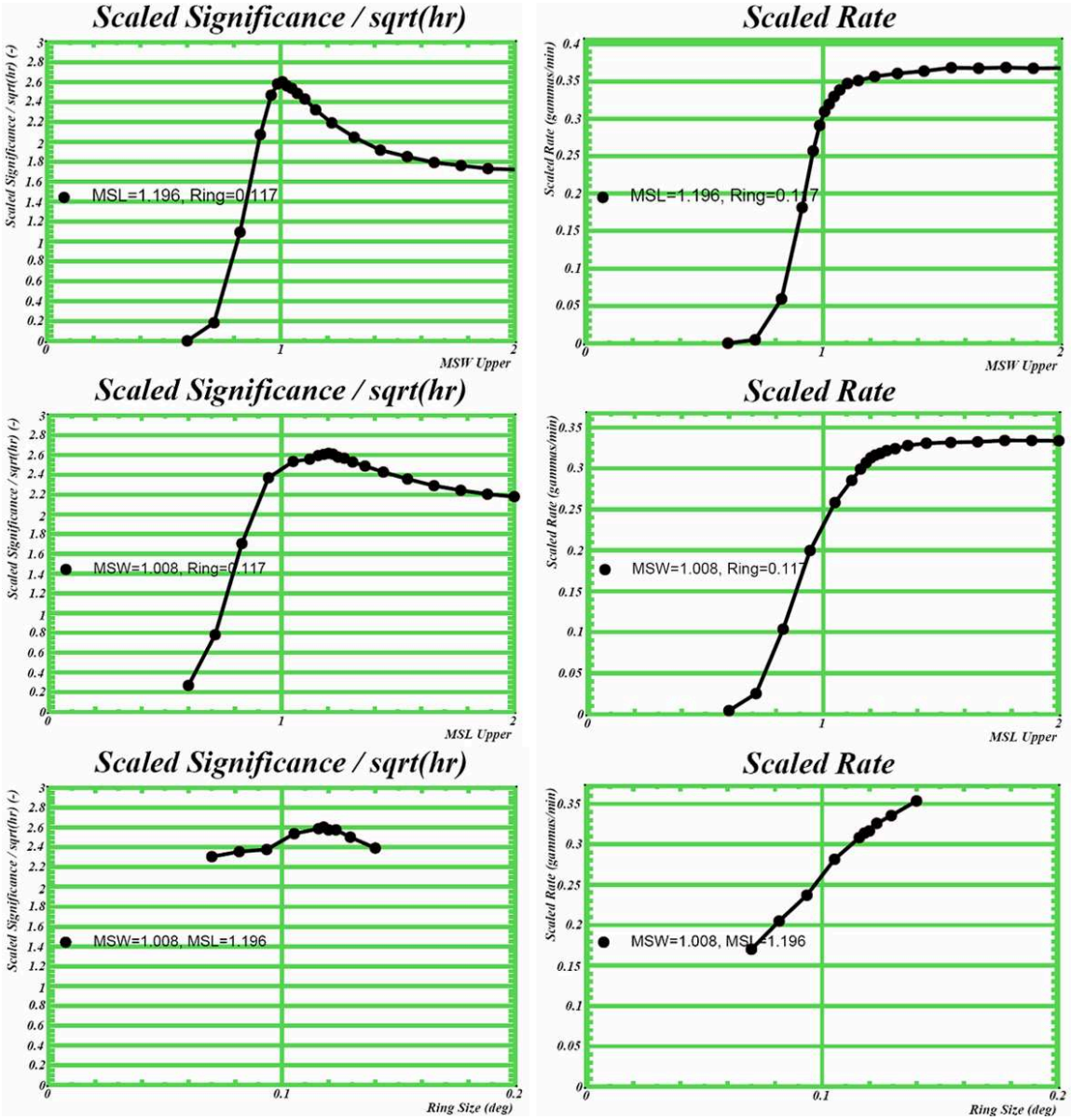

Figure 6.22: Cuts optimization scans for a 5% Crab-like source. Here only the final single-variable scans are shown, with the other parameters adjusted very close to their optimal value, as found in previous steps of the optimization. Scaled significances and rates refer to the significances and rates for the scaled-down excesses obtained from the Crab source. Top row: sensitivity and rate as a function of MSW; the maximal sensitivity is attained at 1.00. Middle row: sensitivity and rate as a function of MSL; the maximal sensitivity is attained at 1.20. Bottom row: sensitivity and rate as a function of Θ; the maximal sensitivity is attained at 0.116. The background model used was the reflected-regions one and the number of background regions was kept fixed at 10 (found to be the optimal value).

7

Analysis: 1ES 1218 + 30.4 and the Extragalactic Background Light

Having described the phenomenal astrophysical objects that are blazars, how their TeV radiation interacts with the extragalactic background light, and how experiments are designed to record the passage of these rare photons, everything only truly concretizes when a real case is analyzed. In this chapter, observations of the source 1ES 1218 + 30.4, using the VERITAS apparatus, are studied. The chapter is divided in two. First the data are searched for evidence of γ-ray emission from the location of 1ES 1218 + 30.4, so as to confirm the MAGIC detection of the source as a TeV emitter. Then the spectrum of 1ES 1218 + 30.4 is used to put a limit on the density of the extragalactic background light.

7.1 TeV Emission from 1ES 1218 + 30.4

7.1.1 Data Set

VERITAS observations of 1ES 1218 + 30.4 started on December 20, 2006 and ended on March 20, 2007. Although the source was also indirectly observed as part of the intermediate-energy-peaked BL Lac object W Comae campaign in 2008 (the two sources are only 2° apart in declination), these data are not used here because of the complications implied by the change of configuration of the array between the two epochs and the possibility, although small, of contamination of the background regions with significant γ-ray emission from the latter object. In fact, W Comae, which is normally undetected at TeV energies in its quiescent state, was caught in

two distinct flaring episodes during this period, see [185], [186] and [187]. In the 2006-2007 season W Comae was not flaring and only in some of the runs, those wobbled in the South direction, would it be included in the field of view, so it is not a problem; this will nevertheless be verified later in this chapter.

In total then, 128 observing runs were attempted on 1ES 1218 + 30.4 in 2006-2007. As this was a time of construction (the third telescope, T3, had just been brought online), the system was in an unstable state and the observing crew was still inexperienced with the new setup; many things could go wrong. 27 of the runs were completely unusable for any kind of study because of trouble with the acquisition system, observer errors or poor weather conditions. Since the weather monitoring system was not operational all the time, many of the observing conditions were judged by eye only. Only nights rated as B+ or better were used. For those nights when the FIR monitoring was available (see section 5.5), it was checked that its readings were stable throughout the run, which indicates that no clouds were present along the line of sight of the telescopes. Further data diagnostic checks were performed after application of stage 1 of the analysis to the runs. In particular, the L3 rate was verified to be stable and above 150 Hz, indicating that the acquisition system was working correctly. Some runs that included some rate dips, but are otherwise fine had to be thrown away because of the inability of the analysis to recalculate properly the livetime after a cut in time. Two livetime calculators were compared to detect any clock problems. Various data quality reports comparing the performance of different parts of the system were also consulted and any run containing an anomaly was rejected from the analysis. Most of the data were taken in wobble tracking mode. Due to the too few runs taken in alternate configurations (pairs mode or two-telescope observations), it was decided that it was not worth trying to include those in the analysis and to concentrate only on the good three-telescope wobble-mode observations. During the quality checks it was discovered that the T3 pointing was slightly off for the majority of the December data. This did not affect a lot of useful data because most of the December data were rejected on other grounds anyway. Still,

software correction of the pointing allowed recovery of 8 runs that would otherwise have been lost. What remained after all these quality checks were 64 good runs (16 wobbled South, 17 North, 15 East and 16 West, a good mix of wobble directions, which reduces the possibility of biases due to some anomaly in the field of view) for a total livetime of 1162 min (=19.37 h); the dead time was approximately 10%.

The daily laser data taken to calibrate the camera were similarly checked for quality. Programs like those described in section 5.6 showed that the laser pulse reaching T3 was too weak for reliable calibration for some of the January runs. In those cases, the T3 data were calibrated using the nearest successful laser run available. A detailed account of the data and corresponding laser runs used can be found in tables B.1-B.3 of appendix B.

7.1.2 Detection

Because the *VEGAS* analysis package has been under intense development for the past few years (and still is evolving today), it has really been like trying to hit a moving target than to obtain reliable analysis results. They have been difficult to obtain and trust at first, but they have increasingly improved in quality over time as algorithms were reviewed by different collaboration members and bugs were fixed. One of the tasks of the author was to confirm the analysis of the 1ES 1218 + 30.4 data made by a colleague with another package, called *Event Display*, in preparation for a publication [42], [43]. Unfortunately, at the time this was undertaken, no spectral or light curve analysis of the data could be done with *VEGAS* because of some problems in the code. Nevertheless the confirmation of 1ES 1218 + 30.4 as a source of γ rays was successfully established by the author. Since then, the *VEGAS* implementation has evolved sufficiently that the spectral and light curve analyses have become more reliable; these will be presented in the next subsections. In the process of making the code more robust, the detection of sources itself has also improved. Presented here are the updated detection results, obtained with the version of *VEGAS* dated from June 27, 2008, with some additional bug fixes.

Due to the evolution of *VEGAS*, the γ-ray selection cuts from table 6.3, that were

Optimized selection cuts for a 3% Crab-like source
$MSW < 1.16$
$MSL < 1.36$
$\Theta^2 < (0.115\,^\circ)^2 = 0.0132\,^{\circ 2}$
Number of reflected background regions automatically chosen by code

Table 7.1: Optimized selection cuts for a 3% Crab-like source

obtained at the beginning of 2008, are no longer optimized for the new analysis. The reason is twofold. Firstly, the *distance* quality cut has been found to give superior results if it is relaxed from 1.3 to 1.43, to allow for more events near the edge of the camera to survive the analysis (the event reconstruction efficiency increased from 21% to 28%). Secondly, improved lookup tables that include interpolation over different noise levels have been implemented, and they were generated under the new *distance* quality cut scheme. Because of time constraints a cuts optimization for the new analysis conditions could not be performed by the author. This was however done by another collaboration member using a technique similar to that discussed in section 6.7. The new selection cuts, optimized for a 3% Crab Nebula-like source are given in table 7.1. One thing to note is that the lookup tables that were actually used for the analysis, although they include the improvements mentioned above, were also generated specifically for three-telescope data, which is ideal for the analysis of 1ES 1218 + 30.4. The cuts in table 7.1 were however optimized on four-telescope data, so there may still be room for more improvement on the selection of optimal cuts.

With the new cuts, there were 837 signal events for 4069 background events, yielding a significance of detection of $12.47\,\sigma$ for the reflected-regions model. For the ring-background model, there were 848 signal and 10 918 background events, for a significance of $13.48\,\sigma$. The γ-ray detection rates were $(0.29 \pm 0.03)\,\gamma$/min for both models. There is no possible doubt about the detection since the significance is well

above the critical value $5\,\sigma$ [1] for both models. The slight difference in significance is irrelevant as discussed in section 6.6.3 and can probably be attributed to the fact that both models use different effective sizes for the background regions[2]; in the reflected-regions model α was 0.124 [3] while α was 0.046 for the ring-background model. With the cuts of table 6.3, the significances would have been $6.81\,\sigma$ and $8.00\,\sigma$ for the reflected-regions and ring models respectively, more than 40% decreases that show the effect that an unoptimized analysis can have. Having a look at the MSW and MSL distributions shows why the new optimized cuts are so different from the previous ones. Figure 7.1 shows that the MSW and MSL peaks extend to larger values than what was suggested by figures 6.15 and 6.16, which were obtained with the old *distance* cut and old lookup tables. Hence, the new scheme really benefitted from a re-optimization of the selection cuts.

Examining now the results of the detection in more detail, figure 7.2 shows the Θ^2 plots for the reflected-regions background models. The statistical excess of counts at low values of Θ^2 indicates clearly a γ-ray source. The Θ^2 cut captures a little more than the first bin of this plot. Although it would appear that a larger value for the cut, maybe $\Theta^2 < 0.03$ would have increased the significance, this does not follow immediately because changing a cut has repercussions on the distributions of the other parameters, MSW and MSL, probably rendering their cut values sub-optimal, as was seen in section 6.7. Nevertheless, there is a good reason to suspect that the

[1] There is nothing truly critical about the $5\,\sigma$ value; as discussed in section 6.6.3, this is just the standard used in the field of γ-ray astronomy.

[2] Here the signal counts are not independent, they are basically the same between the two background models. Therefore, the $1\,\sigma$ expected difference discussed in section 6.6.3 does not necessarily apply here. This is why the difference in significances is rather attributed to the difference in α values. Note, however, that the standard deviation of the significance values of the runs having a 0.5° wobble offset in the table of appendix B is $1.01\,\sigma$, in perfect agreement with the expectations from section 6.6.3. This is as it should since they are independent measurements analyzed in the same way.

[3] This α value results from a mix of runs having 3 background regions, for the 0.3° wobble runs, and a majority of runs having 9 background regions, for the 0.5° wobble runs.

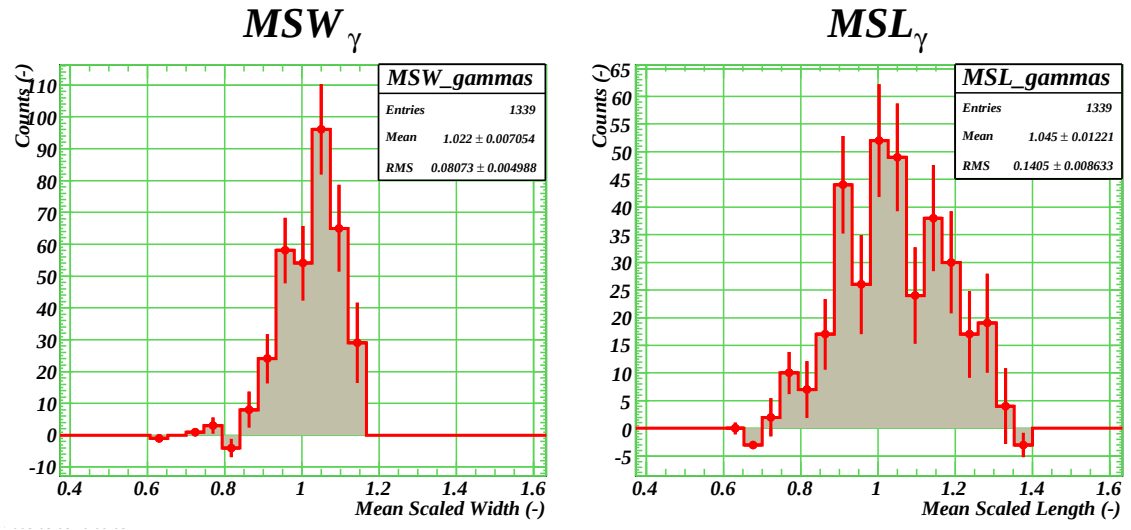

Figure 7.1: MSW and MSL distributions for 1ES 1218 + 30.4 observations using the complete set of files. These are the distributions for γ-ray-like events only, *i.e.* with the background counts subtracted, which explains the few bins with negative contents. The number of entries represent the signal and normalized background counts that were used in the making of these histograms.

Θ^2 cut is not perfectly optimized for the source at hand: this is three-telescope data whereas the optimization was performed for four-telescope data; therefore, it can be expected that the γ-ray location reconstruction is less precise in our case, resulting in larger Θ^2's. Since it is not fair to change the cuts once the data have been looked at (doing so would introduce an unjustified bias), the analysis is pursued with the initial choice of cuts, which are still appropriate since they yield a strong detection. At larger values of Θ^2, the plot shows that the signal counts match well with the background counts, as they should for a point-like source[4]. In this region of the plot, the tendency of counts to slowly decrease with increasing Θ^2 is due to acceptance effects.

A more complete picture of the detection is obtained by looking at the results

[4]Actually, upon closer inspection, the signal counts have a tendency to be above the background counts. This could indicate a systematic effect or a problem in the analysis code. The author suggests that maybe the signal region is excluded from the background counts calculations but that the background regions are not excluded from the signal counts calculations. If the two types of counts are not renormalized properly to take this into account, then this could lead to the behaviour observed here.

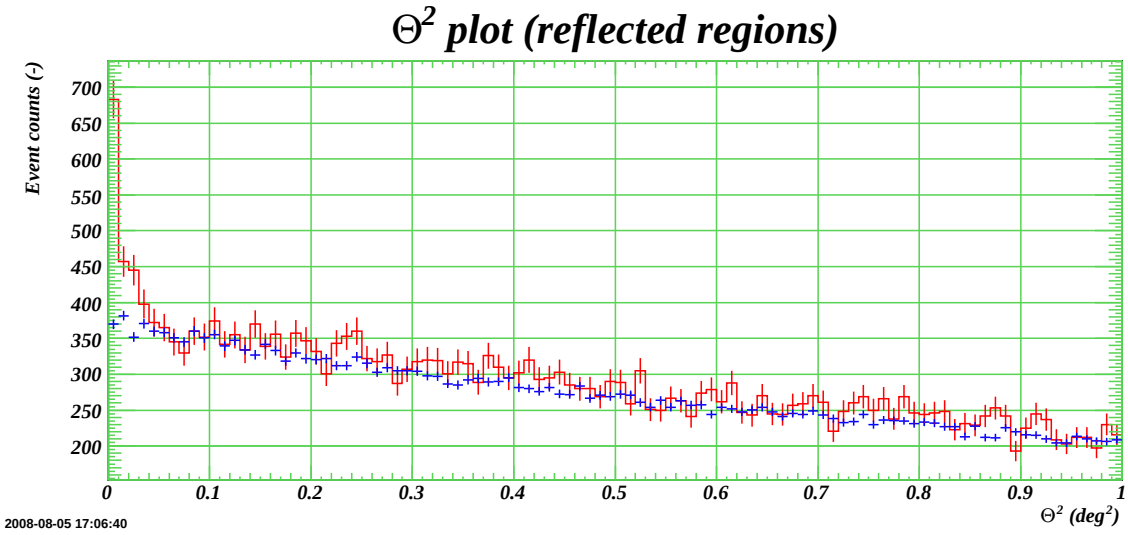

Figure 7.2: Θ^2 plot for 1ES 1218 + 30.4 observations using the reflected-regions background model on the complete set of files. The red histogram represents the signal counts, while the blue data points represent the background counts. Note that the error bars on the background counts are smaller because the background is estimated from several reflected regions (here 8.08 on average, the exact number depending on the wobble offset of the particular run). The statistical excess of counts at low values of Θ^2 indicates a γ-ray source. At larger values, the signal counts match well with the background counts, as it should for a point-like source.

from the ring-background model analysis. First the events are binned in a sky map according to their arrival direction. This raw map is shown in figure 7.3. Already, there are indications that there may be more events originating from the nominal location of 1ES 1218 + 30.4, shown by the crosshair, than from elsewhere in the map. To ascertain this, the background counts are extracted from rings around the tentative source locations as described in section 6.6.2. Every bin in the map is taken as a possible source location. Disks of radius 0.3 ° around the locations of 1ES 1218 + 30.4 and W Comae have been excluded from the computation of the background counts in order to avoid introducing biases. These counts, weighted by their acceptance relative to that of the bin to which they report, are then subtracted from the raw map to yield the excess map shown in figure 7.4.

What is more interesting, however, is not the excess in every bin, but the total excess in the signal region centered on each bin. To get that, one reassigns to each bin's value of the raw counts map the sum of the values of its neighboring bins that are inside a circle of radius equal to the value of the Θ-cut, which amounts to

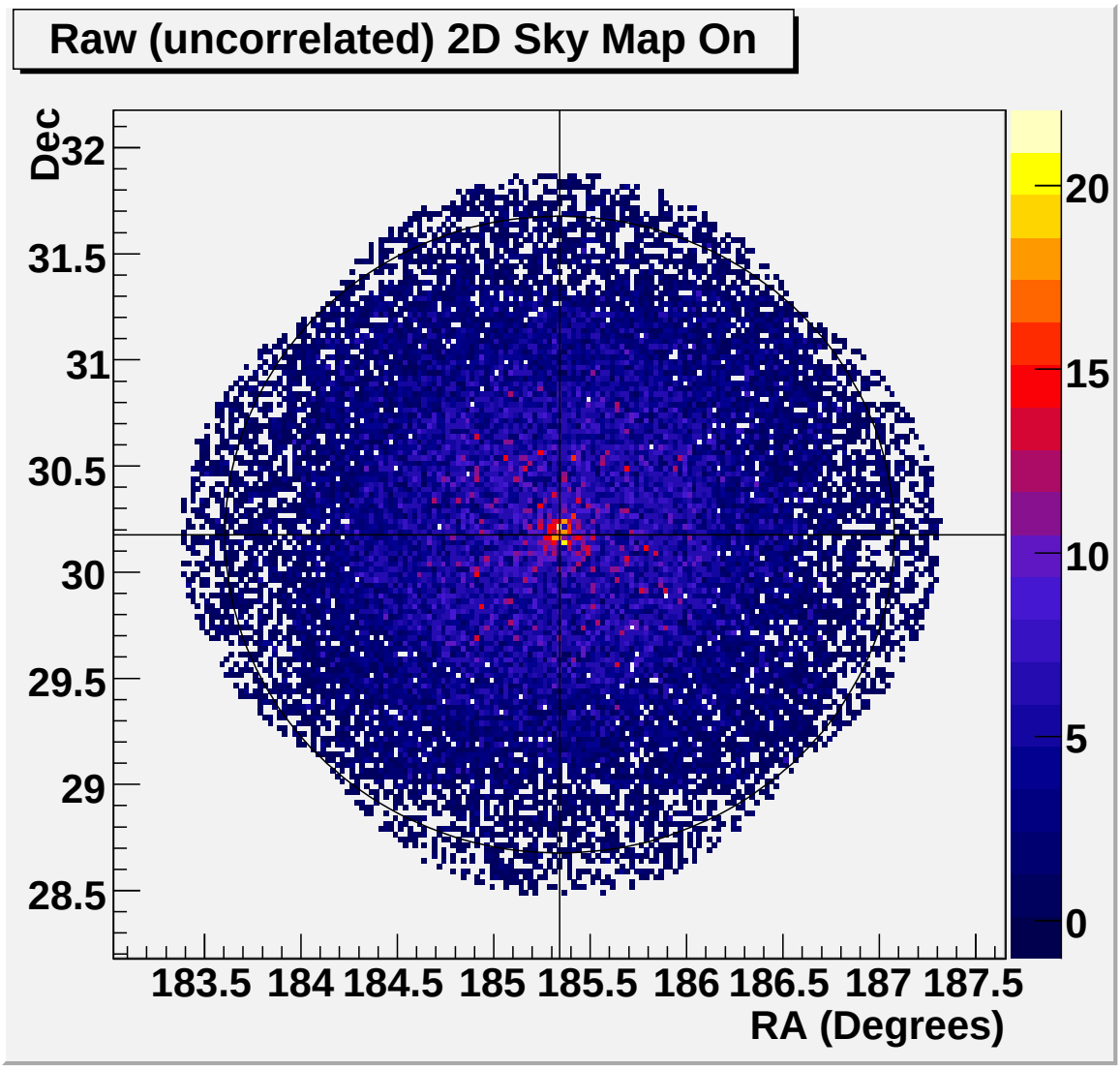

Figure 7.3: Raw counts map for 1ES 1218 + 30.4 observations using the complete set of files. The arrival directions of the reconstructed γ-ray-like showers are histogrammed in square bins of side 0.025 ° length. The crosshair shows the nominal location of 1ES 1218 + 30.4.

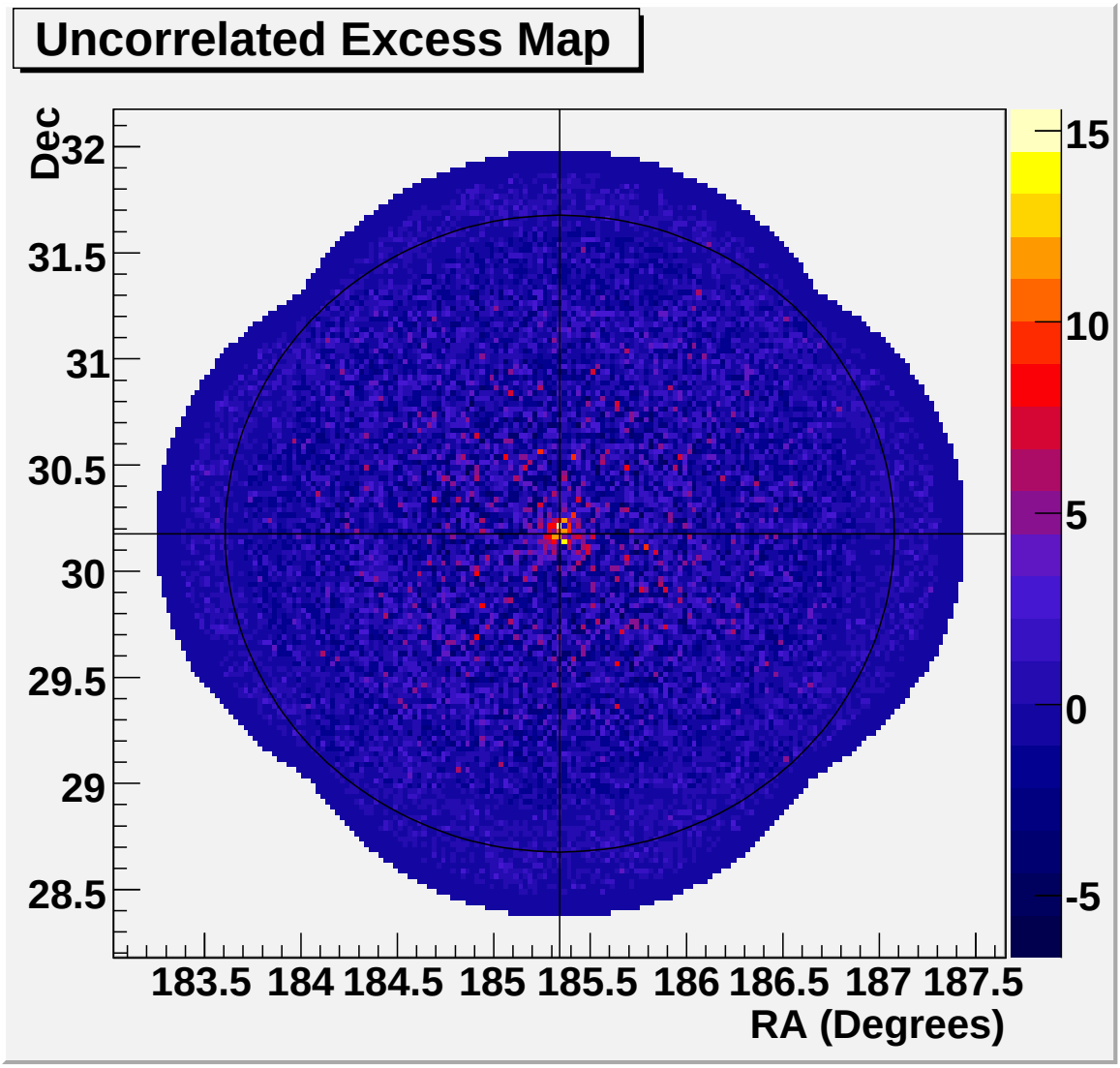

Figure 7.4: Uncorrelated excess map for 1ES 1218 + 30.4 observations for the complete set of files. This map is obtained from figure 7.3 using the ring-background model in the way explained in section 6.6.2, but with the signal region consisting of only 1 bin.

integrating over the signal region[5]. As a result, the maps derived from this integrated raw counts map[6] get a smoothed-like appearance. The result for the excess map is shown in figure 7.5. The 'smoothing' procedure can be thought of as a way of taking into account the fact that the arrival direction of a γ ray is only reconstructed up to a finite precision. By smoothing, it is hoped that the fluctuations due to this imprecision will average out and that the final result will be more precise. Regions of the unsmoothed map containing many bins that have large excesses form structures in the smoothed image that really stand out. The excess at 1ES 1218 + 30.4's location in figure 7.5 is now unquestionable.

Similarly, one can apply equation 6.8 to get a map of the significance of the excesses of the bins of the previous image. This is shown in figure 7.6. This map shows that the bin having the highest significance has a value of 14.15 and is located at 0.0125 ° down from the center of the map. This is consistent with the nominal location of 1ES 1218 + 30.4, since it is just a half-bin away (the position of 1ES 1218 + 30.4 falls at the edge between two bins of the map). It is still possible to compute the significance at the nominal location of 1ES 1218 + 30.4, and in that case one obtains 13.48, the value mentioned previously.

As a check that the background was well estimated and that the computations were well carried, it is a common practice to plot the distribution of the significances of figure 7.6. This is shown in figure 7.7. If there was no source in the field of view, the distribution of significances would be expected to follow a Gaussian centered on zero and having unit width [179]. Here, this is clearly not the case as there is an obvious excess of bins having large significances indicating the presence of a source. However, there still is a population in this histogram that is well described by a Gaussian fit having parameters close to the predicted ones. This population comes from the parts of the field-of-view that do not include the source. It indicates that the background

[5] A side effect of the integration procedure is that the map's bins become correlated.

[6] Note that a different acceptance ratio (α) is used when dealing with the integrated counts maps rather than with the raw counts map because the former has a signal region of radius Θ and the latter has an effective signal region of only one bin.

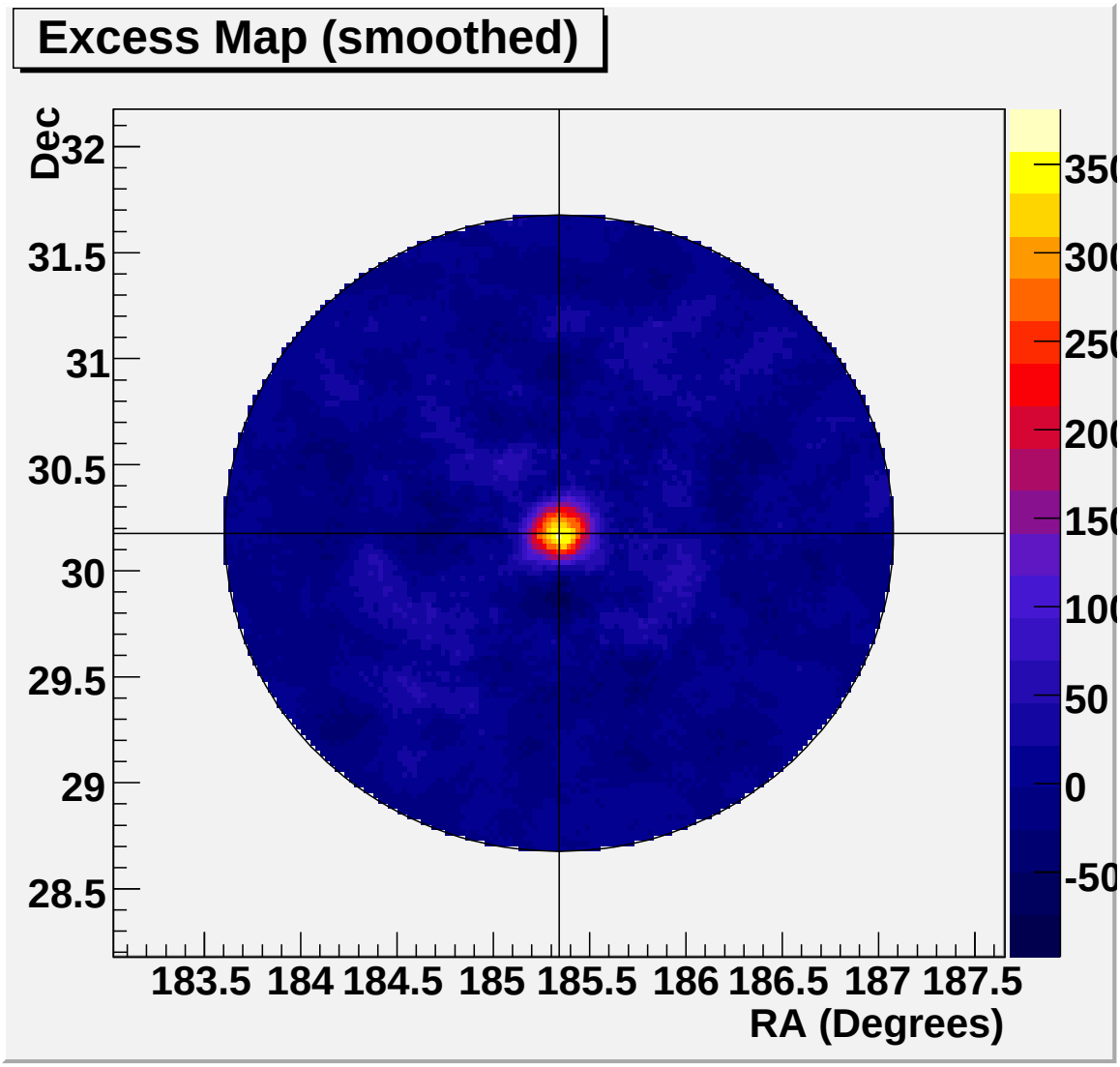

Figure 7.5: Excess map for 1ES 1218 + 30.4 observations using the ring-background model on the complete set of files. This map is obtained from the version of the map of figure 7.3 that is integrated over a signal region of radius equal to the Θ-cut value. This results in a map whose bins are correlated, but that is visually more representative. It is also a way of taking into account the fact that the arrival direction of a γ ray is only reconstructed up to a finite precision. By smoothing, it is hoped that the fluctuations average out and that the final result is more precise.

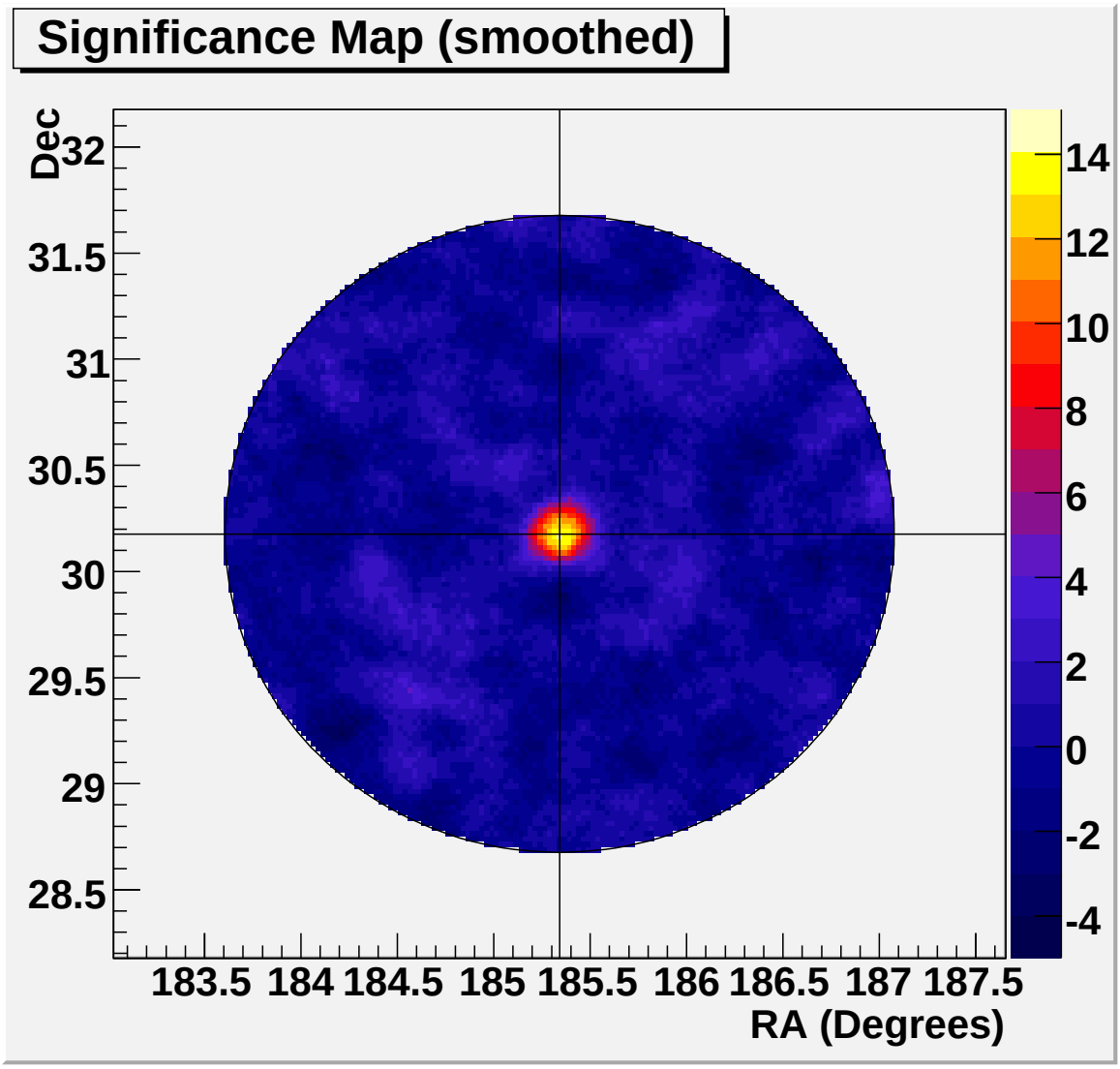

Figure 7.6: Significance map for 1ES 1218 + 30.4 observations using the ring-background model on the complete set of files. There is obviously a γ-ray source at the position of 1ES 1218 + 30.4. The maximal significance is 14.15 and is located a half-bin down from the center. The significance at the center is 13.48.

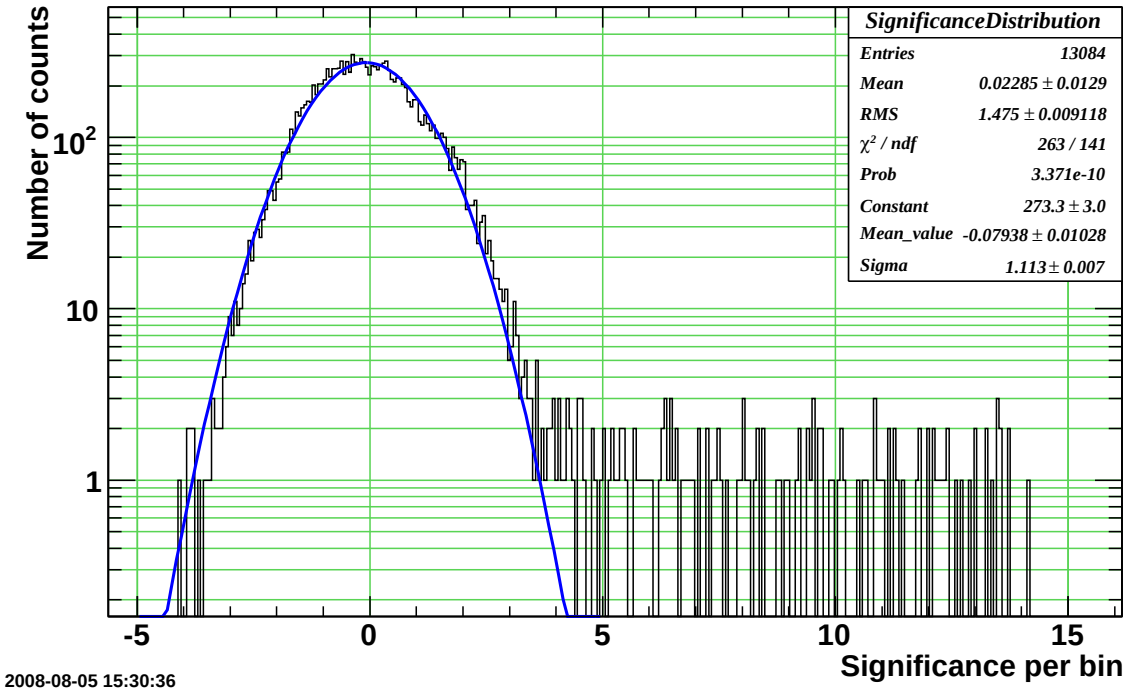

Figure 7.7: Distribution of significances for the bins of the sky map shown in figure 7.6 for 1ES 1218 + 30.4 observations. If there was no source in the field of view, the distribution of significances in each bin would be expected to follow a Gaussian distribution because of random fluctuations in the number of background counts. This is what happens for the majority of the bins as can be shown by the Gaussian fit (solid blue curve). However, the unusually large number of bins having significances greater than 5 and not following the Gaussian distribution indicates the presence of a γ-ray source.

is behaving as expected, with normal fluctuations due to counting statistics.

Having established the emissivity of 1ES 1218 + 30.4 at TeV energies with high significance with two background models, it is interesting to go back and see the effect of some of the choices that were made in preparing the analysis. Two of them are of interest: 1) the decision to apply tracking corrections to the December 2006 data and 2) the exclusion of a region around the W Comae location from the background evaluation.

Effect of tracking corrections

In order to best address the question of the effect of applying tracking corrections to the December 2006 runs, the run list was shortened to include only these data (8

runs). Figure 7.8 shows the excess map for the case where no tracking corrections have been applied. The maximal excess is found to have a $7.83\,\sigma$ significance and is located 0.066° away from the nominal position of 1ES 1218 + 30.4, where the significance is $6.34\,\sigma$. This is not a huge pointing error since the radius of the signal region (Θ) is larger than that, but it still represents a large fraction of it.

When corrections are applied to the tracking[7], the excess map of figure 7.9 is obtained. In this case, the maximal excess is found 0.045° away from the center of the map, and it has a $8.34\,\sigma$ significance value. The significance at 1ES 1218 + 30.4's location slightly increased to $6.89\,\sigma$. The ring-background model then confirms that the tracking corrections helped in obtaining better results. The significance at the center of the map increased slightly and the distance from nominal of the maximal excess diminished. Moreover, the fact that the significance of the maximal excess also increased might mean that the reconstructed arrival directions were less spread out than before the corrections. More detailed studies would be required to verify this. Using the reflected-regions background model, the significance went from $4.80\,\sigma$ (strong hint of a detection), for the case with no corrections, to $5.94\,\sigma$ (a solid detection) with the corrections.

Although there is improvement with the tracking corrections applied, as demonstrated with the two background models, it is more difficult to claim that it is a *significant* improvement. Nevertheless, the pointing error was small to start with, so it is harder to demonstrate significant changes in this case. The well-behaved excess map shown in figure 7.9 shows that the inclusion of the corrected December 2006 runs within the final run list poses no problem and they do contribute to increase the detection statistics.

Effect of W Comae

The exclusion of the region surrounding the location of W Comae from the background counts evaluation was really done as an extra-precautious measure. In fact, regarding

[7]The corrections consisted in the application of revised parameters for the tracking model, which were obtained from pointing checks made at the end of December 2006.

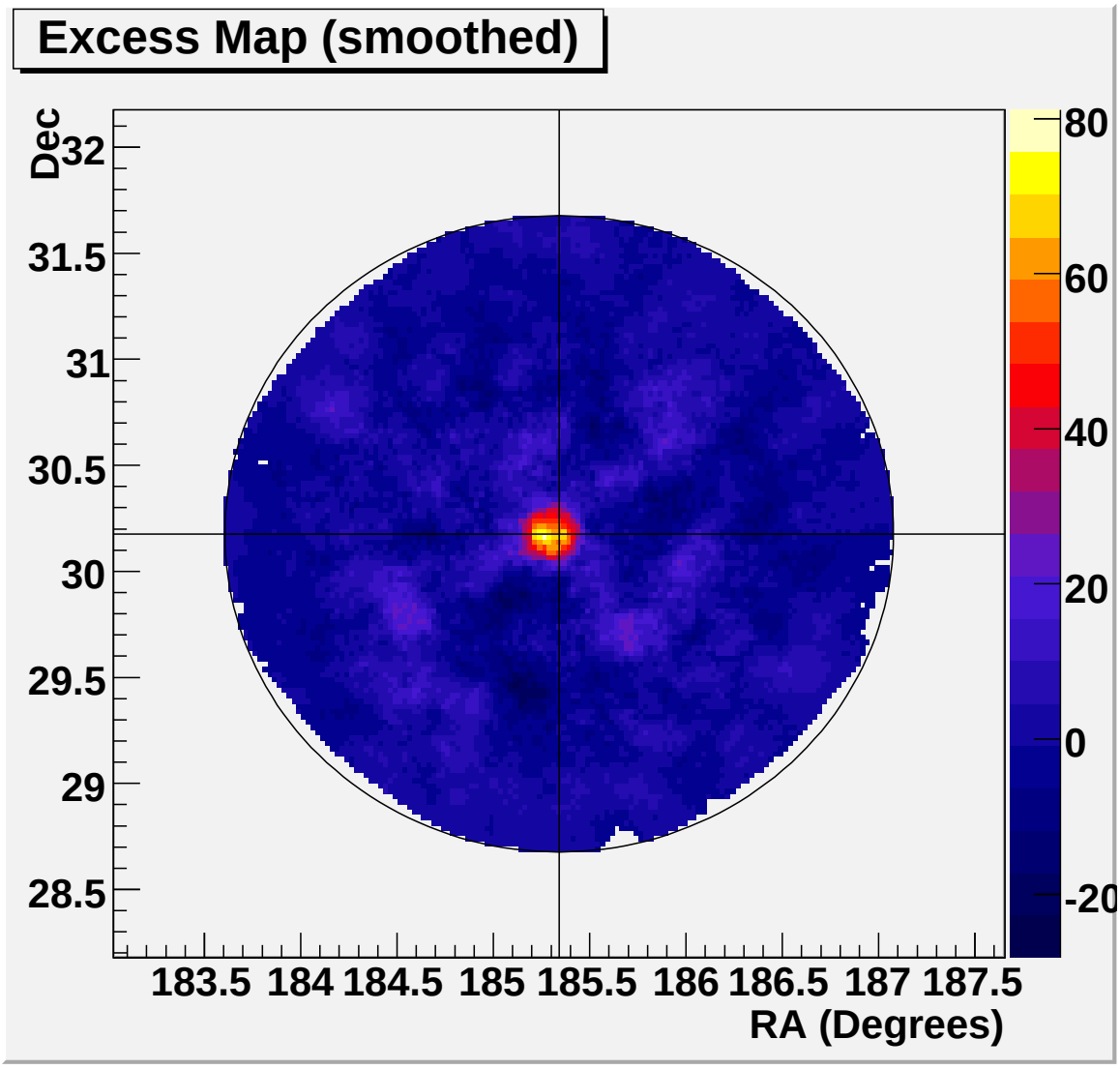

Figure 7.8: Excess map for 1ES 1218 + 30.4 using the ring-background model on the set of files from December 2006. No tracking corrections were applied. It can be seen that the position of the greatest excess is slightly off-center. This is due to the bad tracking of one of the telescopes, T3, during this time.

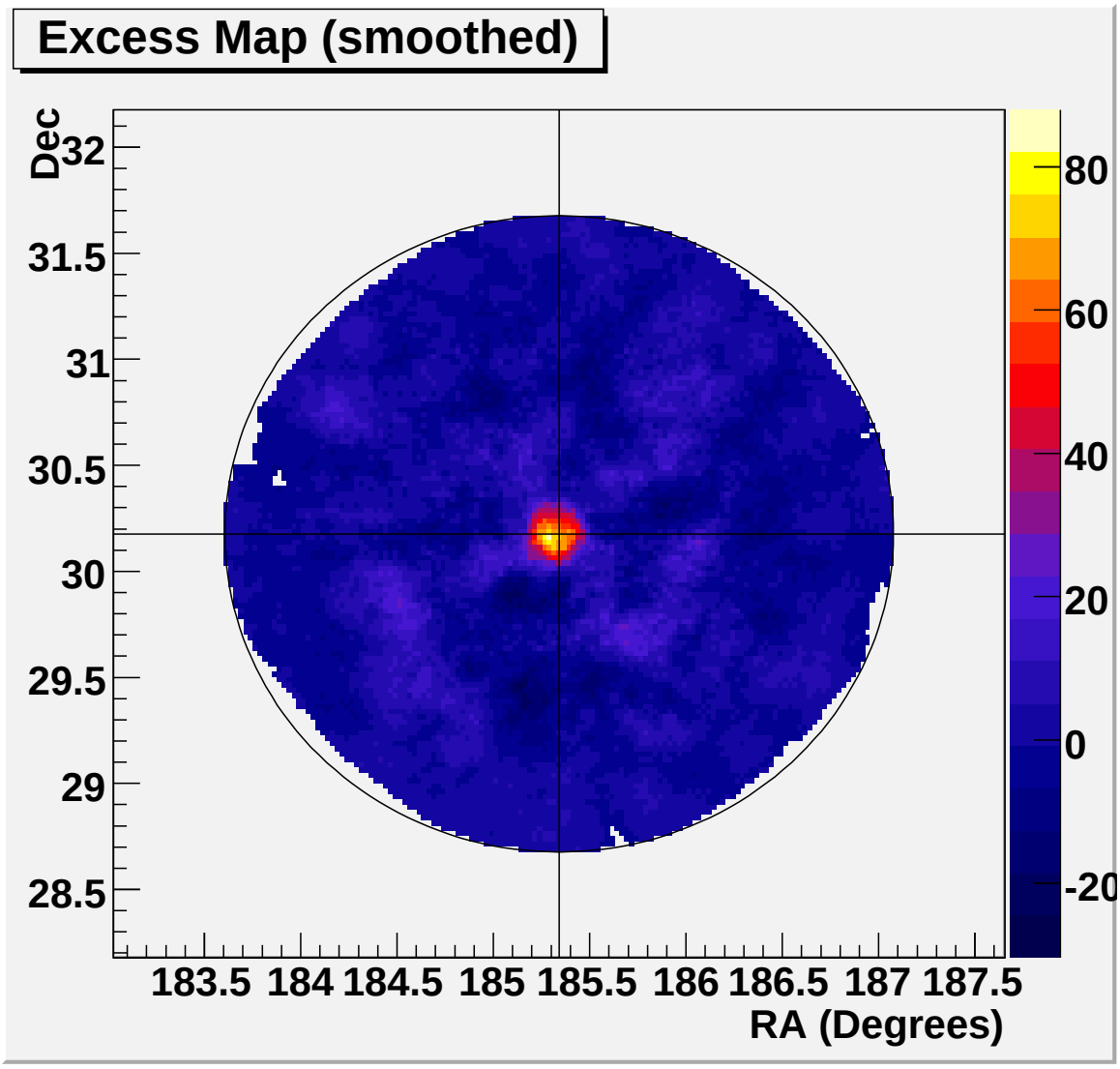

Figure 7.9: Excess map for 1ES 1218 + 30.4 using the ring-background model on the set of files from December 2006. Tracking corrections were applied. The position of the greatest excess is now closer to the nominal position of 1ES 1218 + 30.4 indicated by the crosshair. This indicates that the bad tracking of T3 during this time has been compensated for.

the analysis at the location of 1ES 1218 + 30.4, there is little chance that γ rays from W Comae could have affected the background counts at all, unless it had been in a strong flaring state. The reason is that the distance between the two sources, being of $2\,^\circ$, is sufficiently great for the two sources not to interfere with each other. For example, for a run where the wobble offset, with respect to 1ES 1218 + 30.4, is $0.5\,^\circ$ in the South direction, the most southern point of a reflected background region of radius Θ will still be $0.885\,^\circ$ away from the position of W Comae, which is greater than the radius of a region from where a signal from a point source would be expected. For the ring-background model, the outer radius of the annulus used for the background estimation measures $0.8\,^\circ$; again, there is no danger for contamination of the 1ES 1218 + 30.4 background counts with W Comae's γ rays. Where there could possibly be any such contamination is for test positions at other parts of the field-of-view, mostly in between the two sources. Let us now investigate whether the exclusion region was a necessary precaution or not for these parts of the field-of-view, *i.e.* whether a significant signal could be detected from the location of W Comae.

To accomplish this, a run list made up only of the runs wobbled South was used (these 16 runs are marked with an asterisk in the table of appendix B). The test position for the analysis was set to the location of W Comae and both background models were used. For the reflected-regions analysis, the significance obtained was $0.84\,\sigma$. For the ring-background analysis, it was 1.59, far from what is needed to claim a detection. Therefore, the exclusion of a region around the location of W Comae was not strictly necessary since no abnormal excess of γ rays were observed from this source during these observations. Figure 7.10 shows the significance map for this analysis. Although there are some regions that have a slightly higher significance than others (apart for the region around 1ES 1218 + 30.4), these are not unexpected given the large number of bins in the map; they are just random fluctuations and all of them indicate a significances less than 4.0.

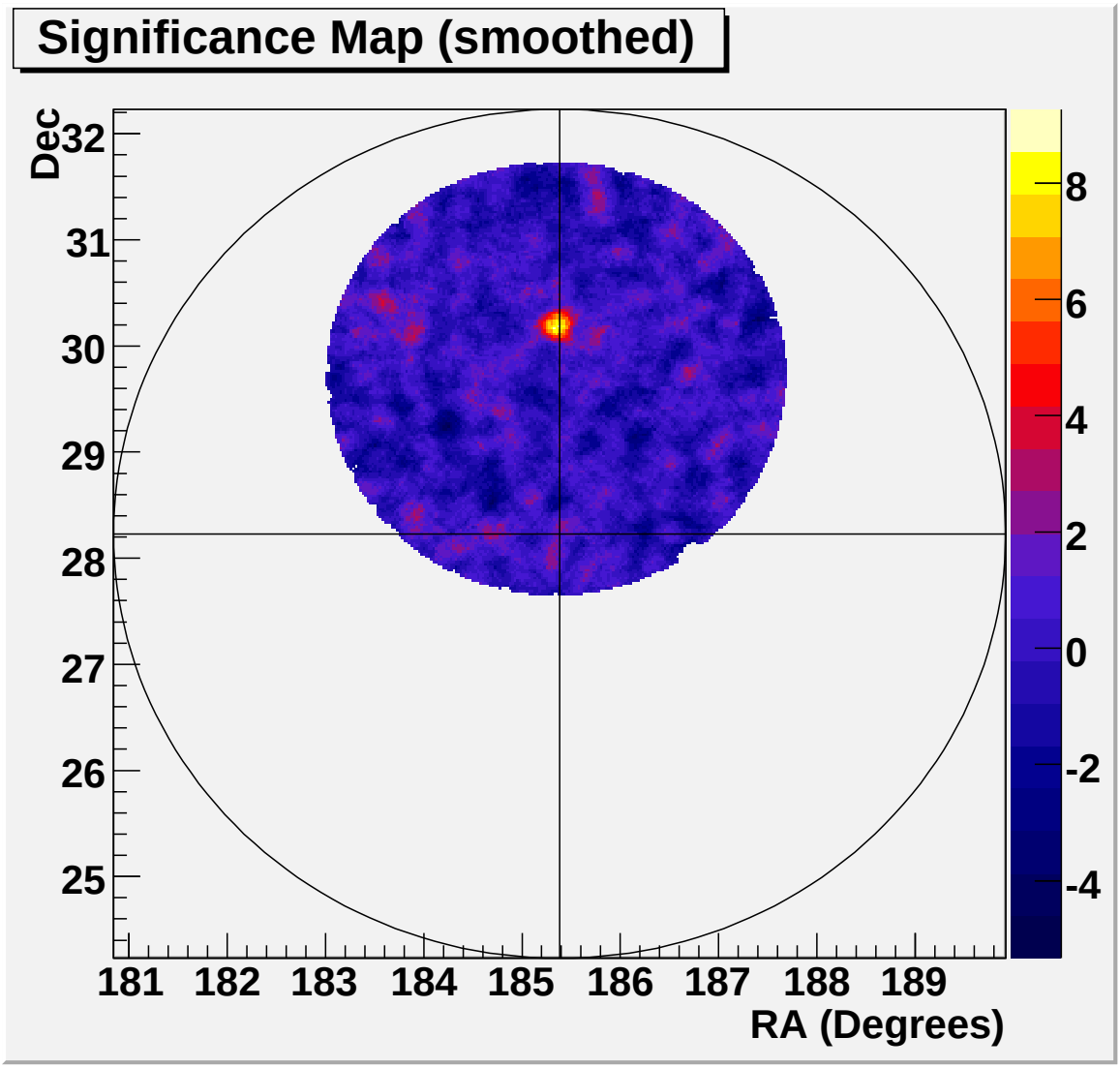

Figure 7.10: Significance map for W Comae using the ring-background model on the set of files that included this source in the field of view. No significant excess is found at the nominal position of W Comae indicated by the center of the crosshair. The significant blob above it is due to 1ES 1218 + 30.4.

7.1.3 Spectrum

Now equipped with a solid detection of 1ES 1218 + 30.4, a spectral reconstruction of this source can be attempted. As mentioned previously, the *VEGAS* code to do this analysis has been evolving a lot and only recently has it produced more convincing results. The code is still not perfect; studies of the Crab Nebula's spectrum indicate that its shape is well reconstructed but that there are still some small unresolved issues regarding its normalization [188]. Despite this, it is interesting to see what one gets for the case of 1ES 1218 + 30.4 and compare the results to those obtained with *Event Display*, the alternative analysis package.

To reconstruct the spectrum, one usually opens up the cuts. Although this reduces the significance, because more noise is accepted in the measurement, the total number of signal events increases. Of course, the background events count also increases (so that the additional noise in the signal counts can be subtracted), but less so than the signal counts. The result is an increase of the rate of detected γ rays (this effect can be seen in figure 6.22). Here, the cuts shown in table 7.2 are used. They were not specifically optimized for spectral reconstruction (no such optimization has been performed yet by the collaboration), but rather for significance on full-strength Crab Nebula data. These cuts were used because they are indeed relaxed compared to those shown in table 7.1, so the rate is expected to increase, but also, the effective area file that was used had been generated from these cuts[8]. The effective area file was generated specifically for 3-telescope data and for a source with an expected power-law type of spectrum with index 3.0.

The reflected-regions analysis was chosen because it introduces less complications (and thus less uncertainty) in the spectral reconstruction, compared with the ring-background analysis that requires an acceptance curve. The significance obtained with the relaxed cuts was $11.46\,\sigma$ (1882 signal events for 6042 background events, $\alpha \sim 0.227$) and the rate was $(0.46 \pm 0.04)\,\gamma$/min, 59% more than with the detection

[8] During a spectral analysis, the cuts used have to be the same ones that were used for the generation of the effective area curve for the analysis to make sense.

Spectrum Selection Cuts
$MSW < 1.20$
$MSL < 1.49$
$\Theta^2 < (0.158\,^\circ)^2 = 0.0250\,^{\circ 2}$
Number of reflected background regions automatically chosen by code

Table 7.2: Spectrum selection cuts

cuts. As described in section 6.6.4, the detected γ rays are separated in energy bands and the differential flux is obtained from[9]

$$\boxed{\phi_\gamma(E_i) = \frac{R_\gamma}{\Delta E_i \; A_{\gamma,\mathrm{eff}}(E_i)}}, \tag{7.1}$$

where ΔE_i is the width of bin i and the other symbols are defined as previously. The statistical uncertainty on the flux is given by[10,11]

$$\delta\phi_\gamma(E_i) = \frac{\sqrt{N_{\gamma,\mathrm{s}} + \alpha^2 N_{\gamma,\mathrm{bg}}}}{\Delta E_i \; A_{\gamma,\mathrm{eff}}(E_i) \; t_{\mathrm{live}}}, \tag{7.2}$$

Applying this to the data, the results shown in table 7.3 are obtained. A power law fit $C(\frac{E}{0.8\,\mathrm{TeV}})^{-\Gamma}$ is applied to the data, resulting in a reduced χ^2 of 0.39, with an associated probability of 76%, indicating that the points are well described by the fit. The power law index is $\Gamma = 2.8 \pm 0.2$ and the normalization constant is $C = (2.2 \pm 0.3) \times 10^{-12}\gamma/(\mathrm{cm}^2\,\mathrm{s}\,\mathrm{TeV})$. The spectrum points and fit are plotted in figure 7.11, along with the spectrum from *Event Display*, obtained by another collaboration member [43], and the spectrum measured by the MAGIC collaboration [41]. Within statistical uncertainties, all the spectra are compatible. Even the normalization, which was expected to possibly be the cause of discrepancies, agrees (when the energy values, at which the fits are normalized, are taken to be the same).

[9] In reality, it is not a single effective area value that is used for each bin; each event is weighted by the effective area corresponding to its energy.

[10] This is based on equation 5 of [179], since the assumption of no source in the field-of-view can no longer be made.

[11] The uncertainty on the flux measurement was badly implemented in *VEGAS*, a bug that was fixed by the author.

$\mathbf{E_i}$	$\phi(\mathbf{E_i})/(1\times10^{-12})$	$\delta\phi(\mathbf{E_i})/(1\times10^{-12})$
(TeV)	$(\gamma/(\mathrm{cm^2\,s\,TeV}))$	$(\gamma/(\mathrm{cm^2\,s\,TeV}))$
0.347	21	4
0.527	8.4	1.4
0.801	2.3	0.5
1.23	0.60	0.19
1.93	0.16	0.08

Table 7.3: Spectrum points for 1ES 1218 + 30.4 using the *VEGAS* analysis package.

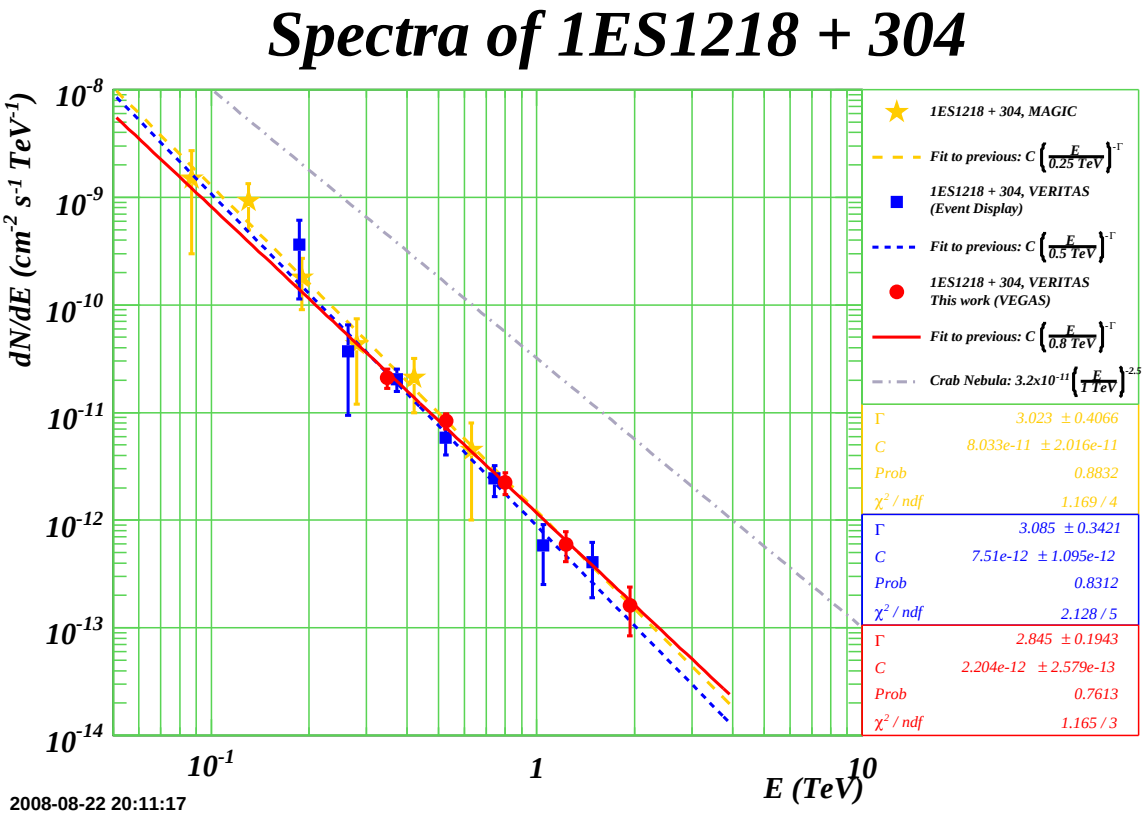

Figure 7.11: Spectra of 1ES 1218 + 30.4 from different analyses: the stars are the MAGIC collaboration's points [41], squares are from an independent VERITAS analysis [43], circles are the result of the work presented in this thesis. All the spectra agree within statistical uncertainties. The Crab Nebula spectrum is also plotted for reference [175].

A notable difference between the *Event Display* spectrum and the *VEGAS* one is the two supplemental points that *Event Display* can produce at lower energies. There are two reasons why this is so. Firstly, the quality cut on the *size* parameter is lower for *Event Display* than for *VEGAS*; this allows more of the lower energy showers to survive the cuts. The current *VEGAS* value was chosen as a conservative starting point until future studies show that it can be lowered. *Event Display* is a package that has evolved more rapidly and therefore more time has been taken to optimize its parameters. Secondly, looking at the energy bias curve of figure 7.12, which shows how precisely the energy is reconstructed for simulated events, one sees that the bias is within 10% only between 0.350 TeV and 25 TeV. *VEGAS* does not include events having a larger bias than this in the spectrum calculation to avoid the introduction of uncertainties. Admittedly, the curve shown was for a zenith angle of 30 °, whereas most of the data were taken at higher elevations where the acceptable region of the energy bias curve extends to slightly lower energies. Still this shows that statistics are being lost for energies $\sim 0.350\,\mathrm{TeV}$ and lower. The combination of this loss of statistics at low energies with the large *size* cut is what prevents *VEGAS* from computing the two leftmost points of the 1ES 1218 + 30.4 spectrum.

At the other end of the spectrum, *VEGAS* is able to compute the last point at a higher energy. The last point is defined by the requirement of having a detection with significance greater than 2.0 for that energy bin. The author optimized the binning in order to push this limit at the highest possible energy. The fact that more runs were used for the analysis presented in this work than were used for the analysis from [43] may explain why the rightmost point is achieved at higher energies here.

With the fit obtained above, one can compute the integral flux above the minimum point in the spectrum. One gets $\Phi_{\gamma,E>0.35\,\mathrm{TeV}} = (4.4 \pm 0.6) \times 10^{-12}\gamma/(\mathrm{cm}^2\,\mathrm{s})$. This represents $\sim$ 4.3% of the Crab Nebula integral flux above the same energy, which justifies the use of cuts optimized for a source having 3% of the Crab Nebula's strength for the detection analysis. The integral flux computed above 0.3 TeV is $\Phi_{\gamma,E>0.3\,\mathrm{TeV}} = (5.8 \pm 0.8) \times 10^{-12}\gamma/(\mathrm{cm}^2\,\mathrm{s})$, which falls in the range of predictions

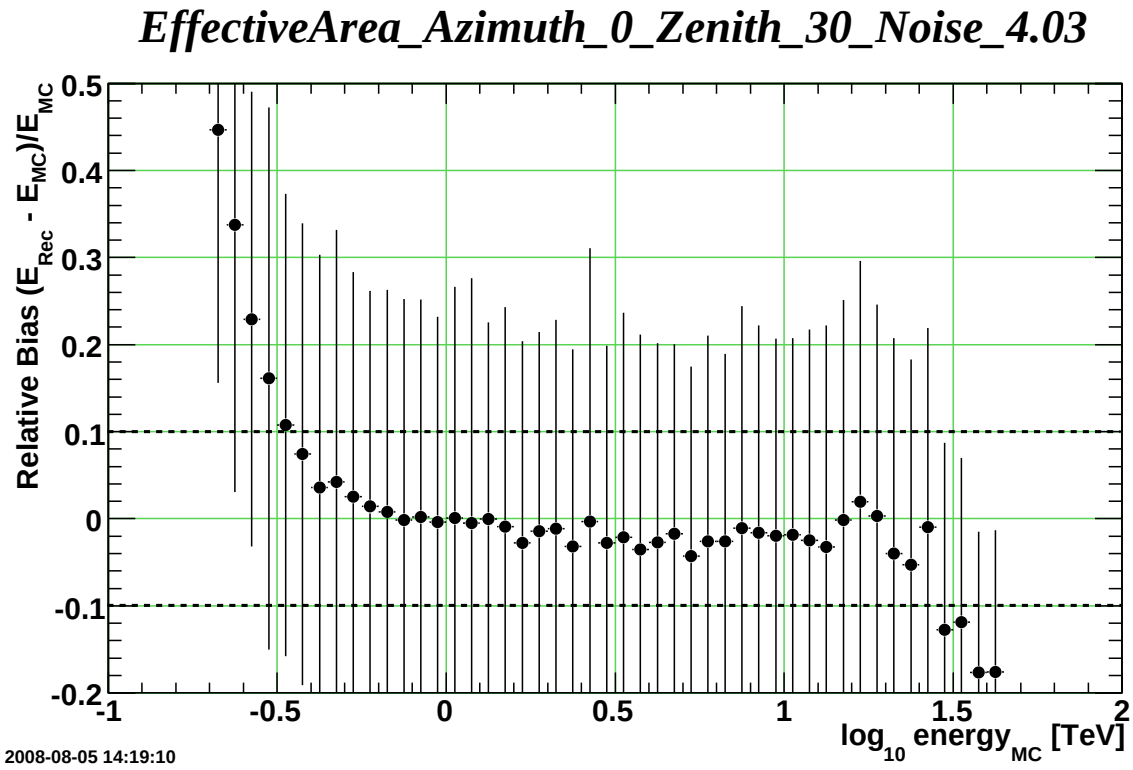

Figure 7.12: Plot of the energy bias curve. This compares the reconstructed energy of an event to its true value set in Monte Carlo simulations (MC). Only a bias less than 10% is deemed acceptable for a *VEGAS* spectral reconstruction; this is the region on the plot between the two dashed lines. At low energies the bias is large because, near the detection threshold, there will be more higher energy events filling the lookup table bins than lower energy ones that do not all pass the trigger. At high energies it drops off because of loss of statistics at high energies and because images of large showers get truncated and thus the energy is underestimated. The error bars do not represent the uncertainty on the points themselves, but the spread in the data.

presented in section 2.4.1 ($1.6\times10^{-12}\,\gamma/(\mathrm{cm}^2\,\mathrm{s})$ to $6.7\times10^{-12}\,\gamma/(\mathrm{cm}^2\,\mathrm{s})$ [12] [27]).

Concerning the systematic uncertainties on the spectrum's parameters, these are still not completely studied. The main sources of systematics can be divided into four categories: the atmosphere, the optical response of the telescopes, the camera response and the analysis software [189]. Uncertainties may arise because of variations in the observing conditions (night-sky background fluctuations, atmospheric changes, telescope degradation, etc.), because of improper modeling (shower interactions, telescope system, etc.) or because of the way the analysis is implemented (background models, selection cuts, etc.). How these uncertainties affect the final results is a difficult question to answer. To tackle it, a lot of simulations need to be made, with slight changes in the parameters. For example, one can use different interaction models to generate the showers, different atmospheric models to propagate the Čerenkov photons to the telescopes. All the detector parameters (reflectivities, point-spread function, collection efficiencies) can also be varied around their nominal specifications to see what the effect is on the biases in energy reconstruction and on the calculated effective areas. Such a study has been performed by a VERITAS member using *Event Display* [190]. Because *VEGAS* is still under development, the uncertainties associated with analyses made with this package are still not fully investigated. However, based on uncertainty analyses obtained with *Event Display*, and because the spectrum obtained here with *VEGAS* agrees with the one obtained with *Event Display*, it is likely that the dominant contributions to the systematic uncertainties come not from the analysis packages, but from the variations and modeling of the atmosphere and of the detector. Therefore, assuming that **the conclusions reached in [190] are applicable to the current analysis**, the systematic uncertainty in the flux normalization will be estimated to be 20% and the one associated with the photon index will be estimated to be 0.2.

[12] Note, however, that these predictions do not take into account the absorption due to the extragalactic background light.

7.1.4 Light Curve

Finally, before closing the section on the TeV emission of 1ES 1218 + 30.4, let us present its **light curve**, *i.e.* the time dependence of its integral flux. The following reasoning is followed in producing the light curve.

Let $\Phi_{\gamma,E>E_{\rm th}}(t)$ be the integral flux above the threshold energy $E_{\rm th}$ at time t:

$$\Phi_{\gamma,E>E_{\rm th}}(t) := \int_{E_{\rm th}}^{\infty} \phi_\gamma(E,t)\, dE, \tag{7.3}$$

where $\phi_\gamma(E,t)$ is the differential flux at energy E and at time t. $\Phi_{\gamma,E>E_{\rm th}}(t)$ is what we are looking for, but it cannot be obtained solely from equation 7.3 in small time bins because the low statistics collected over small periods of time make it impossible to reconstruct $\phi_\gamma(E,t)$ properly in these time bins.

Let $R_{\gamma,E>E_{\rm th}}(t)$ be the measured rate above the threshold. Let $A_{\gamma,\rm eff}(E,t)$ be the effective area at energy E, which has a dependence on t via the zenith and azimuth angles of observation. Then

$$R_{\gamma,E>E_{\rm th}}(t) = \int_{E_{\rm th}}^{\infty} \phi_\gamma(E,t) A_{\gamma,\rm eff}(E,t)\, dE. \tag{7.4}$$

Dividing 7.3 by 7.4 and isolating $\Phi_{\gamma,E>E_{\rm th}}(t)$, one gets

$$\Phi_{\gamma,E>E_{\rm th}}(t) = \frac{R_{\gamma,E>E_{\rm th}}(t) \int_{E_{\rm th}}^{\infty} \phi_\gamma(E,t)\, dE}{\int_{E_{\rm th}}^{\infty} \phi_\gamma(E,t) A_{\gamma,\rm eff}(E,t)\, dE} \tag{7.5}$$

$$\approx \frac{R_{\gamma,E>E_{\rm th}}(t) \int_{E_{\rm th}}^{\infty} \phi_\gamma(E)\, dE}{\int_{E_{\rm th}}^{\infty} \phi_\gamma(E) A_{\gamma,\rm eff}(E,t)\, dE}, \tag{7.6}$$

where the time dependence of $\phi_\gamma(E,t)$ has been dropped in the second line under the assumption that **the shape of the spectrum does not vary significantly in time, but only the normalization**, which cancels out. In other words, the time dependence of the integral flux is taken from the time dependence of the rate divided by a time-dependent effective area, which is an averaged effective area weighted by the spectrum shape (obtained from accumulated statistics over a longer time).

The *VEGAS* code to do this analysis is still under development at the time of writing[13]. Figure 7.13 nevertheless presents the preliminary result obtained. For now, the

[13] The author is actively helping the developers by testing the code and he has made an important suggestion regarding the implementation of the algorithm presented above.

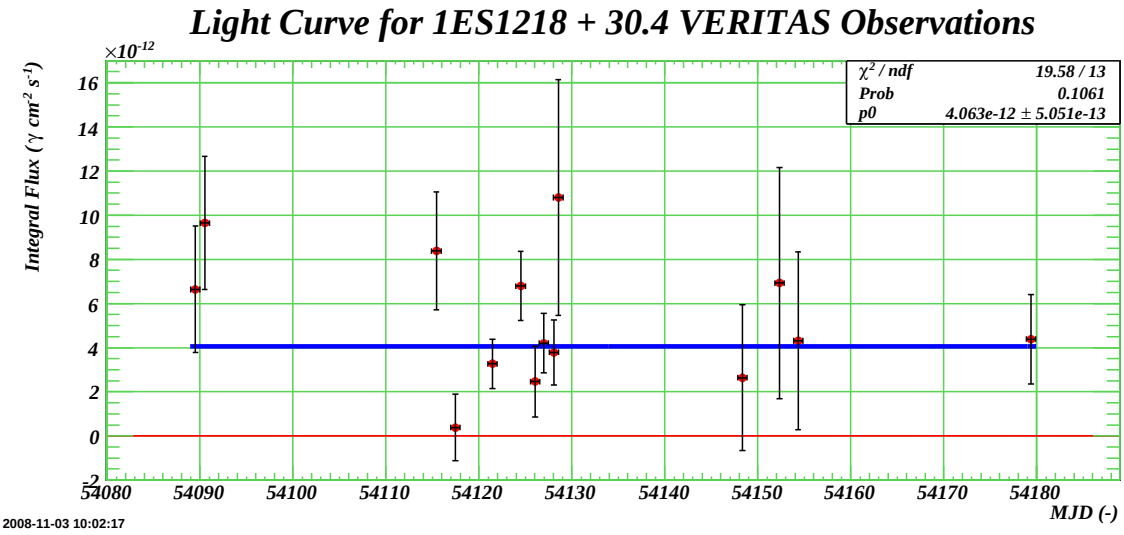

Figure 7.13: Light curve for 1ES 1218 + 30.4 VERITAS observations. The daily fluxes are shown for $E > 350\,\mathrm{GeV}$. The data are consistent with a steady emission rate.

code is limited by the facts that only one default noise level is assumed and that only the average zenith angle in each bin is used when accessing the effective area file. This might have some small effects (maybe more for the nights where there were various runs attempted), but overall the results seem good; in particular, a fit to a constant indicates a mean flux above 350 GeV of $(4.1 \pm 0.5) \times 10^{-12} \gamma/(\mathrm{cm}^2\,\mathrm{s})$, in agreement with the integral flux derived above. None of the points deviates significantly from the fit. In consequence, no claim for variability can be made.

7.2 1ES 1218 + 30.4 and the Extragalactic Background Light

It is interesting, now that the observed spectrum of 1ES 1218 + 30.4 has been measured, to use it as a tool to address other physical questions. In chapter 3, it was inferred that there are two main possibilities. One of them is to assume a certain form for the spectral density of the extragalactic background light (EBL) and compute the attenuation that it creates. This allows one to recover the intrinsic spectrum of the source, which can be useful to study the emission mechanisms of blazars. The other possibility is, on the contrary, to assume a certain form for the intrinsic spectrum and

use it to help constrain the EBL density, which is not known with great precision. The two approaches have their supporters. The first one is attempted in [43]. Here, the second one is investigated. In order to do so, the innovative technique developed by Mazin and Raue in [64] is used; a program that replicates their algorithm was independently written by the author and applied to the spectral measurements of 1ES 1218 + 30.4 derived in section 7.1.3.

7.2.1 Algorithm and Implementation

As may be recalled from section 3.3 where the algorithm of Mazin and Raue was briefly outlined, the idea is to make use of the computing power of modern computers to calculate the intrinsic spectrum of a source for a large collection of EBL constructs that span the range of possibilities allowed by measurements and limits imposed by experiments not involving blazar observations. Each intrinsic spectrum obtained is examined and judged as being physically possible or impossible according to the current theoretical understanding of blazars. All EBL constructs that lead to an impossible intrinsic spectrum are rejected from the collection. The envelope of the remaining possibilities is interpreted as a new limit on the extragalactic background light density. Here, the details of the implementation of this scheme are discussed.

B-Splines Parameterization

The first step consists in building the collection of EBL constructs that will serve as testing probes. To do that, the current measurements and limits on the EBL density are used; these are shown in figure 7.14. A two-dimensional grid is then overlaid on this space. The grid's first point is at $\lambda = 0.1\,\mu\text{m}$ and the last point at $\lambda = 1000\,\mu\text{m}$; there are 16 points equally spaced in $\log(\lambda)$ [14]. In the other dimension, there are 12 points, from $\nu I_\nu = 0.1\,\text{nW}\,\text{m}^{-2}\,\text{sr}^{-1}$ to $\nu I_\nu = 100\,\text{nW}\,\text{m}^{-2}\,\text{sr}^{-1}$, also equally spaced in $\log(\nu I_\nu)$. Only the grid points that are roughly within the boundaries defined by the EBL limits are kept. An EBL construct is then built by selecting one point for

[14] Note that the spacing of the grid points was chosen such that the sharpest expected features in an EBL spectrum can be achieved by the constructs [64].

each x-position of the remaining part of the grid. The construct is completed by utilizing the selected points to parameterize a cubic spline, which is a smooth curve passing close to each of the selected points. The advantage of using splines rather than another kind of parameterization will become clear in the next section. A total of 8 064 000 different constructs can be made with the usable grid points shown in figure 7.14.

Explicitly, the splines are parameterized in the following way[15]. First a basis-spline, or **B-spline**, is defined on each interval of five consecutive grid points. Let us temporarily rescale the x-axis of such an interval i such that it spans the range $[0, 4]$ (thus, there are grid points at $x = 0, 1, 2, 3$ and 4). On this interval, the B-spline has the form

$$s_i(x) := \begin{cases} \frac{3}{8}x^2 - \frac{1}{8}x^3; & x \in [0, 2] \\ \frac{3}{8}(-x+4)^2 - \frac{1}{8}(-x+4)^3; & x \in [2, 4] \\ 0; & x \notin [0, 4]. \end{cases} \tag{7.7}$$

This looks like the shape of a Gaussian as can be seen in figure 7.14, but it does not have the same properties. Instead, notice that at each wavelength, there are three or four non-zero B-splines (three if the chosen wavelength is at the position of one of the grid points, four if it is in between two grid points). The sum of the B-splines at that wavelength is exactly 1.0 [16]. Therefore, the values of the B-splines at a particular wavelength can be used to form a parameterized curve $\nu I_\nu(\lambda)$ by serving as weights for the contributions of the selected grid points (control points) of a construct:

$$\nu I_\nu(\lambda) := \sum_{i=0}^{k-1} g_i s_i(\lambda), \tag{7.8}$$

where k is the number of control points and g_i is the y-value (in $\mathrm{nW\,m^{-2}\,sr^{-1}}$) of

[15] The author believes that the B-spline formula given in [64] is not the one actually used to generate their EBL constructs. All attempts at using it resulted in curves that did not agree with the ones presented in that paper. This is what motivates the use of the alternate B-spline formula derived by the author and used in this thesis; with the new parameterization, the curves agree almost perfectly.

[16] Actually this is not true for the wavelengths between the first and second leftmost points of the grid; $s_0(x)$ and $s_1(x)$ have been slightly modified on this interval to implement a special boundary condition in order to mimic the behaviour of the curves in [64].

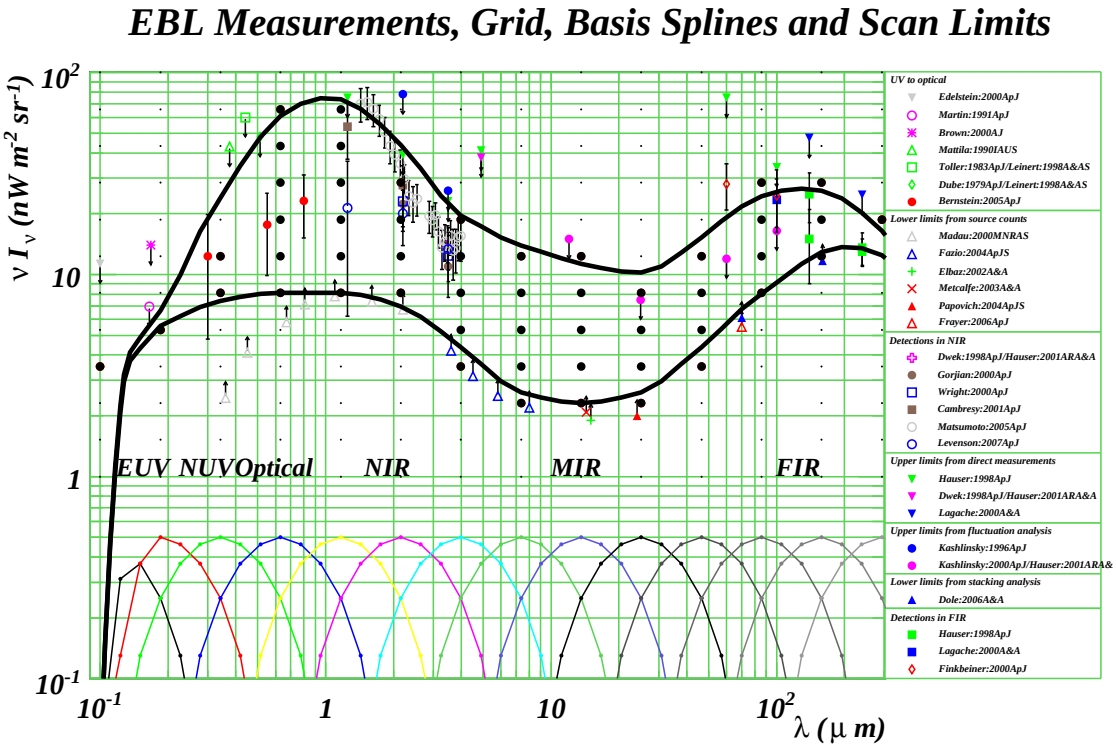

Figure 7.14: The elements necessary to implement a scan of EBL shapes using splines. The data points are EBL measurements and limits from non-blazar experiments. The grid is shown by black dots. The heavy black dots are the grid points that are selected to act as control points for the splines. The basis splines are shown as Gaussian-like functions in the lower part of the graph. The peak of a basis spline is located at a grid point's x-position and its width spans an interval equal to the distance between 5 consecutive grid points (although this cannot be seen here because of the log scale). The first two basis splines are truncated to implement a special boundary condition. When the spline parameterization is applied to the highest and lowest selected grid points in each column, the top and bottom thick black curves are obtained, respectively. These are the upper and lower limits of the scan. The references for the data points are as follow: Upper limits in the UV to optical: [191], [192], [193], [194], [195]-[196], [197]-[196]; Tentative detection in the UV to optical: [198]; Lower limits from source counts: [199], [200], [201], [202], [203], [204], [205]; Detections in the NIR: [206]-[54], [207], [208], [209], [210], [211]; Upper limits from direct measurements: [212], [206], [213]; Upper limits from fluctuation analysis: [214], [215]-[54]; Lower limits from stacking analysis in the FIR: [204]; Detections in the FIR: [212], [213], [216].

the i^{th} grid point in the construct. Note that the spline given by equation 7.8 does not necessarily pass directly through the selected grid points; it only passes relatively close to them, depending on what the neighbor control points are. This is a desirable feature since it makes the collection of EBL curves more diverse and realistic.

Intrinsic Spectrum Unfolding

With an EBL construct as given by equation 7.8, the associated intrinsic spectrum can be recovered by applying equation 3.5 in reverse, *i.e.* by removing the absorption from the left-hand side of the equation rather than applying it on the right-hand side. In section 3.1, where this equation was first introduced, the optical thickness was however given in a simplified version. Introducing more details in the calculation, and switching from energy to wavelength variables for the low-energy photon, equation 3.6 becomes [60]

$$\tau(E,z) = 10^{-15}\frac{4\pi}{hc^2}\int_0^z \left(\frac{dl}{dz^*}\right) dz^* \int_{-1}^{+1} d\mu \frac{1-\mu}{2} \int_0^{\lambda'_{\text{threshold}}} \nu I_\nu(\lambda')\,\sigma_{\gamma\gamma}(E',\lambda',\mu)\,d\lambda', \tag{7.9}$$

where the integral over distance has been replaced by an integral over redshift, the primed quantities are red-shifted values and the cross-section is no longer assumed to be pre-integrated over the different possible angles of interaction. In this equation, νI_ν has units of $\text{nW}\,\text{m}^{-2}\,\text{sr}^{-1}$, λ is in µm, $\sigma_{\gamma\gamma}$ is in m^2 and hc^2 is in $\text{J}\,\text{m}^2\,\text{s}^{-1}$; this explains the factor 1×10^{-15}. Note that $\lambda'_{\text{threshold}}$ depends on μ, where $\mu=\cos(\theta)$ and θ is the angle between the photons in the pair production interaction. This is why the μ integration is not performed in advance as was suggested in section 3.1, although it makes little difference in practice. The only assumption made in equation 7.9 is that **the evolution of EBL density with redshift can be ignored**, *i.e.* the difference between the background of photons seen today and that at the source redshift is negligible (νI_ν does not have an explicit dependence on z). This assumption is almost always made and was shown to be a very small effect, *e.g.* see [65].

The cross-section is computed from quantum electro-dynamics and is given by

[217]

$$\sigma_{\gamma\gamma}(E,\lambda,\mu) = \frac{3\sigma_{\mathrm{T}}}{16}(1-\beta^2)\left[2\beta(\beta^2-2)+(3-\beta^4)\ln\left(\frac{1+\beta}{1-\beta}\right)\right], \tag{7.10}$$

where $\beta := \sqrt{1-\frac{2\lambda m_{\mathrm{e}}^2 c^3}{Eh(1-\mu)}}$ and $\sigma_{\mathrm{T}} := 6.65\times10^{-29}\,\mathrm{m}^2$ is the Thomson cross-section.

The relation between distance and redshift is implemented by [218]

$$\left(\frac{dl}{dz}\right) = \frac{c}{H_0(1+z)\sqrt{(1+z)^2(\Omega_{\mathrm{m}}z+1)+z(2+z)\left[(1+z)^2\Omega_{\mathrm{r}}-\Omega_\Lambda\right]}}, \tag{7.11}$$

where $H_0 = 71.0\,\mathrm{km/(s\,Mpc)}$ is the Hubble constant, $\Omega_{\mathrm{m}} \approx 0.3, \Omega_{\mathrm{r}} \approx 0$ are the energy densities of matter and radiation normalized to the critical density of the universe, and $\Omega_\Lambda \approx 0.7$ is the dimensionless cosmological constant.

The triple integral of equation 7.9 needs to be performed for all the EBL constructs. This could take a considerably long time. However, the splines implementation of the EBL curves greatly simplifies the problem. In fact, substituting equation 7.8 in equation 7.9, one gets

$$\tau(E,z) \propto \int_0^z \left(\frac{dl}{dz^*}\right) dz^* \int_{-1}^{+1} d\mu \frac{1-\mu}{2} \int_0^{\lambda'_{\mathrm{threshold}}} \sum_{i=0}^{k-1} g_i s_i(\lambda')\,\sigma_{\gamma\gamma}(E',\lambda',\mu)\,d\lambda' \tag{7.12}$$

$$= \sum_{i=0}^{k-1} g_i \left[\int_0^z \left(\frac{dl}{dz^*}\right) dz^* \int_{-1}^{+1} d\mu \frac{1-\mu}{2} \int_0^{\lambda'_{\mathrm{threshold}}} s_i(\lambda')\,\sigma_{\gamma\gamma}(E',\lambda',\mu)\,d\lambda'\right] \tag{7.13}$$

The quantity within square brackets is the same for all EBL constructs since it depends not on the particular grid points chosen, but only on the the interaction cross-section and the basis splines, which are completely defined by the grid points spacings only. Figure 7.15 illustrates this. Hence, the advantage of using splines is that only k triple integrals need to be performed for each energy point, one for each basis spline that can be defined on the grid. These can be pre-calculated and saved. To get the opacity due to a particular EBL construct, all that is needed then is a simple sum of the control points' y-values, weighted by the pre-calculated integrals. This is much faster.

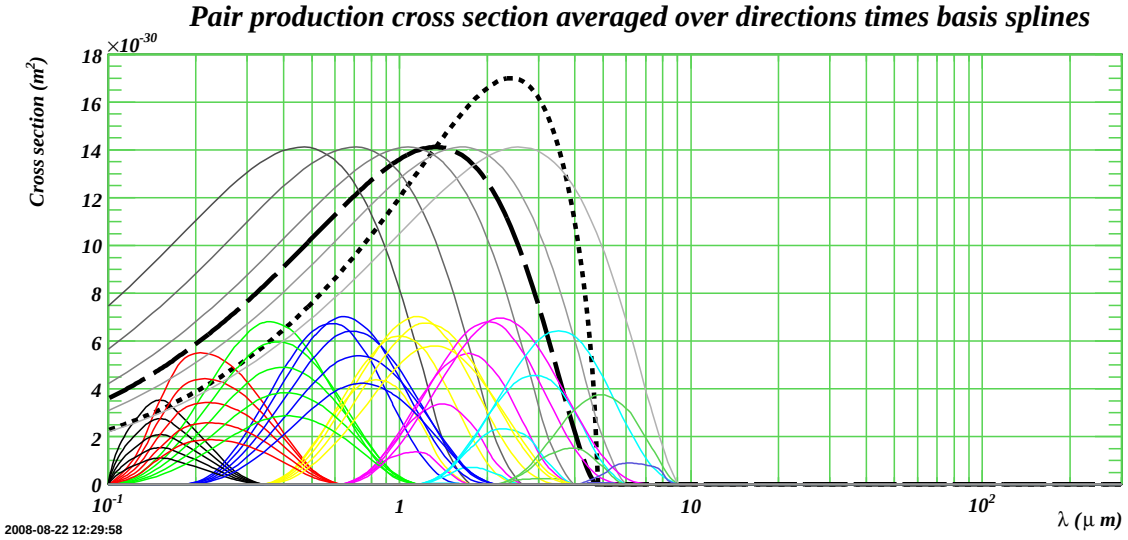

Figure 7.15: Pair production cross-section's effect on the B-splines. The integrand of equation 7.13 are the B-splines of figure 7.14 modulated by the interaction cross-section. Here, the thick dotted black line is the cross-section for a head-on collision with a 1 TeV photon. Temporarily omitting the redshift integral and performing the μ integral by inversing the order of integration, for illustration purposes only, one obtains the direction-averaged cross-section shown by the thick dashed curve. The thin curves with gray shadings are similarly obtained, but for the different energies of the points in the 1ES 1218 + 30.4 spectrum. The colored curves in the lower part are the B-Splines of figure 7.14 convolved with each different gray curve. The quantity in square brackets in equation 7.13 is then the integral of these colored curves, which can be computed without knowledge of the particular control points that are chosen during the scan. Another thing that this figure illustrates is that the last point in the 1ES 1218 + 30.4 spectrum can interact with low-energy photons with wavelengths up to 9 μm. Therefore, the limit on the EBL to be derived is not expected to constrain longer wavelengths.

Rejection Criterion

The intrinsic spectrum associated with each of the EBL shapes is then examined to decide if it is physically admissible or not. According to theory, there is a limit to how hard a spectrum can be. The hardness of a spectrum is judged by its photon index Γ. As mentioned in section 3.3, two limit cases are examined. The first one is $\Gamma_{\text{realistic}} = 1.5$ and is called the *realistic* case because it represents the ideas of mainstream theory [65]. The second one, the *extreme* case, is $\Gamma_{\text{extreme}} = 2/3$ and is explored because some alternate theories imply that the photon index can be lower than expected from conventional models, *e.g.* see [219]. Similarly, an exponential pile-up at high energies is also expected to be unphysical. Consequently, if an intrinsic spectrum is found to be harder than these limits imply, or to have part of its curve described by an exponential, then the EBL shape that is responsible for this inadmissible intrinsic spectrum is rejected from the set of EBL constructs. The limit on the EBL is constructed by looping over the surviving possibilities and keeping the highest density value at each wavelength. The logic behind this being that since all the EBL curves passing above this envelope were rejected, then it must be that the true EBL spectrum cannot pass above this limit.

Intrinsic Spectrum Parameterization

In order to quantify the shape of a spectrum, to assess if it is or not harder than the limits that were set, or if it presents an exponential behaviour, an analytical representation of it is desired. This is obtained by fitting one of the following functions:

$$\text{PL} \quad N_0 E^{-\Gamma}; \tag{7.14}$$

$$\text{BPL} \quad N_0 E^{-\Gamma} \left[1 + \left(\frac{E}{E_b}\right)^f\right]^{\frac{\Gamma_1-\Gamma_2}{f}}; \tag{7.15}$$

$$\text{BPLSE} \quad N_0 E^{-\Gamma} \left[1 + \left(\frac{E}{E_b}\right)^f\right]^{\frac{\Gamma_1-\Gamma_2}{f}} e^{\frac{E}{E_p}}; \tag{7.16}$$

$$\text{DBPL} \quad N_0 E^{-\Gamma} \left[1 + \left(\frac{E}{E_{b_1}}\right)^{f_1}\right]^{\frac{\Gamma_1-\Gamma_2}{f_1}} \left[1 + \left(\frac{E}{E_{b_2}}\right)^{f_2}\right]^{\frac{\Gamma_2-\Gamma_3}{f_2}}; \tag{7.17}$$

$$\text{DBPLSE} \qquad N_0 E^{-\Gamma} \left[1 + \left(\frac{E}{E_{b_1}}\right)^{f_1}\right]^{\frac{\Gamma_1-\Gamma_2}{f_1}} \left[1 + \left(\frac{E}{E_{b_2}}\right)^{f_2}\right]^{\frac{\Gamma_2-\Gamma_3}{f_2}} e^{\frac{E}{E_p}}; \quad (7.18)$$

where PL stands for Power Law, BPL for Broken Power Law, BPLSE for Broken Power Law with Super-Exponential pile-up, DBPL for Double Broken Power Law and DBPLSE for Double Broken Power Law with Super-Exponential pile-up. The photon indices are given by the Γ parameters, the positions of the breaks, by the E_b parameters and the start of a super-exponential pile-up region, by the E_p parameters. Note that there are transition regions to smooth the breaks when two power laws are joined; the intensity of the smoothing is governed by the f parameters.

Since it is on the basis of the analytical representation of an intrinsic spectrum that it is decided if the spectrum is physically admissible or not, a good fit is necessary to make a good judgment. Also, the simplest function that appropriately describes the data points should be preferred over more complex functions for the analysis to be as conservative as possible. These requirements are achieved by fitting the functions in order of complexity, which is the order in which they were presented here, and by asking that the probability of a fit be greater than 5%. The first function to attain this mark is then examined. If it does not lead to a rejection, then the next function is fitted to see if a significantly better description of the data can be attained by the more complex function. To make this objective, a likelihood ratio test is used to compare the fits [64]. If

$$\int_0^{\frac{\chi^2_A-\chi^2_B}{2}} PDF_{(\chi^2,\nu)} d\chi^2 \geq 0.95, \quad (7.19)$$

where $PDF_{(\chi^2,\nu)}$ is the probability density function of the χ^2 distribution with $\nu := \nu_A - \nu_B$ degrees of freedom, then the more complex fit function B is preferred over the fit A. This can only be achieved if fit B is obviously superior to fit A. If the more complex function is preferred, then it is this one that is evaluated for exclusion. Of course, depending on the number of points in a spectrum not all functions can be fitted. The requirement is that there be at least one more point in the spectra than there are parameters in the fitting function. For cases where the number of

parameters is only one too many to permit fitting, f is fixed to give the extra degree of freedom, since this is not a critical parameter.

The rejection of a curve then takes the following explicit form. If the preferred function is BPLSE or DBPLSE, then the intrinsic spectrum shows sign of a super exponential pile-up and so the EBL shape is excluded. If the preferred fit is from another one of the functions, then the photon indices Γ_i are each compared to the realistic and extreme limiting cases: if $\Gamma_i + \sigma_{(i,\mathrm{stat})} + \sigma_{\mathrm{sys.}} < \Gamma_{\mathrm{limit}}$, where $\sigma_{(i,\mathrm{stat})}$ and $\sigma_{\mathrm{sys.}}$ are the statistical and systematic uncertainties on the spectral slope, then the EBL shape is rejected. If no fit was a satisfactory description of the intrinsic spectrum, then the EBL construct is not rejected because it cannot be said with certainty that it leads to abnormal blazar spectra. Important in this technique is therefore to have reliable fits, with well estimated errors on the parameters. A non-reliable fit can lead to acceptance of a curve that would otherwise be rejected and can result in an EBL upper limit unnecessarily high. The analysis framework *ROOT 5.19c* was used to implement this analysis and perform the fitting (more reliable than in earlier versions). Despite the rapidity of *ROOT*'s routines and the time gain obtained with the spline implementation, the fitting still demands considerable time, especially for spectra having many points.

The confidence level associated with the limit is hard to state. As estimated in [64], it is likely to range from 68% to 95% because the EBL shapes are rejected based on their photon index with a $1\,\sigma$ criterion, while the likelihood ratio test to give preference to a more complex function has $2\,\sigma$ level requirement. The systematic uncertainties are associated to the grid setup (30%), evolution of the EBL (10%), the absolute energy scale for the blazar spectra (15% that leads to a 3% effect on the limit) and the numerical uncertainties (2%). Adding these contributions in quadrature yields a 32% total systematic uncertainty.

7.2.2 Limits on the Extragalactic Background Light

Applying this scheme to blazar data, limits on the EBL are now derived. First the 1ES 1218 + 30.4 spectrum measured earlier is analyzed, then the limit is comple-

mented by combining the results from the blazars that were found to be the most constraining in [64], namely 1ES 1101 - 23.2, H 1426 + 428 and Mrk 501. The spectra of these sources were shown earlier in figure 3.8 and their data points are obtained from [65], [220] and [221], respectively.

1ES 1218 + 30.4

In [64], the MAGIC collaboration's spectrum of 1ES 1218 + 30.4 was analyzed, resulting in a very low percentage of curves being rejected[17]. It is therefore interesting to see if the VERITAS spectrum of the same source can perform better, since it extends to higher energies. Note that because the spectrum derived in this work has only five points, $f \equiv 7.0$ is set in equation 7.15 to permit fitting with this function[18].

As examples of the computation, consider figures 7.16 and 7.17. The first figure shows a case where the intrinsic spectrum is unsatisfactorily fitted by the PL function (the fit probability is only 2.5%), so the BPL fit is invoked to give a better description of the data. Although the first photon index has a value of -1.4, its uncertainty is large (± 6.8). Therefore, the conditions for rejection are not met, for either the realistic or extreme cases, and the EBL shape that led to this spectrum is kept (the second index has a value of 1.9 and is not challenging the criteria). The final EBL limit will then necessarily be at least above this shape.

In the second example, the PL fit is acceptable, with a probability of 25%. The photon index is (0.30 ± 0.17) . Adding the systematic uncertainty of the fit (0.2), the condition for rejection is attained for the realistic case, but not for the extreme case. One therefore sees that the limit on the EBL will be set higher for the extreme case than for the realistic one.

At the end of the scan, 64% of the 8 064 000 curves were rejected in the realistic case and 30% in the extreme case. Only 251 EBL shapes resulted in an intrinsic

[17] The author confirmed that no limit on the EBL could be set with the MAGIC spectrum.

[18] $f \equiv 7.0$ was chosen because it allows the transition region between the two power laws to be of the order of the spacing between the spectrum points. Later, $f \equiv 4.0$, will be a more appropriate value for the case of H 1426 + 428 because of the larger spacings between the points.

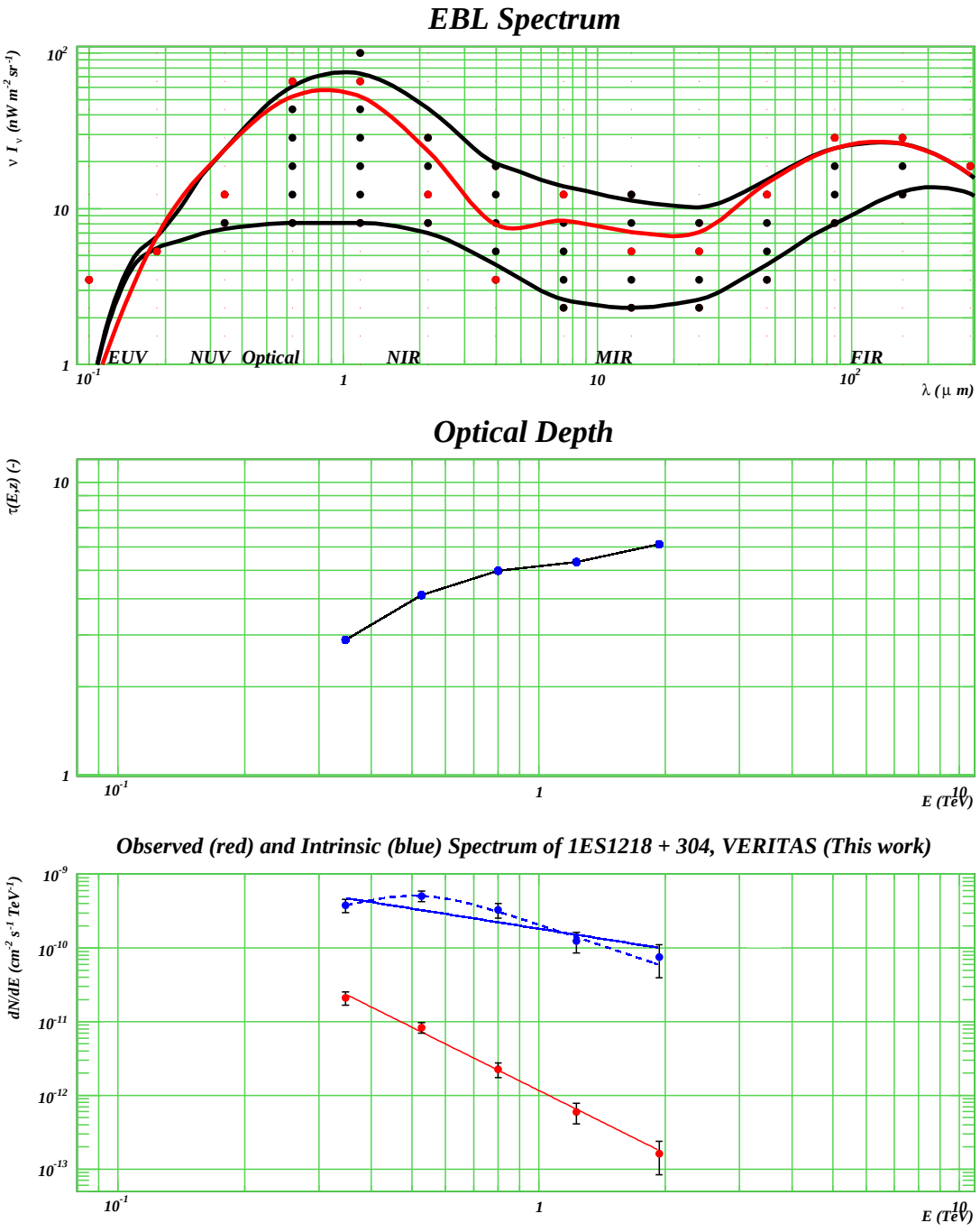

Figure 7.16: Example from the EBL scan, where the shape is not rejected. The top panel shows the particular EBL shape under investigation. The red dots are the control points and the red curve is the resulting spline. The black curves are the scan limits. The middle panel shows the optical thickness computed from equation 7.13. The bottom panel shows both the observed and intrinsic spectra. The intrinsic spectra is fitted by the PL (solid blue curve) and BPL functions (dashed blue curve). The latter one describes the data better with a 50% fit probability *vs* 2.5% for PL, which is insufficient. The shape is not rejected because of the large uncertainty on Γ_1 in equation 7.15.

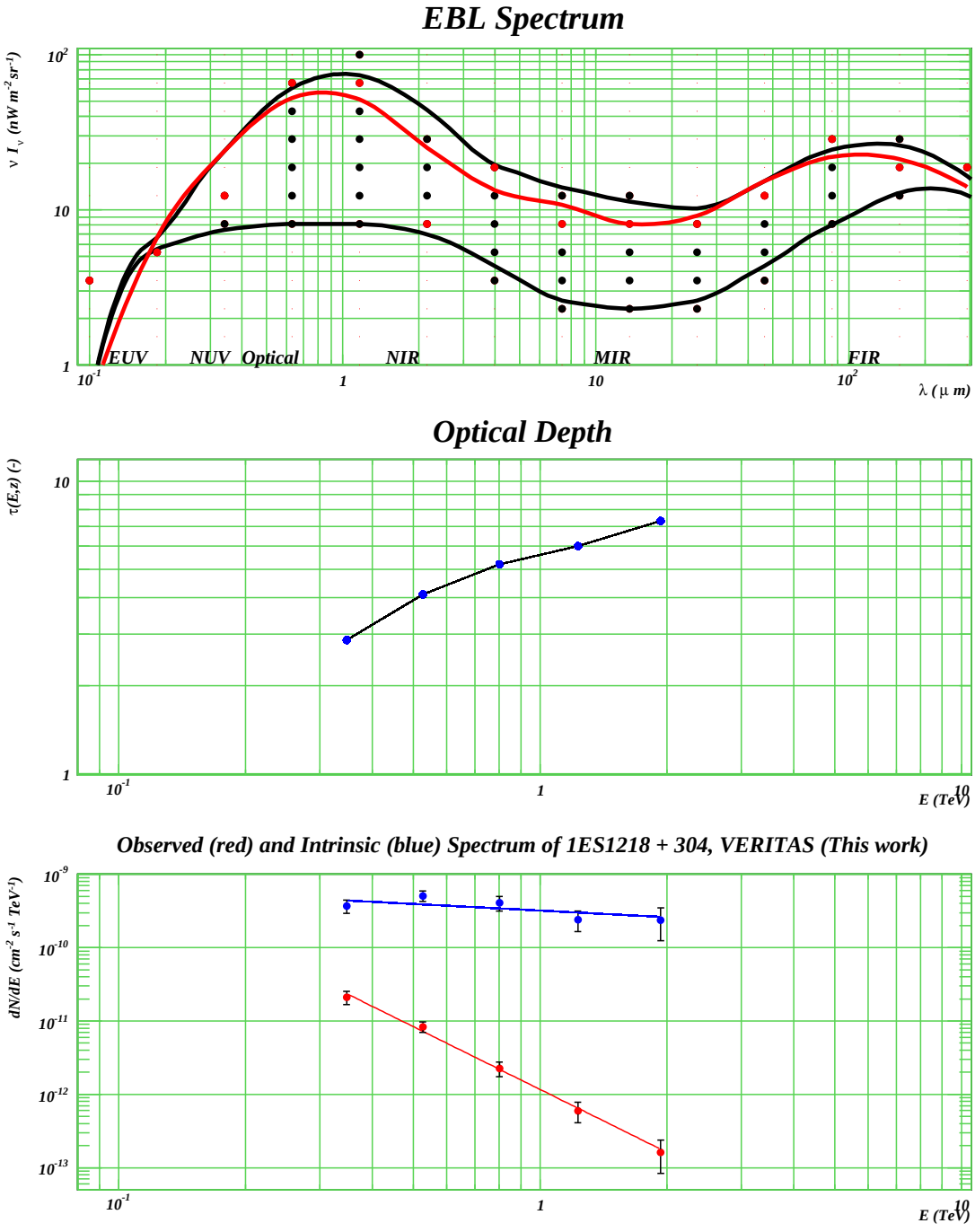

Figure 7.17: Example from the EBL scan, where the shape is rejected in the realistic case, but not in the extreme one. Refer to figure 7.16 for an explanation of the different panels. Here the PL fit is satisfactory and the BPL one cannot yield a significant improvement. The photon index is (0.30 ± 0.17), with a 0.2 systematic uncertainty.

spectrum that could not be appropriately fitted, but these did not have the consequence of altering the end results. Figure 7.18 shows the upper limit that can be set on the EBL (the permissible EBL spectrum lies below the green curves). Only the range of wavelengths over which the green curves are defined is being constrained. The limit for the realistic and extreme cases are almost the same, differing only at the longest wavelengths of the range. It is not a very strong constraint, but it is better than the null result obtained with the MAGIC spectrum. Interestingly, the exercise can be repeated with the spectrum obtained with *Event Display*. This gives greater arm leverage because of the additional points at low energy. Doing so results in the limits shown in figure 7.19. In this case, less EBL shapes were rejected (43% for the realistic case and 15% for the extreme case), perhaps because of the slightly larger error bars and the slightly lower maximal energy point. However, the realistic limit is pushed further down, probably because of the lower energy points of the spectrum. The extreme limit on the other hand becomes less constraining than before, most probably because of the larger error bars that render the PL fits more frequently satisfactory and easier to accept for the extreme case. Combining the MAGIC and VERITAS spectra together did not result in an improved limit because of the increased systematic uncertainties.

1ES 1101 - 23.2, H 1426 + 428 and Mrk 501

Now, the true power of the technique is revealed when the limits imposed by various blazars are combined. The individual results for 1ES 1101 - 23.2, H 1426 + 428 and Mrk 501 are presented in figure 7.20 (only the realistic case is shown for clarity) and the combined limit is formed in the next subsection.

The range of wavelengths constrained by 1ES 1101 - 23.2 is similar to that constrained by 1ES 1218 + 30.4. This could be expected, since the two spectra are similar and the sources are at almost the same redshift (0.186 for 1ES 1101 - 23.2 *vs* 0.182 for 1ES 1218 + 30.4). The higher precision on the 1ES 1101 - 23.2 points, and their greater number, makes the limit more constraining however. Surprisingly, less curves were rejected than for the case of 1ES 1218 + 30.4 with the *VEGAS* spectrum:

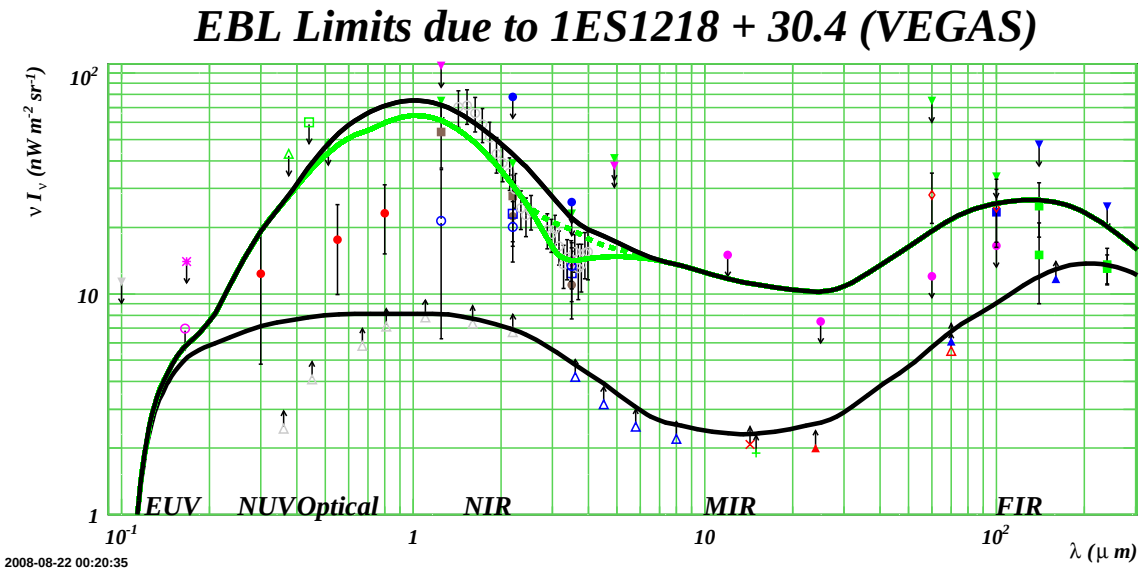

Figure 7.18: Limits on the EBL due to 1ES 1218 + 30.4 (spectrum from *VEGAS* analysis). The solid green curve shows the limit for the realistic case, while the dashed curve shows it for the extreme case. The permissible EBL spectrum lies below these curves.

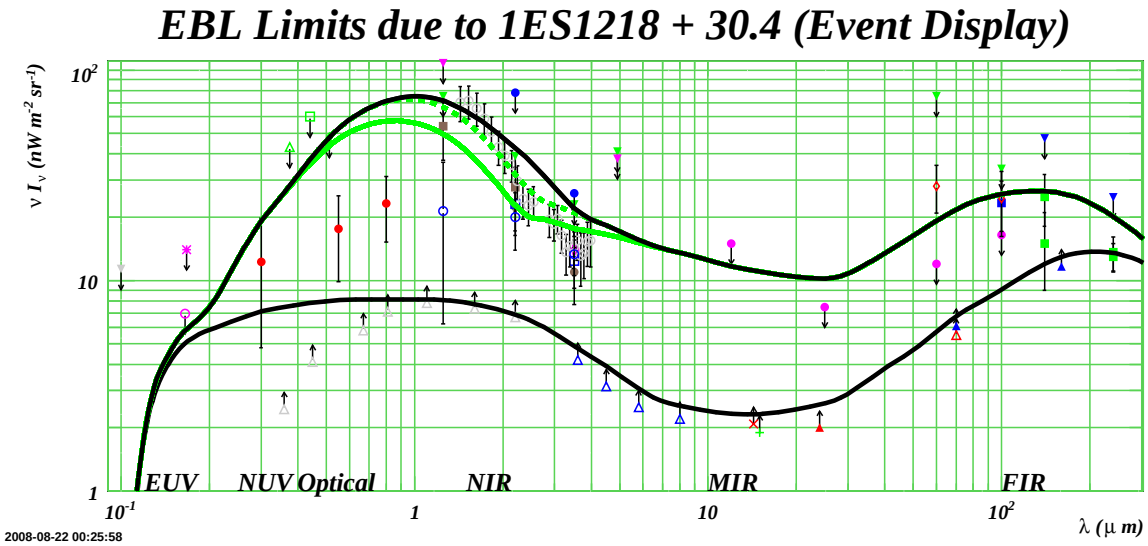

Figure 7.19: Limits on the EBL due to 1ES 1218 + 30.4 (spectrum from *Event Display* analysis). The solid green curve shows the limit for the realistic case, while the dashed curve shows it for the extreme case. The permissible EBL spectrum lies below these curves.

56% of the shapes were rejected for the realistic case and 24% for the extreme case and all of the spectra could be fitted.

For H 1426 + 428, the analysis resulted in a 58% rejection rate in the realistic case and 32% in the other case; only 134 intrinsic spectra could not be fitted. This blazar is less distant with a redshift of 0.129, but its spectrum has been measured up to 10 TeV. This means that it has the potential to constrain the EBL at longer wavelengths. This is the case; as can be seen in the figure the limit is imposed in the mid-infrared range. The limit is not very constraining, a result of the large error bar on the last point of this spectrum and the low number of points ($f \equiv 4.0$ was imposed to allow fitting with the BPL function).

Mrk 501, at a redshift of 0.034, is even closer to us, but its spectrum is very well measured and it extends to more than 20 TeV. This allows for probing the far-infrared range. Although the most EBL constructs were rejected in this analysis (70% for the realistic case and 66% for the extreme case), the limit imposed is barely constraining and almost coincides with the upper limit of the scan. Only 631 intrinsic spectra could not be fitted. But to obtain this, the error bars of the observed spectrum had to be scaled up by a factor 1.4, otherwise the fitter would return too many unreliable results.

Also shown in figure 7.20 are the limits derived in [64] for the same sources. The fact that mostly the same wavelength ranges are being constrained for the different cases indicates that the program is performing a sensible job. However, the limits derived in this thesis are more conservative. The source of this discrepancy is not clear. As stressed before, the quality of the imposed constraint is highly dependent on obtaining good fits with correctly evaluated uncertainties on the parameters. This proved to be difficult to obtain in some cases. The fits were sometimes returned with obviously too large uncertainties[19]. These led to acceptance of EBL shapes that should have been rejected. To err in this direction only makes the constraint

[19]Some experiments with having a criterion of goodness on parameter errors were attempted, but it did not result in significantly different results and the introduction of such criteria was questionable. It was preferred not to use this to avoid introducing unwanted biases.

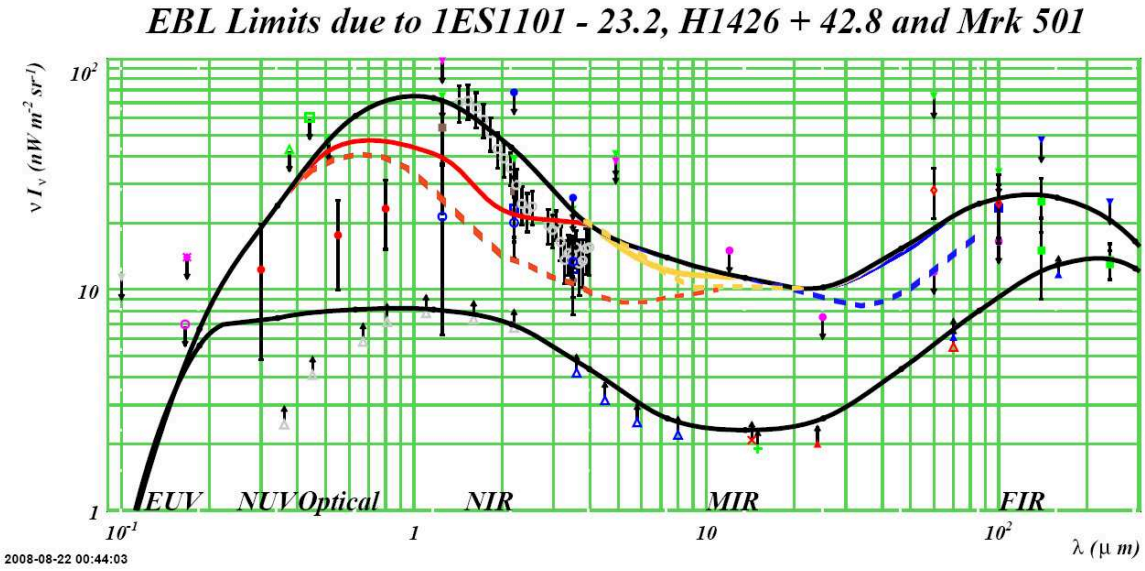

Figure 7.20: Limits on the EBL due to 1ES 1101 - 23.2 (red), H 1426 + 428 (orange) and Mrk 501 (blue). Only the realistic case is shown for clarity (similar conclusions hold for the extreme case). The solid curves are the limits derived in this work, while the dashed curves are the limits derived in [64] using a similar technique. The limits derived here are more conservative, but mostly on the same wavelength ranges.

more conservative, not more aggressive, so it does not invalidate the results presented here. Other possibilities are that the details of the intrinsic spectrum unfolding or of the spline implementations differ in the two cases[20]. Comparing the two programs more carefully in a longer study might reveal why the results obtained are not in closer agreement. Nonetheless, the results are sufficiently probing that it can be said with certainty that the 1ES 1218 + 30.4 VERITAS spectrum has an undeniable constraining power for the EBL, to a level close to that of 1ES 1101 - 23.2. More observations of 1ES 1218 + 30.4 could reduce the uncertainty in the spectrum and provide higher energy points. Improving the *VEGAS* analysis may also allow recovery of some of the low-energy points. This would contribute to increase the constraining power achievable with this rare high-redshift source (by TeV astronomy standards) observable from the northern hemisphere.

[20] This is not the preferred explanation of the author because comparison with some of the figures in [64] suggests that the intrinsic spectra are comparable.

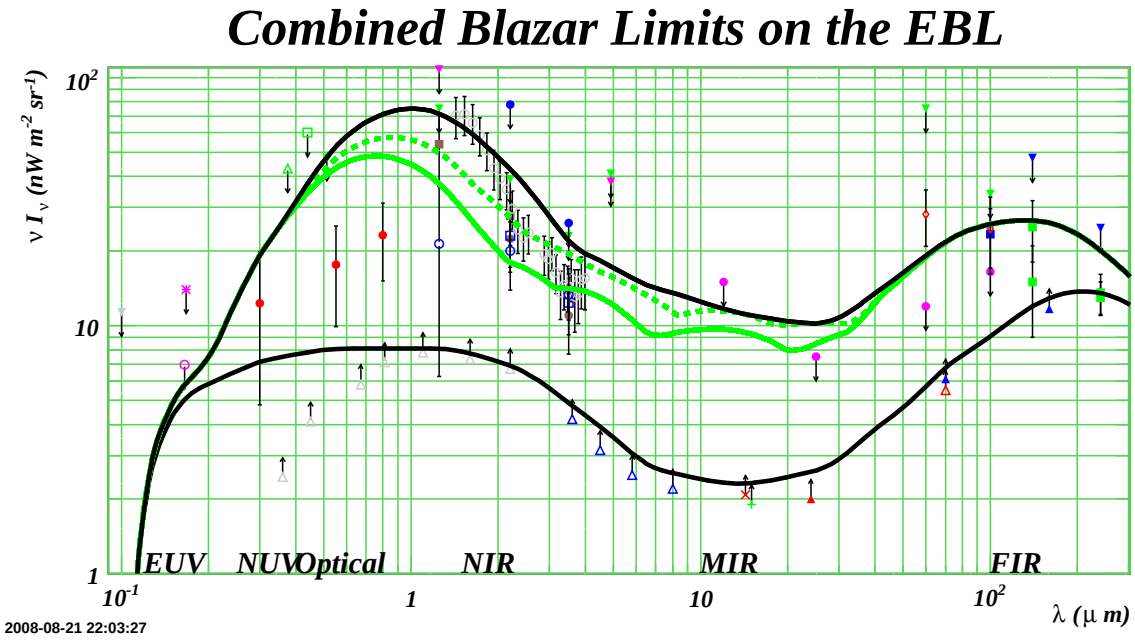

Figure 7.21: Combined blazar limits on the EBL. The spectra used are those of 1ES 1218 + 30.4 (from this work), 1ES 1101 - 23.2 [65], H 1426 + 428 [220] and Mrk 501 [221]. The solid green curve is for the realistic case and the dashed curve is for the extreme case.

Combined Limit

The combined limit is not just the juxtaposition of the different limits of figure 7.20. An EBL shape that survived the analysis for a particular blazar might be rejected for another one. Therefore, the total number of excluded shapes from all blazars must be used and the envelope of the surviving ones recomputed. Figure 7.21 shows the combined limit so obtained. For the realistic case, 96% of the EBL shapes are rejected and 85% for the extreme case. The limits are now clearly defined over a wide range of wavelengths. The EBL measurements in the near-infrared region, that were mentioned to be questionable in section 3.3, were only mildly challenged by the limits set by 1ES 1218 + 30.4 taken individually. In the combined limit this becomes a real challenge for the realistic case and a slightly less important one for the extreme case. In the near to mid-infrared range, the limit from blazars is lower than those set from direct measurements and fluctuation analysis. This shows the strength of the blazar approach in this region of the spectrum difficult to measure by other techniques.

Comparing the combined limits with that derived in [64] (figure 7.22), one of

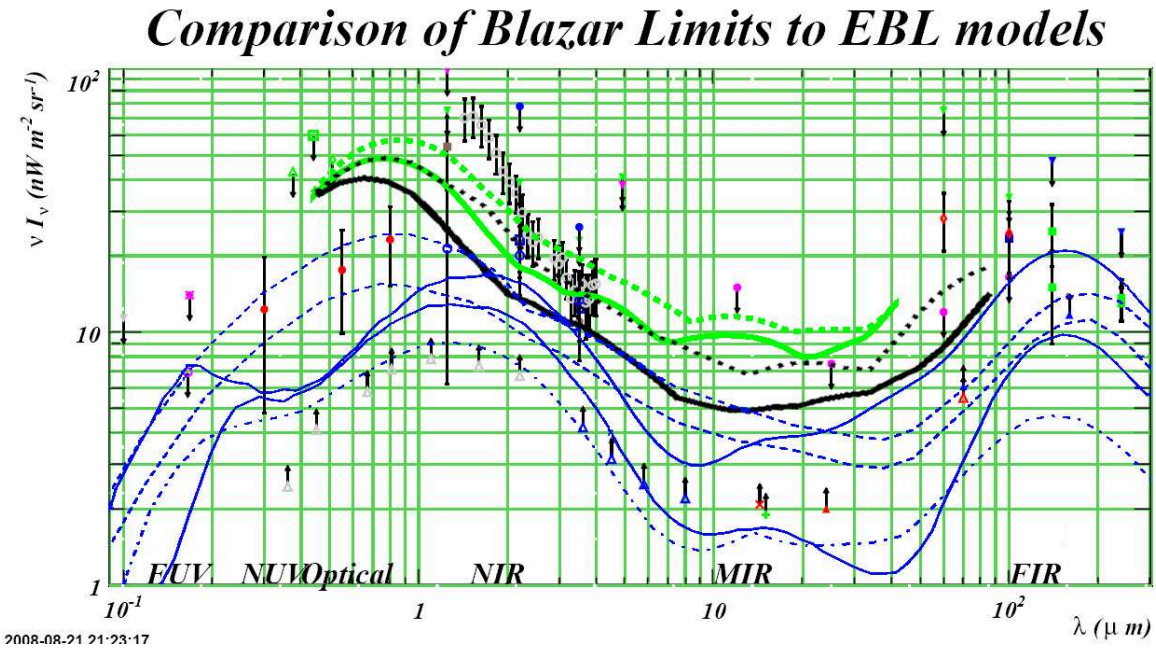

Figure 7.22: Comparison of blazar limits with models of the EBL. The green curves are the same as in figure 7.21 and the black curves are the corresponding limits derived in [64]. The blue curves are EBL models plotted from [64]. They are the updated high and low models of Kneiske (solid curve) [222], the fast and baseline evolution models of Stecker (dashed) [56], and the Primack model (dashed-dotted) [223].

course concludes again that a more conservative result is obtained here. The figure also shows comparisons with some of the most popular models for the EBL density. The derived limit is unable to favor one of them since they all remain unchallenged.

CONCLUSIONS

8

Conclusions

A lot of terrain has been covered throughout the development of this thesis. First the AGN phenomenon was described with emphasis on the blazar class and the possible mechanisms that can explain their γ-ray emission. The object central to this thesis, 1ES 1218 + 30.4, was then introduced by examining its emission properties at many wavelengths. Theoretical motivations for studying this object were given and the one concerning the absorption of its flux by the extragalactic background light was investigated in greater detail. Emphasis was put on the pair production process and on how the absorption factor is computed, on the different constituents of the EBL and on how blazar observations can help in constraining it in a region where it has proven difficult to be measured directly. In order to help in this regard, a way of detecting γ rays is needed. Therefore, various experiments designed to do so, by taking advantage of the different ways in which γ rays interact, were described in an order that naturally led to the imaging atmospheric Čerenkov technique that the VERITAS collaboration exploits. Every aspect of its apparatus was explained, from the reasons for the telescopes design to the electronic acquisition system. Observing and hardware monitoring strategies were also discussed. Then the details of the analysis procedure were presented in a way that progressively establishes the link between the FADC traces that are actually measured and the differential γ-ray flux that one ultimately wants to derive. The importance of the analysis cuts was highlighted and a search for their optimal value was undertaken. The analysis techniques were then applied to the VERITAS observations of 1ES 1218 + 30.4 to confirm its detection and evaluate its spectrum. The spectrum was finally used to impose a constraint on the EBL density

and in doing so accomplish the goal set by the theoretical motivations underlying this thesis.

Specifically, the major results obtained are

- a detection of 1ES 1218 + 30.4 at TeV energies with a significance of $13.48\,\sigma$ and a γ-ray detection rate of $(0.29 \pm 0.03)\,\gamma/\mathrm{min}$;
- a spectrum measurement of this source's emission having the form $(2.2{\pm}0.3_{\mathrm{stat.}}{\pm}0.4_{\mathrm{sys.}}){\times}10^{-12}\mathrm{cm}^{-2}\,\mathrm{s}^{-1}\,\mathrm{TeV}^{-1}(\frac{E}{0.8\,\mathrm{TeV}})^{-2.8\pm0.2_{\mathrm{stat.}}\pm0.2_{\mathrm{sys.}}}$ in the 350 GeV to 1.9 TeV energy range;
- an integral flux measurement $\Phi(E > 0.35\,\mathrm{TeV}) = (4.4 \pm 0.6) \times 10^{-12}\gamma/(\mathrm{cm}^2\,\mathrm{s})$;
- a light curve that is consistent with no variability in the observed flux;
- an upper limit on the EBL density in the optical to near-infrared wavelengths range, derived from the 1ES 1218 + 30.4 observations;
- an upper limit on the EBL density in the optical to far-infrared wavelengths range, derived from the spectra of four different blazars.

Even though the EBL unfolding code written for this work produced more conservative results than those presented in [64], the limits obtained still challenge the direct measurements of the EBL made in the near-infrared region and improve the limits from direct measurements and fluctuation analysis in the near to mid-infrared wavelengths range. In order to resolve the apparent discrepancy between the two implementations of the algorithm, closer comparisons at intermediate steps of the calculations would be required. It is also suggested to review the fitting procedure to improve the fit accuracy and robustness that seemed deficient in some cases. It might also be interesting to see if other analytical functions could result in an improved description of the data or in easier and more reliable fitting. A further improvement that could be made is to take into account the evolution of the EBL density with redshift, which was neglected here. Studies of the kind that was presented in [224] might help in doing that.

It may be recalled that the generation of these limits relied on the assumption that **there is a limit to the hardness of the intrinsic spectrum of a source**. Two cases were investigated, a realistic one where the limit on the photon index was set to 1.5 and an extreme one where the limit was set to 2/3. Recently, papers have been published that revisit this assumption and seem to imply that the intrinsic spectra of blazars might actually not be limited in the way previously thought [225], [71]. This could invalidate the results presented here and of other EBL studies made with the help of blazar spectra. Furthermore, the recent detection of the flat spectrum radio quasar 3C 279 at a redshift of 0.536 by the MAGIC collaboration [226] generated some debates within the community regarding the transparency of the Universe to TeV radiation, with people arriving at other possible explanations than a very low EBL density [227], [228], [229]. All this shows that the problem of constraining the EBL density remains a difficult one.

Future research focused on understanding better the emission from blazars should help in our ability to draw stronger conclusions. In this respect, multi-wavelength observation efforts are encouraged since they seem to be the key to understand the complex objects that are blazars. Data from the recently launched GLAST satellite are also greatly awaited since it will help increase the wavelength coverage. On the VERITAS side, things that could improve the experiment include implementing a better procedure for aligning the mirror facets (this will improve the point-spread functions, which will allow for better background rejection and a lower energy threshold), using photomultiplier tubes with a higher quantum efficiency (this has an effect similar to increasing the mirror area and helps lower the energy threshold and improves the sensitivity), increasing the field of view, or even adding telescopes to the array, with possibly larger size reflectors. Of course, the few known problems with the analysis procedure also need to be resolved, but work is already being made in this direction and more robust results should be available soon.

APPENDICES

A

VERITAS Specifications

Array:

FLWO location 31°40′30.21″ N, 110°57′07.77″ W (Southern Arizona, USA)
Number of telescopes 4
Pattern Four-sided shape with sides of lengths 85 m, 35 m, 85 m and 109 m
Altitude 1275 m

Reflector:

Type Composite
Shape Spherical
Design Davies-Cotton
Diameter 12 m
Curvature radius 12 m
Focal length 12 m
Alignment position 24 m
Alignment dispersion 0.5 cm
F number 1.0

Number of facets 345
Shape of facets Hexagonal
Material of facets Glass, front anodized aluminum
Thickness of facets (11.5 ± 1.0) mm
Diameter of facets (60.96 ± 0.3) cm
Curvature radius of facets (23.97 ± 0.01) m
Focal length of facets 12 m
Focal length dispersion of facets 8.6 cm
Area of facets 0.322 m^2
Thickness of aluminum layer 180 nm
Thickness of anodized layer 80 nm
Reflectivity $\geq 85\,\%$ in the 280-450 nm range, $\geq 90\,\%$ at 320 nm
Reflectivity loss 3 % per year at 320 nm
Spot size of facets (diameter of circle containing 90% of light) (6.0 ± 0.5) mm

Area of reflector $\sim 110\,m^2$
Point Spread Function 0.06 °, at 70 ° elevation with bias alignment

Camera:

Number of pixels 499
Field of view diameter 3.5 °
Number of current monitor boards 16

photomultiplier tubes:

Brand Photonis XP2970/02
Tube diameter 29 mm
Peak quantum efficiency at 420 nm
Number of stages 10
Maximum supply voltage 1800 V
Temperature range −30 °C to 50 °C
Typical voltage 850 V
Typical gain 2×10^5
Typical anode current 3-6 μA for dark to bright fields of view
Dynamic range of current monitor 0-127 μA
Plate-Scale 0.148 °/PMT
Pre-amplifier gain 6.6
Pre-amplifier current to voltage conversion 500 Ω

Light Cones:

Type Hybrid hexagonal entrance to Winston cone exit
Increase in light collection efficiency ∼ 30%
Camera dead-space with cones 25 %
Reflectivity > 85 % above 260 nm

Electronics:

Number of channels per telescope 500
Trigger level 1 CFD at each channel at the 6-7 photoelectrons level for single telescope operation, 4-5 photoelectrons for stereo.
Trigger level 2 Pattern detection of any coincidence of three neighboring pixels
Trigger level 3 Array trigger
Coincidence L2 window ∼ 5 ns
Coincidence L3 window ∼ 100 ns
Number of bits 8
Rate 500 MHz
Number of samples per event 24
Event size 13.5 kb
Telescope readout time ∼ 400 μs
Dead time at nominal single telescope trigger rate 10%
Nominal single telescope trigger rate 150 Hz
Cable Loss 0.75
FADC conversion 256 counts per 2 V
FADC gain 7.26
Memory 32 μs
QI frequency range 1 Hz - 1 MHz

QI pulse height range 85 dB
QI pulse width range 1 ns - 10 ms

Tracking System:

Mount Altitude-over-Azimuth
Slew rate 1 °/s
Tracking error $< 0.01\,^\circ$

VERITAS Member Institutions:

Smithsonian Astrophysical Observatory
Purdue University
Iowa State University
Washington University in St. Louis
University of Chicago
University of Utah
University of California, Los Angeles
McGill University
University College Dublin
University of Leeds
Adler Planetarium
Argonne National Lab
Barnard College
DePauw University
Grinnell College
University of California, Santa Cruz
University of Iowa
University of Massachussetts
Cork Institute of Technology
Galway-Mayo Institute of Technology
National University of Ireland, Galway
$\sim$ 20 Associate Members

Other:

Energy range 100 GeV - 50 TeV
Effective Area at 1 TeV $> 1\times10^5\,\mathrm{m}^2$
Crab Nebula detection rate $\sim 7\,\gamma/\mathrm{min}$
Angular Resolution to γ rays $0.15\,^\circ$
Core Location Resolution $\sim 7.5\,\mathrm{m}$
Analysis Energy Threshold is about 150 GeV for observations near the zenith. It increases to 300 GeV at 40 ° zenith angle.

B

Run List for 1ES 1218 + 30.4 Observations

Run	**Date**	$\mathbf{L_{T1-T2}}$	$\mathbf{L_{T3}}$	**W.**	**Wob.**	**L3**	θ_{Zn}	**Sig.**	**Rate**
(#)	(yyyymmdd)	(#)	(#)	(-)	(°)	**(Hz)**	(°)	(σ)	**(γ/min)**
*32992	20061220	32967	32967	A	0.3 S	164	29.6	2.30	0.44 ± 0.22
32993	20061220	32967	32967	A	0.3 W	168	24.2	1.35	0.29 ± 0.23
32994	20061220	32967	32967	A	0.3 N	172	19.9	2.21	0.49 ± 0.25
32995	20061220	32967	32967	A	0.3 E	173	15.6	2.23	0.53 ± 0.26
33026	20061221	32996	32996	A	0.3 N	165	25.8	3.66	0.91 ± 0.29
*33027	20061221	32996	32996	A	0.3 S	167	21.3	0.09	0.02 ± 0.21
33028	20061221	32996	32996	A	0.3 W	170	16.3	3.12	0.73 ± 0.27
33029	20061221	32996	32996	A	0.3 E	171	12.0	1.51	0.31 ± 0.22
33386	20070115	33369	33369	A	0.5 N	172	31.9	1.19	0.20 ± 0.19
*33387	20070115	33369	33369	A	0.5 S	176	27.5	3.36	0.61 ± 0.23
33388	20070115	33369	33369	A	0.5 E	179	23.3	2.15	0.39 ± 0.22
33389	20070115	33369	33369	A	0.5 W	180	17.8	1.10	0.20 ± 0.20
33453	20070117	33441	33401	A	0.5 W	172	20.7	0.68	0.11 ± 0.18
33454	20070117	33441	33401	A	0.5 E	172	17.1	2.37	0.44 ± 0.22
33456	20070117	33441	33401	A	0.5 N	176	5.9	1.31	0.22 ± 0.19
*33458	20070117	33441	33401	A	0.5 S	173	2.4	0.23	0.04 ± 0.16

Table B.1: 1ES 1218 + 30.4 run list. The column headers are the run number, the date, the laser file used to calibrate T1 and T2, the laser file used to calibrate T3, the weather grade, the wobble offset, the L3 rate, the zenith angle, the significance and the detection rate. Runs marked by an asterisk are used in the search for a signal from W Comae. All runs have a 20 min duration, except 33575 and 33576, which are 10 min long. The cuts of table 7.1 are used for the significances and rates quoted.

Run	**Date**	$\mathbf{L_{T1-T2}}$	$\mathbf{L_{T3}}$	**W.**	**Wob.**	**L3**	θ_{Zn}	**Sig.**	**Rate**
(#)	(yyyymmdd)	(#)	(#)	(-)	(°)	**(Hz)**	(°)	(σ)	**(γ/min)**
*33517	20070121	33515	33401	B-	0.5 S	157	33.9	3.06	0.51 ± 0.21
33518	20070121	33515	33401	B	0.5 N	164	29.0	3.36	0.61 ± 0.23
33519	20070121	33515	33401	B	0.5 E	169	25.0	1.70	0.28 ± 0.19
33520	20070121	33515	33401	B	0.5 W	173	19.4	0.76	0.13 ± 0.19
33521	20070121	33515	33401	A-	0.5 N	175	15.1	0.19	0.04 ± 0.19
*33522	20070121	33515	33401	A-	0.5 S	176	10.7	3.02	0.61 ± 0.25
33524	20070121	33515	33401	A-	0.5 E	177	3.0	0.80	0.13 ± 0.18
33525	20070121	33515	33401	B	0.5 W	174	3.7	1.90	0.32 ± 0.20
33526	20070121	33515	33401	B	0.5 N	175	7.6	0.79	0.14 ± 0.19
*33528	20070121	33515	33401	B	0.5 S	173	14.8	1.57	0.26 ± 0.19
33569	20070124	33562	33401	A-	0.5 W	181	10.4	2.71	0.54 ± 0.24
33570	20070124	33562	33401	A-	0.5 E	181	6.5	1.72	0.31 ± 0.21
*33571	20070124	33562	33401	A-	0.5 S	178	2.6	1.19	0.20 ± 0.19
33572	20070124	33562	33401	A-	0.5 N	176	3.6	1.52	0.27 ± 0.20
33573	20070124	33562	33401	A-	0.5 E	176	8.9	1.64	0.29 ± 0.20
33574	20070124	33562	33401	A-	0.5 W	175	14.4	1.16	0.20 ± 0.19
33575	20070124	33562	33401	A-	0.5 N	175	17.4	1.64	0.43 ± 0.32
*33576	20070124	33562	33401	A-	0.5 S	172	20.0	1.51	0.37 ± 0.29
33605	20070125	33595	33401	A-	0.5 N	181	6.9	0.52	0.08 ± 0.16
*33606	20070125	33595	33401	A-	0.5 S	180	3.1	2.45	0.42 ± 0.21
33620	20070126	33616	33401	B+	0.5 E	178	21.0	0.55	0.10 ± 0.20
33621	20070126	33616	33401	B+	0.5 W	180	15.4	-0.19	-0.03 ± 0.15
*33622	20070126	33616	33401	B+	0.5 S	181	11.5	1.76	0.32 ± 0.21
33623	20070126	33616	33401	B+	0.5 N	181	6.7	2.49	0.46 ± 0.22

Table B.2: 1ES 1218 + 30.4 run list (continued).

Run	**Date**	$\mathbf{L_{T1-T2}}$	$\mathbf{L_{T3}}$	**W.**	**Wob.**	**L3**	θ_{Zn}	**Sig.**	**Rate**
(#)	(yyyymmdd)	(#)	(#)	(-)	(°)	**(Hz)**	(°)	(σ)	**(γ/min)**
33625	20070126	33616	33401	B	0.5 W	176	3.3	1.87	0.31 ± 0.19
33626	20070126	33616	33401	B	0.5 E	178	6.6	0.40	0.07 ± 0.17
33627	20070126	33616	33401	B	0.5 N	175	11.6	0.91	0.16 ± 0.19
*33628	20070126	33616	33401	B	0.5 S	176	17.7	3.34	0.59 ± 0.23
33632	20070127	33636	33401	A	0.5 E	182	19.1	2.32	0.42 ± 0.22
33633	20070127	33636	33401	A	0.5 W	182	13.5	-0.32	-0.05 ± 0.16
*33634	20070127	33636	33401	A	0.5 S	181	9.5	3.13	0.59 ± 0.24
33635	20070127	33636	33401	A	0.5 N	182	4.7	-0.27	-0.05 ± 0.17
33638	20070127	33636	33401	A	0.5 N	179	2.8	0.52	0.08 ± 0.17
*33640	20070127	33636	33401	A	0.5 S	179	11.5	2.89	0.51 ± 0.22
33641	20070127	33636	33401	A	0.5 E	177	15.6	0.37	0.06 ± 0.17
33642	20070127	33636	33401	A	0.5 W	174	21.2	3.64	0.74 ± 0.26
33645	20070128	33651	33401	A	0.5 W	185	5.8	1.88	0.34 ± 0.21
33646	20070128	33651	33401	A	0.5 E	183	2.6	1.70	0.28 ± 0.19
33647	20070128	33651	33401	A	0.5 N	178	3.9	0.99	0.17 ± 0.19
*33648	20070128	33651	33401	A	0.5 S	174	8.8	1.88	0.34 ± 0.21
33650	20070128	33651	33401	A	0.5 W	174	19.7	0.26	0.05 ± 0.19
*33897	20070217	33894	33993	A	0.5 S	169	25.4	1.32	0.23 ± 0.19
33898	20070217	33894	33993	A	0.5 E	170	21.2	0.93	0.17 ± 0.20
33958	20070221	none	none	A	0.5 W	165	21.7	0.18	0.03 ± 0.17
34010	20070223	34019	34019	A	0.5 N	164	20.2	1.27	0.21 ± 0.19
34444	20070320	34432	34432	A-	0.5 N	168	5.0	0.87	0.15 ± 0.19
34446	20070320	34432	34432	A-	0.5 E	164	13.7	0.92	0.15 ± 0.18
34447	20070320	34432	34432	A	0.5 W	160	19.3	1.24	0.22 ± 0.19

Table B.3: 1ES 1218 + 30.4 run list (continued).

C

Night-Sky Background at VERITAS Sites

C.1 The Night-Sky Background

As with other types of astronomy, the **night-sky background**, *i.e.* the background light in the night sky which is due to unresolved stars and galaxies, zodiacal light, airglow, auroras, light pollution, etc. (see table C.1 and [230] for a discussion of the night-sky background), is a determining factor in the choice of the site where telescopes are to be installed. As it is remarked in [6], it is possible to reduce the background light up to a limiting natural level dominated by starlight and airglow by appropriate choice of observing site (far from the poles and from manmade activities) and observing times (clear moonless nights). Although it is fairly easy to choose the observing times, it is less trivial to choose an observing site. Undoubtedly, many different factors, other than the level of the night-sky background, enter the choice for an appropriate site: access, facilities, budget, etc. Still, measures of the night-sky background are required to help in the decision. Other than site selection, a good knowledge of the night-sky background is useful in understanding the VERITAS experiment. In fact, the presence of background light reaching the photomultiplier tubes of the telescopes cameras not only blurs the images, but also induces a DC current that can shorten their lifetime and it also affects the threshold at which the experiment can operate. A knowledge of the night-sky background may help in understanding and overcoming these limitations by suggesting the use of light cones, for example, to limit the field of view of the photomultiplier tubes and hence the amount of sky noise they can see. An understanding that the night-sky background varies during the night also leads to the use of padding techniques to make sure

the amount of sky noise is the same between ON and OFF runs. The night-sky background level also serves as an input in simulations of the experiment and is thus a very important parameter because it defines the baseline against which signals are compared in the search for a reliable detection of Čerenkov light from extensive air showers.

Although the night-sky background level might be available from external sources, it is preferable to make our own measurements because the result will be more suited to the use of an atmospheric Čerenkov telescope. Moreover, by using the same instrument at various sites, we ensure that the results are directly comparable and that any systematic effects, if present, will be the same in all data sets.

This report presents results obtained from measurements of the night-sky background at different sites considered for the VERITAS experiment. The work presented here is mostly based on [231], which describes the night-sky background measurements performed by the H.E.S.S. collaboration, and on [232], which describes the construction of an instrument similar to the one that the H.E.S.S. team used. After an introduction to the experiment's method and a characterization of the instrument, comparison measurements of the night-sky background between various sites are given.

C.2 Instrument

The photon flux at a certain wavelength, or **differential photon flux**, is defined as

$$\phi(\lambda) := \frac{dN}{dA\, d\Omega\, dt\, d\lambda}, \tag{C.1}$$

i.e. the number of photons N per unit area A, solid angle Ω, time t and wavelength λ. Of course any real instrument will measure only intervals of wavelengths, so the output from such an instrument will be given by the integral, over the wavelength window, of the differential photon flux admitted in the instrument through its area and solid angle $A_{\text{eff}}\Omega_{\text{eff}}$, reduced by its transmission $T(\lambda)$ and photon counting efficiency $\varepsilon_{\text{PMT}}(\lambda)$ characteristics at the relevant wavelengths. In practice, an instrument will need to

Component	**Source**	**Coordinate system**	**Intensity (S_{10})**	**Timescale**
Night Airglow	Excitation of upper-atmosphere atoms and molecules. OH (381.7-4470.2 nm), O_2 (260-380 nm), NO_2 (500 650 nm continuum), O (557.7, 630, 636.4 nm), Na (589, 589.6 nm), N (519.8, 520.1 nm)	Horizon (Z, A)	50	Few minutes - few hours; Seasonal; Solar activity
Zodiacal light	Sunlight scattering by interplanetary dust particles. Thermal emission from these particles	Ecliptic $(\beta, \lambda - \lambda_\odot)$	117	Seasonal
Integrated starlight (Mag. 5 to infinity)	Combined unresolved stars of our Galaxy	Galactic (b, l)	28	Earth's rotation
Diffuse galactic light	Scattered light from interstellar dust particles	Galactic (b, l)	9	Earth's rotation
Extragalactic light	Redshifted photons from unresolved galaxies. Scattered light from dust in the intergalactic space	Isotropic	0.9	
Aurora	Excitation of upper-atmosphere atoms and molecules by energetic particles. O (557.7, 630nm), N (475 nm).	Local	$>$ Night airglow	Seasonal; Solar cycle; Magnetic activity
Light Pollution	Urban lighting scattered by the troposphere. Mercury and Sodium lamps.	Local	Depends	Seasonal

Table C.1: The different components contributing to the night-sky background light.

amplify the signal by a gain G and convert it to charge so that a current I_{sky} can be measured. In equation,

$$I_{\text{sky}} = e^{-} G \int_{\lambda - d\lambda}^{\lambda + d\lambda} \varepsilon_{\text{PMT}}(\lambda') T(\lambda') A_{\text{eff}} \Omega_{\text{eff}} \phi(\lambda')\, d\lambda'. \tag{C.2}$$

If the wavelength window is sufficiently small, we can assume that $\phi(\lambda')$ **is approximately constant** and pull it out of the integral, such that we can deduce it from the output current and known characteristics of the instrument using the following formula:

$$\boxed{\phi(\lambda) = \frac{I_{\text{sky+dark}} - I_{\text{dark}}}{e^{-} G\, A_{\text{eff}} \Omega_{\text{eff}} \int_{\lambda - d\lambda}^{\lambda + d\lambda} T(\lambda') \varepsilon_{\text{PMT}}(\lambda')\, d\lambda'}}, \tag{C.3}$$

with the understanding that $I_{\text{sky}} = I_{\text{sky+dark}} - I_{\text{dark}}$, *i.e.* the effect of dark currents in the instrument are subtracted from the output to get only the signal from the sky.

Now, let us define the **integral photon flux** over a large wavelength window as

$$\phi := \int_{\lambda_1}^{\lambda_2} \phi(\lambda')\, d\lambda' = \frac{dN}{dA\, d\Omega\, dt}, \tag{C.4}$$

and assume there is no mechanism selecting a particular wavelength in the instrument such that the **transmission of the instrument is unity in this window**, then

$$\boxed{\phi = \frac{I_{\text{sky+dark}} - I_{\text{dark}}}{e^{-} G\, A_{\text{eff}} \Omega_{\text{eff}} \int_{\lambda_1}^{\lambda_2} \frac{\phi(\lambda')}{\phi} \varepsilon_{\text{PMT}}(\lambda')\, d\lambda'}}, \tag{C.5}$$

where $\phi(\lambda')$ could no longer be taken as constant over this wider window. It may seem bizarre that the quantity ϕ we are looking for is included in the denominator in the right hand side of the equation, but what one truly needs is the quantity $S(\lambda) := \frac{\phi(\lambda')}{\phi}$, which is the shape of the spectrum, and is measurable without an explicit, *a priori*, knowledge of ϕ.

An instrument, similar to the one described in [231], built at McGill University[1], fulfills the requirements needed to measure the differential and integral photon fluxes from the night-sky background. Figure C.1 shows a schematic of the instrument. It

[1] Design and construction by Jean-Phillipe Gagnon [232], a former master's student at McGill University.

consists of a magnetically shielded photomultiplier tube that is exposed to the night-sky background through a long baffled tube, which defines the area and solid angle. The baffles are placed such as to reduce reflections inside the instrument. A filter wheel, comprising 8 different filters, can be placed in the light path to measure the differential photon flux. The photomultiplier tube is biased by a high voltage supply at -1700 V, and the output current is read off a picoammeter, with dark current readings typically around 1 nA and sky readings of a few nA.

Although a computerized acquisition system was built to take the measurements, no such device was used for the results presented here because of the difficulties involved in transporting the system at different sites.

C.2.1 Quantum Efficiency

Although it would have been preferable to use the exact same photomultiplier tube in the night-sky background instrument as those that are used in the VERITAS experiment, the photomultiplier tube used is of the kind being used at the STACEE experiment, *i.e.* it is a Photonis XP2282B. This choice comes from the original purpose of the apparatus, which was to be used primarily at the STACEE site, and from the availability of these tubes at McGill University. The main characteristics of this tube are given in table C.2. The **quantum efficiency**, *i.e.* the probability with which a photon of a certain wavelength produces a photoelectron, was not directly measured for the instrument's tube, hence the Photonis specifications for that tube have been used (see figure C.2). Based on a study[2] of the variance of VERITAS photomultiplier tubes quantum efficiencies, it was estimated that a 20% error was probably reasonable for values extracted from this curve. Another possible source of uncertainty about the quantum efficiency of that tube is the fact that the STACEE experiment changed the window material of their tubes from lime glass to borosilicate at some point to get more sensitivity in the UV. The tube maker made the requested change without providing a new model number for the new tubes. It could not

[2]Private communication between Jean-Phillipe Gagnon and John P. Finley from the VERITAS collaboration.

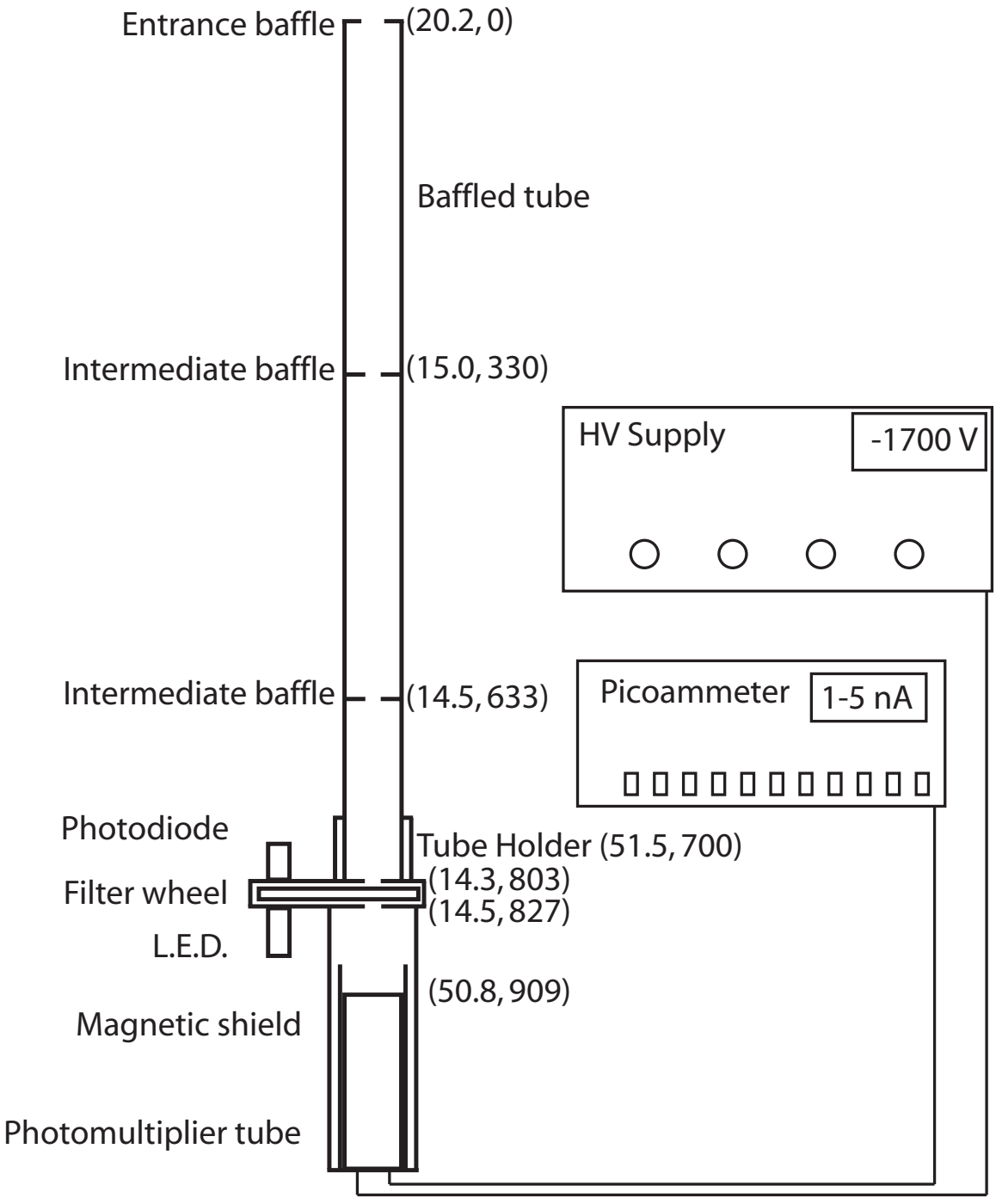

Figure C.1: Schematics and wiring of the night-sky background instrument. Numbers in parenthesis represent the diameters of apertures and their position along the optical axis, in mm.

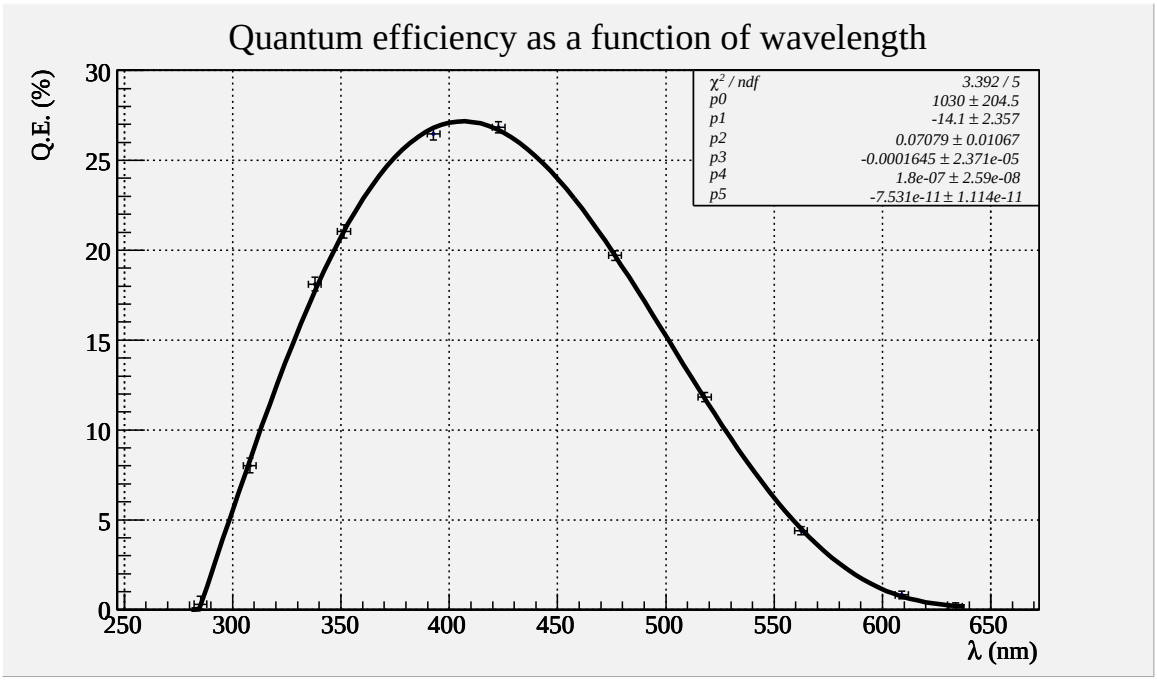

Figure C.2: Quantum efficiency of the photomultiplier tube used in the night-sky background instrument. A fifth order polynomial has been fitted in order to interpolate values between data points. Data come from the tube's specification sheet; error bars refer to the reading errors of the graph on the specification sheet. A 20% error will be allowed on extracted values from the fit to allow for tube aging, photocathode non-uniformity and for variance from the specifications within a group of tubes.

be traced back whether the tube used in the night-sky background instrument is of the former or latter type. The curve shown in figure C.2 assumes a lime glass photocathode material. This remains to be verified.

C.2.2 Gain

Of course, in order to use C.3 and C.5, we need a knowledge of the gain of the instrument. The **gain** of the photomultiplier tube is defined as the ratio of electrons collected at the anode to the number of photoelectrons generated at the photocathode. This definition, as formulated here, is however inapplicable in practice since the number of photoelectrons generated due to a pulse of light is not directly measurable or deducible when a calibrated light source is unavailable, as was the case in this experiment. Hence, it is a tricky challenge to compute the needed gain from the sole output of the anode; another input seems to be missing. What saves us

Specification	**Value**
Model number	Photonis XP2282B
Serial number	19562
Base number	901012
Diameter	51 mm
Length	145 mm
Mass	150 g
Material	lime glass
Photocathode	bi-alkali
Structure	linear focused
Number of dynodes	8
Maximum supply voltage	3000 V
Maximum gain	5×10^6
Maximum continuous anode current	0.2 mA
Typical dark current	5 nA
Rise time	1.5 ns
Temperature range	-30 to +50 °C
Sensitivity deviation with temperature (at 400 nm)	-0.2 %/K
Spectral range	290-650 nm
Quantum efficiency at maximum sensitivity (420 nm)	28%
Refractive index at 420 nm	1.54

Table C.2: Specifications for the Photonis XP2282B photomultiplier tube used in the night-sky background instrument

here is the recognition that the photoelectrons are generated randomly following a **Poisson distribution**. In fact, as photons hit the photocathode, photoelectrons are produced with a given probability (the quantum efficiency). The number of photoelectrons generated by light pulses of equal intensity will vary from pulse to pulse, but their distribution will follow the binomial distribution. Since the quantum efficiency is relatively small, it can be expected that **the Poisson distribution is a good approximation** for the binomial distribution in this case. Now, using the property that the variance of the Poisson distribution equals its mean, and using the fact that μ/σ **is scale invariant** as the population of photoelectrons is amplified by the gain of the photomultiplier tube, allows us to finally relate the unmeasurable number of photoelectrons to the measurable number of electrons collected at the anode and the spread of this number over many tries. Thus, our other handle on the problem of the gain measurement is the repeatability of the experiment. By repeating the experiment a great number of times, the variance of the population becomes measurable and this knowledge is used in place of the knowledge of the initial number of photoelectrons. This method for the gain calculation, dubbed the **statistical method**, was successfully used at McGill to measure the gain of the STACEE photomultiplier tubes; results and details can be found in [159].

In equations, let G be the gain of the photomultiplier tube, μ_i be the mean total charge of the photoelectrons, σ_i be the standard deviation on the total charge of the photoelectrons[3], μ_f be the mean total charge of the population of electrons measured at the anode end of the photomultiplier tube, and σ_f be its standard deviation. Then,

$$\begin{aligned} G &:= \frac{\#_f(e^-)}{\#_i(e^-)}, && \text{by definition of gain;} \\ &= \frac{\mu_f/e^-}{\mu_i/e^-}, && \text{using the charge values;} \\ &= \frac{\mu_f/e^-}{\frac{(\mu_i/e^-)^2}{(\sigma_i/e^-)^2}}, && \text{since } \tfrac{\mu_i}{e^-} = (\tfrac{\sigma_i}{e^-})^2, \text{ according to Poisson statistics;} \\ &= \frac{\mu_f/e^-}{\frac{(\mu_f/e^-)^2}{(\sigma_f/e^-)^2}}, && \text{from a scale invariant of the population;} \end{aligned} \tag{C.6}$$

[3] What should be used for the Poisson distribution parameters are not μ_i and σ_i, which have units of charge, but μ_i/e^- and σ_i/e^-, which are unitless numbers of photoelectrons.

that is,

$$\boxed{G = \frac{\sigma_f^2}{\mu_f}\frac{1}{e^-}} \quad \text{in term of measurable properties.} \tag{C.7}$$

To apply this method to the case at hand, a blue light-emitting diode (uncalibrated light source) was used to illuminate the face of the photomultiplier tube, which was held at high voltage by a PD HV-1547 power supply. The color of the light-emitting diode is irrelevant since the derivation above does not depend on wavelength; the gain is the the multiplication factor after the photons have been converted to electrons. Still, the color independence of the method was experimentally confirmed in [159]. For the gain measurements, as for the night-sky background measurements, the photomultiplier tube was allowed to warm up for at least half an hour, as was found to be the necessary stabilization time by looking at dark current curves over time . The photomultiplier tube was also covered by a magnetic shield, whose effectiveness was demonstrated in [232], to avoid unwanted effects from the Earth's magnetic field. The light-emitting diode was driven to give small pulses of light of 0.1 µs width at a frequency of 100 kHz by a BNC-8010 pulse generator whose output was also used to trigger a LeCroy 2323A gate generator. The resulting pulse output from the photomultiplier tube were verified to sit well inside the time window defined by the gate, as can be seen in figure C.3. The tube's pulse and accompanying gate were then fed to a LeCroy 2249W Analog-to-Digital Converter (ADC) for digitization of the pulse over the gate's duration. A computer program read and stored a total of 5000 digitized values per run.

To get a precise value for the gain, the experiment is repeated for different light levels. For each of those, the distributions of digitized charges are fitted with a Gaussian[4], see figure C.4. The means and standard deviations of these fits are extracted, converted to charge units[5] and are plotted in figure C.5. In this plot, the means have been corrected to remove the pedestal contribution, which we get from a special run

[4] Another fitting scheme was investigated in [159], where it is shown that the systematic errors introduced by using a Gaussian fit are less than 1%.

[5] The conversion factor is $1.56 \times 10^6 e^-$ per ADC count for the LeCroy 2249W [233].

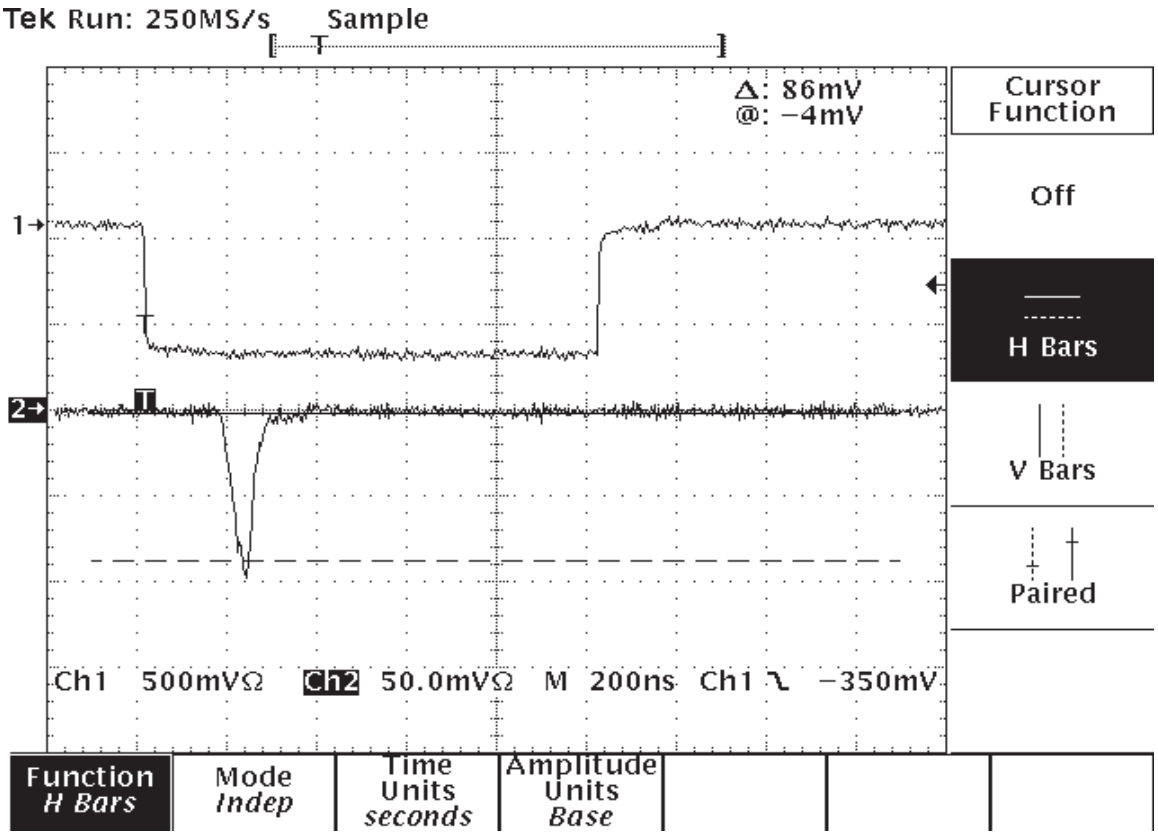

Figure C.3: Oscilloscope screen capture showing the pulse from the photomultiplier tube and the gate used to digitize the charge. The photomultiplier tube was biased at a high voltage of 1700 V.

where the light source was kept disconnected. Points for very low light levels, *i.e.* for which the distribution falls in only a few bins, have been discarded as these can cause deviations from linearity because of rounding errors introduced by the ADC, as shown in [159]. Equation (C.7) can then be applied by taking σ_f^2/μ_f to be the slope of a linear fit[6] through the data points. This way of proceeding discards any y-intercept that would result from noise in the system. Actually, equation (C.7) needs a small correction. The derivation assumed that $\mu_i/\sigma_i = \mu_f/\sigma_f$, but in reality this is not the case. When an electron hits a dynode it produces a number of additional electrons. This number, however, varies a little from hit to hit. This has the effect of adding an additional source of variance to the number of electrons collected at the output. Hence, the σ_f that we measure is overestimated with respect to the one that appears in equation (C.7). Simulations made in [159] show that this is a 9% effect and it has been corrected for in the gain values presented here.

Because of difficulty in seeing the signal from the night-sky background when the filters were being used, different high voltage values were experimented with. Thus, the gain calculation was performed for many different high voltage values to be able to tackle any situation that may arise in the field. Results are shown in figure C.6. A curve was fitted to the data points to be able to interpolate for other high voltage values; it has the form

$$G = kV^{\gamma} \tag{C.8}$$

where V is the applied voltage, k and γ are constants. The motivation for this model comes from the way a photomultiplier tube is constructed and its dynodes connected together. Basically, the gain elements provided by each dynode stage get multiplied and each of these gains is proportional to the voltage applied. Of course the geometry of the assembly and the way that the dynodes are connected to the resistor network in the base of the tube will complicate any simple derivation of the above formula. Therefore, γ should not be expected to be an integer number, and k should

[6] A polynomial fit of higher order was considered in [159] to take into account possible variations from linearity at high light levels, but it was shown to be a negligible effect.

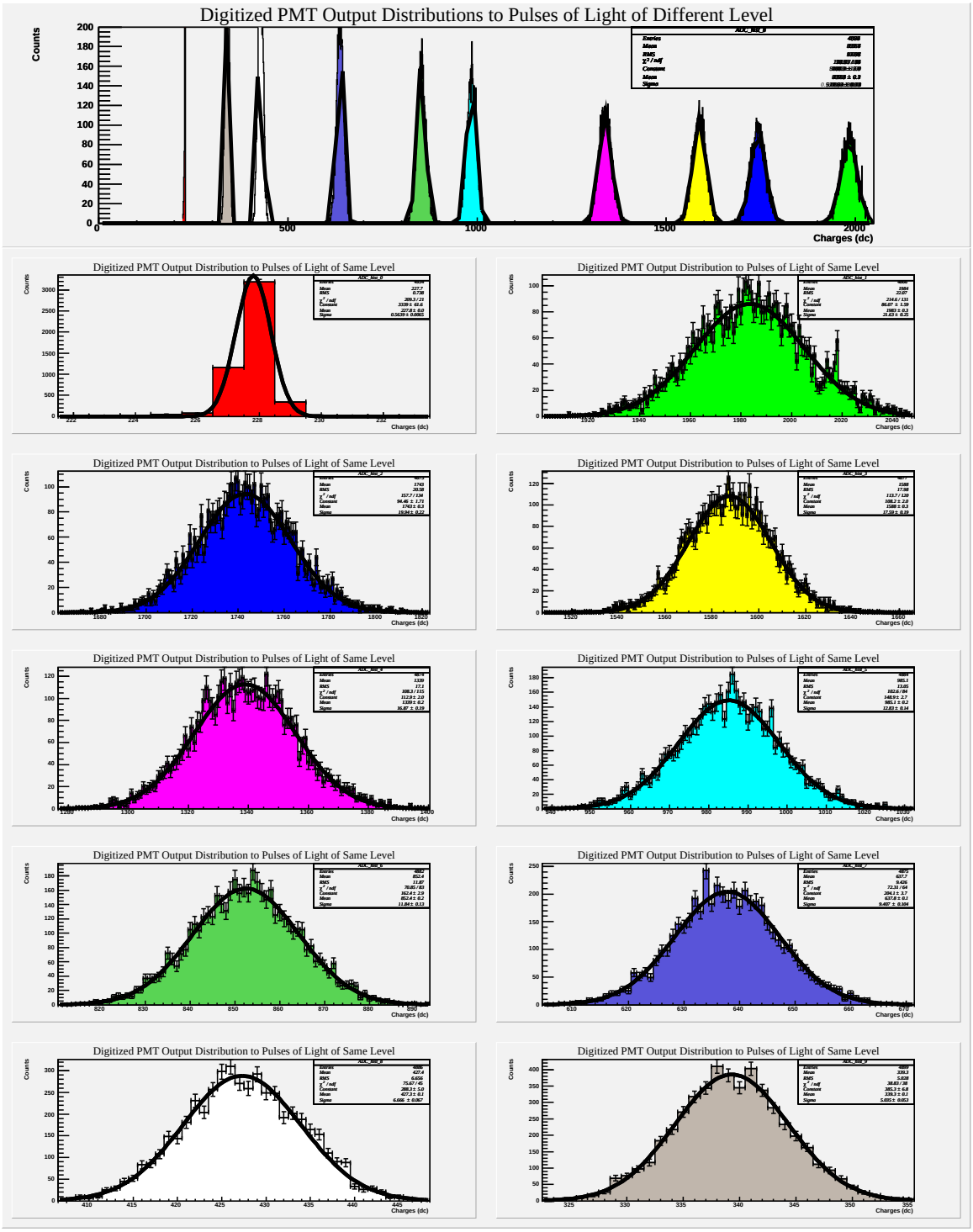

Figure C.4: Digitized charge distributions collected at the anode of the night-sky background instrument's photomultiplier tube for a series of light pulses. Each distribution represents a different light level. The first distribution represents the pedestal value, when no light source is used. The photomultiplier tube was biased at a high voltage of 1700 V.

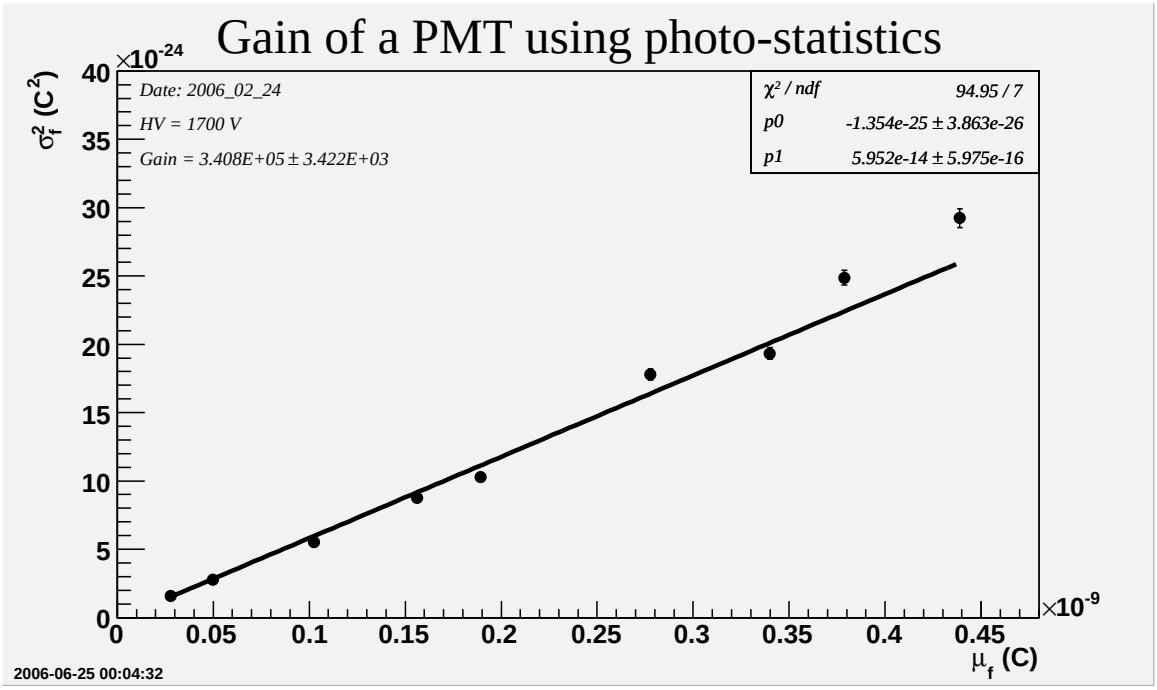

Figure C.5: Variance as a function of the mean of the charge distributions collected at the anode of the night-sky background instrument's photomultiplier tube for a series of light pulses. Each point represents a different light level. Error bars from the Gaussian fit results are too small to see. A linear fit is applied to the data. The slope of the line is related to the gain of the instrument. The photomultiplier tube was biased at a high voltage of 1700 V.

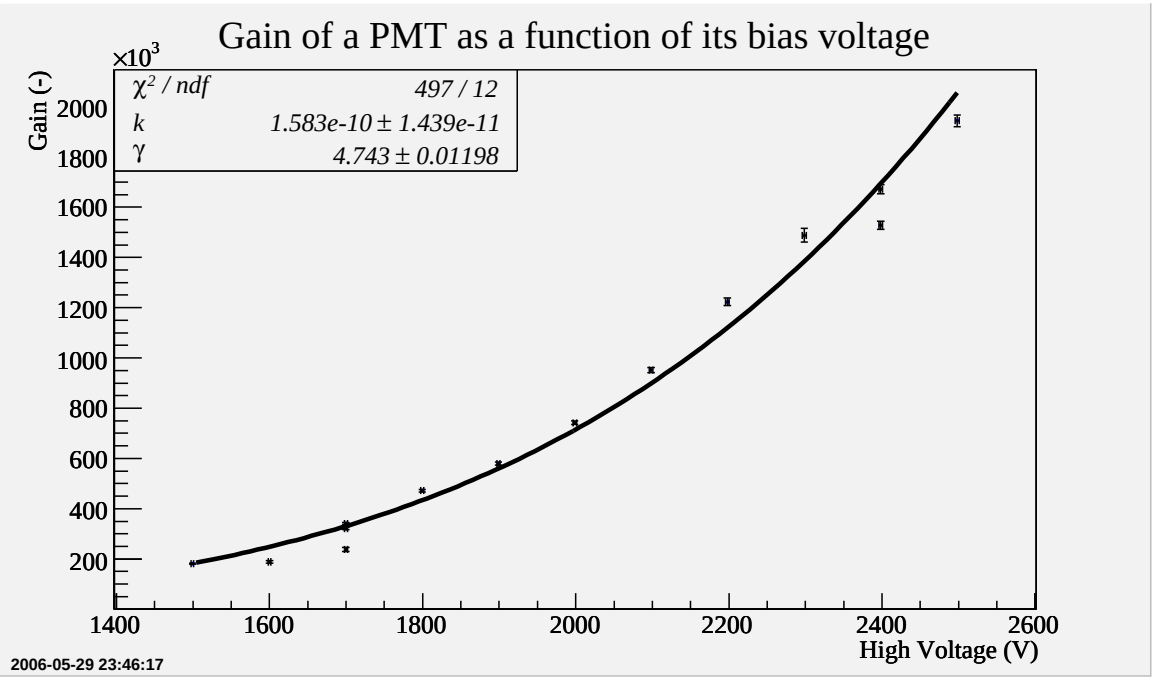

Figure C.6: Gain curve for the night-sky background instrument's photomultiplier tube. Error bars are smaller than the markers.

be understood as having units that will make the gain unitless, even though we won't explicitly write them. Here, we get $k = (1.58 \pm 0.14) \times 10^{-10}$ and $\gamma = 4.74 \pm 0.01$. Hence, the gain value that will be used in the following sections for experiments with the high voltage set at 1700 V is

$$\boxed{G_{1700\mathrm{V}} = (3.2 \pm 0.4) \times 10^5} \tag{C.9}$$

The values for k and γ are in reasonable agreement with the values obtained in experiments done previously at McGill and at the University of Chicago [159], considering the tube has aged a little. The value for the gain is also in good agreement with the specification sheet for that tube. This value is however not in agreement, by almost an order of magnitude, with the one deduced in [232], and explains partly why the night-sky background results obtained in that thesis seemed a little off. As for the uncertainty on the gain, it was obtained from error propagation on (C.8). This includes the variations from experiment to experiment whereas the smaller uncertainty shown in figure C.5 does not include it and should not be used. Our uncertainty is in reasonable agreement with the one quoted in [159] for the method used. One thing that was not investigated is the effect of temperature on the gain. According to the specification sheet of the tube, this is around $-0.2\%/\mathrm{K}$. The temperature on the field was not carefully monitored during data taking, but was generally between $10\,^\circ$ and $15\,^\circ$ less than the laboratory temperature where the gain measurements took place. Corrections that would need to be made to the above number for the gain are therefore of the order of 2 or 3% and are inside the quoted uncertainty.

C.2.3 Area and Solid Angle

Another important consideration in the use of equations (C.3-C.5) is the geometry that will define the area A_{eff} and solid angle Ω_{eff} subtended by the night-sky background instrument. The way the instrument was designed (see figure C.1), this cannot be answered in a straightforward manner. The detector is extended in this case, being of size comparable to the different apertures used, and cannot be approximated by a simple cone, which would make the determination of the solid angle easy. Also, the

different apertures are not all of the same size and it is not obvious which one should be used to compute the area.

The solid angle is usually defined as the area of the surface of a unit sphere seen by a point at its origin. Here this definition is inapplicable due to the extended nature of the instrument; there is no single point that can be used as the origin. Moreover not all points on the photomultiplier tube surface see the same portion of the sky; the center point of the photomultiplier tube sees a much larger portion of the sky than a point near its edge. An external point of view is required where a sphere at infinity is projected onto the instrument. To simulate this, a ray tracing program was written to examine the transmission of light rays generated at the entrance aperture and traveling through the instrument with a given angle of incidence with respect to the direction defined by the optical axis. The ratio $\varepsilon(\theta)$ of surviving rays at the photocathode to the number of generated rays, as a function of angle of incidence, is used to weight the integral that gives the solid angle in spherical coordinates:

$$\Omega_{\text{eff}} := 2\pi \int \varepsilon(\theta) \sin(\theta)\, d\theta. \tag{C.10}$$

The blue curve in figure C.7 shows $\varepsilon(\theta)$ obtained from the simulation. The resulting solid angle is $\Omega_{\text{sim}} = (4.6 \pm 0.2) \times 10^{-4}\text{sr}$, corresponding to the field of view seen by a cone of apex angle $1.39^\circ \pm 0.03^\circ$. The quoted uncertainty is not the ideal one given by the simulation, as quoted in the figure, but the spread in values gotten from running various simulations with the dimensions of the instrument shaken around their tolerances.

An unfortunate observer mistake during data taking, however, led the author to doubt about the accuracy of the simulations. During one of the runs, the instrument was mounted with the baffled tube reversed with respect to the normal configuration. To correct these data, a calibration run was taken to measure the ratio of a night sky measurement with the tube in its reversed position to the same night sky measurement with the tube in the normal position. This ratio could also be predicted by running the simulations for the mis-configured apparatus, but was found to disagree greatly with the experimental ratio (0.80 in simulations *vs* 2.27 experimentally). Thus the

simulations appeared to be wrong. In fact, the simulations do not take possible reflections inside the tube into account. Reflections are supposed to be blocked by the baffles in the tube, but what if they were inadvertently placed in a non-optimal position? Then they would allow some reflected light to reach the photomultiplier tube. One possibility, to explain the discording experimental and simulated ratios, is that, in the normal position, the baffles are placed optimally to reduce reflections to a minimal amount, but that with the tube in its inverted position, the baffles are shifted to another position which lets a lot of reflected light pass through the instrument. To verify that this is indeed plausible, the $\varepsilon(\theta)$ curve was experimentally measured by using a light-emitting diode to simulate a point-like light source at infinity. The light-emitting diode was held 7.6 meters in front of the instrument and was displaced perpendicularly to the optical axis by increments of a few centimeters. At each position, the output of the photomultiplier tube was measured and compared to the one when the light-emitting diode was aligned with the optical axis. The setup was extremely crude and explains the variations in the data and the large error bars (points with visible error bars in figure C.7). What one must understand is that the shape of the $\varepsilon(\theta)$ curve depends greatly on the diameters and positions of the baffles apertures along the optical axis, and presumably on the presence or absence of reflections inside the tube. The data were compared with various simulated curves for configurations that approach that of the night-sky background instrument, but no comparison was better than the one shown in figure C.7, which uses the best known dimensions of the instrument. These experiments showed how easy it is to get the solid angle value wrong by factors up to 2 or 3 by making simplifying assumptions about the geometry of the apparatus; the exact dimensions really need to be used. The fact that here data agrees well with the simulated curve then implies that there were minimal reflections and that the simulations can be trusted when the instrument is mounted in its normal configuration. Even though the data agrees rather well with the simulated curve, there is still a systematic overshoot of the data at higher angle values. This may be due to a very small amount of reflections inside the tube and

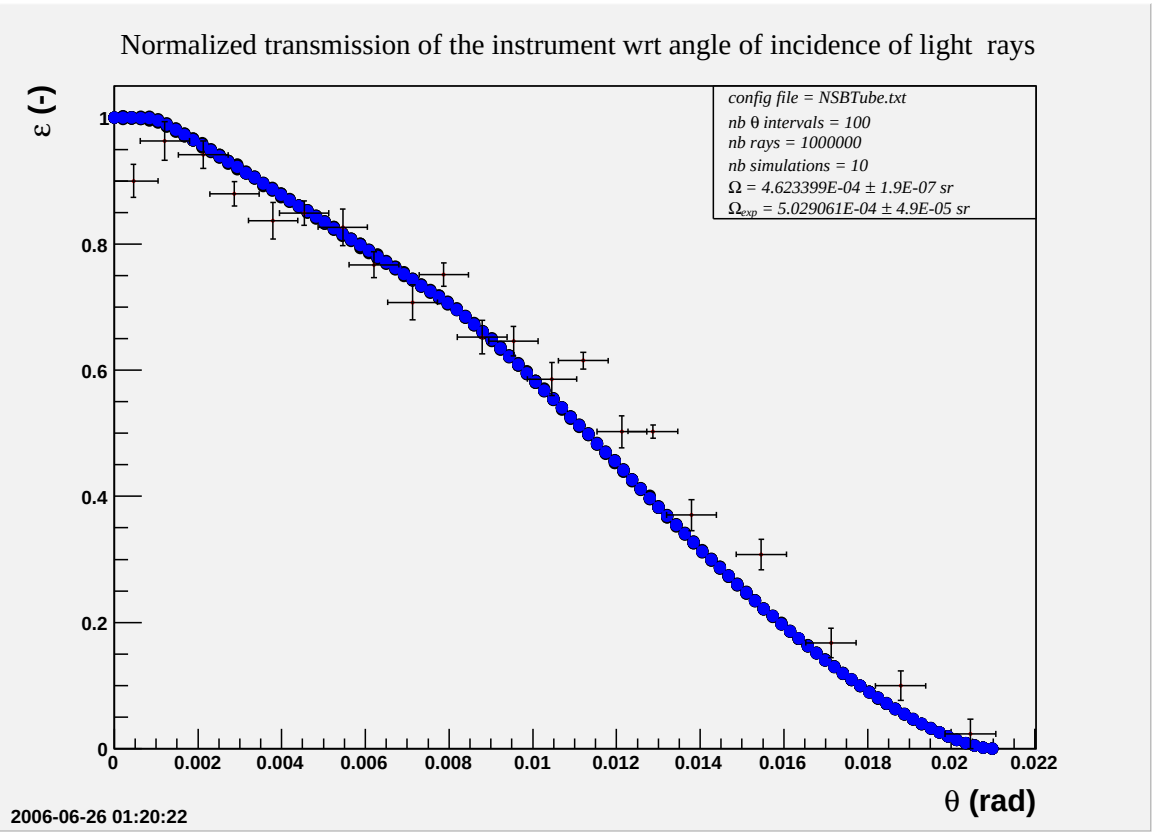

Figure C.7: Transmission curve for the night-sky background instrument. $\varepsilon(\theta)$ is the ratio of the amount of light reaching the photocathode to the amount of light entering the instrument. Kinks in the curve are due to the baffles affecting the propagation of light rays in the instrument. Each blue point is the average of 10 simulations. Error bars are smaller than the markers for these. Points with the visible error bars correspond to experimental data.

increases slightly the solid angle. From the data, we get $\Omega_{\text{exp}} = (5.0 \pm 0.5) \times 10^{-4}$ sr. This is a 9% difference with the previous estimate and agrees within error bars. This value is more than twice that found in [232] by a much cruder method and contributes to explaining why the results seemed off in that thesis. Whether the instrument with the baffled tube upside down is profoundly affected by reflections on the wall of the tube remains to be proved (no attempt was made to measure its $\varepsilon(\theta)$ curve), but remains the principal hypothesis to explain the discording ratios[7]. What matters most is that the instrument in its normal configuration behaves as expected.

[7]This hypothesis has been proved correct by Michael McCutcheon who took pictures of the reflections inside the night-sky background instrument with a camera placed at the position where the photomultiplier tube normally sits.

As for the effective area, it cannot be computed independently from the solid angle. We can, however, compute the entangled quantity $A_{\text{eff}} \cdot \Omega_{\text{eff}}$ and use our previous result for the solid angle to deduce the effective area. The photocathode surface can be divided in many elemental annuli of known area and sufficiently small enough width that the solid angle that each of these rings subtends is approximately constant over their surface. The solid angle seen by each annulus can be computed using a different ray tracing simulation, which generates rays for the given annulus over a known solid angle. The ratio of the number of rays that can escape the instrument to the number of generated rays at the annulus is a measure of the sought solid angle. The sum of the $A_i \cdot \Omega_i$'s, where i indicates the ring index, gives the quantity we are looking for. Figure C.8 shows the results of this simulation[8], namely $[A_{\text{eff}} \cdot \Omega_{\text{eff}}]_{\text{Normal configuration}} = (0.074 \pm 0.003)\,\text{mm}^2 \cdot \text{sr}$. Again, the quoted uncertainty is the result from shaking the instrument's dimensions around their nominal value. This number can be trusted, since we have shown previously that simulations for the tube in its normal position are not plagued by many unwanted reflections. Still, we will apply the 9% increase discussed above to correct for the small amount of reflections and obtain a better estimate. We will use the result

$$\boxed{[A_{\text{eff}} \cdot \Omega_{\text{eff}}]_{\text{Normal configuration}} = (0.074 \pm 0.003)\,\text{mm}^2 \cdot \text{sr}.} \tag{C.11}$$

With the previous results, we deduce that the effective area is $A_{\text{eff}} = (147 \pm 16)\,\text{mm}^2$.

When the filters were used to get the spectrum (see next section), a problem occurred in that the signal from the night sky was so much reduced that it was buried in the fluctuations of the dark current. In order to get an acceptable signal, the solution was found to remove the long baffled tube, leaving only the short tube holder to define the solid angle, see figure C.1. The area and solid angles in this configuration are thus also needed to interpret the differential flux of the night-sky background. A calibration run was taken to compute the $\frac{[A_{\text{eff}} \cdot \Omega_{\text{eff}}]_{\text{No tube}}}{[A_{\text{eff}} \cdot \Omega_{\text{eff}}]_{\text{Normal configuration}}}$ ratio.

[8] An independent simulation, utilizing a different method was conducted by D. Hanna. Results are identical.

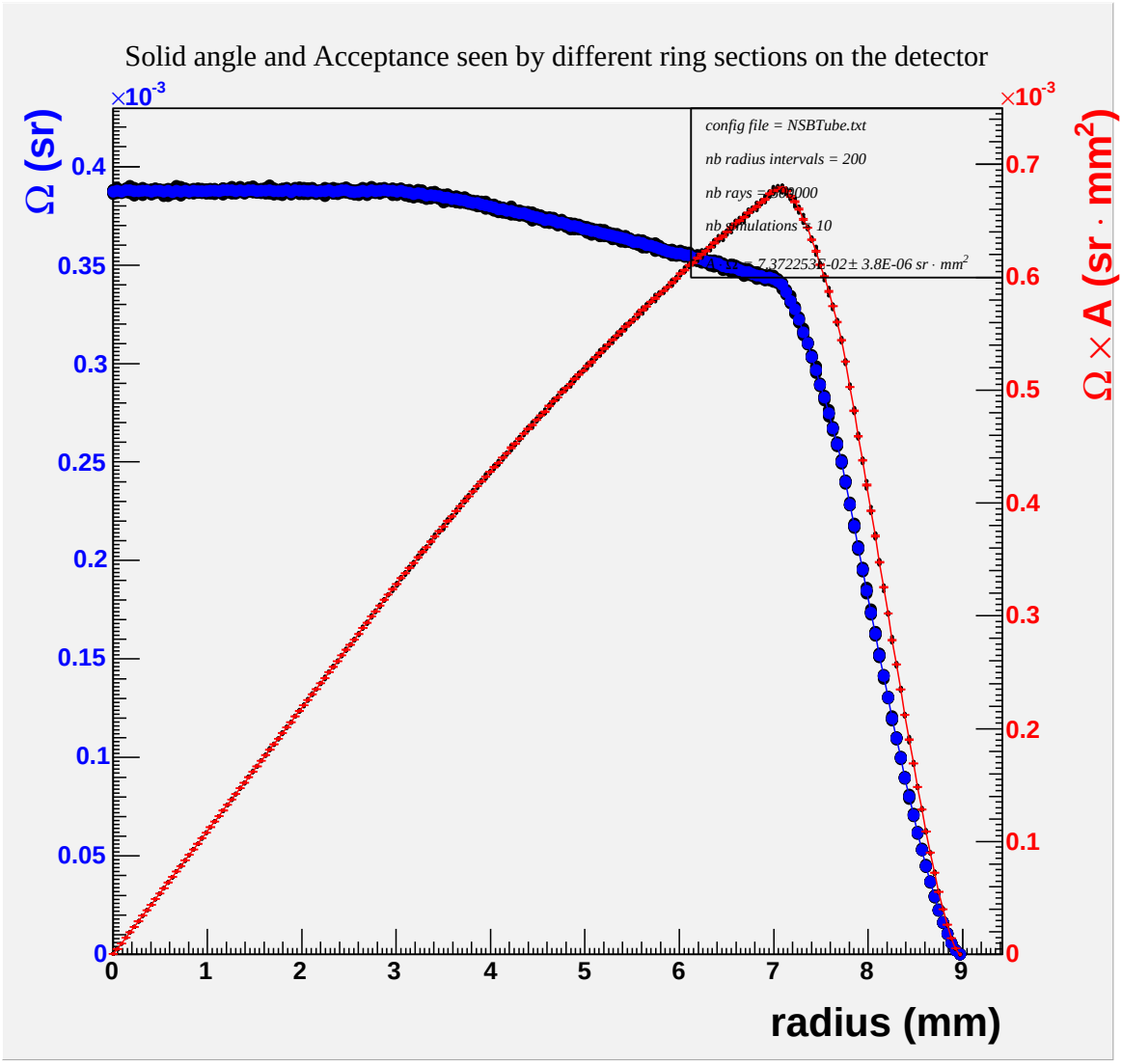

Figure C.8: Solid angle (blue curve) and acceptance (red curve) for ring sections on the photomultiplier tube face of the night-sky background instrument. Total acceptance is the integral of the red curve. Each point is the average of 10 simulations. Error bars are smaller than the markers.

It was found to be 240 ± 20, in good agreement with the simulated value this time, indicating that the no tube configuration does not suffer from too many reflections. With this ratio, and the acceptance value for the normal configuration, we deduce

$$\boxed{[A_{\text{eff}} \cdot \Omega_{\text{eff}}]_{\text{No tube}} = (17.8 \pm 1.7)\,\text{mm}^2 \cdot \text{sr}}. \tag{C.12}$$

No attempt was made to measure the transmission curve experimentally, the setup used previously being unadapted for such a wide opening angle. Trusting the simulations, it can be estimated that the solid angle in this configuration is around (0.103 ± 0.005) sr, corresponding to the solid angle subtended by a cone of $20.8\,^\circ \pm 0.5\,^\circ$ opening angle.

C.3 Differential Photon Flux

The night-sky background instrument includes a wheel where 8 different filters can be inserted to measure the photon flux at different wavelengths. In order to get a measure of the differential photon flux, equation (C.3) tells us that the quantum efficiency must be convolved with the transmission of the filter being used. While the transmission curves for the 550 and 580 nm filters were included in their shipment, the transmission curves of all the other filters remained unavailable and assumptions needed to be made about those. From the Edmund Optics website [234], very vague information about their narrow band filters is available. It can, however, be concluded that their central wavelength tolerance is ± 2 nm, their full width at half maximum (FWHM) is around (10 ± 2) nm and there is some indication that the transmission peak is increasing with wavelength value, starting at around 25% in the UV to around 45% in the yellow. The two transmission curves that we had showed that assuming those suggested transmission values can result in large errors since the true transmissions were around 60% compared to the suggested 45% from the website. This 33% discrepancy was thus used as an error estimate for the transmission peaks of the filters with unknown transmission curves. The estimates for the FWHM are in good agreement with the provided transmission curves. To perform the convolution with the quantum efficiency curve (figure C.2), Gaussian functions with these assumed FWHM

λ_{center}	**Transmission Peak**	**FWHM**	$\varepsilon_{\text{PMT}}(\lambda_{\text{center}})$	$\int_{\lambda-d\lambda}^{\lambda+d\lambda} T(\lambda')\varepsilon_{\text{PMT}}(\lambda')\,d\lambda'$
(nm)	**(%)**	**(nm)**	**(%)**	**(nm)**
365 ± 2	25 ± 8	10 ± 2	24 ± 5	0.6 ± 0.3
400 ± 2	30 ± 10	10 ± 2	27 ± 5	0.9 ± 0.4
430 ± 2	40 ± 13	10 ± 2	26 ± 5	1.1 ± 0.5
458 ± 2	45 ± 15	10 ± 2	23 ± 5	1.1 ± 0.5
492 ± 2	45 ± 15	10 ± 2	17 ± 3	0.8 ± 0.4
520 ± 2	45 ± 15	10 ± 2	11 ± 2	0.5 ± 0.2
550 ± 2	60 ± 2	10 ± 2	6 ± 1	0.4 ± 0.1
580 ± 2	62 ± 1	8.6 ± 0.3	2.6 ± 0.5	0.15 ± 0.03

Table C.3: Characteristics of the night-sky background instrument when used with the filters

and peak values were used to approximate the transmission curves. Table C.3 lists the center wavelength of the different filters used, along with the assumptions made for their transmission curves and the results of the convolution.

Data were taken at four different sites: at the 10-m building on top of Mount Hopkins (31°40'50"N, 110°52'44"W), at the VERITAS base camp at the base of Mount Hopkins (31°40'29"N, 110°57'11"W), nearby Montosa Canyon on the Mount Hopkins road (31°40'34"N, 110°55'43"W), and at Horseshoe Canyon on Kitt Peak (31°57'15"N, 111°37'15"W). The 10-m and base camp sites were investigated during the fall of 2005 and the base camp, Montosa Canyon and Kitt Peak sites were investigated during the spring of 2006. The procedure consisted in pointing the instrument at only one place in the sky, usually at zenith, and taking 10 consecutive current measurements with each filter. The 10 measurements were averaged, the dark current subtracted and eq. (C.3) applied with the parameters described in previous sections. Early data showed that measurements with the filters and the baffled tube always resulted in data indistinguishable from the dark current. In an attempt to measure something with the filters, the end baffle was removed, but this did not improve the situation. Increasing the high voltage also did not help. The only way a

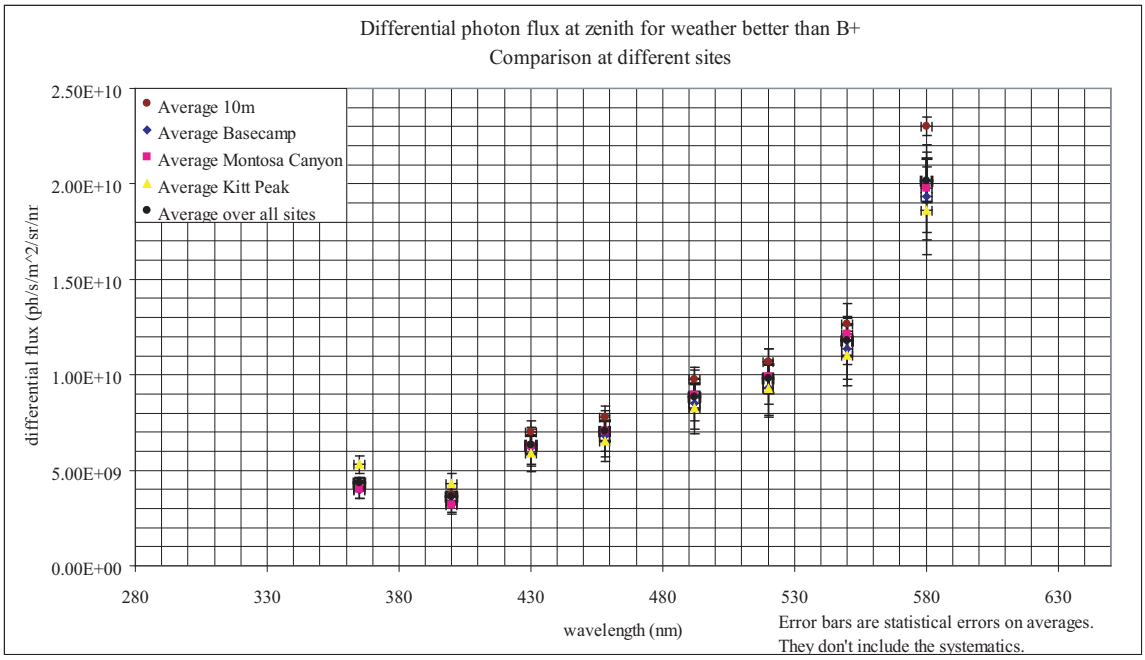

Figure C.9: The differential photon flux at different sites.

measurement above dark current could be obtained with the filters in place was to remove the baffled tube entirely, as mentioned in a previous section. The increased acceptance angle in this configuration has the effect of introducing an additional uncertainty; the transmission of filters is angle dependent and they are meant to be used with a collimated beam. With our wider opening angle, we might be violating this condition, but simulations show that the maximum acceptance angle is about 14°, thus the effect must be small compared to other systematic uncertainties.

Figure C.9 shows a comparison of the differential photon flux measurements taken with the instrument pointing at zenith for the different sites. Only data taken in weather graded B+ or better was retained and averaged. Since we are interested in comparing sites, the error bars plotted reflect the statistical uncertainties due to the averaging over the night to night fluctuations and do not include the systematic uncertainties discussed in previous sections since these are the same for all sites. For the sites where there were not enough data runs to estimate a reasonable statistical error, the uncertainty from the base camp measurements have been assumed.

It is apparent that the shape of the spectrum is the same at all sites. It should not,

however, be concluded immediately that all sites are equal in terms of light pollution. Firstly, the filters were chosen to avoid the main emission lines, so as to get the general shape of the spectrum[9]. Light pollution will be more easily tackled in the next section where integral photon flux measurements are discussed. Secondly, these are measurements taken while pointing at zenith, where light pollution should be minimum. Ideally, differential photon flux measurements should be taken at various elevation and azimuth angles to see how the night-sky background spectrum changes with terrestrial coordinates due to the local light pollution. Since the data were taken manually in a lengthy process, this could only be done partially. We restricted ourselves to spectrum measurements at zenith, at 60° elevation facing North and at 60° elevation facing South. Results are displayed in figure C.10 for the base camp site. Within statistical uncertainties, no elevation dependence can be deduced, any discrepancy can be explained by night to night fluctuations alone. This is even more the case for the Kitt Peak site, which is believed to be even less light polluted. Of course, it is possible that the spectrum might change at elevations lower than 60°. More measurements would be needed to confirm that.

C.4 Integral Photon Flux; North-South Scans

Now that the shape of the spectrum is known to be similar at all sites and over at least a large range of elevations, it can be used to compute the needed integral quantum efficiency in equation (C.5). Figure C.11 shows the zenith spectrum, $S(\lambda)$, averaged over different nights at different sites, normalized so that its integral is unity. The convolution of that curve with the quantum efficiency curve for the photomultiplier tube gives us the integral quantum efficiency. Here the systematic uncertainties of the spectrum were used to see by how much the spectrum shape could change due to the unknown transmissions of the filters. An additional 10% systematic uncertainty is

[9]Recently, a new filter has been purchased to measure the sodium double line. This will allow us to better measure the difference in light pollution attributable to sodium lights near the different sites. Measurements to come...

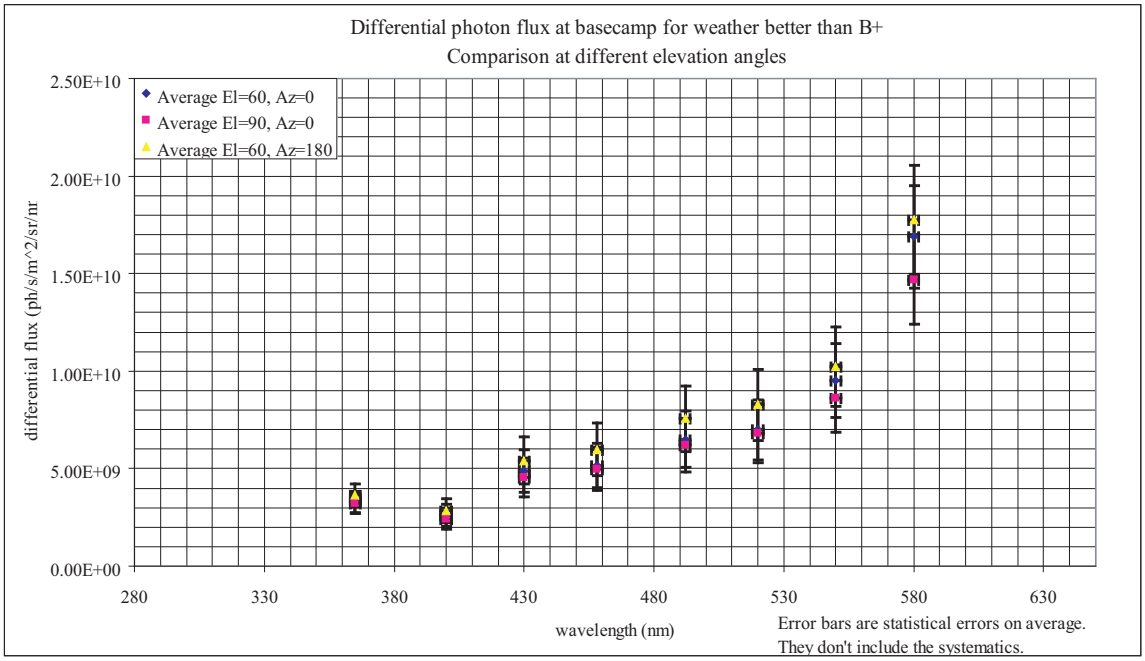

Figure C.10: The differential photon flux at different elevations.

estimated to account for the fact that the peaks in the spectrum curve, due to sodium line emission for example, have been neglected. The result is an integral quantum efficiency of

$$\boxed{\int_{\lambda_1}^{\lambda_2} \frac{\phi(\lambda')}{\phi} \varepsilon_{\mathrm{PMT}}(\lambda')\, d\lambda' = (7.4 \pm 1.5)\%} \tag{C.13}$$

Figure C.12 shows averages of integral photon flux measurements taken at different sites in a North to South scan of the sky. These data were taken without filter. The instrument is first pointed in the North direction, then the elevation angle is increased by 10° steps until zenith is reached. At zenith the instrument is rotated by 180° to scan the South direction, again by 10° steps. Each data point consists of an average of ten current measurements taken at a rate of 3 readings per second. The dark current was monitored a few times during the scan to ensure the stability of the tube. Data points affected by the Milky Way, or by clouds, or a bright star being present in the sky, have been removed as much as possible from the average to smooth out any bumps. Error bars in the graph are the statistical uncertainties from the average calculations. The systematic errors are the same for all sites and are not shown to

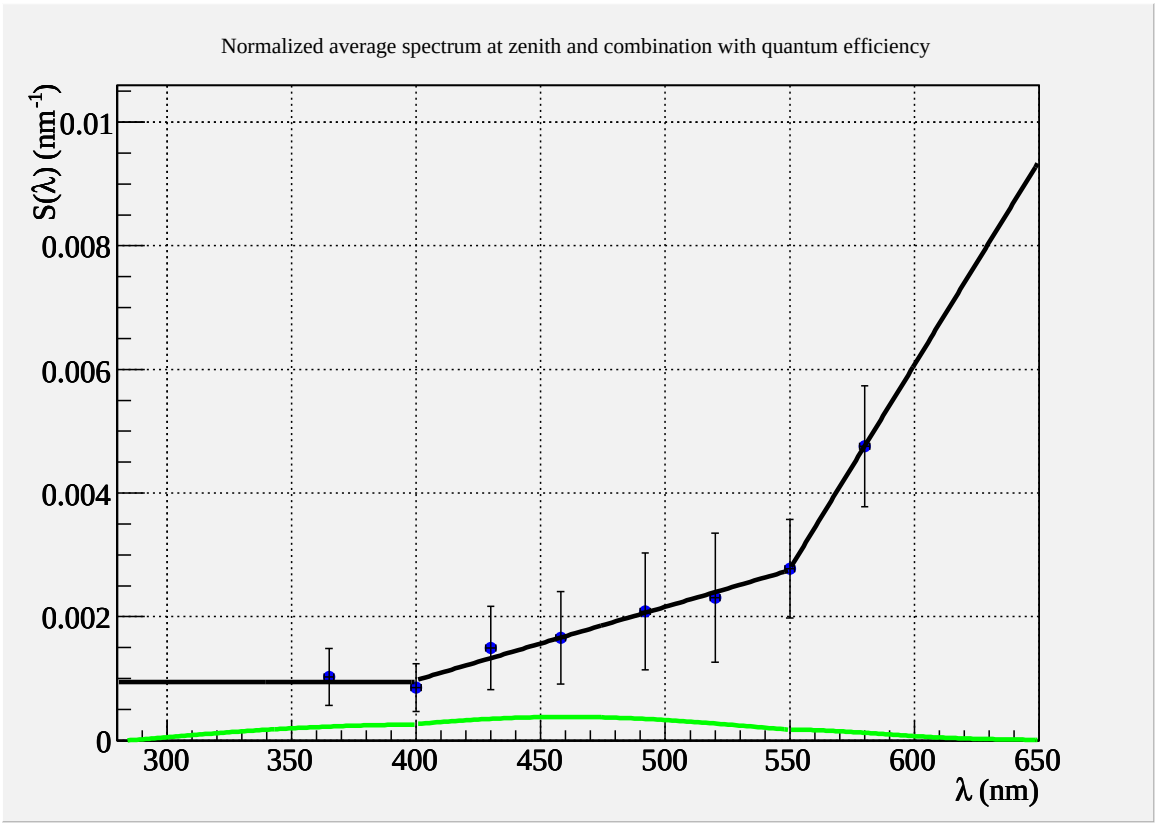

Figure C.11: Spectrum used in the calculation of the integral quantum efficiency (blue points). Three linear functions have been used to approximate the spectrum and compute the integrals. Error bars here include the systematic uncertainties resulting from the unknown transmission curves of the filters. The green curve is the multiplication by the quantum efficiency curve. Its integral is the quantum efficiency averaged over the shape of the spectrum.

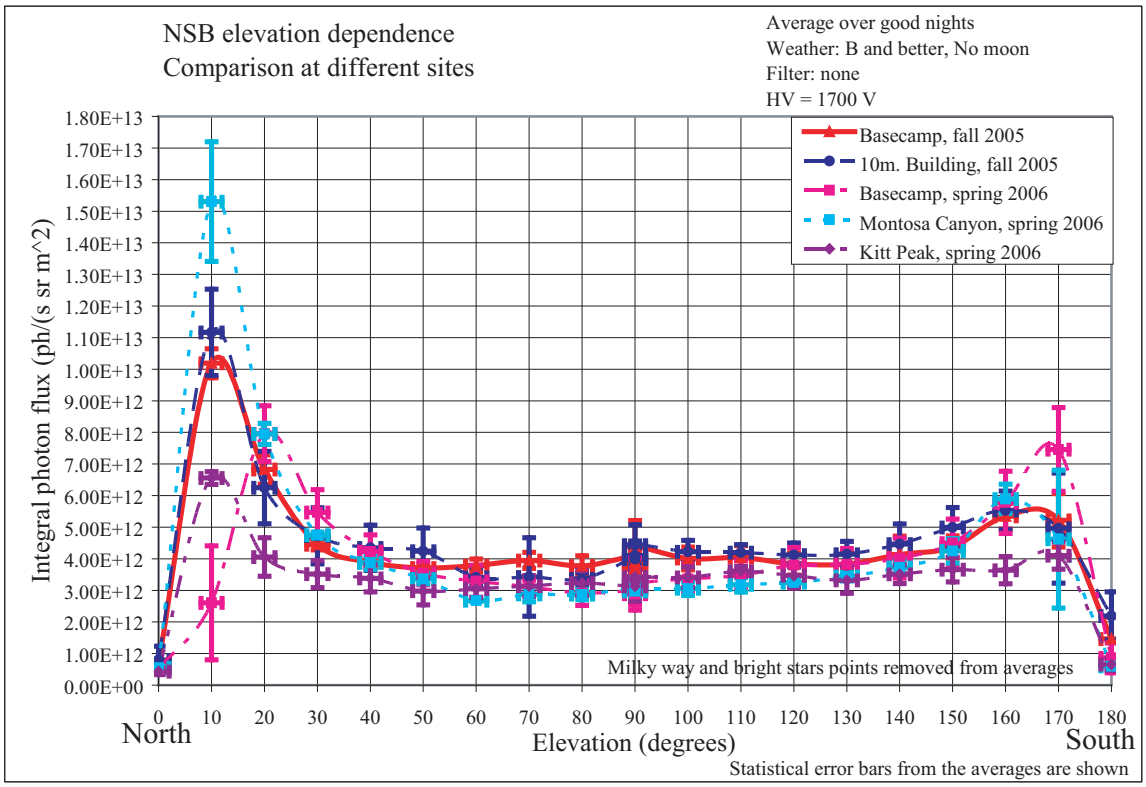

Figure C.12: Integral photon flux for different elevation angles in a North to South scan of the night sky at different sites. Elevations $> 90\,^\circ$ should be understood as really being $180\,^\circ - El$ with $Az = 180\,^\circ$. Error bars are statistical from the average calculations. When there were not enough quality points to compute an uncertainty, an average uncertainty was used. Smooth lines are only to guide the eye.

make the comparison easier. Near zero measurements at the extremes on the graph are due to hills and trees in the viewing path of the instrument. The big bump around $10\,^\circ$ is mainly due to the Tucson lights and the smaller bump near the South horizon is due to a combination of nightglow and the lights from Nogales. The Kitt Peak site being to the West of the Tucson-Nogales line, it is not affected by their light pollution in the North and South directions, hence the smaller bumps in its curve at low elevations. At higher elevations, all sites show a fairly flat curve, showing a relatively stable night-sky background far from the Milky Way. Moreover, all sites show approximately the same level of night-sky background, with differences that can be explained by night to night fluctuations alone.

Site	Absolute Photon Flux	Relative Photon Flux
(-)	(photons/(s sr m^2))	(-)
Basecamp, Spring 2006	$(3.19 \pm 0.08) \times 10^{12}$	1
Basecamp, Fall 2005	$(3.90 \pm 0.06) \times 10^{12}$	1.22 ± 0.03
10-m building, Fall 2005	$(3.94 \pm 0.11) \times 10^{12}$	1.24 ± 0.05
Montosa Canyon, Spring 2006	$(3.04 \pm 0.06) \times 10^{12}$	0.95 ± 0.03
Kitt Peak, Spring 2006	$(3.31 \pm 0.05) \times 10^{12}$	1.04 ± 0.03

Table C.4: Average photon flux levels at different sites for elevations greater or equal to 60 °. Statistical uncertainties are quoted.

C.5 Discussion

Since the integral photon flux curves are flat at high elevations, it is appropriate to average them to get a mean value for each site. The average night-sky background for elevations above 60 °, with Milky Way contributions excluded as much as possible, in A/B weather, is given in table C.4 for the different sites. Again, only statistical uncertainties are quoted to make the comparison easier. The night-sky background level relative to the base camp site during the spring 2006 measurements is also shown.

Keeping in mind that it is hard to precisely compare sites with only a few good nights of measurements, results during the spring of 2006 confirm that the base camp, Montosa Canyon and Kitt Peak sites are equivalent at high elevation and that there certainly are no orders of magnitude differences between them. However, the flux seems a little higher during the fall 2005, for the 10-m building and base camp sites, than during the spring 2006. Whether this is seasonal variability or instability in the apparatus is hard to say and would require measurements over several years to confirm.

The absolute integral photon flux at the base camp site, in the wavelength region appropriate for atmospheric Čerenkov telescopes, including systematic uncertainty is

$$\boxed{\overline{\phi}_{\mathrm{El}\geq 60^\circ} = (3.2 \pm 0.8) \times 10^{12} \mathrm{photons}/(\mathrm{s\,sr\,m}^2)}. \qquad \text{(C.14)}$$

It is interesting to note that the values obtained for the differential and integral photon fluxes are comparable to the results presented in the H.E.S.S. paper [231] for the sites of Namibia ($(2.21 \pm_{\text{random}} 0.22 \pm_{\text{systematic}} 8.8\%) \times 10^{12}\text{photons}/(\text{s sr m}^2)$) and La Palma ($(2.60 \pm_{\text{random}} 0.35 \pm_{\text{systematic}} 8.8\%) \times 10^{12}\text{photons}/(\text{s sr m}^2)$). This confirms that the apparatus is understood to an acceptable level.

The largest uncertainties in the calculation presented here come from the assumed quantum efficiency and assumed transmissions for the filters. These should really be measured in the lab.

The experiment shows that light pollution due to the Tucson lights can increase the photon flux up to a factor 5, but only at very low elevations. With a minimum of shielding at low elevations, this should not be a real issue for the telescopes. The Milky Way was found to increase the flux by a factor of about 40%, and similarly for bright stars that crossed the field of view. Clouds on the other hand, could decrease or increase the flux, depending on their location with respect to the city lights.

It is probably appropriate to close this report by mentioning, as was done in [231], that the night-sky background is a complicated thing that varies according to various coordinate systems and on various time scales. The measurements presented above are however believed to be taken under typical conditions and the results are not expected to change much if the experiment was to be repeated.

Here are some other interesting things that could be tried with the night-sky background instrument:

- Scans with filters to lower elevations to see if the shape of the spectrum eventually changes.
- Inclusion of a filter for the sodium double line.
- Azimuth scans.
- Following a point in the sky to truly see the effect of elevation on the night-sky background, rather than the effect of different parts of the sky.
- Study the evolution of the NSB with time during a night.

- Confirm that the effects of temperature on the gain of PMT are negligible.
- Study the effect of the presence of the moon on the night-sky background.
- Perform albedo measurement to see how much background light is reflected from the ground.

Acknowledgments: Many thanks to David Hanna, Jean-Phillipe Gagnon, Michael McCutcheon, John Kildea, Audrey MacLeod, Jamie Holder and Hakima Manseri for either help in understanding the instrument or help in taking the measurements during long cold and dark nights.

D

Programs

Here is, for future students of the McGill group, the documentation concerning the programs that the author wrote during the course of this thesis. The programs are saved either in the McGill CVS repository, or the VERITAS one. For almost all of these programs, more information can be found by typing

`programname -help`

or by reading the source code, which is well documented. The program whose names are not starting by the letter "L" have benefited from additional code provided by M. McCutcheon for inclusion into the daily data quality monitoring (DQM) scheme. For the programs supporting the `batch` option, this is what it means:

```
batch tells Root to work in batch mode so that the program runs faster.
      Useful when working remotely.  The default interactive (non
      batch) mode is useful for easy zooming and editing of graphs,
      but makes the program run slower, especially while working from
      a remote location.
```

LRunScript

```
Usage:   LRunScript <Script> [Email] [ResultsFile]
```

This is an extremely useful script. It is used to run other scripts (equivalent of a `source` command) and saves the screen outputs to a text file that is optionally sent by email at the end of the execution. Every command executed is echoed in the output file, is time stamped and is made visually easy to find against the other text outputs; this makes LRunScript an ideal tool for logging the results of a script execution.

Lrootlogon.C

Lrootlogon.C is a set of useful preferences that ROOT loads at initialization. It makes the ROOT plotting more enjoyable and sets the stat boxes to display more useful information.

LTools

LTools is a library of tools that are used by the other programs of the suite. It must be compiled and the resulting library must be placed in an accessible location for the other programs to find. LTools can also be used in a non-compiled fashion within an interactive ROOT session.

LEvent

LEvent defines an event object custom made to store VERITAS data. Other programs of the DQM suite use it.

LSolidAngle

```
Usage: LSolidAngle  <filename.txt> [--grid --nbrays=<int>
         --nbtheta=<even int> --nbsimulations=<int > 1>
         --batch --help]
Each option can be substituted by its first letter, e.g. -h for --help.

Ray tracing simulation to compute the solid angle subtended by an
instrument having cylindrical symmetry, e.g. the NSB instrument
with its various circular baffles.
INPUTS:
        filename.txt   contains the dimensions of the apparatus for
              which we want to compute the solid angle.  Any units
              can be used and should not be specified.  The units
              chosen must be consistent throughout.  The format is a
              number on each line, representing respectively d0, z0,
              blank line, d1, z1, blank line, etc... di is the
              diameter of baffle i, zi is its position along the
              optical axis, with z=0 at the entrance baffle, i.e.
              z0 = 0, and z+ going into the instrument (following path
              of light rays).  Baffles need to be inputted in
              increasing order of z.  Comments in this file begin with //
              See example files Cone.txt, StraightTube.txt,
              HessTube.txt, NSBTube.txt.
        grid      The light rays will be generated on a square grid
```

```
                rather than randomly.
        nbrays    Number of rays to be generated in each simulation.
        nbtheta   Number of theta intervals to use to compute the
                  integral of the transmission curve.
                  Must be an even number.
        nbsimulations  Number of simulations to average over.  Must be
                  greater than 1.
OUTPUTS:
        Graph of the transmission curve used in the solid angle
        calculation.
        Drawing of the instrument.
        Value of the solid angle is printed to screen.
        The error quoted is the result of running the simulation a
        number of times with the number of specified rays and computing
        the statistics of these simulations.  The error does not
        include the uncertainties in the measurement of the instrument.
```

LAreaSolidAngle

```
Usage: LAreaSolidAngle  <filename.txt> [--nbrays=<int>
          --nbradius=<even int> --nbsimulations=<int > 1>
          --batch --help]
Each option can be substituted by its first letter, e.g. -h for --help.

Ray tracing simulation to compute the acceptance subtended by an
instrument having cylindrical symmetry, e.g. the NSB instrument
with its various circular baffles.
INPUTS:
        filename.txt   contains the dimensions of the apparatus for
              which we want to compute the solid angle.
              Units of mm should be used and should not be specified.
              The units must be consistent throughout.  The format is
              a number on each line, representing respectively d0, z0,
              blank line, d1, z1, blank line, etc... di is the diameter
              of baffle i, zi is its position along the optical axis,
              with z=0 at the entrance baffle, i.e. z0 = 0, and z+
              going into the instrument (following path of light rays).
              Baffles need to be inputted in increasing order of z.
              Comments in this file begin with //
              See example files Cone.txt, StraightTube.txt,
              HessTube.txt, NSBTube.txt.
        nbrays    Number of rays to be generated in each simulation.
        nbradius  Number of radius intervals to use to compute the
                  integral of the acceptance curve.
                  Must be an even number.
        nbsimulations  Number of simulations to average over.
                       Must be greater than 1.
```

```
OUTPUTS:
        Graph of the solid angle and acceptance curves as a function
        of radius on the detector.
        Drawing of the instrument.
        Value of the total acceptance is printed to screen.
        The error quoted is the result of running the simulation a
        number of times with the number of specified rays and
        computing the statistics of these simulations. The error does
        not include the uncertainties in the measurement of the
        instrument.
```

LFADCSummer

```
Usage: LFADCSummer <filename> [--telnum=<telescope_number>
           --event=<event_number> --avg --threshold=<threshold_value>
           --gif --eps --help]
Each option can be substituted by its first unambiguous abbreviation,
e.g. -te for --telnum.
Example: LFADCSummer 1190.vbf -ev=1000 -avg -th=50 -gif

Displays a graph of the sum of FADC pulses over the camera channels
for the specified event number.  This can be used to determine
which window to use to integrate under the pulse.
Note: the sum goes over all hit channels, including those receiving
the L2 and laser diode signals.
INPUTS:
        filename  is the VERITAS Bank Format file to use as input
                  (.vbf or .cvbf).
        telnum    is the telescope number for which we want the
                  charges (default = 1).
        event     is the event number to be summed (default = 0,
                  i.e. all).
                  If this flag is set to 0, then all of them are
                  summed and displayed in sequence.  Otherwise
                  only the specified event is summed and displayed.
        avg       asks to display the average pulse rather than the
                  sum of them.
        threshold is the value against which the sum of the traces
                  is to be compared.
                  If the absolute value of sample number 13 (a sample
                  number that should be in the peak region) in the
                  summed FADC trace is higher than the threshold value,
                  then the graph is displayed (and printed if requested).
                  The threshold value must be between 0 and 127500 (or
                  0 and 255 if --avg is used).
        gif       specifies to print the resulting graph(s) to
                  .gif file(s).
```

```
        eps       specifies to print the resulting graph(s) to
                  .eps file(s).
OUTPUTS:
        SumTracefilename_event_telnum.gif       gif file(s) of the
                                                summed event(s).
        SumTracefilename_event_telnum.eps       eps file(s) of the
                                                summed event(s).
        AvgTracefilename_event_telnum.gif       gif file(s) of the
                                                averaged event(s).
        AvgTracefilename_event_telnum.eps       eps file(s) of the
                                                averaged event(s).
```

DataTree

```
Usage: DataTree <filename> [--telnum=<telescope_number>
            --printevent[=<event_number>] --fillmethod=<method_number>
            --help]
Each option can be substituted by its first unambiguous abbreviation,
e.g. -t for --telnum.
Example: DataTree 31190.cvbf -t=1 -p=3 -f=2.

Creates a ROOT tree to store the charges, max sample height and
position, pedestals and gain switches of each channel, for each event
of a VERITAS run.
Each of these quantities are stored both as given by the hardware,
and as extracted in software from the FADC trace for comparison
purposes.  For each channel, a histogram of the pedestals from
pedestal events and a vector containing the average trace are also
created.
INPUTS:
        filename.vbf   is the VERITAS Bank Format file to use as input
                       (.vbf or .cvbf).
        telnum         is the telescope number for which we want the
                       charges (default = 1).
        printevent     makes the program print the event's number as
                       it fills the tree.
                       If this flag is set to 0, or no event number
                       is specified, then all of them are printed,
                       otherwise only the specified event's info is
                       printed.
        fillmethod     is the method (default = 2) used to calculate
                       SWCharge and SWPulseHeight by subtraction of
                       a pedestal.
                       1 == Uses the first few samples of the trace to
                       compute the pedestal:
                       this quantity is called the SWPedestal.
                       The calculation yields a different pedestal for
```

```
                        each tube, for each event.
                        2 == Uses the pedestal events and averages
                        them for each tube to get the pedestal.
                        This results in the same pedestal for each event,
                        but will be different for each tube.
OUTPUTS:
        filename.root           contains the ROOT tree.
```

Diagnosis

```
Usage:  Diagnosis <filename.root> [--minevent=<event_number>
           --Maxevent=<event_number>
           --printevent[=<event_number>] --printcode[=<print_code>]
           --cameraplot[=<camera_code>] --fadctraces --distributions
           --laserphotodiodechannel=<channel> --selectL2Channels
           --batch --writetodb --help]

Each option can be substituted by its first unambiguous abbreviation,
(e.g. -m for --minevent).

Example:  Diagnosis 2212_2.root -m=1 -M=5 -printe=3 -printc=11 -d -l=499

Reads a VERITAS ROOT tree, created with LDataTree, and finds the best
working channels.  This is done by comparing the distributions, for
laser events, of various parameters (MeanHWCharges, RMSHWCharges,
MeanSWCharges, RMSSWCharges, MeanSWPedestals, RMSSWPedestals) for each
channel to the standard (or mean) distribution over all channels.
The diagnosis is done in various steps:
First the laser photodiode channel is removed from the set of channels,
then the L2 channels, then the dead channels, and finally, Chauvenet's
criterion is used to reject any channel that has a parameter not
fitting into one of the standard distributions.
The surviving channels are labelled as good.
A color code, defined in the LTools library, is used in the output to
identify the different kinds of channels.
Note: channels labelled as nonstandard are not necessarily bad channels,
they simply
do not fit perfectly inside one or more of the distributions mentioned
earlier.
INPUTS:
  filename.root  is the VERITAS ROOT file to use as input, created
                 with LDataTree.
  minevent    is the starting value for the event reading loop
              (Default = 0).
              If this option is used without the Maxevent option, then
              only the specified event is examined, i.e. there is no
              loop.
```

```
  Maxevent     is the ending value for the event reading loop
               (Default = total number of events).
               If this option is not specified, but minevent is used,
               then Maxevent will be set to the same value as minevent.
               If this option is used without the minevent option, then
               the reading loop starts at 0 and ends at Maxevent.
  printevent   prints the event's information as specified by print_code.
               If this flag is set to 0, or no event number is specified,
               then all of them are printed, otherwise only the specified
               event is printed.
  printcode    is a number made up of 1 and 0's, each 1 beeing a flag to
               print a specific set of info. If print_code is not
               specified, or is 0, then all infos are printed.
               (1->Event number; 10->Event header; 100->HW properties;
               1000->SW properties; 10000->Charges; 100000->Pedestals;
               100000->GainSwitches; 1000000->PulseHeights;
               10000000->PulsePosition.)
  cameraplot   makes the program produce camera plots of the quantities
               specified by camera_code.
               camera_code is a number made up of 1 and 0's, each 1
               being a flag to plot a specific quantity.
               If camera_code is not specified, or is 0, then all
               plots are produced.
               (as above for printcode).
  fadctraces   probably prints average fadctrace of all channels

  distributions  makes the program print 500 histograms: one for each
                 of HWCharges, SWCharges and SWPedestals distributions
                 for laser events.
  laserphotodiodechannel  tells the program which channel is that of
                          the photodiode.
                          If left unspecified, the program assumes
                          this is channel 499.
                          Select -1 to use no photodiode.
  selectL2channels  (flag) causes the program to ignore the default
                    L2 channels and select them based on laser run
                    properties.
  writetodb    If this flag is set, the program will only simulate
               writing to the DB.  By default the program writes to
               database and this flag should be used only when one
               wants to use the program for quick testing purposes.
  keepdistributons  In the spirit of writetodb, set this flag if you
               don't want to save the individual distributons for every
               property and channel; speeds things up for testing
               purposes.
OUTPUTS:
```

```
filename.root  the input file is updated with 500 distributions for
               HWCharges; HWPedestals; HWPulseHeights;
               HWPulsePositions; HWGainSwitch; SWCharges;
               SWPedestals; SWPulseHeights; SWGainSwitch for all
               events, and the same distributions for laser
               events only (except, of course, for the pedestal
               events histograms).
               The input file is also updated with a vector
               containing the status of each channel, according to
               the color code in LTools.
runid_PedestalEvtsParameters.pdf   graphs showing the parameters
               describing the standard Pedestal Events histogram.
runid_HWChargesParameters.pdf      graphs showing the parameters
               describing the standard HWCharges histogram.
runid_HWPulseHeightParameters.pdf  graphs showing the parameters
               describing the standard HWPulseHeight histogram.
runid_HWPulsePositionParameters.pdf graphs showing the parameters
               describing the standard HWPulsePosition histogram.
runid_SWChargesParameters.pdf       graphs showing the parameters
               describing the standard SWCharges histogram.
runid_SWPedestalsParameters.pdf     graphs showing the parameters
               describing the standard SWPedestals histogram.
runid_SWPulseHeightParameters.pdf   graphs showing the parameters
               describing the standard SWPulseHeight histogram.
runid_ChannelDiagnosis.gif   a camera plot color coded to the
               channel status.
runid_HWChargesDistributions_laser.pdf 500 histograms of HWCharges
               of laser events (if -d is used)
runid_SWChargesDistributions_laser.pdf 500 histograms of SWCharges
               of laser events (if -d is used)
runid_SWPedestalsDistributions_laser.pdf 500 histograms of
               SWPedestals of laser events (if -d is used)
CamHWChargesfilename_event_telnum.pdf     a camera plot of the
               hardware calculated charges (if the -c option is
               used).
CamHWPedestalsfilename_event_telnum.pdf   a camera plot of the
               hardware calculated pedestals (if the -c option
               is used).
CamHWGainSwitchfilename_event_telnum.pdf  a camera plot of the
               hardware calculated gain switches (if the -c
               option is used).
CamSWChargesfilename_event_telnum.pdf    a camera plot of the
               software calculated charges (if the -c option
               is used).
CamSWPedestalsfilename_event_telnum.pdf  a camera plot of the
               software calculated pedestals (if the -c option
```

```
                is used).
  CamSWGainSwitchfilename_event_telnum.pdf a camera plot of the
                software calculated gain switches (if the -c
                option is used).
```

RelGain_Max

```
Usage: RelGain_Max <filename.root> [--minevent=<event_number>
           --Maxevent=<event_number>
           --printevent[=<event_number>] --printcode[=<print_code>]
           --cameraplot[=<camera_code>] --batch --writetodb --help]
Each option can be substituted by its first unambiguous abbreviation,
e.g. -r for --run.
Example: RelGain_Max 2211_2.root -m=1 -M=5 -printe=3 -printc=11

Reads a VERITAS ROOT tree, created with DataTree and processed with
Diagnosis, and computes the relative gains.  In addition the three
pixels with the largest charge in each event are determined and the
relative frequency with which each channel attains this status is
recorded.  The relative gain is computed by comparing the charge
in each PMT to the mean charge across the camera.  These relative
gains are computed for all laser events found in the requested events.
The final result is their average.  Only good channels, as given by
Diagnosis, are used in the computation of the mean charge across the
camera.
INPUTS:
  filename.root  is the VERITAS ROOT file to use as input, created
                 with LDataTree and diagnosed with Diagnosis.
  writetodb   If this flag is set, the program will only simulate
              writing to the DB.  By default the program writes to
              database and this flag should be used only when one
              wants to use the program for quick testing purposes.
OUTPUTS:
  filename.root  the input file is updated with the 500 distributions
                 of relative gains.
  RelGain_Max.txt  a text file of space seperated variables, ready
                   for input into the database.  The first line
                   consists of the run number and each following line
                   gives, for each channel in turn: relative gain;
                   standard deviation of relative gain; diagnosis status;
                   relative frequency of largest charge in an event;
                   relative frequency of second to largest charge in
                   an event;
                   relative frequency of third to largest charge in
                   an event;
                   relative frequency of top three charge in an event;
  MeanRelGain_filename_hist.gif   an histogram of the distribution
```

```
                of mean relative gains.
  MeanRelGain_filename_cam.gif    a camera plot of the mean relative
                gains.
  RelGain_filename_distributions.ps   the 500 channel distributions of
                relative gains used in computing the mean rel. gains.
  Max_Pixel1_filename_cam.gif   Camera plot of relative frequency of
                largest charge in an event.
  Max_Pixel2_filename_cam.gif   Camera plot of relative frequency of
                second largest charge in an event.
  Max_Pixel3_filename_cam.gif   Camera plot of relative frequency of
                third largest charge in an event.
  Max_PixelAll_filename_cam.gif Camera plot of relative frequency of
                top three charge in an event.
```

AbsGain

```
Usage: AbsGain <filename.root | runlist.txt> [--minevent=<event_number>
          --Maxevent=<event_number>
          --printevent[=<event_number>] --printcode[=<print_code>]
          --cameraplot[=<camera_code>] --channeltoanalyze=<channelnb>
          --batch --writetodb --help]
Each option can be substituted by its first unambiguous abbreviation,
e.g. -m for --minevent.
Example: AbsGain 2211_2.root -ch=1

Reads a VERITAS ROOT tree (or set of trees if the runlist option is
used), created with DataTree and processed with Diagnosis, and computes
the Absolute Gains for laser events using the sigma^2 over mu technique.
In computing the charge distributions, the laser fluctuations are
removed by monitoring the intensity of the laser pulses using the
average response of the good tubes in the camera.  The output of each
tube is scaled, for each event, according to the correction implied
by the laser monitor.  If a single file, with a single attenuation, is
used the graph of sigma^2 vs mu is assumed to pass through (0, 0) and
the gain computed accordingly.  If a runlist is used, with different
attenuations for each of the files, the gain is obtained from the
slope to the best fit of a straight line to the sigma^2 vs mu points,
without assuming a 0 intercept.  It's believed that this results in
more reliable gain estimates, the intercept being interpreted as NSB
or electronic noise contributions to the width of the charge
distributions when there is no laser light.  If the RelGain_Max
program was run on the last file of the runlist, then a comparison to
the relative gains obtained from this source is provided.
INPUTS:
  filename.root  is the VERITAS ROOT file to use as input, created
        with DataTree and diagnosed with Diagnosis.  Optionally may
        have been passed through RelGain_Max.
```

```
  runlist.txt is a text file containing a list of filename.root files
        as described above.  Each file should be specified on a
        different line.  Lines starting with // are ignored.  Sigma^2
        and mu from the different files are combined if a runlist is
        used and results in a better estimate for the gains.  A
        relevant name for this file, e.g. including the date, is a
        good idea, since the name of this file will be the base for
        the name of the output files.
  channeltoanalyze  asks the program to produce some plots regarding
        the specified channel.
  writetodb   If this flag is set, the program will only simulate
        writing to the DB.  By default the program writes to database
        and this flag should be used only when one wants to use the
        program for quick testing purposes.
OUTPUTS:
  filename.root  the input file is updated with vectors for the
        absolute and relative gains, number of photoelectrons, sigma
        and mu values for each channel.  There also are histograms
        for the distributions of gains and distributions of software
        charges before and after corrections for laser fluctuations,
        and profiles for the response of each channel wrt to the
        laser monitor.  All these outputs are in the AbsGain folder
        created in the root file.
  AbsGain_filename.txt  a text file of tab seperated values.  The
        columns are channel number, absolute gain, uncertainty,
        relative gain, uncertainty and channel status (as given by
        Diagnosis)
  Sigma2VSMu500_filename_Tx.ps  a plot showing the sigma^2 vs mu
        graphs for all channels.
```

LGradientFinder

```
Usage: LGradientFinder <filename.root | runlist.txt> [--GoodOnly
             --AllTests --RidiculousProbabilityCriterion=<Double_t>
             --batch --help]
Each option can be substituted by its first unambiguous abbreviation,
e.g. -b for --batch.
Example: LGradientFinder 2211_2.root -b -R=0.001 -G -A

Reads a VERITAS ROOT tree (or set of trees if the runlist option is
used), created with DataTree and processed with Diagnosis, RelGain_Max
and AbsGain, and compares the output of those programs in different
parts of the camera to verify that the quantities thesse programs
compute are uniformly distributed across the pixels of the cameras.
If uniformity is statistically improbable, the program gives the
probability for that to be the case, suggests a direction for a
possible gradient and displays diagnostic histograms showing the
```

```
comparisons made, as well as camera plots of the quantities where
evidence for gradients was found.  The program will only show up to 5
different gradients for each input file, in order to limit the number
of plots.
INPUTS:
  filename.root  is the VERITAS ROOT file to use as input, created
        with DataTree and diagnosed with Diagnosis, RelGain_Max and
        AbsGain.
  runlist.txt is a text file containing a list of filename.root files
        as described above.  Each file should be specified on a
        different line.  Lines starting with // are ignored.
  GoodOnly    A flag that specifies to do the comparisons only using
        the good tubes as given by Diagnosis.  If the flag is not
        specified, good tube and non-standard ones are used, but
        not the ones with L2 or the photodiode, or those that are dead.
  AllTests    A flag that specifies to compare all possible quantities
        across the different parts of the camera.  This can be long
        and produce many many plots.  So the default is not to use
        this flag, which will perform test of the basic quantities
        only.  Look at the code to find which ones.
  RidiculousProbabilityCriterion  is a number that specifies the
        boundary between the existence of a gradient or not.
        The smaller this number, the stronger the gradient will need
        to be before the program decides it's worth displaying it.
        The program actually computes the probability that the
        distribution of some quantity is uniform across some part of
        the camera and compares it to this criterion.
OUTPUTS:
   Nothing written to file for now.  Save any displayed graph
   manually if you want to keep them.
```

LEBL

```
Usage: LEBL <SpectrumName> [--limits --init --sorted --batch --help]
Each option can be substituted by its first unambiguous abbreviation,
Example: LEBL 1ES1218Luis -b

Computes the intrinsic spectrum of the given source for many different
realizations of the EBL photon density.  The algorithm is a recreation
of that used in Mazin&Raue: astro-ph/0701694.
Use the complementary program LEBL_Results to derive an upper limit on
the EBL photon density.  Important in this technique is to have
reliable fits.  A non-reliable fit can lead to acceptance of a curve
that would otherwise be rejected and can result in a EBL UL higher
than expected.  It is up to the user to try different values of the
options, and possibly to hack into the code in order to get a very
high percentage of reliable fits.
```

```
INPUTS:
  SpectrumName  is the observed spectrum to be used.
  Current options are:
     TestSpectrum
     1ES1218Luis
     1ES1218Pascal
     1ES1218MAGIC
     1ES1218Combined
     H1426HEGRA1999
     1ES1101HESS
     Mrk501HEGRA
  limits   Toggles between using limits for fits parameters, or not.
  init     Toggles between using custom initialisation for fits
           parameters, for every fit, or not.
           This can slow down the program quite a bit.
  sorted   Toggles between using sorted break points or allowing them
           to be arranged whatever way the fitter wants them, or not.
  viewlimitbuildup    Toggles between showing the limit on the EBL
           building up or not.  Slows down the calculation but useful
           in debugging.
  pause    Toggles between pausing and waiting for user input when a
           build up of the limit occurs, or not.
           This flag automatically enable the showlimitbuildup flag.
OUTPUTS:
  LEBLResults_SpectrumName.root  Contains the results of the fit and
           status of rejection or acceptance.
           Run LEBL_Results on this file to derive an upper limit.
  PPSplineIntegrals_SpectrumNamePrecision.root  Contains computed
           values of integrals of basis splines with pair produnction
           cross section.  Once computed, these integrals are reused
           the next time the program is run.  This saves
           initialization time.
```

LEBL_Results

```
Usage: LEBL_Results <FileName.root/txt> [--batch --help]
Each option can be substituted by its first unambiguous abbreviation,
Example: LEBL_Results LEBLResults_1ES1218Luis.root -b

Derive an upper limit on the EBL photon density from the results file
produced by LEBL
INPUTS:
  FileName.root/txt  is the root file or list of root files containing
  the results to be used.
OUTPUTS:
  Limits_FileName.root  Contains the derived limit on the EBL density.
```

E

Acronyms

In reading papers, one quickly gets lost with all the acronyms in use. Here is a compiled list of acronyms that may be useful in the field of astro-particle physics in general.

γ-ray Collaborations:

VERITAS Very Energetic Radiation Imaging Telescope Array System
FLWO Fred Lawrence Whipple Observatory
H.E.S.S. High Energy Stereoscopic System
HEGRA High Energy Gamma-Ray Astronomy
MAGIC Major Atmospheric Gamma-ray Imaging Čerenkov (Telescope)
CANGAROO Collaboration of Australia and Nippon (Japan) for a Gamma Ray Observatory in the Outback
CAT Čerenkov Array at Themis
STACEE Solar Tower Atmospheric Čerenkov Effect Experiment
CTA Čerenkov Telescope Array
AGIS Advanced Gamma ray Imaging System

Cosmic Rays:

UHECR Ultra-High Energy Cosmic Ray
CASA-MIA Chicago Air Shower Array - MIchigan muon Array
HiRes High Resolution Fly's Eye experiment
AGASA Akeno Giant Air Shower Array
KASCADE KArlsruhe Shower Core and Array DEtector
GZK Greisen-Zatsepin-K'uzmin

Satellites:

ESA European Space Agency
NASA National Aeronautics and Space Administration
ASCA Advanced Satellite for Cosmology and Astrophysics
RXTE Rossi X-ray Timing Explorer
EUVE Extreme UltraViolet Explorer
CGRO Compton Gamma Ray Observatory
- **BATSE** Burst And Transient Source Experiment
- **EGRET** Energetic Gamma Ray Experiment Telescope
- **OSSE** Oriented Scintillation Spectrometer Experiment

COMPTEL COMPTon TELescope

GLAST Gamma-ray Large Area Space Telescope
LAT Large Area Telescope
GBM Gamma-ray Burst Monitor

ASM All-Sky Monitor
IUE International Ultraviolet Explorer
EUVE Extreme Ultraviolet Explorer
RHESSI Reuven Ramaty High Energy Solar Spectroscopic Imager
AGILE Astro-rivelatore Gamma a Immagini LEggero
HETE-2 High Energy Transient Explorer 2
FREGATE French Gamma Telescope

INTEGRAL INTErnational Gamma-Ray Astrophysics Laboratory
IRAS InfraRed Astronomical Satellite
COBE COsmic Background Explorer
NIRS Near InfraRed Spectrometer
DIRBE Diffuse Infrared Background Experiment
OSO Orbiting Solar Observatory
SAS Small Astronomy Satellite
HST Hubble Space Telescope

Other Observatories:

UKIRT United Kingdom Infrared Telescope
UMRAO University of Michigan Radio Astronomy Observatory
JCMT James Clerk Maxwell Telescope
CAO Crimean Astrophysical Observatory
LOPES LOFAR PrototypE Station
LOFAR LOw Frequency ARray
HAWC High Altitude Water Čerenkov
OWL Orbiting Wide-field Light-collectors
EUSO Extreme-Universe Space Observatory
TrICE Track Imaging Čerenkov Experiment
MACE Major Atmospheric Cerenkov Experiment
GRATIS Gamma-Ray Astrophysical Telescope Imaging System
GAW Gamma Air Watch
VLA Very Large Array
VLBA Very Long Baseline Array
NRAO National Radio Astronomy Observatory
OMM Observatoire du Mont Mégantic
NSTTF National Solar Thermal Test Facility

Sources:

NSB Night Sky Background
LONS Light Of the Night Sky
SNR SuperNovae Remnant
QSO Quasi-Stellar Object
SSRQ Steep-Spectrum Radio Quasar
BLRG Broad-Line Radio Galaxies
FSRQ Flat-Spectrum Radio Quasar
NELG Narrow-Line-Emission X-ray Galaxies
NLRG Narrow-Line Radio Galaxies

AGN Active Galactic Nuclei
FR Faranhoff-Reilly
GRB Gamma-Ray Burst
CR Cosmic Ray

Blazars:
BL-Lac BL Lacertae
BLR Broad Line Region
HBL High energy peaked BL-Lac
XBLs X-ray selected BL-Lac
LBL Low energy peaked BL-Lac

Emission Processes:

IC(S) Inverse Compton (Scattering)
SSC Synchrotron Self Compton
EC External Compton
ERC External Radiation Compton
SEC Synchrotron External Compton
SPB Synchrotron Proton Blazar
BAL Broad-Absorption Line

Electronics and Computers:

PMT Photo Multiplier Tube
MAPMT Multi-Anode Photo Multiplier Tube
pe photoelectron
HV High Voltage
SSD Silicon Strip Detector
DACQ Data ACQuisition
VDAQ VME Data Acquisition
ADC Analog-to-Digital Converter
QADC Charge (Q) Analog-to-Digital Converter
FADC Flash Analog-to-Digital Converter
SCI Scalable Coherent Interface
PST Pattern Selection Trigger
GIT Gain Inference Technique
FGIT Flash Gain Inference Technique
RF Radio Frequency
CFD Constant Fraction Discriminator
RFB Rate Feed-Back
DATs Digital Asynchronous Transceiver modules
PPG Programmable Pulse Generator
PDM Pulse Delay Module
SAT SubArray Trigger board
PCB Printed Circuit Board
VME Virtual Machine Environment
CPU Central Processing Unit
POSIX Portable Operating System Interface for UNIX
PC Personal Computer
CORBA Common Object Request Broker Architecture
Gbps GigaBits Per Second
Kbps KiloBits Per Second
Mbps MegaBits Per Second

SBC Single Board Computer

Energy Bands, Energy Units and Related Backgrounds:

CBR Cosmic Background Radiation
DEBRA Diffuse Extragalactic Background RAdiation
EBL Extragalactic Background Light
EGL ExtraGalactic Light
IBL Intergalactic Background Light
CRB Cosmic Radio Background
CMB Cosmic Microwave Background
CMBR Cosmic Microwave Background Radiation
CIB Cosmic Infrared Background
IR InfraRed
IRB InfraRed Background
NIR Near InfraRed
MIR Mid InfraRed
FIR Far InfraRed
CUVOB Cosmic UV and Optical Background
UV Ultra Violet
CXB Cosmic X-ray Background
CGB Cosmic Gamma-ray Background
LE Low Energy
HE High Energy
VHE Very High Energy
UHE Ultra High Energy
eV Electron Volt ($1\ \mathrm{eV} = 1.602176462(63) \times 10^{-19}$ J)
keV Kilo-electron Volt ($= 1 \times 10^3$ eV $= 160.2$ aJ)
MeV Mega-electron Volt ($= 1 \times 10^6$ eV $= 160.2$ fJ)
GeV Giga-electron Volt ($= 1 \times 10^9$ eV $= 160.2$ pJ)
TeV Tera-electron Volt ($= 1 \times 10^{12}$ eV $= 160.2$ nJ)
PeV Peta-electron Volt ($= 1 \times 10^{15}$ eV $= 160.2\ \mu$J)
EeV Exa-electron Volt ($= 1 \times 10^{18}$ eV $= 160.2$ mJ)

Telescope:

ZA Zenith Angle
LZA Large Zenith Angle
LOS Line Of Sight
OSS Optical Support Structure
FOV Field Of View
IACT Imaging Atmospheric Čerenkov Telescope (or Technique)
ACT Atmospheric Čerenkov Telescope (or Technique)

VERITAS:

VEGAS VERITAS Experiment Gamma-Analysis Suite
VBF VERITAS Bank Format
HVAC High Voltage Array Control
DQM Daily Quality Monitoring

GRISU Gamma-Ray Instruments Simulation Utility, the Grinnell-ISU simulation and analysis package
SWG Science Working Group
TAC Time Allocation Committee
VPC VERITAS Publications Committee
VAC VERITAS Array Control
VEC VERITAS Executive Committee
MRS Mean Reduced Scaled
MSP Mean Scaled Parameter
MSW Mean Scaled Width
MSL Mean Scaled Length
RMS Reduced Mean Scaled
WRMS Weighted Reduced Mean Scaled

General Astrophysics:

EAS Extensive Air Shower
PIC Proton Induced Cascade
ISM InterStellar Medium
MC Monte Carlo
MJD Modified Julian Date
SED Spectral Energy Distribution
EM ElectroMagnetic
GCN Gamma-ray burst Coordinate Network
GPS Global Positioning System
TOO Targets Of Opportunity
PSF Point Spread Function
PBH Primordial Black Hole
NED NASA/IPAC Extragalactic Database
CDS Centre de Donnes astronomiques de Strasbourg
FITS Flexible Image Transport System
CASCA Canadian Astronomical Society/ Société Canadienne d'Astronomie

Quantum Gravity:

LI Lorentz Invariance
LIV Lorentz Invariance Violation
LSV Lorentz Symmetry Violation
MAV Maximum Attainable Velocity
LDRK Linearly Deformed Relativistic Kinematics
QDRK Quadratically Deformed Relativistic Kinematics
DLS Deformed Lorentz Symmetry

Other:

FTE Full Time Equipment
QE Quantum Efficiency
QED Quantum Electro-Dynamics
QED Quod Erat Demonstrandum
QI Charge (Q) Injection
TBD To Be Determined
TBR To Be Resolved
DOE Department Of Energy
NSF National Science Foundation

REFERENCES

Bibliography

[1] John Kildea, *γ-ray Astronomy*, September 2003. Talk given at McGill University.

[2] Deirdre Horan and Scott Wakely , *TeVCat: Online Catalog for TeV Astronomy*, *http://tevcat.uchicago.edu/*, 2007. [LINK].

[3] Julian H. Krolik. *Active Galactic Nuclei: From the Central Black Hole to the Galactic Environment*. Princeton University Press, 41 William Street, Princeton, New Jersey 08540, first edition, 1999.

[4] Deirdre Horan. *The Discovery of TeV γ rays from the BL Lacertae object, 1H1426+428*. PhD thesis, School of Physics, University College Dublin, September 2001.

[5] C. M. Urry and P. Padovani. *The Unification of Radio-Loud AGN*. In R. D. Ekers, C. Fanti, and L. Padrielli, editors, *Extragalactic Radio Sources*, volume 175 of *IAU Symposium*, pages 379–+, 1996. [ADS].

[6] Trevor C. Weekes. *Very High Energy Gamma-Ray Astronomy*. Institute of Physics Publishing, The Public Ledger Building, Suite 929, 150 South Independence Mall West, Philadelphia, PA 19106, U.S.A., first edition, 2003.

[7] M. J. Rees, *Appearance of Relativistically Expanding Radio Sources*, Nature, 211:468–+, July 1966. [ADS].

[8] A. R. Whitney, I. I. Shapiro, A. E. E. Rogers, D. S. Robertson, C. A. Knight, T. A. Clark, R. M. Goldstein, G. E. Marandino, and N. R. Vandenberg, *Quasars Revisited: Rapid Time Variations Observed Via Very-Long-Baseline Interferometry*, *Science*, 173:225–230, July 1971. [ADS].

[9] Michael J. Carson. *Astrophysical Limits On Quantum Gravity Energy Scales*. PhD thesis, School of Physics, University College Dublin, July 2000.

[10] M. Catanese and T. C. Weekes, *Very High Energy Gamma-Ray Astronomy*, PASP, 111:1193–1222, October 1999, arXiv:astro-ph/9906501. [ADS].

[11] M. Punch, C. W. Akerlof, M. F. Cawley, M. Chantell, D. J. Fegan, S. Fennell, J. A. Gaidos, J. Hagan, A. M. Hillas, Y. Jiang, A. D. Kerrick, R. C. Lamb, M. A. Lawrence, D. A. Lewis, D. I. Meyer, G. Mohanty, K. S. O'Flaherty, P. T. Reynolds, A. C. Rovero, M. S. Schubnell, G. Sembroski, T. C. Weekes, and C. Wilson, *Detection of TeV photons from the active galaxy Markarian 421*, Nature, 358:477–+, August 1992. [ADS].

[12] J. Quinn, C. W. Akerlof, S. Biller, J. Buckley, D. A. Carter-Lewis, M. F. Cawley, M. Catanese, V. Connaughton, D. J. Fegan, J. P. Finley, J. Gaidos, A. M. Hillas, R. C. Lamb, F. Krennrich, R. Lessard, J. E. McEnery, D. I. Meyer, G. Mohanty, A. J. Rodgers, H. J. Rose, G. Sembroski, M. S. Schubnell, T. C. Weekes, C. Wilson, and J. Zweerink, *Detection of Gamma Rays with $E > 300$ GeV from Markarian 501*, ApJ, 456:L83+, January 1996. [ADS].

[13] F. Krennrich, S. D. Biller, I. H. Bond, P. J. Boyle, S. M. Bradbury, A. C. Breslin, J. H. Buckley, A. M. Burdett, J. B. Gordo, D. A. Carter-Lewis, M. Catanese, M. F. Cawley, D. J. Fegan, J. P. Finley, J. A. Gaidos, T. Hall, A. M. Hillas, R. C. Lamb, R. W. Lessard, C. Masterson, J. E. McEnery, G. Mohanty, P. Moriarty, J. Quinn, A. J. Rodgers, H. J. Rose, F. W. Samuelson, G. H. Sembroski, R. Srinivasan, V. V. Vassiliev, and T. C. Weekes, *Measurement of the Multi-TEV Gamma-Ray Flare Spectra of Markarian 421 and Markarian 501*, ApJ, 511:149–156, January 1999, arXiv:astro-ph/9808333. [ADS].

[14] J. A. Gaidos, C. W. Akerlof, S. D. Biller, P. J. Boyle, A. C. Breslin, J. H. Buckley, D. A. Carter-Lewis, M. Catanese, M. F. Cawley, D. J. Fegan, J. P. Finley, A. M. Hillas, F. Krennrich, R. C. Lamb, R. Lessard, J. McEnery, G. Mohanty, P. Moriarty, J. Quinn, A. Rodgers, H. J. Rose, F. Samuelson, M. S. Schubnell, G. Sembroski, R. Srinivasan, T. C. Weekes, C. L. Wilson, and J. Zweerink, *Very Rapid and Energetic Bursts of TeV Photons from the Active Galaxy Markarian 421.*, Nature, 383:319–+, 1996. [ADS].

[15] F. Aharonian, A. G. Akhperjanian, A. R. Bazer-Bachi, B. Behera, M. Beilicke, W. Benbow, D. Berge, K. Bernlöhr, C. Boisson, O. Bolz, V. Borrel, T. Boutelier, I. Braun, E. Brion, A. M. Brown, R. Bühler, I. Büsching, T. Bulik, S. Carrigan, P. M. Chadwick, A. C. Clapson, L.-M. Chounet, G. Coignet, R. Cornils, L. Costamante, B. Degrange, H. J. Dickinson, A. Djannati-Ataï, W. Domainko, L. O. Drury, G. Dubus, J. Dyks, K. Egberts, D. Emmanoulopoulos, P. Espigat, C. Farnier, F. Feinstein, A. Fiasson, A. Förster, G. Fontaine, S. Funk, S. Funk, M. Füßling, Y. A. Gallant, B. Giebels, J. F. Glicenstein, B. Glück, P. Goret, C. Hadjichristidis, D. Hauser, M. Hauser, G. Heinzelmann, G. Henri, G. Hermann, J. A. Hinton, A. Hoffmann, W. Hofmann, M. Holleran, S. Hoppe, D. Horns, A. Jacholkowska, O. C. de Jager, E. Kendziorra, M. Kerschhaggl, B. Khélifi, N. Komin, K. Kosack, G. Lamanna, I. J. Latham, R. Le Gallou, A. Lemière, M. Lemoine-Goumard, J.-P. Lenain, T. Lohse, J. M. Martin, O. Martineau-Huynh, A. Marcowith, C. Masterson, G. Maurin, T. J. L. McComb, R. Moderski, E. Moulin, M. de Naurois, D. Nedbal, S. J. Nolan, J.-P. Olive, K. J. Orford, J. L. Osborne, M. Ostrowski, M. Panter, G. Pedaletti, G. Pelletier, P.-O. Petrucci, S. Pita, G. Pühlhofer, M. Punch, S. Ranchon, B. C. Raubenheimer, M. Raue, S. M. Rayner, M. Renaud, J. Ripken, L. Rob, L. Rolland, S. Rosier-Lees, G. Rowell, B. Rudak, J. Ruppel, V. Sahakian, A. Santangelo, L. Saugé, S. Schlenker, R. Schlickeiser, R. Schröder, U. Schwanke, S. Schwarzburg, S. Schwemmer, A. Shalchi, H. Sol, D. Spangler, Ł. Stawarz, R. Steenkamp, C. Stegmann, G. Superina, P. H. Tam, J.-P. Tavernet, R. Terrier, C. van Eldik, G. Vasileiadis, C. Venter, J. P. Vialle, P. Vincent,

M. Vivier, H. J. Völk, F. Volpe, S. J. Wagner, M. Ward, and A. A. Zdziarski, *An Exceptional Very High Energy Gamma-Ray Flare of PKS 2155-304*, ApJ, 664:L71–L74, August 2007, arXiv:0706.0797. [ADS].

[16] J. Albert, E. Aliu, H. Anderhub, P. Antoranz, A. Armada, C. Baixeras, J. A. Barrio, H. Bartko, D. Bastieri, J. K. Becker, W. Bednarek, K. Berger, C. Bigongiari, A. Biland, R. K. Bock, P. Bordas, V. Bosch-Ramon, T. Bretz, I. Britvitch, M. Camara, E. Carmona, A. Chilingarian, J. A. Coarasa, S. Commichau, J. L. Contreras, J. Cortina, M. T. Costado, V. Curtef, V. Danielyan, F. Dazzi, A. De Angelis, C. Delgado, R. de los Reyes, B. De Lotto, E. Domingo-Santamaría, D. Dorner, M. Doro, M. Errando, M. Fagiolini, D. Ferenc, E. Fernández, R. Firpo, J. Flix, M. V. Fonseca, L. Font, M. Fuchs, N. Galante, R. J. García-López, M. Garczarczyk, M. Gaug, M. Giller, F. Goebel, D. Hakobyan, M. Hayashida, T. Hengstebeck, A. Herrero, D. Höhne, J. Hose, D. Hrupec, C. C. Hsu, P. Jacon, T. Jogler, R. Kosyra, D. Kranich, R. Kritzer, A. Laille, E. Lindfors, S. Lombardi, F. Longo, J. López, M. López, E. Lorenz, P. Majumdar, G. Maneva, K. Mannheim, O. Mansutti, M. Mariotti, M. Martínez, D. Mazin, C. Merck, M. Meucci, M. Meyer, J. M. Miranda, R. Mirzoyan, S. Mizobuchi, A. Moralejo, D. Nieto, K. Nilsson, J. Ninkovic, E. Oña-Wilhelmi, N. Otte, I. Oya, D. Paneque, M. Panniello, R. Paoletti, J. M. Paredes, M. Pasanen, D. Pascoli, F. Pauss, R. Pegna, M. Persic, L. Peruzzo, A. Piccioli, E. Prandini, N. Puchades, A. Raymers, W. Rhode, M. Ribó, J. Rico, M. Rissi, A. Robert, S. Rügamer, A. Saggion, T. Saito, A. Sánchez, P. Sartori, V. Scalzotto, V. Scapin, R. Schmitt, T. Schweizer, M. Shayduk, K. Shinozaki, S. N. Shore, N. Sidro, A. Sillanpää, D. Sobczynska, A. Stamerra, L. S. Stark, L. Takalo, F. Tavecchio, P. Temnikov, D. Tescaro, M. Teshima, D. F. Torres, N. Turini, H. Vankov, V. Vitale, R. M. Wagner, T. Wibig, W. Wittek, F. Zandanel, R. Zanin, and J. Zapatero, *Variable Very High Energy γ-Ray Emission from Markarian 501*, ApJ, 669:862–883, November 2007, arXiv:astro-ph/0702008. [ADS].

[17] T. Weekes, *Astrophysics: Photons from a hotter hell*, Nature, 448:760–762, August 2007. [ADS].

[18] M. C. Begelman, A. C. Fabian, and M. J. Rees, *Implications of very rapid TeV variability in blazars*, *ArXiv e-prints*, 709, September 2007, 0709.0540. [ADS].

[19] G. Fossati, L. Maraschi, A. Celotti, A. Comastri, and G. Ghisellini, *A unifying view of the spectral energy distributions of blazars*, MNRAS, 299:433–448, September 1998, arXiv:astro-ph/9804103. [ADS].

[20] G. Ghisellini, A. Celotti, G. Fossati, L. Maraschi, and A. Comastri, *A theoretical unifying scheme for gamma-ray bright blazars*, MNRAS, 301:451–468, December 1998, arXiv:astro-ph/9807317. [ADS].

[21] M. Böttcher, *Modeling the emission processes in blazars*, Ap&SS, 309:95–104, June 2007, arXiv:astro-ph/0608713. [ADS].

[22] P. Padovani, *The blazar sequence: validity and predictions*, Ap&SS, 309:63–71, June 2007, arXiv:astro-ph/0610545. [ADS].

[23] W. Cui, *TeV Astrophysics, A Review*, *ArXiv Astrophysics e-prints*, August 2006, astro-ph/0608042. [ADS].

[24] The Pierre Auger Collaboration, *Correlation of the highest energy cosmic rays with nearby extragalactic objects*, *Science*, 318:939, 2007. [LINK].

[25] J. H. Buckley, *ASTROPHYSICS: What the Wild Things Are*, *Science*, 279:676–+, January 1998. [ADS].

[26] G. Colla, C. Fanti, A. Ficarra, L. Formiggini, E. Gandolfi, G. Grueff, C. Lari, L. Padrielli, G. Roffi, P. Tomasi, and M. Vigotti, *A catalogue of 3235 radio sources at 408 MHz*, A&AS, 1:281–+, March 1970. [ADS].

[27] L. Costamante and G. Ghisellini, *TeV candidate BL Lac objects*, A&A, 384:56–71, March 2002, arXiv:astro-ph/0112201. [ADS].

[28] R. L. White, R. H. Becker, M. D. Gregg, S. A. Laurent-Muehleisen, M. S. Brotherton, C. D. Impey, C. E. Petry, C. B. Foltz, F. H. Chaffee, G. T. Richards, W. R. Oegerle, D. J. Helfand, R. G. McMahon, and J. E. Cabanela, *The FIRST Bright Quasar Survey. II. 60 Nights and 1200 Spectra Later*, ApJS, 126:133–207, February 2000, arXiv:astro-ph/9912215. [ADS].

[29] N. Bade, V. Beckmann, N. G. Douglas, P. D. Barthel, D. Engels, L. Cordis, P. Nass, and W. Voges, *On the evolutionary behaviour of BL Lac objects*, A&A, 334:459–472, June 1998, arXiv:astro-ph/9803204. [ADS].

[30] D. Weistrop, R. F. Mushotzky, D. B. Shaffer, H. J. Reitsema, and B. A. Smith, *CCD photometry of the BL Lacertae objects 1218+304, 1219+28, and 1727+50 - Point sources, associated nebulosity, and broad-band spectra*, ApJ, 249:3–12, October 1981. [ADS].

[31] J. D. Finke, J. C. Shields, M. Boettcher, and S. Basu, *Redshift Limits of BL Lacertae Objects from Optical Spectroscopy*, *ArXiv e-prints*, 711, November 2007, 0711.2089. [ADS].

[32] M. Giroletti, G. Giovannini, G. B. Taylor, and R. Falomo, *A Sample of Low-Redshift BL Lacertae Objects. I. The Radio Data*, ApJ, 613:752–769, October 2004, arXiv:astro-ph/0406255. [ADS].

[33] C. M. Urry, R. Scarpa, M. O'Dowd, R. Falomo, J. E. Pesce, and A. Treves, *The Hubble Space Telescope Survey of BL Lacertae Objects. II. Host Galaxies*, ApJ, 532:816–829, April 2000, arXiv:astro-ph/9911109. [ADS].

[34] X.-B. Wu, F. K. Liu, and T. Z. Zhang, *Supermassive black hole masses of AGNs with elliptical hosts*, A&A, 389:742–751, July 2002, arXiv:astro-ph/0203158. [ADS].

[35] J.-H. Woo and C. M. Urry, *Active Galactic Nucleus Black Hole Masses and Bolometric Luminosities*, ApJ, 579:530–544, November 2002, arXiv:astro-ph/0207249. [ADS].

[36] A. J. Blustin, M. J. Page, and G. Branduardi-Raymont, *Intrinsic absorbers in BL Lac objects: The XMM-Newton view*, A&A, 417:61–70, April 2004, arXiv:astro-ph/0312599. [ADS].

[37] R. Sato, J. Kataoka, T. Takahashi, G. M. Madejski, S. Rügamer, and S. J. Wagner, *Suzaku Observation of the TeV Blazar 1ES 1218+304: Clues on Particle Acceleration in an Extreme TeV Blazar*, ApJ, 680:L9–L12, June 2008. [ADS].

[38] D. Horan, H. M. Badran, I. H. Bond, P. J. Boyle, S. M. Bradbury, J. H. Buckley, D. A. Carter-Lewis, M. Catanese, O. Celik, W. Cui, M. Daniel, M. D'Vali, I. de la Calle Perez, C. Duke, A. Falcone, D. J. Fegan, S. J. Fegan, J. P. Finley, L. F. Fortson, J. A. Gaidos, S. Gammell, K. Gibbs, G. H. Gillanders, J. Grube, J. Hall, T. A. Hall, D. Hanna, A. M. Hillas, J. Holder, A. Jarvis, M. Jordan, G. E. Kenny, M. Kertzman, D. Kieda, J. Kildea, J. Knapp, K. Kosack, H. Krawczynski, F. Krennrich, M. J. Lang, S. Le Bohec, E. Linton, J. Lloyd-Evans, A. Milovanovic, P. Moriarty, D. Muller, T. Nagai, S. Nolan, R. A. Ong, R. Pallassini, D. Petry, B. Power-Mooney, J. Quinn, M. Quinn, K. Ragan, P. Rebillot, P. T. Reynolds, H. J. Rose, M. Schroedter, G. H. Sembroski, S. P. Swordy, A. Syson, V. V. Vassiliev, S. P. Wakely, G. Walker, T. C. Weekes, and J. Zweerink, *Constraints on the Very High Energy Emission from BL Lacertae Objects*, ApJ, 603:51–61, March 2004, arXiv:astro-ph/0311397. [ADS].

[39] F. Aharonian, A. Akhperjanian, M. Beilicke, K. Bernlöhr, H.-G. Börst, H. Bojahr, O. Bolz, T. Coarasa, J. L. Contreras, J. Cortina, S. Denninghoff, V. Fonseca, M. Girma, N. Götting, G. Heinzelmann, G. Hermann, A. Heusler, W. Hofmann, D. Horns, I. Jung, R. Kankanyan, M. Kestel, A. Konopelko, H. Kornmeyer, D. Kranich, H. Lampeitl, M. Lopez, E. Lorenz, F. Lucarelli, O. Mang, D. Mazin, H. Meyer, R. Mirzoyan, A. Moralejo, E. Ona-Wilhelmi, M. Panter, A. Plyasheshnikov, G. Pühlhofer, R. de los Reyes, W. Rhode, J. Ripken, G. Rowell, V. Sahakian, M. Samorski, M. Schilling, M. Siems, D. Sobzynska, W. Stamm, M. Tluczykont, V. Vitale, H. J. Völk, C. A. Wiedner, and W. Wittek, *Observations of 54 Active Galactic Nuclei with the HEGRA system of Cherenkov telescopes*, A&A, 421:529–537, July 2004. [ADS].

[40] STACEE Collaboration: R. Mukherjee, N. Akhter, J. Ball, J. E. Carson, C. E. Covault, D. D. Driscoll, P. Fortin, D. M. Gingrich, D. S. Hanna, A. Jarvis, J. Kildea, T. Lindner, C. Mueller, R. A. Ong, K. Ragan, D. A. Williams, and J. Zweerink, *STACEE Observations of 1ES 1218+304*, *ArXiv e-prints*, 710, October 2007, 0710.4170. [ADS].

[41] J. Albert, E. Aliu, H. Anderhub, P. Antoranz, A. Armada, M. Asensio, C. Baixeras, J. A. Barrio, M. Bartelt, H. Bartko, D. Bastieri, S. R. Bavikadi, W. Bednarek, K. Berger, C. Bigongiari, A. Biland, E. Bisesi, R. K. Bock, T. Bretz, I. Britvitch, M. Camara, A. Chilingarian, S. Ciprini, J. A. Coarasa,

S. Commichau, J. L. Contreras, J. Cortina, V. Curtef, V. Danielyan, F. Dazzi, A. De Angelis, R. de los Reyes, B. De Lotto, E. Domingo-Santamaría, D. Dorner, M. Doro, M. Errando, M. Fagiolini, D. Ferenc, E. Fernández, R. Firpo, J. Flix, M. V. Fonseca, L. Font, N. Galante, M. Garczarczyk, M. Gaug, M. Giller, F. Goebel, D. Hakobyan, M. Hayashida, T. Hengstebeck, D. Höhne, J. Hose, P. Jacon, O. Kalekin, D. Kranich, A. Laille, T. Lenisa, P. Liebing, E. Lindfors, F. Longo, J. López, M. López, E. Lorenz, F. Lucarelli, P. Majumdar, G. Maneva, K. Mannheim, M. Mariotti, M. Martínez, K. Mase, D. Mazin, M. Meucci, M. Meyer, J. M. Miranda, R. Mirzoyan, S. Mizobuchi, A. Moralejo, K. Nilsson, E. Oña-Wilhelmi, R. Orduña, N. Otte, I. Oya, D. Paneque, R. Paoletti, M. Pasanen, D. Pascoli, F. Pauss, N. Pavel, R. Pegna, M. Persic, L. Peruzzo, A. Piccioli, M. Poller, E. Prandini, W. Rhode, J. Rico, B. Riegel, M. Rissi, A. Robert, S. Rügamer, A. Saggion, A. Sánchez, P. Sartori, V. Scalzotto, R. Schmitt, T. Schweizer, M. Shayduk, K. Shinozaki, S. N. Shore, N. Sidro, A. Sillanpää, D. Sobczyńska, A. Stamerra, L. S. Stark, L. Takalo, P. Temnikov, D. Tescaro, M. Teshima, N. Tonello, A. Torres, D. F. Torres, N. Turini, H. Vankov, A. Vardanyan, V. Vitale, R. M. Wagner, T. Wibig, W. Wittek, and J. Zapatero, *Discovery of Very High Energy Gamma Rays from 1ES 1218+30.4*, ApJ, 642:L119–L122, May 2006, arXiv:astro-ph/0603529. [ADS].

[42] P. Fortin, *Observations of the high-frequency-peaked BL Lac object 1ES 1218+304 with VERITAS*, *ArXiv e-prints*, 709, September 2007, 0709.3657. [ADS].

[43] P. Fortin, *VERITAS observations of the BL Lac object 1ES 1218+304*, *To be published in* ApJ, July 2008. [LINK].

[44] Thomas Bretz. *Observations of the Active Galactic Nucleus 1ES 1218 + 30.4 with the MAGIC-telescope.* PhD thesis, Bayerischen Julius-Maximilians-Universitat Wurzburg, 2006.

[45] Luis Valcarcel. *Gravitational Lorentz violations in 5D black hole background: A Numerical investigation.* Master's thesis, McGill University, August 2003. UMI-MQ-98756.

[46] G. Amelino-Camelia, John Ellis, N. E. Mavromatos, D. V. Nanopoulos, and Subir Sarkar, *Tests of quantum gravity from observations of γ-ray bursts*, *Nature*, 393:763–765, 06 1998.

[47] J. Albert, for the MAGIC Collaboration, J. Ellis, N. E. Mavromatos, D. V. Nanopoulos, A. S. Sakharov, and E. K. G. Sarkisyan, *Probing Quantum Gravity using Photons from a Mkn 501 Flare Observed by MAGIC*, *ArXiv e-prints*, 708, August 2007, 0708.2889. [ADS].

[48] Robert J. Gould and Gérard P. Schréder, *Pair Production in Photon-Photon Collisions*, *Phys. Rev.*, 155(5):1404–1407, Mar 1967.

[49] F. A. Aharonian, A. M. Atoian, and A. M. Nagapetian, *Photoproduction of electron-positron pairs in compact X-ray sources*, *Astrofizika*, 19:323–334, April 1983. [ADS].

[50] F. A. Aharonian. *Very High Energy Cosmic Gamma Radiation: A Crucial Window on the Extreme Universe*. World Scientific, 5 Toh Tuck Link, Singapore 596224, 2004.

[51] A. J. Nikishov, *Soviet Phys.-JETP*, 14:393, 1962.

[52] Robert J. Gould and Gerald Schréder, *Opacity of the Universe to High-Energy Photons*, *Phys. Rev. Lett.*, 16(6):252–254, Feb 1966. [LINK].

[53] J. V. Jelley, *High-Energy γ-Ray Absorption in Space by a 3.5° K Microwave Field*, *Phys. Rev. Lett.*, 16(11):479–481, Mar 1966. [LINK].

[54] M. G. Hauser and E. Dwek, *The Cosmic Infrared Background: Measurements and Implications*, ARA&A, 39:249–307, 2001, arXiv:astro-ph/0105539. [ADS].

[55] J. R. Primack, R. S. Somerville, J. S. Bullock, and J. E. G. Devriendt. *Probing Galaxy Formation with High-Energy Gamma Rays*. In F. A. Aharonian and H. J. Völk, editors, *American Institute of Physics Conference Series*, volume 558 of *American Institute of Physics Conference Series*, pages 463–+, 2001. [ADS].

[56] F. W. Stecker, M. A. Malkan, and S. T. Scully, *Intergalactic Photon Spectra from the Far-IR to the UV Lyman Limit for $0 < z < 6$ and the Optical Depth of the Universe to High-Energy Gamma Rays*, ApJ, 648:774–783, September 2006, arXiv:astro-ph/0510449. [ADS].

[57] E. Dwek, R. G. Arendt, and F. Krennrich, *The Near-Infrared Background: Interplanetary Dust or Primordial Stars?*, ApJ, 635:784–794, December 2005, arXiv:astro-ph/0508262. [ADS].

[58] F. Krennrich, I. H. Bond, S. M. Bradbury, J. H. Buckley, D. A. Carter-Lewis, W. Cui, I. de la Calle Perez, D. J. Fegan, S. J. Fegan, J. P. Finley, J. A. Gaidos, K. Gibbs, G. H. Gillanders, T. A. Hall, A. M. Hillas, J. Holder, D. Horan, M. Jordan, M. Kertzman, D. Kieda, J. Kildea, J. Knapp, K. Kosack, M. J. Lang, S. LeBohec, P. Moriarty, D. Müller, R. A. Ong, R. Pallassini, D. Petry, J. Quinn, N. W. Reay, P. T. Reynolds, H. J. Rose, G. H. Sembroski, R. Sidwell, N. Stanton, S. P. Swordy, V. V. Vassiliev, S. P. Wakely, and T. C. Weekes, *Discovery of Spectral Variability of Markarian 421 at TeV Energies*, ApJ, 575:L9–L13, August 2002, arXiv:astro-ph/0207184. [ADS].

[59] F. Aharonian, A. Akhperjanian, M. Beilicke, K. Bernlöhr, H. Börst, H. Bojahr, O. Bolz, T. Coarasa, J. Contreras, J. Cortina, L. Costamante, S. Denninghoff, V. Fonseca, M. Girma, N. Götting, G. Heinzelmann, G. Hermann,

A. Heusler, W. Hofmann, D. Horns, I. Jung, R. Kankanyan, M. Kestel, J. Kettler, A. Kohnle, A. Konopelko, H. Kornmeyer, D. Kranich, H. Krawczynski, H. Lampeitl, M. Lopez, E. Lorenz, F. Lucarelli, O. Mang, H. Meyer, R. Mirzoyan, M. Milite, A. Moralejo, E. Ona, M. Panter, A. Plyasheshnikov, G. Pühlhofer, G. Rauterberg, R. Reyes, W. Rhode, J. Ripken, G. Rowell, V. Sahakian, M. Samorski, M. Schilling, M. Siems, D. Sobzynska, W. Stamm, M. Tluczykont, H. J. Völk, C. A. Wiedner, W. Wittek, and R. A. Remillard, *Variations of the TeV energy spectrum at different flux levels of Mkn 421 observed with the HEGRA system of Cherenkov telescopes*, A&A, 393:89–99, October 2002. [ADS].

[60] E. Dwek and F. Krennrich, *Simultaneous Constraints on the Spectrum of the Extragalactic Background Light and the Intrinsic TeV Spectra of Markarian 421, Markarian 501, and H1426+428*, ApJ, 618:657–674, January 2005, arXiv:astro-ph/0406565. [ADS].

[61] A. Imran and F. Krennrich, *Detecting a unique EBL signature with TeV gamma rays*, *ArXiv e-prints*, 708, August 2007, 0708.3104. [ADS].

[62] M. Schroedter, *Upper Limits on the Extragalactic Background Light from the Very High Energy Gamma-Ray Spectra of Blazars*, ApJ, 628:617–628, August 2005, arXiv:astro-ph/0504397. [ADS].

[63] M. Persic and A. De Angelis, *Intergalactic absorption and blazar gamma-ray spectra*, *ArXiv e-prints*, 711, November 2007, 0711.2317. [ADS].

[64] D. Mazin and M. Raue, *New limits on the density of the extragalactic background light in the optical to the far infrared from the spectra of all known TeV blazars*, A&A, 471:439–452, August 2007, arXiv:astro-ph/0701694. [ADS].

[65] F. Aharonian, A. G. Akhperjanian, A. R. Bazer-Bachi, M. Beilicke, W. Benbow, D. Berge, K. Bernlöhr, C. Boisson, O. Bolz, V. Borrel, I. Braun, F. Breitling, A. M. Brown, P. M. Chadwick, L.-M. Chounet, R. Cornils, L. Costamante, B. Degrange, H. J. Dickinson, A. Djannati-Ataï, L. O. Drury, G. Dubus, D. Emmanoulopoulos, P. Espigat, F. Feinstein, G. Fontaine, Y. Fuchs, S. Funk, Y. A. Gallant, B. Giebels, S. Gillessen, J. F. Glicenstein, P. Goret, C. Hadjichristidis, D. Hauser, M. Hauser, G. Heinzelmann, G. Henri, G. Hermann, J. A. Hinton, W. Hofmann, M. Holleran, D. Horns, A. Jacholkowska, O. C. de Jager, B. Khélifi, S. Klages, N. Komin, A. Konopelko, I. J. Latham, R. Le Gallou, A. Lemière, M. Lemoine-Goumard, N. Leroy, T. Lohse, J. M. Martin, O. Martineau-Huynh, A. Marcowith, C. Masterson, T. J. L. McComb, M. de Naurois, S. J. Nolan, A. Noutsos, K. J. Orford, J. L. Osborne, M. Ouchrif, M. Panter, G. Pelletier, S. Pita, G. Pühlhofer, M. Punch, B. C. Raubenheimer, M. Raue, J. Raux, S. M. Rayner, A. Reimer, O. Reimer, J. Ripken, L. Rob, L. Rolland, G. Rowell, V. Sahakian, L. Saugé, S. Schlenker, R. Schlickeiser, C. Schuster, U. Schwanke, M. Siewert, H. Sol, D. Spangler, R. Steenkamp, C. Stegmann, J.-P. Tavernet, R. Terrier, C. G. Théoret, M. Tluczykont, C. van Eldik, G. Vasileiadis, C. Venter, P. Vincent, H. J. Völk, and S. J. Wagner, *A*

low level of extragalactic background light as revealed by γ-rays from blazars, Nature, 440:1018–1021, April 2006, arXiv:astro-ph/0508073. [ADS].

[66] F. Aharonian, A. G. Akhperjanian, A. R. Bazer-Bachi, M. Beilicke, W. Benbow, D. Berge, K. Bernlöhr, C. Boisson, O. Bolz, V. Borrel, I. Braun, E. Brion, A. M. Brown, R. Bühler, I. Büsching, T. Boutelier, S. Carrigan, P. M. Chadwick, L.-M. Chounet, G. Coignet, R. Cornils, L. Costamante, B. Degrange, H. J. Dickinson, A. Djannati-Ataï, L. O'C. Drury, G. Dubus, K. Egberts, D. Emmanoulopoulos, P. Espigat, C. Farnier, F. Feinstein, E. Ferrero, A. Fiasson, G. Fontaine, S. Funk, S. Funk, M. Füßling, Y. A. Gallant, B. Giebels, J. F. Glicenstein, B. Glück, P. Goret, C. Hadjichristidis, D. Hauser, M. Hauser, G. Heinzelmann, G. Henri, G. Hermann, J. A. Hinton, A. Hoffmann, W. Hofmann, M. Holleran, S. Hoppe, D. Horns, A. Jacholkowska, O. C. de Jager, E. Kendziorra, M. Kerschhaggl, B. Khélifi, N. Komin, K. Kosack, G. Lamanna, I. J. Latham, R. Le Gallou, A. Lemière, M. Lemoine-Goumard, T. Lohse, J. M. Martin, O. Martineau-Huynh, A. Marcowith, C. Masterson, G. Maurin, T. J. L. McComb, E. Moulin, M. de Naurois, D. Nedbal, S. J. Nolan, A. Noutsos, J.-P. Olive, K. J. Orford, J. L. Osborne, M. Panter, G. Pelletier, P.-O. Petrucci, S. Pita, G. Pühlhofer, M. Punch, S. Ranchon, B. C. Raubenheimer, M. Raue, S. M. Rayner, J. Ripken, L. Rob, L. Rolland, S. Rosier-Lees, G. Rowell, V. Sahakian, A. Santangelo, L. Saugé, S. Schlenker, R. Schlickeiser, R. Schröder, U. Schwanke, S. Schwarzburg, S. Schwemmer, A. Shalchi, H. Sol, D. Spangler, F. Spanier, R. Steenkamp, C. Stegmann, G. Superina, P. H. Tam, J.-P. Tavernet, R. Terrier, M. Tluczykont, C. van Eldik, G. Vasileiadis, C. Venter, J. P. Vialle, P. Vincent, H. J. Völk, S. J. Wagner, and M. Ward, *Detection of VHE gamma-ray emission from the distant blazar 1ES 1101-232 with HESS and broadband characterisation*, A&A, 470:475–489, August 2007, arXiv:0705.2946. [ADS].

[67] L. Costamante, *A low density of the extragalactic background light revealed by the H.E.S.S. spectra of the BL Lac objects 1ES 1101-232 and H 2356-309*, Ap&SS, 309:487–495, June 2007, arXiv:astro-ph/0612709. [ADS].

[68] F. Aharonian, A. G. Akhperjanian, U. Barres de Almeida, A. R. Bazer-Bachi, B. Behera, M. Beilicke, W. Benbow, K. Bernlöhr, C. Boisson, O. Bolz, V. Borrel, I. Braun, E. Brion, A. M. Brown, R. Bühler, T. Bulik, I. Büsching, T. Boutelier, S. Carrigan, P. M. Chadwick, L.-M. Chounet, A. C. Clapson, G. Coignet, R. Cornils, L. Costamante, M. Dalton, B. Degrange, H. J. Dickinson, A. Djannati-Ataï, W. Domainko, L. O'C. Drury, F. Dubois, G. Dubus, J. Dyks, K. Egberts, D. Emmanoulopoulos, P. Espigat, C. Farnier, F. Feinstein, A. Fiasson, A. Förster, G. Fontaine, S. Funk, M. Füßling, Y. A. Gallant, B. Giebels, J. F. Glicenstein, B. Glück, P. Goret, C. Hadjichristidis, D. Hauser, M. Hauser, G. Heinzelmann, G. Henri, G. Hermann, J. A. Hinton, A. Hoffmann, W. Hofmann, M. Holleran, S. Hoppe, D. Horns, A. Jacholkowska, O. C. de Jager, I. Jung, K. Katarzyński, E. Kendziorra, M. Kerschhaggl, B. Khélifi, D. Keogh, N. Komin, K. Kosack, G. Lamanna, I. J. Latham, A. Lemière,

M. Lemoine-Goumard, J.-P. Lenain, T. Lohse, J. M. Martin, O. Martineau-Huynh, A. Marcowith, C. Masterson, D. Maurin, G. Maurin, T. J. L. McComb, R. Moderski, E. Moulin, M. de Naurois, D. Nedbal, S. J. Nolan, S. Ohm, J.-P. Olive, E. de Oña Wilhelmi, K. J. Orford, J. L. Osborne, M. Ostrowski, M. Panter, G. Pedaletti, G. Pelletier, P.-O. Petrucci, S. Pita, G. Pühlhofer, M. Punch, S. Ranchon, B. C. Raubenheimer, M. Raue, S. M. Rayner, M. Renaud, J. Ripken, L. Rob, L. Rolland, S. Rosier-Lees, G. Rowell, B. Rudak, J. Ruppel, V. Sahakian, A. Santangelo, R. Schlickeiser, F. Schöck, R. Schröder, U. Schwanke, S. Schwarzburg, S. Schwemmer, A. Shalchi, H. Sol, D. Spangler, Ł. Stawarz, R. Steenkamp, C. Stegmann, G. Superina, P. H. Tam, J.-P. Tavernet, R. Terrier, C. van Eldik, G. Vasileiadis, C. Venter, J. P. Vialle, P. Vincent, M. Vivier, H. J. Völk, F. Volpe, S. J. Wagner, M. Ward, A. A. Zdziarski, and A. Zech, *Discovery of VHE γ-rays from the distant BL Lacertae 1ES 0347-121*, A&A, 473:L25–L28, October 2007, arXiv:0708.3021. [ADS].

[69] F. Aharonian, A. G. Akhperjanian, U. Barres de Almeida, A. R. Bazer-Bachi, B. Behera, M. Beilicke, W. Benbow, K. Bernlöhr, C. Boisson, O. Bolz, V. Borrel, I. Braun, E. Brion, A. M. Brown, R. Bühler, T. Bulik, I. Büsching, T. Boutelier, S. Carrigan, P. M. Chadwick, L.-M. Chounet, A. C. Clapson, G. Coignet, R. Cornils, L. Costamante, M. Dalton, B. Degrange, H. J. Dickinson, A. Djannati-Ataï, W. Domainko, L. O'C. Drury, F. Dubois, G. Dubus, J. Dyks, K. Egberts, D. Emmanoulopoulos, P. Espigat, C. Farnier, F. Feinstein, A. Fiasson, A. Förster, G. Fontaine, S. Funk, M. Füßling, Y. A. Gallant, B. Giebels, J. F. Glicenstein, B. Glück, P. Goret, C. Hadjichristidis, D. Hauser, M. Hauser, G. Heinzelmann, G. Henri, G. Hermann, J. A. Hinton, A. Hoffmann, W. Hofmann, M. Holleran, S. Hoppe, D. Horns, A. Jacholkowska, O. C. de Jager, I. Jung, K. Katarzyński, E. Kendziorra, M. Kerschhaggl, B. Khélifi, D. Keogh, N. Komin, K. Kosack, G. Lamanna, I. J. Latham, A. Lemière, M. Lemoine-Goumard, J.-P. Lenain, T. Lohse, J. M. Martin, O. Martineau-Huynh, A. Marcowith, C. Masterson, D. Maurin, G. Maurin, T. J. L. McComb, R. Moderski, E. Moulin, M. de Naurois, D. Nedbal, S. J. Nolan, S. Ohm, J.-P. Olive, E. de Oña Wilhelmi, K. J. Orford, J. L. Osborne, M. Ostrowski, M. Panter, G. Pedaletti, G. Pelletier, P.-O. Petrucci, S. Pita, G. Pühlhofer, M. Punch, S. Ranchon, B. C. Raubenheimer, M. Raue, S. M. Rayner, M. Renaud, J. Ripken, L. Rob, L. Rolland, S. Rosier-Lees, G. Rowell, B. Rudak, J. Ruppel, V. Sahakian, A. Santangelo, R. Schlickeiser, F. Schöck, R. Schröder, U. Schwanke, S. Schwarzburg, S. Schwemmer, A. Shalchi, H. Sol, D. Spangler, Ł. Stawarz, R. Steenkamp, C. Stegmann, G. Superina, P. H. Tam, J.-P. Tavernet, R. Terrier, C. van Eldik, G. Vasileiadis, C. Venter, J. P. Vialle, P. Vincent, M. Vivier, H. J. Völk, F. Volpe, S. J. Wagner, M. Ward, A. A. Zdziarski, and A. Zech, *New constraints on the mid-IR EBL from the HESS discovery of VHE γ-rays from 1ES 0229+200*, A&A, 475:L9–L13, November 2007, arXiv:0709.4584. [ADS].

[70] F. W. Stecker, *The Spectrum of 1ES0229 + 200 and the Cosmic Infrared Background*, *ArXiv e-prints*, 710, October 2007, 0710.2252. [ADS].

[71] F. W. Stecker, M. G. Baring, and E. J. Summerlin, *Blazar γ-Rays, Shock Acceleration, and the Extragalactic Background Light*, ApJ, 667:L29–L32, September 2007, arXiv:0707.4676. [ADS].

[72] R. Wagner, D. Dorner, M. Hayashida, T. Hengstebeck, D. Kranich, D. Mazin, D. Tescaro, for the MAGIC Collaboration, and N. Nowak, *Detection of Very-High Energy Gamma-Rays from the BL Lac Object PG 1553+113 with the MAGIC Telescope*, *ArXiv e-prints*, 711, November 2007, 0711.1586. [ADS].

[73] T. Kifune, *Invariance Violation Extends the Cosmic-Ray Horizon?*, ApJ, 518:L21–L24, June 1999, arXiv:astro-ph/9904164. [ADS].

[74] S. Coleman and S. L. Glashow, *High-energy tests of Lorentz invariance*, Phys. Rev. D, 59(11):116008–+, June 1999, arXiv:hep-ph/9812418. [ADS].

[75] F. W. Stecker and S. L. Glashow, *New tests of Lorentz invariance following from observations of the highest energy cosmic /γ-rays*, *Astroparticle Physics*, 16:97–99, October 2001, arXiv:astro-ph/0102226. [ADS].

[76] R. J. Protheroe and H. Meyer, *An infrared background-TeV gamma-ray crisis?*, *Physics Letters B*, 493:1–2, November 2000, arXiv:astro-ph/0005349. [ADS].

[77] F. W. Stecker, *Constraints on Lorentz invariance violating quantum gravity and large extra dimensions models using high energy γ-ray observations*, *Astroparticle Physics*, 20:85–90, November 2003, arXiv:astro-ph/0308214. [ADS].

[78] G. Amelino-Camelia, *Planck-scale Lorentz-symmetry test theories*, *ArXiv Astrophysics e-prints*, October 2004, astro-ph/0410076. [ADS].

[79] F. W. Stecker, *Testing Relativity at High Energies Using Spaceborne Detectors*, *ArXiv Astrophysics e-prints*, June 2006, astro-ph/0606641. [ADS].

[80] Goddard Space Flight Center, *Swift: Catching Gamma Ray Bursts on the Fly, The Burst Alert Telescope*, *http://swift.sonoma.edu/about_swift/instruments/bat.html*. [LINK].

[81] Barbara Jo Mattson, *Gamma-ray Detectors*, *http://www.airynothing.com/high_energy_tutorial/detection/detection05.html*. [LINK].

[82] NASA, *Gamma-Ray Telescopes and Detectors*, *http://imagine.gsfc.nasa.gov/docs/science/how_l2/gamma_detectors.html*. [LINK].

[83] NASA, *Gamma-ray Astronomy Satellites and Missions*, *http://imagine.gsfc.nasa.gov/docs/sats_n_data/gamma_missions.html*. [LINK].

[84] NASA, *The History of Gamma-ray Astronomy*, *http://imagine.gsfc.nasa.gov/docs/science/know_l1/history_gamma.html*. [LINK].

[85] NASA, *CGRO Science Support Center*, *http://cossc.gsfc.nasa.gov/docs/cgro/index.html*. [LINK].

[86] NASA, *INTEGRAL U.S. Guest Observer Facility*, *http://heasarc.gsfc.nasa.gov/docs/integral/inthp_about.html*. [LINK].

[87] AGILE collaboration, *AGILE website*, *http://agile.iasf-roma.inaf.it/*. [LINK].

[88] NASA, *GLAST The Gamma Ray Large Area Space Telescope*, *http://www-glast.stanford.edu/mission.html*. [LINK].

[89] NASA, *GLAST Burst Monitor* , *http://f64.nsstc.nasa.gov/gbm/*. [LINK].

[90] M. Amenomori, S. Ayabe, P. Y. Cao, Danzengluobu, L. K. Ding, Z. Y. Feng, Y. Fu, H. W. Guo, M. He, K. Hibino, N. Hotta, Q. Huang, A. X. Huo, K. Izu, H. Y. Jia, F. Kajino, K. Kasahara, Y. Katayose, Labaciren, J. Y. Li, H. Lu, S. L. Lu, G. X. Luo, X. R. Meng, K. Mizutani, J. Mu, H. Nanjo, M. Nishizawa, M. Ohnishi, I. Ohta, T. Ouchi, J. R. Ren, T. Saito, M. Sakata, T. Sasaki, Z. Z. Shi, M. Shibata, A. Shiomi, T. Shirai, H. Sugimoto, K. Taira, Y. H. Tan, N. Tateyama, S. Torii, T. Utsugi, C. R. Wang, H. Wang, X. W. Xu, Y. Yamamoto, G. C. Yu, A. F. Yuan, T. Yuda, C. S. Zhang, H. M. Zhang, J. L. Zhang, N. J. Zhang, X. Y. Zhang, Zhaxisangzhu, Zhaxiciren, W. D. Zhou, and The Tibet As Γ Collaboration, *Observation of Multi-TEV Gamma Rays from the Crab Nebula using the Tibet Air Shower Array*, ApJ, 525:L93–L96, November 1999, arXiv:astro-ph/9909172. [ADS].

[91] J. Linsley, *MIT Air Shower Project (1)*, *Journal of the Physical Society of Japan Supplement*, 17:C148+, 1962. [ADS].

[92] A. Borione, M. Catanese, and et al. *A Search for 100 TeV Gamma-Ray Emission from Cygnus X-3 and Hercules X-1 with CASA-MIA*. In *International Cosmic Ray Conference*, volume 1 of *International Cosmic Ray Conference*, pages 385–+, 1993. [ADS].

[93] J. Wochele, *KASCADE-Grande* , *http://www-ik.fzk.de/KASCADE_home_g.html*. [LINK].

[94] AGASA Collaboration, *AGASA (Akeno Giant Air Shower Array) the Akeno Observatory* , *http://www-akeno.icrr.u-tokyo.ac.jp/AGASA/*. [LINK].

[95] Auger Collaboration, *Pierre Auger Observatory, studying the universe's highest energy particles*, *http://www.auger.org/*. [LINK].

[96] J. V. Jelley. *Čerenkov Radiation and its applications*. Pergamon Press, 122 E. 55th Street, New York 22, N.Y., 1958.

[97] V. P. Zrelov. *Cherenkov Radiation in High-Energy Physics, Part I Cherenkov Radiation in Isotropic and Anisotropic Media: Theory and Experimental Verification*. Keter Press, Jerusalem, 1970.

[98] N. C. Gerson, *Variations in the index of refraction of the atmosphere*, *Pure and Applied Geophysics*, 13:88–101, September 1948. [LINK].

[99] G. Maier, *Private communication.*, November 2007. Data for the figure obtained with MODTRAN. [LINK].

[100] A. M. Hillas, *Differences between Gamma-Ray and Hadronic Showers*, *Space Science Reviews*, 75:17–30, January 1996. [ADS].

[101] John Kildea. *Studies of the Crab Nebula and Pulsar at TeV Energies.* PhD thesis, School of Physics, University College Dublin, November 2002.

[102] D. S. Hanna, D. Bhattacharya, L. M. Boone, M. C. Chantell, Z. Conner, C. E. Covault, M. Dragovan, P. Fortin, D. T. Gregorich, J. A. Hinton, R. Mukherjee, R. A. Ong, S. Oser, K. Ragan, R. A. Scalzo, D. R. Schuette, C. G. Théoret, T. O. Tümer, D. A. Williams, and J. A. Zweerink, *The STACEE-32 ground based gamma-ray detector*, *Nuclear Instruments and Methods in Physics Research A*, 491:126–151, September 2002, arXiv:astro-ph/0205510. [ADS].

[103] T. C. Weekes, *The Atmospheric Cherenkov Imaging Technique for Very High Energy Gamma-ray Astronomy*, *ArXiv Astrophysics e-prints*, August 2005, astro-ph/0508253. [ADS].

[104] J. V. Jelley, *Heaviside-Mallet Radiation?*, *Nature*, 247:401, February 1974. [LINK].

[105] A. S. Lidvansky, *Air Cherenkov methods in cosmic rays: Review and some history*, *Radiation Physics and Chemistry*, 75:891–898, August 2006, arXiv:astro-ph/0504269. [ADS].

[106] A. M. Hillas. *Cerenkov light images of EAS produced by primary gamma.* In F. C. Jones, editor, *International Cosmic Ray Conference*, volume 3 of *International Cosmic Ray Conference*, pages 445–448, August 1985. [ADS].

[107] T. C. Weekes, M. F. Cawley, D. J. Fegan, K. G. Gibbs, A. M. Hillas, P. W. Kowk, R. C. Lamb, D. A. Lewis, D. Macomb, N. A. Porter, P. T. Reynolds, and G. Vacanti, *Observation of TeV gamma rays from the Crab nebula using the atmospheric Cerenkov imaging technique*, ApJ, 342:379–395, July 1989. [ADS].

[108] J. Kildea, R. W. Atkins, H. M. Badran, G. Blaylock, I. H. Bond, S. M. Bradbury, J. H. Buckley, D. A. Carter-Lewis, O. Celik, Y. C. K. Chow, W. Cui, P. Cogan, M. K. Daniel, I. de La Calle Perez, C. Dowdall, C. Duke, A. D. Falcone, D. J. Fegan, S. J. Fegan, J. P. Finley, L. F. Fortson, D. Gall, G. H. Gillanders, J. Grube, K. J. Gutierrez, J. Hall, T. A. Hall, J. Holder, D. Horan, S. B. Hughes, M. Jordan, I. Jung, G. E. Kenny, M. Kertzman, J. Knapp, A. Konopelko, K. Kosack, H. Krawczynski, F. Krennrich, M. J. Lang, S. Lebohec, J. Lloyd-Evans, J. Millis, P. Moriarty, T. Nagai, P. A. Ogden, R. A. Ong, J. S. Perkins, D. Petry, F. Pizlo, M. Pohl, J. Quinn, M. Quinn, P. F. Rebillot, H. J. Rose, M. Schroedter, G. H. Sembroski, A. W. Smith, A. Syson,

J. A. Toner, L. Valcarcel, V. V. Vassiliev, S. P. Wakely, T. C. Weekes, and R. J. White, *The Whipple Observatory 10 m gamma-ray telescope, 1997 2006*, *Astroparticle Physics*, 28:182–195, October 2007. [ADS].

[109] A. Kohnle, F. Aharonian, A. Akhperjanian, S. Bradbury, A. Daum, T. Deckers, J. Fernandez, V. Fonseca, M. Hemberger, G. Hermann, M. Hess, A. Heusler, W. Hofmann, R. Kankanian, C. Köhler, A. Konopelko, E. Lorenz, R. Mirzoyan, N. Müller, M. Panter, D. Petry, A. Plyasheshnikov, G. Rauterberg, M. Samorski, W. Stamm, M. Ulrich, H. J. Völk, C. A. Wiedner, and H. Wirth, *Stereoscopic imaging of air showers with the first two HEGRA Cherenkov telescopes*, *Astroparticle Physics*, 5:119–131, August 1996. [ADS].

[110] F. Krennrich, C. W. Akerlof, J. H. Buckley, J. Bussóns-Gordo, D. A. Carter-Lewis, M. F. Cawley, M. A. Catanese, V. Connaughton, D. J. Fegan, J. P. Finley, J. A. Gaidos, K. H. Harris, A. M. Hillas, R. C. Lamb, M. J. Lang, G. Mohanty, J. Quinn, A. J. Rodgers, H. J. Rose, A. C. Rovero, M. S. Schubnell, G. H. Sembroski, T. C. Weekes, and C. Wilson, *Stereoscopic observations of gamma rays at the Whipple observatory*, *Astroparticle Physics*, 8:213–221, April 1998. [ADS].

[111] M. Mori, S. A. Dazeley, P. G. Edwards, S. Gunji, S. Hara, T. Hara, J. Jinbo, A. Kawachi, T. Kifune, H. Kubo, J. Kushida, Y. Matsubara, Y. Mizumoto, M. Moriya, H. Muraishi, Y. Muraki, T. Naito, J. R. Patterson, K. Nishijima, M. D. Roberts, G. P. Rowell, T. Sako, K. Sakurazawa, Y. Sato, R. Susukita, T. Tamura, T. Tanimori, S. Yanagita, T. Yoshida, T. Yoshikoshi, and A. Yuki. *The CANGAROO-III Project*. In B. L. Dingus, M. H. Salamon, and D. B. Kieda, editors, *American Institute of Physics Conference Series*, volume 515 of *American Institute of Physics Conference Series*, pages 485–+, 2000. [ADS].

[112] W. Hofmann, *Proceeding towards a major atmospheric Cherenkov detector- V*, August 1997. [LINK].

[113] E. Lorenz and The MAGIC Collaboration. *The MAGIC Telescope Project*. In B. L. Dingus, M. H. Salamon, and D. B. Kieda, editors, *American Institute of Physics Conference Series*, volume 515 of *American Institute of Physics Conference Series*, pages 510–+, 2000. [ADS].

[114] D. Hanna, *VERITAS telescopes celebrate first light*, *CERN Cour.*, 47N6:19–21, 2007. [LINK].

[115] G. Maier, *VERITAS: Status and Latest Results*, *ArXiv e-prints*, 709, September 2007, 0709.3654. Presented at the International Cosmic Ray Conference 2007. [ADS].

[116] H. Krawczynski, for the VERITAS Collaboration, *Blazar Observations with VERITAS*, *ArXiv e-prints*, 710, September 2007, 0710.0089. Presented at the International Cosmic Ray Conference 2007. [ADS].

[117] VERITAS Collaboration: T. B. Humensky, *Observation of the Supernova Remnant IC 443 with VERITAS*, *ArXiv e-prints*, 709, September 2007, 0709.4298. Presented at the International Cosmic Ray Conference 2007. [ADS].

[118] P. Colin, *Observation of M87 with VERITAS*, *ArXiv e-prints*, 709, September 2007, 0709.3663. Presented at the International Cosmic Ray Conference 2007. [ADS].

[119] G. Maier, *Observation of LS I +61 303 with VERITAS*, *ArXiv e-prints*, 709, September 2007, 0709.3661. Presented at the International Cosmic Ray Conference 2007. [ADS].

[120] C. Baixeras and et al. *Magic Phase II*. In *International Cosmic Ray Conference*, volume 5 of *International Cosmic Ray Conference*, pages 227–+, 2005. [ADS].

[121] P. Vincent. *H.E.S.S. Phase II*. In *International Cosmic Ray Conference*, volume 5 of *International Cosmic Ray Conference*, pages 163–+, 2005. [ADS].

[122] W. Hofmann, *Performance Limits for Cherenkov Instruments*, *ArXiv Astrophysics e-prints*, March 2006, astro-ph/0603076. [ADS].

[123] I. de La Calle Pérez and S. D. Biller, *Extending the sensitivity of air Čerenkov telescopes*, *Astroparticle Physics*, 26:69–90, September 2006, arXiv:astro-ph/0602284. [ADS].

[124] G. Hermann, S. Carrigan, B. Glück, and D. Hauser, *A Smart Pixel Camera for future Cherenkov Telescopes*, *ArXiv Astrophysics e-prints*, November 2005, astro-ph/0511519. [ADS].

[125] G. Cusumano, G. Agnetta, A. Alberdi, M. Alvarez, P. Assis, B. Biondo, F. Bocchino, P. Brogueira, J. A. Caballero, M. Carvajal, A. J. Castro-Tirado, O. Catalano, F. Celi, C. Delgado, G. Di Cocco, A. Dominguez, J. M. Espino Navas, M. C. Espirito Santo, M. I. Gallardo, J. E. Garcia, S. Giarrusso, M. Gomez, J. L. Gomez, P. Goncalves, M. Guerriero, A. La Barbera, G. La Rosa, M. Lozano, M. C. Maccarone, A. Mangano, I. Martel, E. Massaro, T. Mineo, M. Moles, F. Perez-Bernal, M. A. Peres-Torres, M. Pimenta, A. Pina, F. Prada, J. M. Quesada, J. M. Quintana, J. R. Quintero, J. Rodriguez, F. Russo, B. Sacco, M. A. Sanchez-Conde, A. Segreto, B. Tome', A. de Ugarte Postigo, and P. Vallania, *GAW - An Imaging Atmospheric Cherenkov Telescope with Large Field of View*, *ArXiv e-prints*, 707, July 2007, 0707.4541. [ADS].

[126] A. Konopelko, J. P. Finley, and G. Urbanski, *Design Study of a Low Energy IACT Array for Ground-Based Gamma-Ray Astronomy*, *ArXiv e-prints*, 708, August 2007, 0708.3865. [ADS].

[127] V. V. Vassiliev and S. J. Fegan, *Schwarzschild-Couder two-mirror telescope for ground-based gamma-ray astronomy*, *ArXiv e-prints*, 708, August 2007, 0708.2741. [ADS].

[128] S. J. Fegan and V. V. Vassiliev, *The performance of an idealized large-area array of moderate-sized IACTs*, *ArXiv e-prints*, 708, August 2007, 0708.2716. [ADS].

[129] F. Aharonian, *Next generation of IACT arrays: scientific objectives versus energy domains*, *ArXiv Astrophysics e-prints*, November 2005, astro-ph/0511139. [ADS].

[130] G. Hermann, W. Hofmann, T. Schweizer, M. Teshima, and f. t. CTA consortium, *Cherenkov Telescope Array: The next-generation ground-based gamma-ray observatory*, *ArXiv e-prints*, 709, September 2007, 0709.2048. [ADS].

[131] P. Colin, S. LeBohec, and J. Holder, *Experimental approaches for 100 TeV gamma-ray astronomy*, *ArXiv Astrophysics e-prints*, October 2006, astro-ph/0610344. [ADS].

[132] H. Krawczynski, J. Buckley, K. Byrum, C. Dermer, B. Dingus, A. Falcone, P. Kaaret, F. Krennrich, M. Pohl, V. Vassiliev, D. A. Williams, and for the White Paper Team, *White Paper on the Status and Future of Ground-based Gamma-ray Astronomy*, *ArXiv e-prints*, 709, September 2007, 0709.0704. [ADS].

[133] S. C. Corbató, H. Y. Dai, J. W. Elbert, D. B. Kieda, E. C. Loh, P. V. Sokolsky, P. Sommers, and J. K. K. Tang, *HiRes, a high resolution Fly's Eye detector.*, *Nuclear Physics B Proceedings Supplements*, 28:36–39, November 1992. [ADS].

[134] *The Pierre Auger observatory design report*, 1997. [LINK].

[135] Robert E. Streitmatter. *Orbiting Wide-angle Light-collectors (OWL): Observing cosmic rays from space.* volume 433, pages 95–107. AIP, 1998. [LINK].

[136] Livio Scarsi. *EUSO: Using high energy cosmic rays and neutrinos as messengers from the unknown universe.* volume 566, pages 113–127. AIP, 2001. [LINK].

[137] H. Falcke, W. D. Apel, A. F. Badea, L. Bähren, K. Bekk, A. Bercuci, M. Bertaina, P. L. Biermann, J. Blümer, H. Bozdog, I. M. Brancus, S. Buitink, M. Brüggemann, P. Buchholz, H. Butcher, A. Chiavassa, K. Daumiller, A. G. de Bruyn, C. M. de Vos, F. di Pierro, P. Doll, R. Engel, H. Gemmeke, P. L. Ghia, R. Glasstetter, C. Grupen, A. Haungs, D. Heck, J. R. Hörandel, A. Horneffer, T. Huege, K.-H. Kampert, G. W. Kant, U. Klein, Y. Kolotaev, Y. Koopman, O. Krömer, J. Kuijpers, S. Lafebre, G. Maier, H. J. Mathes, H. J. Mayer, J. Milke, B. Mitrica, C. Morello, G. Navarra, S. Nehls, A. Nigl, R. Obenland, J. Oehlschläger, S. Ostapchenko, S. Over, H. J. Pepping, M. Petcu, J. Petrovic, S. Plewnia, H. Rebel, A. Risse, M. Roth, H. Schieler, G. Schoonderbeek, O. Sima, M. Stümpert, G. Toma, G. C. Trinchero, H. Ulrich, S. Valchierotti, J. van Buren, W. van Cappellen, W. Walkowiak, A. Weindl, S. Wijnholds, J. Wochele, J. Zabierowski, J. A. Zensus, and D. Zimmermann, *Detection and imaging of atmospheric radio flashes from cosmic ray air showers*, Nature, 435:313–316, May 2005, arXiv:astro-ph/0505383. [ADS].

[138] G. B. Yodh, *Water Cherenkov Detectors: MILAGRO*, *Space Science Reviews*, 75:199–212, January 1996. [ADS].

[139] A. Carraminana, B. Dingus, J. Goodman, M. Gonzalez, and HAWC collaboration. *The HAWC Gamma-ray Observatory*. In *AAS/High Energy Astrophysics Division*, volume 10 of *AAS/High Energy Astrophysics Division*, pages 41.07–+, March 2008. [ADS].

[140] E. Hays. *The Track Imaging Cerenkov Experiment*. In *AAS/High Energy Astrophysics Division*, volume 9 of *AAS/High Energy Astrophysics Division*, pages 21.05–+, September 2006. [ADS].

[141] D. Hanna et al., *First results from VERITAS*, *Nuclear Instruments and Methods in Physics Research Section A: Accelerators, Spectrometers, Detectors and Associated Equipment*, 588(1-2):26–32, April 2008. Proceedings of the First International Conference on Astroparticle Physics - RICAP 07. [LINK].

[142] John M. Davies and Eugene S. Cotton, *Design of the quartermaster solar furnace*, *Solar Energy*, 1:16–22, April 1957. [LINK].

[143] R. Cornils, S. Gillessen, I. Jung, W. Hofmann, G. Heinzelmann, and Hess Collaboration. *Point spread function and long-term stability of the H.E.S.S. reflectors*. In F. A. Aharonian, H. J. Völk, and D. Horns, editors, *High Energy Gamma-Ray Astronomy*, volume 745 of *American Institute of Physics Conference Series*, pages 736–741, February 2005. [ADS].

[144] T. C. Weekes, H. Badran, S. D. Biller, I. Bond, S. Bradbury, J. Buckley, D. Carter-Lewis, M. Catanese, S. Criswell, W. Cui, P. Dowkontt, C. Duke, D. J. Fegan, J. Finley, L. Fortson, J. Gaidos, G. H. Gillanders, J. Grindlay, T. A. Hall, K. Harris, A. M. Hillas, P. Kaaret, M. Kertzman, D. Kieda, F. Krennrich, M. J. Lang, S. LeBohec, R. Lessard, J. Lloyd-Evans, J. Knapp, B. McKernan, J. McEnery, P. Moriarty, D. Muller, P. Ogden, R. Ong, D. Petry, J. Quinn, N. W. Reay, P. T. Reynolds, J. Rose, M. Salamon, G. Sembroski, R. Sidwell, P. Slane, N. Stanton, S. P. Swordy, V. V. Vassiliev, and S. P. Wakely, *VERITAS: the Very Energetic Radiation Imaging Telescope Array System*, *Astroparticle Physics*, 17:221–243, May 2002, arXiv:astro-ph/0108478. [ADS].

[145] E. Roache, R. Irvin, J. S. Perkins, K. Harris, A. Falcone, J. Finley, and T. C. Weekes, *Mirror Facets for the VERITAS Telescopes*, 2007. Presented at the International Cosmic Ray Conference 2007. [LINK].

[146] J. Holder, R. W. Atkins, H. M. Badran, G. Blaylock, S. M. Bradbury, J. H. Buckley, K. L. Byrum, D. A. Carter-Lewis, O. Celik, Y. C. K. Chow, P. Cogan, W. Cui, M. K. Daniel, I. de La Calle Perez, C. Dowdall, P. Dowkontt, C. Duke, A. D. Falcone, S. J. Fegan, J. P. Finley, P. Fortin, L. F. Fortson, K. Gibbs, G. Gillanders, O. J. Glidewell, J. Grube, K. J. Gutierrez, G. Gyuk, J. Hall, D. Hanna, E. Hays, D. Horan, S. B. Hughes, T. B. Humensky, A. Imran,

I. Jung, P. Kaaret, G. E. Kenny, D. Kieda, J. Kildea, J. Knapp, H. Krawczynski, F. Krennrich, M. J. Lang, S. Lebohec, E. Linton, E. K. Little, G. Maier, H. Manseri, A. Milovanovic, P. Moriarty, R. Mukherjee, P. A. Ogden, R. A. Ong, D. Petry, J. S. Perkins, F. Pizlo, M. Pohl, J. Quinn, K. Ragan, P. T. Reynolds, E. T. Roache, H. J. Rose, M. Schroedter, G. H. Sembroski, G. Sleege, D. Steele, S. P. Swordy, A. Syson, J. A. Toner, L. Valcarcel, V. V. Vassiliev, S. P. Wakely, T. C. Weekes, R. J. White, D. A. Williams, and R. Wagner, *The first VERITAS telescope*, *Astroparticle Physics*, 25:391–401, July 2006, arXiv:astro-ph/0604119. [ADS].

[147] J. A. Toner, V. Acciari, A. Cesarini, G. H. Gillanders, D. Hanna, G. E. Kenny, J. Kildea, A. McCann, M. McCutcheon, M. J. Lang, P. T. Reynolds, M. Schroedter, A. Smith, J. E. Ward, T. C. Weekes, and B. Zitzer, *Bias Alignment of the VERITAS Telescopes*, 2007. Presented at the International Cosmic Ray Conference 2007. [LINK].

[148] S.-O. Flyckt and C. Marmonier, editors. *Photomultiplier tubes principles & applications*. Photonis, avenue Roger Roncier, B.P. 520, 19106 Brive Cedex, France, 2002.

[149] VERITAS Collaboration: T. Nagai, R. McKay, G. Sleege, and D. Petry, *Focal Plane Instrumentation of VERITAS*, *ArXiv e-prints*, 709, September 2007, 0709.4517. Presented at the International Cosmic Ray Conference 2007. [ADS].

[150] P. Jordan and F. Krennrich, *The Design of Light Concentrators for a 12 m Cherenkov Telescope*, July 2004. [LINK].

[151] H. Hinterberger and R. Winston, *Efficient Light Coupler for Threshold Čerenkov Counters*, *Review of Scientific Instruments*, 37(8):1094–1095, 1966. [LINK].

[152] L. Valcárcel, *Investigating effects of the lightcones cleaning on T3*, *VERITAS internal note, Elog VERITAS at FLWO-BC 3309*, 2007. [LINK].

[153] O. Celik, for the VERITAS Collaboration, *Observations of the Crab Nebula and Pulsar with VERITAS*, *ArXiv e-prints*, 709, September 2007, 0709.3868. Presented at the International Cosmic Ray Conference 2007. [ADS].

[154] A. Weinstein, for the VERITAS Collaboration, *The VERITAS Trigger System*, *ArXiv e-prints*, 709, September 2007, 0709.4438. Presented at the International Cosmic Ray Conference 2007. [ADS].

[155] V. V. Vassiliev, J. Hall, D. B. Kieda, J. Moses, T. Nagai, and J. Smith. *Veritas CFDs*. In *International Cosmic Ray Conference*, volume 5 of *International Cosmic Ray Conference*, pages 2851–+, July 2003. [ADS].

[156] E. Hays, for the VERITAS Collaboration, *VERITAS Data Acquisition*, *ArXiv e-prints*, 710, October 2007, 0710.2288. Presented at the International Cosmic Ray Conference 2007. [ADS].

[157] D. Hanna and R. Mukherjee, *The laser calibration system for the STACEE ground-based gamma ray detector*, *Nuclear Instruments and Methods in Physics Research Section A: Accelerators, Spectrometers, Detectors and Associated Equipment*, 482(1-2):271–280, April 2002. [LINK].

[158] D. Hanna, *A look at T2 PMT gains with laser data*, *VERITAS internal note, Elog Analysis and Calibration 97*, August 2006. [LINK].

[159] François Vincent. *Photomultiplier tube gain measurements using an uncalibrated light source*. Master's thesis, McGill University, July 2000.

[160] M. K. Daniel, for the VERITAS Collaboration, *The VERITAS standard data analysis*, *ArXiv e-prints*, 709, September 2007, 0709.4006. Presented at the International Cosmic Ray Conference 2007. [ADS].

[161] P. Cogan, for the VERITAS Collaboration, *VEGAS, the VERITAS Gamma-ray Analysis Suite*, *ArXiv e-prints*, 709, September 2007, 0709.4233. Presented at the International Cosmic Ray Conference 2007. [ADS].

[162] Peter Cogan. *Nanosecond Sampling of Atmospheric Cherenkov Radiation Applied to TeV Gamma-Ray Observations of Blazars with VERITAS*. PhD thesis, School of Physics, University College Dublin, December 2006.

[163] D. J. Fegan, *The art and power of Čerenkov imaging*, *Space Science Reviews*, 75:137–151, January 1996. [ADS].

[164] P. Cogan, *An Investigation of New Cleaning Algorithms*, *VERITAS internal note, Elog Analysis and Calibration 503*, 2007. [LINK].

[165] A. Atoyan, J. Patera, V. Sahakian, and A. Akhperjanian, *Fourier transform method for imaging atmospheric Cherenkov telescopes*, *Astroparticle Physics*, 23:79–95, February 2005, arXiv:astro-ph/0409388. [ADS].

[166] A. McCann, *Image Processing with FT*, *VERITAS internal note*, 2006.

[167] P. T. Reynolds, C. W. Akerlof, M. F. Cawley, M. Chantell, D. J. Fegan, A. M. Hillas, R. C. Lamb, M. J. Lang, M. A. Lawrence, D. A. Lewis, D. Macomb, D. I. Meyer, G. Mohanty, K. S. O'Flaherty, M. Punch, M. S. Schubnell, G. Vacanti, T. C. Weekes, and T. Whitaker, *Survey of candidate gamma-ray sources at TeV energies using a high-resolution Cerenkov imaging system - 1988-1991*, ApJ, 404:206–218, February 1993. [ADS].

[168] R. W. Lessard, J. H. Buckley, V. Connaughton, and S. Le Bohec, *A new analysis method for reconstructing the arrival direction of TeV gamma rays using a single imaging atmospheric Cherenkov telescope*, *Astroparticle Physics*, 15:1–18, March 2001, arXiv:astro-ph/0005468. [ADS].

[169] M. Morang, *Shower Reconstruction Algorithms for the VERITAS Gamma Ray Telescope*, *VERITAS internal note, Elog Analysis and Calibration 1080*, 2008. [LINK].

[170] W. Hofmann, I. Jung, A. Konopelko, H. Krawczynski, H. Lampeitl, and G. Pühlhofer, *Comparison of techniques to reconstruct VHE gamma-ray showers from multiple stereoscopic Cherenkov images*, *Astroparticle Physics*, 12:135–143, November 1999, arXiv:astro-ph/9904234. [ADS].

[171] H. Krawczynski, D. A. Carter-Lewis, C. Duke, J. Holder, G. Maier, S. Le Bohec, and G. Sembroski, *Gamma hadron separation methods for the VERITAS array of four imaging atmospheric Cherenkov telescopes*, *Astroparticle Physics*, 25:380–390, July 2006, arXiv:astro-ph/0604508. [ADS].

[172] A. Daum, G. Hermann, M. Hess, W. Hofmann, H. Lampeitl, G. Pühlhofer, F. Aharonian, A. G. Akhperjanian, J. A. Barrio, A. S. Beglarian, K. Bernlöhr, J. J. G. Beteta, S. M. Bradbury, J. L. Contreras, J. Cortina, T. Deckers, E. Feigl, J. Fernandez, V. Fonseca, A. Frass, B. Funk, J. C. Gonzalez, G. Heinzelmann, M. Hemberger, A. Heusler, I. Holl, D. Horns, R. Kankanyan, O. Kirstein, C. Köhler, A. Konopelko, D. Kranich, H. Krawczynski, H. Kornmayer, A. Lindner, E. Lorenz, N. Magnussen, H. Meyer, R. Mirzoyan, H. Möller, A. Moralejo, L. Padilla, M. Panter, D. Petry, R. Plaga, J. Prahl, C. Prosch, G. Rauterberg, W. Rhode, A. Röhring, V. Sahakian, M. Samorski, J. A. Sanchez, D. Schmele, W. Stamm, M. Ulrich, H. J. Völk, S. Westerhoff, B. Wiebel-Sooth, C. A. Wiedner, M. Willmer, and H. Wirth, *First results on the performance of the HEGRA IACT array*, *Astroparticle Physics*, 8:1–2, December 1997. [ADS].

[173] for the VERITAS Collaboration Maier, G., *Monte Carlo studies of the VERITAS array of Cherenkov telescopes*, *ArXiv e-prints*, 709, September 2007, 0709.4195. [ADS].

[174] S. C. Commichau, A. Biland, J. L. Contreras, R. de los Reyes, A. Moralejo, J. Sitarek, and D. Sobczynska, *Monte Carlo Studies of Geomagnetic Field Effects on the Imaging Air Cherenkov Technique for the MAGIC Telescope Site*, *ArXiv e-prints*, 802, February 2008, 0802.2551. [ADS].

[175] G. Mohanty, S. Biller, D. A. Carter-Lewis, D. J. Fegan, A. M. Hillas, R. C. Lamb, T. C. Weekes, M. West, and J. Zweerink, *Measurement of TeV gamma-ray spectra with the Cherenkov imaging technique*, *Astroparticle Physics*, 9:15–43, June 1998. [ADS].

[176] D. Berge, S. Funk, and J. Hinton, *Background modelling in very-high-energy γ-ray astronomy*, A&A, 466:1219–1229, May 2007, arXiv:astro-ph/0610959. [ADS].

[177] R. Guenette, *Acceptance curve studies*, *VERITAS internal note, Elog Analysis and Calibration 1095*, 2008. [LINK].

[178] R. Guenette, *The field of view background model, a new background model implemented for the analysis*, *VERITAS internal note, Elog Analysis and Calibration 984*, March 2008. [LINK].

[179] T.-P. Li and Y.-Q. Ma, *Analysis methods for results in gamma-ray astronomy*, *Astrophys. J.*, 272:317–324, September 1983. [ADS].

[180] S. Gillessen and H. L. Harney, *Significance in gamma-ray astronomy - the Li & Ma problem in Bayesian statistics*, A&A, 430:355–362, January 2005, arXiv:astro-ph/0411660. [ADS].

[181] J. Linnemann. *Measures of Significance in HEP and Astrophysics.* In *Statistical Problems in Particle Physics, Astrophysics, and Cosmology*, pages 35–+, 2003. [ADS].

[182] G. Sembroski, *Spectrum Analysis*, *VERITAS internal note, wiki Spectrum Analysis*, May 2008. [LINK].

[183] M. Beilicke, *Cut optimization*, *VERITAS internal note, Elog Blazar-SWG 895*, February 2008. [LINK].

[184] L. Valcárcel, *Cut optimization*, *VERITAS internal note, Elog Blazar-SWG 960*, February 2008. [LINK].

[185] S. Swordy, *VERITAS discovers TeV gamma rays from W Comae*, *The Astronomer's Telegram*, 1422:1–+, March 2008. [ADS].

[186] VERITAS Collaboration: V. A. Acciari, E. Aliu, M. Beilicke, W. Benbow, S. M. Bradbury, J. H. Buckley, V. Bugaev, Y. Butt, O. Celik, A. Cesarini, L. Ciupik, Y. C. K. Chow, P. Cogan, P. Colin, W. Cui, M. K. Daniel, T. Ergin, A. D. Falcone, S. J. Fegan, J. P. Finley, G. Finnegan, P. Fortin, L. F. Fortson, A. Furniss, D. Gall, G. H. Gillanders, J. Grube, R. Guenette, G. Gyuk, D. Hanna, E. Hays, J. Holder, D. Horan, C. M. Hui, T. B. Humensky, A. Imran, P. Kaaret, N. Karlsson, M. Kertzman, D. B. Kieda, A. Konopelko, H. Krawczynski, F. Krennrich, M. J. Lang, S. LeBohec, K. Lee, G. Maier, A. McCann, M. McCutcheon, P. Moriarty, R. Mukherjee, T. Nagai, J. Niemiec, R. A. Ong, D. Pandel, J. S. Perkins, D. Petry, M. Pohl, J. Quinn, K. Ragan, L. C. Reyes, P. T. Reynolds, E. Roache, H. J. Rose, M. Schroedter, G. H. Sembroski, A. W. Smith, D. Steele, S. P. Swordy, J. A. Toner, V. V. Vassiliev, R. Wagner, S. P. Wakely, J. E. Ward, T. C. Weekes, A. Weinstein, R. J. White, D. A. Williams, S. A. Wissel, M. Wood, and B. Zitzer, *VERITAS Discovery of > 200GeV Gamma-ray Emission from the Intermediate-frequency-peaked BL Lac Object W Comae*, *ArXiv e-prints*, 808, August 2008, 0808.0889. [ADS].

[187] S. Swordy, *TeV Outburst from W Comae*, *The Astronomer's Telegram*, 1565:1–+, June 2008. [ADS].

[188] O. Celik, *Crab spectrum with 4T, 4T-CutT4 and 3T Data*, *VERITAS internal note, Elog Offline Analysis Working Group 5634*, July 2008. [LINK].

[189] F. Aharonian, A. G. Akhperjanian, A. R. Bazer-Bachi, M. Beilicke, W. Benbow, D. Berge, K. Bernlöhr, C. Boisson, O. Bolz, V. Borrel, I. Braun, F. Breitling, A. M. Brown, R. Bühler, I. Büsching, S. Carrigan, P. M. Chadwick, L.-M.

Chounet, R. Cornils, L. Costamante, B. Degrange, H. J. Dickinson, A. Djannati-Ataï, L. O'C. Drury, G. Dubus, K. Egberts, D. Emmanoulopoulos, P. Espigat, F. Feinstein, E. Ferrero, A. Fiasson, G. Fontaine, S. Funk, S. Funk, Y. A. Gallant, B. Giebels, J. F. Glicenstein, P. Goret, C. Hadjichristidis, D. Hauser, M. Hauser, G. Heinzelmann, G. Henri, G. Hermann, J. A. Hinton, W. Hofmann, M. Holleran, D. Horns, A. Jacholkowska, O. C. de Jager, B. Khélifi, N. Komin, A. Konopelko, K. Kosack, I. J. Latham, R. Le Gallou, A. Lemière, M. Lemoine-Goumard, T. Lohse, J. M. Martin, O. Martineau-Huynh, A. Marcowith, C. Masterson, T. J. L. McComb, M. de Naurois, D. Nedbal, S. J. Nolan, A. Noutsos, K. J. Orford, J. L. Osborne, M. Ouchrif, M. Panter, G. Pelletier, S. Pita, G. Pühlhofer, M. Punch, B. C. Raubenheimer, M. Raue, S. M. Rayner, A. Reimer, O. Reimer, J. Ripken, L. Rob, L. Rolland, G. Rowell, V. Sahakian, L. Saugé, S. Schlenker, R. Schlickeiser, U. Schwanke, H. Sol, D. Spangler, F. Spanier, R. Steenkamp, C. Stegmann, G. Superina, J.-P. Tavernet, R. Terrier, C. G. Théoret, M. Tluczykont, C. van Eldik, G. Vasileiadis, C. Venter, P. Vincent, H. J. Völk, S. J. Wagner, and M. Ward, *Observations of the Crab nebula with HESS*, A&A, 457:899–915, October 2006, arXiv:astro-ph/0607333. [ADS].

[190] G. Maier, *Systematic errors in spectral energy reconstruction*, *VERITAS internal note, Elog Analysis And Calibration 595*, October 2007. [LINK].

[191] J. Edelstein, S. Bowyer, and M. Lampton, *Reanalysis ofVoyager Ultraviolet Spectrometer Limits to the Extreme-Ultraviolet and Far-Ultraviolet Diffuse Astronomical Flux*, ApJ, 539:187–190, August 2000, arXiv:astro-ph/0003208. [ADS].

[192] C. Martin, M. Hurwitz, and S. Bowyer, *Spectroscopic limits to an extragalactic far-ultraviolet background*, ApJ, 379:549–563, October 1991. [ADS].

[193] T. M. Brown, R. A. Kimble, H. C. Ferguson, J. P. Gardner, N. R. Collins, and R. S. Hill, *Measurements of the Diffuse Ultraviolet Background and the Terrestrial Airglow with the Space Telescope Imaging Spectrograph*, AJ, 120:1153–1159, August 2000, arXiv:astro-ph/0004147. [ADS].

[194] K. Mattila. *Observations of the extragalactic background light.* In S. Bowyer and C. Leinert, editors, *The Galactic and Extragalactic Background Radiation*, volume 139 of *IAU Symposium*, pages 257–268, 1990. [ADS].

[195] G. N. Toller, *The extragalactic background light at 4400 A*, ApJ, 266:L79–L82, March 1983. [ADS].

[196] C. Leinert, S. Bowyer, L. K. Haikala, M. S. Hanner, M. G. Hauser, A.-C. Levasseur-Regourd, I. Mann, K. Mattila, W. T. Reach, W. Schlosser, H. J. Staude, G. N. Toller, J. L. Weiland, J. L. Weinberg, and A. N. Witt, *The 1997 reference of diffuse night sky brightness*, A&AS, 127:1–99, January 1998. [ADS].

[197] R. R. Dube, W. C. Wickes, and D. T. Wilkinson, *Upper limit on the extragalactic background light*, ApJ, 232:333–340, September 1979. [ADS].

[198] R. A. Bernstein, W. L. Freedman, and B. F. Madore, *Corrections of Errors in "The First Detections of the Extragalactic Background Light at 3000, 5500, and 8000 Å. I, II, and III" (ApJ, 571; 56, 85, 107 [2002])*, ApJ, 632:713–717, October 2005, arXiv:astro-ph/0507033. [ADS].

[199] P. Madau and L. Pozzetti, *Deep galaxy counts, extragalactic background light and the stellar baryon budget*, MNRAS, 312:L9–L15, February 2000, arXiv:astro-ph/9907315. [ADS].

[200] G. G. Fazio, M. L. N. Ashby, P. Barmby, J. L. Hora, J.-S. Huang, M. A. Pahre, Z. Wang, S. P. Willner, R. G. Arendt, S. H. Moseley, M. Brodwin, P. Eisenhardt, D. Stern, E. V. Tollestrup, and E. L. Wright, *Number Counts at 3 $\mu m < \lambda <$ 10 μm from the Spitzer Space Telescope*, ApJS, 154:39–43, September 2004, arXiv:astro-ph/0405595. [ADS].

[201] D. Elbaz, C. J. Cesarsky, P. Chanial, H. Aussel, A. Franceschini, D. Fadda, and R. R. Chary, *The bulk of the cosmic infrared background resolved by ISOCAM*, A&A, 384:848–865, March 2002, arXiv:astro-ph/0201328. [ADS].

[202] L. Metcalfe, J.-P. Kneib, B. McBreen, B. Altieri, A. Biviano, M. Delaney, D. Elbaz, M. F. Kessler, K. Leech, K. Okumura, S. Ott, R. Perez-Martinez, C. Sanchez-Fernandez, and B. Schulz, *An ISOCAM survey through gravitationally lensing galaxy clusters. I. Source lists and source counts for A370, A2218 and A2390*, A&A, 407:791–822, September 2003, arXiv:astro-ph/0305400. [ADS].

[203] C. Papovich, H. Dole, E. Egami, E. Le Floc'h, P. G. Pérez-González, A. Alonso-Herrero, L. Bai, C. A. Beichman, M. Blaylock, C. W. Engelbracht, K. D. Gordon, D. C. Hines, K. A. Misselt, J. E. Morrison, J. Mould, J. Muzerolle, G. Neugebauer, P. L. Richards, G. H. Rieke, M. J. Rieke, J. R. Rigby, K. Y. L. Su, and E. T. Young, *The 24 Micron Source Counts in Deep Spitzer Space Telescope Surveys*, ApJS, 154:70–74, September 2004, arXiv:astro-ph/0406035. [ADS].

[204] H. Dole, G. Lagache, J.-L. Puget, K. I. Caputi, N. Fernández-Conde, E. Le Floc'h, C. Papovich, P. G. Pérez-González, G. H. Rieke, and M. Blaylock, *The cosmic infrared background resolved by Spitzer. Contributions of mid-infrared galaxies to the far-infrared background*, A&A, 451:417–429, May 2006, arXiv:astro-ph/0603208. [ADS].

[205] D. T. Frayer, M. T. Huynh, R. Chary, M. Dickinson, D. Elbaz, D. Fadda, J. A. Surace, H. I. Teplitz, L. Yan, and B. Mobasher, *Spitzer 70 Micron Source Counts in GOODS-North*, ApJ, 647:L9–L12, August 2006, arXiv:astro-ph/0606676. [ADS].

[206] E. Dwek and R. G. Arendt, *A Tentative Detection of the Cosmic Infrared Background at 3.5 μm from COBE/DIRBE Observations*, ApJ, 508:L9–L12, November 1998, arXiv:astro-ph/9809239. [ADS].

[207] V. Gorjian, E. L. Wright, and R. R. Chary, *Tentative Detection of the Cosmic Infrared Background at 2.2 and 3.5 Microns Using Ground-based and Space-based Observations*, ApJ, 536:550–560, June 2000, arXiv:astro-ph/0103101. [ADS].

[208] E. L. Wright and E. D. Reese, *Detection of the Cosmic Infrared Background at 2.2 and 3.5 Microns Using DIRBE Observations*, ApJ, 545:43–55, December 2000, arXiv:astro-ph/9912523. [ADS].

[209] L. Cambrésy, W. T. Reach, C. A. Beichman, and T. H. Jarrett, *The Cosmic Infrared Background at 1.25 and 2.2 Microns Using DIRBE and 2MASS: A Contribution Not Due to Galaxies?*, ApJ, 555:563–571, July 2001, arXiv:astro-ph/0103078. [ADS].

[210] T. Matsumoto, S. Matsuura, H. Murakami, M. Tanaka, M. Freund, M. Lim, M. Cohen, M. Kawada, and M. Noda, *Infrared Telescope in Space Observations of the Near-Infrared Extragalactic Background Light*, ApJ, 626:31–43, June 2005, arXiv:astro-ph/0411593. [ADS].

[211] L. R. Levenson, E. L. Wright, and B. D. Johnson, *DIRBE Minus 2MASS: Confirming the CIRB in 40 New Regions at 2.2 and 3.5 μm*, ApJ, 666:34–44, September 2007, arXiv:0704.1498. [ADS].

[212] M. G. Hauser, R. G. Arendt, T. Kelsall, E. Dwek, N. Odegard, J. L. Weiland, H. T. Freudenreich, W. T. Reach, R. F. Silverberg, S. H. Moseley, Y. C. Pei, P. Lubin, J. C. Mather, R. A. Shafer, G. F. Smoot, R. Weiss, D. T. Wilkinson, and E. L. Wright, *The COBE Diffuse Infrared Background Experiment Search for the Cosmic Infrared Background. I. Limits and Detections*, ApJ, 508:25–43, November 1998, arXiv:astro-ph/9806167. [ADS].

[213] G. Lagache, L. M. Haffner, R. J. Reynolds, and S. L. Tufte, *Evidence for dust emission in the Warm Ionised Medium sing WHAM data*, A&A, 354:247–252, February 2000, arXiv:astro-ph/9911355. [ADS].

[214] A. Kashlinsky, J. C. Mather, S. Odenwald, and M. G. Hauser, *Clustering of the Diffuse Infrared Light from the COBE DIRBE Maps. I. C(0) and Limits on the Near-Infrared Background*, ApJ, 470:681–+, October 1996, arXiv:astro-ph/9604182. [ADS].

[215] A. Kashlinsky and S. Odenwald, *Clustering of the Diffuse Infrared Light from the COBE DIRBE Maps. III. Power Spectrum Analysis and Excess Isotropic Component of Fluctuations*, ApJ, 528:74–95, January 2000, arXiv:astro-ph/9908304. [ADS].

[216] D. P. Finkbeiner, M. Davis, and D. J. Schlegel, *Detection of a Far-Infrared Excess with DIRBE at 60 and 100 Microns*, ApJ, 544:81–97, November 2000, arXiv:astro-ph/0004175. [ADS].

[217] J. M. Jauch and F. Rohrlich. *Theory of Photons and Electrons*. Addison-Wesley Publishing Company, Inc., Massachusetts, U.S.A., 1955.

[218] J. A. Peacock. *Cosmological Physics*. Cambridge University Press, The Edinburgh Building, Cambridge, UK, first edition, 1999.

[219] K. Katarzyński, G. Ghisellini, F. Tavecchio, J. Gracia, and L. Maraschi, *Hard TeV spectra of blazars and the constraints to the infrared intergalactic background*, MNRAS, 368:L52–L56, May 2006, arXiv:astro-ph/0603030. [ADS].

[220] F. Aharonian, A. Akhperjanian, M. Beilicke, K. Bernlöhr, H.-G. Börst, H. Bojahr, O. Bolz, T. Coarasa, J. L. Contreras, J. Cortina, L. Costamante, S. Denninghoff, M. V. Fonseca, M. Girma, N. Götting, G. Heinzelmann, G. Hermann, A. Heusler, W. Hofmann, D. Horns, I. Jung, R. Kankanyan, M. Kestel, A. Kohnle, A. Konopelko, H. Kornmeyer, D. Kranich, H. Lampeitl, M. Lopez, E. Lorenz, F. Lucarelli, O. Mang, D. Mazine, H. Meyer, R. Mirzoyan, A. Moralejo, E. Ona-Wilhelmi, M. Panter, A. Plyasheshnikov, J. Prahl, G. Pühlhofer, R. de los Reyes, W. Rhode, J. Ripken, G. Rowell, V. Sahakian, M. Samorski, M. Schilling, M. Siems, D. Sobzynska, W. Stamm, M. Tluczykont, V. Vitale, H. J. Völk, C. A. Wiedner, and W. Wittek, *Observations of H1426+428 with HEGRA. Observations in 2002 and reanalysis of 1999&2000 data*, A&A, 403:523–528, May 2003. [ADS].

[221] F. A. Aharonian, A. G. Akhperjanian, J. A. Barrio, K. Bernlöhr, H. Bojahr, I. Calle, J. L. Contreras, J. Cortina, A. Daum, T. Deckers, S. Denninghoff, V. Fonseca, J. C. Gonzalez, G. Heinzelmann, M. Hemberger, G. Hermann, M. Heß, A. Heusler, W. Hofmann, H. Hohl, D. Horns, A. Ibarra, R. Kankanyan, J. Kettler, C. Köhler, A. Konopelko, H. Kornmeyer, M. Kestel, D. Kranich, H. Krawczynski, H. Lampeitl, A. Lindner, E. Lorenz, N. Magnussen, H. Meyer, R. Mirzoyan, A. Moralejo, L. Padilla, M. Panter, D. Petry, R. Plaga, A. Plyasheshnikov, J. Prahl, G. Pühlhofer, G. Rauterberg, C. Renault, W. Rhode, A. Röhring, V. Sahakian, M. Samorski, D. Schmele, F. Schröder, W. Stamm, H. J. Völk, B. Wiebel-Sooth, C. Wiedner, M. Willmer, and W. Wittek, *The time averaged TeV energy spectrum of MKN 501 of the extraordinary 1997 outburst as measured with the stereoscopic Cherenkov telescope system of HEGRA*, A&A, 349:11–28, September 1999, arXiv:astro-ph/9903386. [ADS].

[222] T. M. Kneiske, K. Mannheim, and D. H. Hartmann, *Implications of cosmological gamma-ray absorption. I. Evolution of the metagalactic radiation field*, A&A, 386:1–11, April 2002, arXiv:astro-ph/0202104. [ADS].

[223] J. R. Primack, J. S. Bullock, and R. S. Somerville. *Observational Gamma-ray Cosmology*. In F. A. Aharonian, H. J. Völk, and D. Horns, editors, *High Energy Gamma-Ray Astronomy*, volume 745 of *American Institute of Physics Conference Series*, pages 23–33, February 2005. [ADS].

[224] A. Franceschini, G. Rodighiero, and M. Vaccari, *The extragalactic optical-infrared background radiations, their time evolution and the cosmic photon-photon opacity*, *ArXiv e-prints*, 805, May 2008, 0805.1841. [ADS].

[225] F. Aharonian, D. Khangulyan, and L. Costamante, *Formation of hard VHE gamma-ray spectra of blazars due to internal photon-photon absorption*, *ArXiv e-prints*, 801, January 2008, 0801.3198. [ADS].

[226] The MAGIC Collaboration, J. Albert, E. Aliu, H. Anderhub, L. A. Antonelli, P. Antoranz, M. Backes, C. Baixeras, J. A. Barrio, H. Bartko, D. Bastieri, J. K. Becker, W. Bednarek, K. Berger, E. Bernardini, C. Bigongiari, A. Biland, R. K. Bock, G. Bonnoli, P. Bordas, V. Bosch-Ramon, T. Bretz, I. Britvitch, M. Camara, E. Carmona, A. Chilingarian, S. Commichau, J. L. Contreras, J. Cortina, M. T. Costado, S. Covino, V. Curtef, F. Dazzi, A. De Angelis, E. De Cea del Pozo, R. de los Reyes, B. De Lotto, M. De Maria, F. De Sabata, C. Delgado Mendez, A. Dominguez, D. Dorner, M. Doro, M. Errando, M. Fagiolini, D. Ferenc, E. Fernandez, R. Firpo, M. V. Fonseca, L. Font, N. Galante, R. J. Garcia Lopez, M. Garczarczyk, M. Gaug, F. Goebel, M. Hayashida, A. Herrero, D. Hohne, J. Hose, C. C. Hsu, S. Huber, T. Jogler, T. M. Kneiske, D. Kranich, A. La Barbera, A. Laille, E. Leonardo, E. Lindfors, S. Lombardi, F. Longo, M. Lopez, E. Lorenz, P. Majumdar, G. Maneva, N. Mankuzhiyil, K. Mannheim, L. Maraschi, M. Mariotti, M. Martinez, D. Mazin, M. Meucci, M. Meyer, J. M. Miranda, R. Mirzoyan, S. Mizobuchi, M. Moles, A. Moralejo, D. Nieto, K. Nilsson, J. Ninkovic, N. Otte, I. Oya, M. Panniello, R. Paoletti, J. M. Paredes, M. Pasanen, D. Pascoli, F. Pauss, R. G. Pegna, M. A. Perez-Torres, M. Persic, L. Peruzzo, A. Piccioli, F. Prada, E. Prandini, N. Puchades, A. Raymers, W. Rhode, M. Ribo, J. Rico, M. Rissi, A. Robert, S. Rugamer, A. Saggion, T. Y. Saito, M. Salvati, M. Sanchez-Conde, P. Sartori, K. Satalecka, V. Scalzotto, V. Scapin, R. Schmitt, T. Schweizer, M. Shayduk, K. Shinozaki, S. N. Shore, N. Sidro, A. Sierpowska-Bartosik, A. Sillanpaa, D. Sobczynska, F. Spanier, A. Stamerra, L. S. Stark, L. Takalo, F. Tavecchio, P. Temnikov, D. Tescaro, M. Teshima, M. Tluczykont, D. F. Torres, N. Turini, H. Vankov, A. Venturini, V. Vitale, R. M. Wagner, W. Wittek, V. Zabalza, F. Zandanel, R. Zanin, and J. Zapatero, *Very-High-Energy Gamma Rays from a Distant Quasar: How Transparent Is the Universe?*, *Science*, 320(5884):1752–1754, 2008, http://www.sciencemag.org/cgi/reprint/320/5884/1752.pdf. [LINK].

[227] S. Razzaque, C. D. Dermer, and J. D. Finke, *The stellar contribution to the extra-galactic background light and absorption of TeV gamma-rays*, *ArXiv e-prints*, 807, July 2008, 0807.4294. [ADS].

[228] A. De Angelis, O. Mansutti, M. Persic, and M. Roncadelli, *Photon propagation and the VHE gamma-ray spectra of blazars: how transparent is really the Universe?*, *ArXiv e-prints*, 807, July 2008, 0807.4246. [ADS].

[229] F. W. Stecker and S. T. Scully, *Is the Universe More Transparent to Gamma Rays Than Previously Thought?*, *ArXiv e-prints*, 807, July 2008, 0807.4880. [ADS].

[230] F.E. Roach and Janet L. Gordon. *The Light of the Night Sky*, volume 4. D. Reidel Publishing Company, Dordrecht, Holland, 306 Dartmouth Street, Boston, Mass. 02116, U.S.A., cloth edition, 1973.

[231] S. Preuss, G. Hermann, W. Hofmann, and A. Kohnle, *Study of the photon flux from the night sky at La Palma and Namibia, in the wavelength region relevant for imaging atmospheric Cherenkov telescopes*, *Nucl. Instrum. Meth.*, A481:229–240, 2002, astro-ph/0107120.

[232] Jean-Phillipe Gagnon. *An instrument to study the photon flux from the night sky in the wavelength region relevant for atmospheric Cherenkov telescopes*. Master's thesis, McGill University, September 2005.

[233] LeCroy Research Systems Corporation. *CAMAC Model 2249W 12 Channel Analog-to-Digital Converter*. 700 South Main Street, Spring Valley, N.Y. 10977, 1984.

[234] Edmund Optics. *Metric Sized Narrow Bandpass Interference Filters*. http://www.edmundoptics.com/onlinecatalog/displayproduct.cfm?productID=1903, 2006.

Web Sites

Author's home page http://www.physics.mcgill.ca/~vluis/
VERITAS http://veritas.sao.arizona.edu/
McGill VERITAS http://www.physics.mcgill.ca/~veritas/
H.E.S.S. http://www.mpi-hd.mpg.de/hfm/HESS/HESS.html
MAGIC http://magic.mppmu.mpg.de/
CANGAROO http://icrhp9.icrr.u-tokyo.ac.jp/
CANGAROO III http://icrhp9.icrr.u-tokyo.ac.jp/c-iii.html
HEGRA http://www-hfm.mpi-hd.mpg.de/CT/CT.html
CLUE http://www.pi.infn.it/clue/
CAT http://lpnp90.in2p3.fr/~cat/index.html
STACEE http://www.astro.ucla.edu/~stacee/
CACTUS http://ucdcms.ucdavis.edu/solar2/
Milagro http://www.lanl.gov/milagro
GAW http://gaw.iasf-palermo.inaf.it/
ARGO http://argo.na.infn.it/
Tibet AS-gamma http://www.icrr.u-tokyo.ac.jp/em/index.html
HiRes http://hires.physics.utah.edu/
Auger http://www.auger.org/
TeVCat: Online catalog for TeV Astronomy http://tevcat.uchicago.edu/
GCN http://gcn.gsfc.nasa.gov/
CGRO http://heasarc.gsfc.nasa.gov/docs/cgro/index.html
GLAST http://glast.gsfc.nasa.gov/